Alma Mater Studiorum – Università di Bologna

DOTTORATO DI RICERCA IN

Ingegneria Civile, Chimica, Ambientale e dei Materiali

Ciclo XXXI

Settore Concorsuale: 03/B2

Settore Scientifico Disciplinare: CHIM/07

Design of new biopolymers for biomedicine and food-packaging

Presentata da: Giulia Guidotti

Coordinatore Dottorato

Prof. Luca Vittuari

Supervisore

Prof. ssa Nadia Lotti

Co-supervisore

Dott. ssa Michelina Soccio

Esame finale anno 2019

Abstract

The limited fossil fuels reserves, as well as serious pollution problems, have led to a continuously growing interest in the use of sustainable materials obtained from renewable sources for many different applications. Among these materials, biopolymers, and in particular the class of biopolyesters, could potentially replace traditional plastics. Their versatility and their ability to undergo degradation in the environment where they are disposed, is of particular interest both for food packaging (when recycling is not possible due to organic matter contamination as well as multi-layered structures) and for biomedicine, in case of temporary applications, such as controlled drug release or tissue engineering. If these materials hydrolyse in the human body, it is possible to avoid the removal of the implant through surgery.

In this framework, aim of the present research project was the synthesis and characterization of new bio-based and biodegradable polyesters and copolyesters, with tailored properties in relation to the intended use, in the fields of food packaging, which is one of the most demanding in terms of plastic sources, and regenerative medicine, as it represents the new frontier of biomedicine. The synthetic routes adopted (i.e. two-step melt polycondensation, ring opening polymerization and chain extension) are solvent-free, simple and economic, and can be easily used for industrial scale-up. Monomers from renewable sources were preferred over the ones obtained from fossil fuels.

Moreover, copolymerization turned out to be a winning strategy to modify the polymers of interest. Starting from polyesters, the aliphatic (i.e. polylactic acid, poly(butylene succinate), polymers containing cyclohexane ring) and aromatic ones (i.e. polymers containing furan and thiophene rings), all characterized by high stiffness and low degradation rates, it was possible to obtain more flexible materials with higher biodegradation rates, particularly suitable for soft tissue engineering and for the realization of flexible food packaging films.

For all these materials, after the solid-state and mechanical characterization, biodegradability and biocompatibility was checked for the first kind of applications, while barrier properties and compostability were evaluated in the latter case.

Table of Contents

1.INTRODUCTION

1.1 A brief history of plastics

The widespread use of plastic in everyday life makes it hard to believe that it entered the scene for the first time in 1856, when the English metallurgist Alexander Parkes invented Parkesine, the first man-made plastic, derived from cellulose [British Plastics Federation].

The real success of plastics started in the 20th century, when materials like Bakelite (1907), Cellophanne (1908), Polyethylene (1933) and Nylon (1935) were invented. During the II World War, large scale plastic production was started for military purposes, like gunner's enclosures, cockpit windows, mortar fuses, helmet liners, goggles, raincoats, waterproof tents and parachutes. It was only after the II World War that the production potential exploded into consumer market. Plastics were employed for textiles, packaging, toys, furniture and domestic uses: Nylon stockings, Polyethylene (PE) bags, Polyethylene Terephthalate (PET) bottles, Lego made of cellulose-acetate and Barbie dolls appeared for the first time on the market [British Plastics Federation].

Starting from this moment, synthetic polymeric materials have become progressively one of the most important domains in the field of materials science. The '60s saw the definitive affirmation of plastic as an irreplaceable instrument of everyday life and as a "new frontier", also in the fields of fashion, design and art. During the following decades, the development of the high-performance plastics (such as polymethylpentene, polyimides, ionomers, polysulfones, …) led to their progressive affirmation for increasingly sophisticated applications in the fields of informatics, electronics, biomedicine and nanotechnologies. For example, cars and aircrafts engine components, helmets for astronauts, items for clinical laboratories, prosthetic parts, music devices, bulletproof shields, solar cells components and flexible screens, are nowadays commonly produced starting from polymers.

1.2 Worldwide production of plastics

Synthetic polymers have become the key materials in every aspect of everyday life and industrial production (i.e. packaging, buildings, transportation, renewable energy, medical devices), thanks to their low cost, reproducibility, versatility, and their resistance to physical aging and biological attacks. Moreover, they are lightweight, easily workable with low energy consumption (for example, a temperature of about 1000 ° C is needed to produce a glass bottle,

while a temperature of 250 ° C is enough to produce a plastic bottle) and, last but not least, they can be quite easily collected and recycled [Vert et al., 2005] (Figure 1.1).

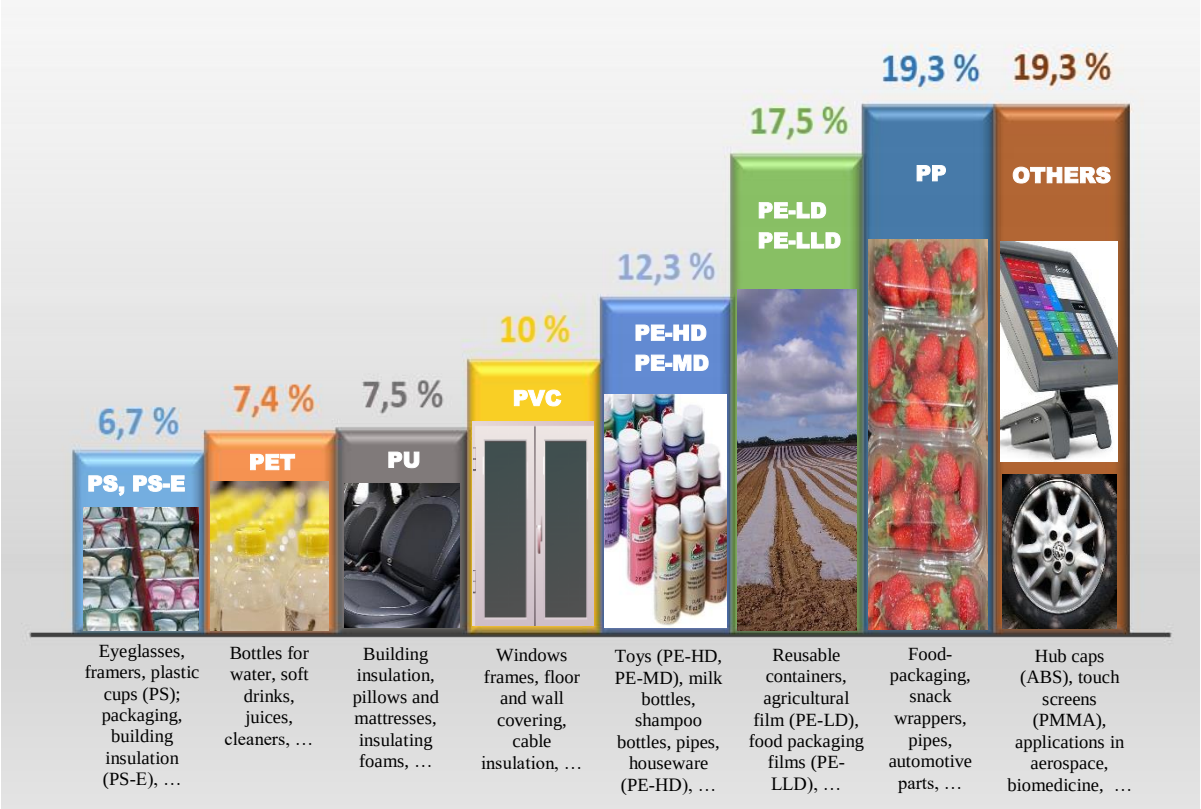

Figure 1.1. European plastics demand by polymer type in 2016.
Source: Plastic Europe

It is therefore not surprising that in 2016, around 335 million tons of plastics have been produced worldwide, and 60 million tons only in Europe. These values include thermoplastics, thermosets, polyurethanes, adhesives, coatings and sealants (PET, polyamides PA, PP and polyacrylic fibers are not included) [Plastics – the Facts 2017]. The main market sector in which plastics are used is packaging, followed by construction, automotive and electronics (Figure 1.2).

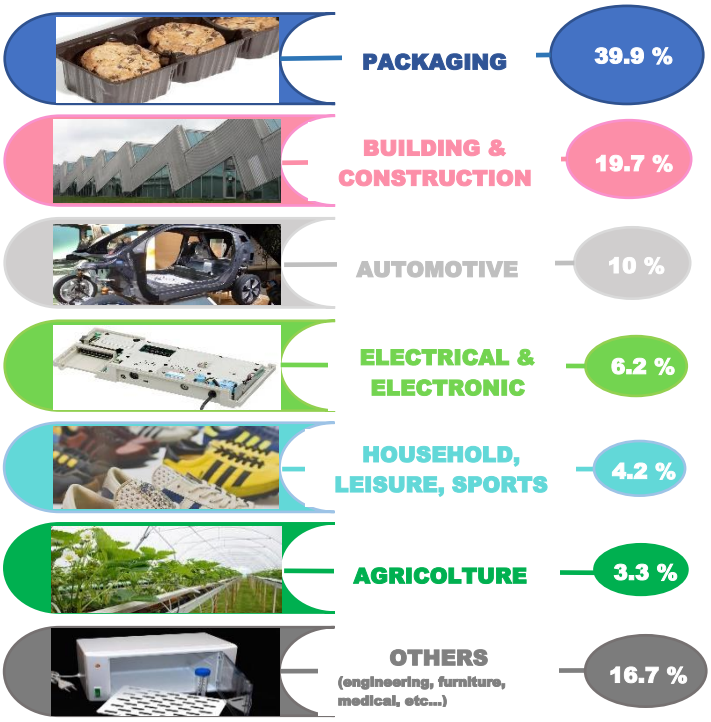

Figure 1.2. European plastics demand by segment in 2016.
Source: Plastic Europe

1.3 Environmental impact

Not all plastic products have the same shelf life: for some of them it is less than one year, for some others it is more than 15 years, and some persist in the environment for 50 years or even more.

Only in 2016, 27.1 million tonnes of plastic waste were collected in Europe, but for the first time more plastic waste was recycled than landfilled (Figure 1.3) [Plastics – the Facts 2017]. The main source of plastic waste is represented by packaging, with 16.7 million of tonnes (around 62%), an application whose growth was accelerated by a global shift from reusable to single-use containers [Geyer et al., 2017].

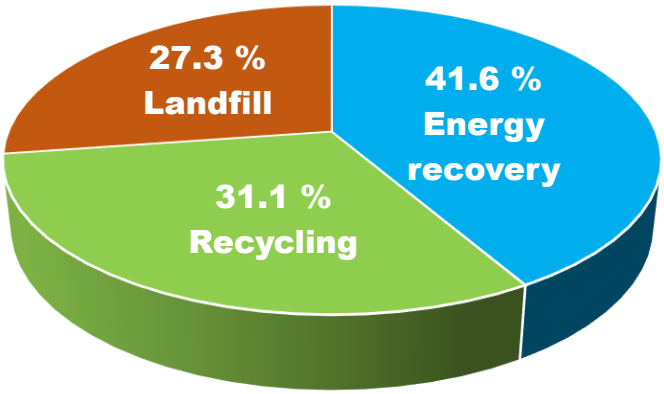

Figure 1.3. Treatment for post-consumer plastics waste in Europe.
Source: Plastic Europe

As regards plastic waste treatment, in ten years, from 2006 to 2016, recycling increased by 79%, energy recovery increased by 61% and landfill decreased by 43%. Even though these data are very promising, it is also true that in many southern and eastern European countries landfill is still the first solution.

The extended and intensive use of plastics has caused environmental pollution problems due to the dispersion of littering in both the land and the aquatic environment. Moreover, the useful plastic properties, such as durability and low density, represent a big problem when plastic waste is inappropriately handled, creating relevant environmental threat. Plastics indeed persist in the environment for many years because of their durability, while their low density determines the easy dispersion by water and wind, sometimes travelling thousands of kilometres from source areas [Ryan et al.,2009]. As a result, plastic wastes are now ubiquitous pollutants, even on the most remote areas of the planet: floating macro- and microplastics islands can be found for example in the Mediterranean Sea, in Southwest England, in the Atlantic, Pacific and Indian Oceans, in the Southern Korean coasts, in the Black Sea and near the Arctic Circle (Figure 1.4) [Ioakeimidis et al., 2017]. As an example, the so-called "Great Pacific garbage patch", which is the biggest accumulation of ocean plastic in the world, located between California and Hawaii, has an extension of 1.6 million square kilometres and contains about 80,000 metric tons of plastic [Lebreton et Al., 2018].

Living organisms, in particular marine animals, can also be affected by entanglement, direct ingestion of plastic waste, or by exposure to chemicals within plastics that cause interruptions in their biological functions.

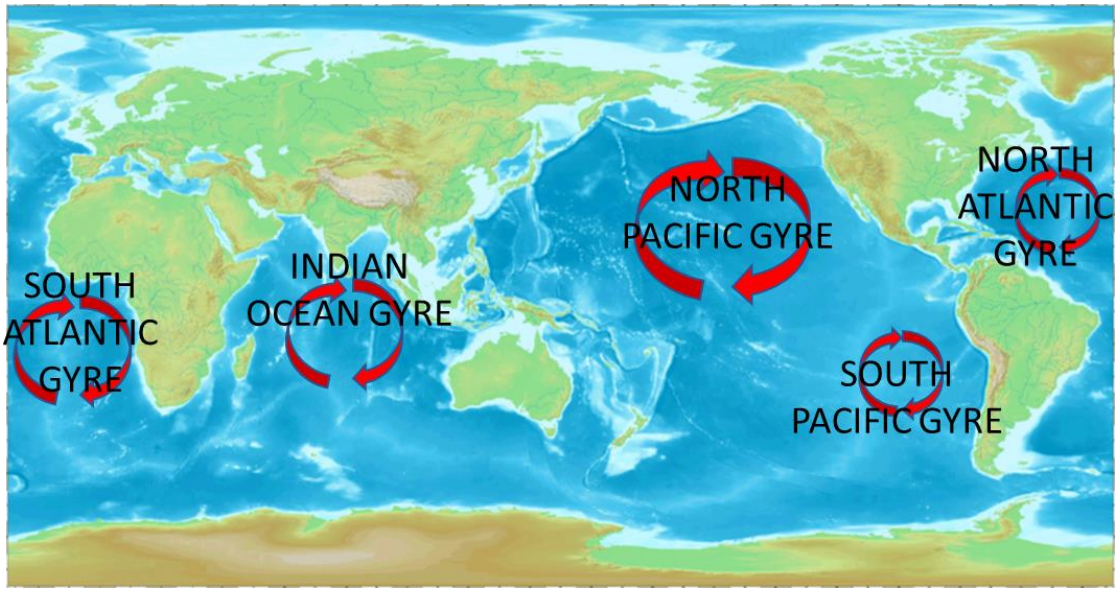

Figure 1.4. Garbage islands world map.
Source: National Geographic

Considering this alarming situation, there are many actions aimed to get the public opinion more aware of this crucial problem. For example, if we consider only this year, the Earth Day was focused on plastic pollution, the organization Plastic Change has promoted the World Clean Up Day [Plastic Change, 2018] against the accumulation of plastic bags in the environment, and in July there was also the International Plastic Bag Free Day [A plastic Bag Free World, 2018]. Moreover, over the last 30 years, the European Union has developed a long-term waste management policy consisting of a series of legislations that aims to reduce environmental and health impacts and create a recycling and resource-efficient economy [Being wise with waste: the EU's approach to waste management, 2010]. The 2008/98/EC Directive introduced a multi-step hierarchy, which classifies the different waste treatment strategies (prevention, re-use, recycling, other forms of recovery and landfill) according to their ability to preserve the limited fossil resources (Figure 1.5).

Figure 1.5. European waste hierarchy.

Source Brochure: Being wise with waste: the EU's approach to waste management, 2010

1.4 Bioplastics

One of the possible strategies that can be adopted to limit pollution problems, preserving in the same time the limited amount of fossil fuels, is the use of bioplastics as alternative to the petrol-based ones. According to the *European Bioplastics Association*, the word "Bioplastics" includes a family of materials, which can be divided in three different categories (Figure 1.6):

- Bio-based but not degradable materials (i.e. bio-PE and bio-PET) [Nakajima et al., 2017];
- Biodegradable materials obtained from non-renewable sources (i.e. poly(butylene adipate terephthalate) PBAT and polycaprolactone PCL);
- Bio-based and biodegradable materials (polylactic acid PLA, polyhydroxyalkanohates PHA, poly(butylene adipate) PBA, poly(butylene succinate) PBS and poly(ethylene furanoate) PEF).

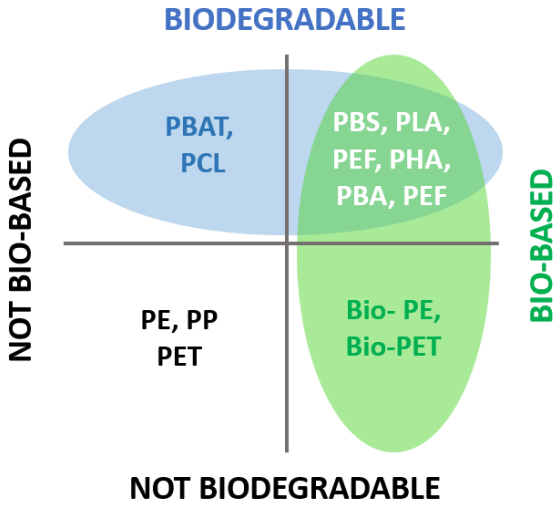

Figure 1.6. Bioplastic categories.
Source: European Bioplastics

Another classification considers their productive process:

- Replacement of traditional plastics with natural biopolymers such as starch, chitin, chitosan and their derivatives;
- Replacement of traditional plastics with polymers obtained by genetically modified bacteria and microorganisms (*Bacillus*, *Rhodococcus* and *Pseudomonas*), such as polyhydroxyalkanohates;
- Use of monomers obtained from renewable sources for polymer synthesis (this is the case of poly(ethylene 2,5-furanoate), PEF).

These materials show properties similar to those of petrochemical-based plastics and can also be manufactured and processed with the same technologies. Nevertheless, they present many advantages, like (a) a cleaner production chain, (b) the lowering of waste management costs, (c) the reduction of dependence on fossil resources, which are not limitless and whose price is subjected to continuous and uncontrolled fluctuations, (d) the decrease of greenhouse gases and toxic fumes (in case of incineration) emissions and (e) the increase of source efficiency, in particular if bioplastics are recycled or used for energy recovery, in order to support the development of a circular economy.

Moreover, biodegradable polymers disposed in the environment can undergo degradation by the action of microorganisms or by hydrolysis. Thanks to these processes, they can be easily converted to CO_2, CH_4, water, biomass and other natural substances. For this reason, they can

be buried in soil or incorporated into the organic waste stream, all together with organic waste, unlike traditional plastic bags, which need to be separated from organic waste through several time consuming and expensive processes.

In this way, biodegradable plastics represent not only a cost-effective disposal solution, but can also give an important contribution to efficient management of organic waste. The principal applications for biodegradable plastics include packaging materials (trash bags, food containers, film wrapping, laminated paper), hygiene products (diaper back sheets, cotton swabs), consumer goods (fast-food tableware, containers, egg cartons, toys), and agricultural tools (mulch films, pots). [Gross et al., 2002; Siracusa et al., 2008]. On the other hand, a considerable number of bioplastics derives from wheat, corn, sugar cane and rice, which are first and fore most foodstuffs. In addition, it has to be taken into consideration that biomass-based products are not *per se* ecologically or economically more efficient than a petrochemical-based one: for example, if processes that consume high quantities of energy are needed to refine the biomass, or the costs for refining biomass are higher than those of oil, benefits can easily become issues. For these reasons, Life Cycle Assessments (LCAs) studies must be conducted, taken into consideration also ethical and moral aspects.

Anyway, although nowadays the global production capacity of biopolymers is only 2.05 million tons per year (about 1% of total production), their market is rapidly growing, thanks to European Union directives and to a greater awareness of public opinion and governments towards environmental preservation.

It is expected that production, which in 2017 was 2.05 million tonnes, will exceed 2.44 million tonnes in 2022 (Figure 1.7) [European Bioplastics, 2017].

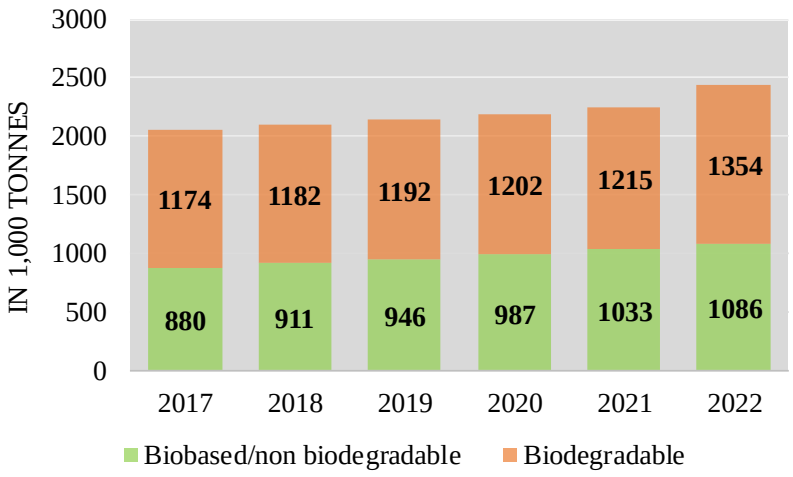

Figure 1.7. Global production capacities of Bioplastics.
Source: European Bioplastics, nova-Institute (2017)

Among biodegradable polymers, PBS, PLA and PHA are the main drivers of this growth, while between bio-based and not biodegradable polymers, bio-based PE, bio-based PET, and bio-based PA currently make up for around 57 percent (1.2 million tonnes) of the global bioplastics production capacities (Figure 1.8).

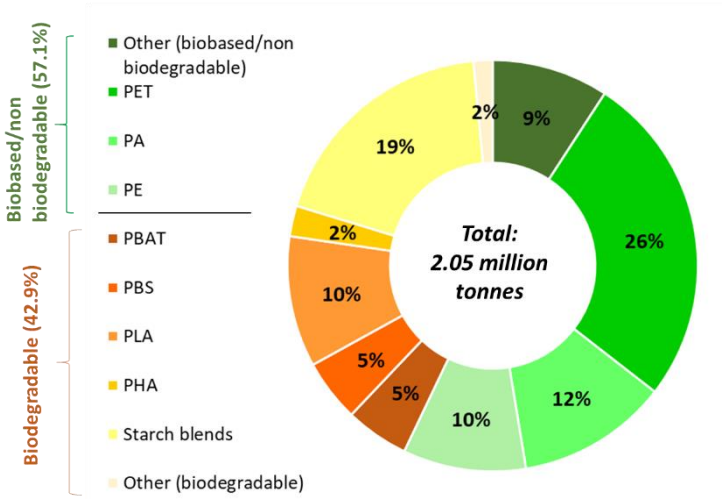

Figure 1.8. Global production capacities of Bioplastics in 2017 by material type.
Source: European Bioplastics, nova-Institute (2017)

1.5 Polyesters

Polyesters are a class of polymers containing ester functional groups along the main chain. They are generally obtained from polycondensation between one or more diacids (or diesters) and one or more diols.

It is a class of extremely versatile materials characterized by interesting properties. The relatively easily accessible raw materials, a great variety of composition, simple synthetic approaches, processability and workability even in complex shapes, the possibility to chemically and/or physically modify the surface and possibility to immobilize biomolecules inside them, make them very interesting candidates, despite some limitations given by the presence of low molecular weight substances, that can be released in the environment (monomers, catalysts, additives, etc.) and the easy absorption of water and biomolecules from

the surroundings (even in applications where it is not required). As just mentioned, it is possible to easily adapt their properties *ad hoc* depending on the intended use.

For these reasons, polyesters are used for the large-scale production of items, like bottles, bags, films, packaging, insulating films and tapes, as well as for more specific applications as parts of electronic components, biomedical devices, technical clothing.

1.5.1 Aliphatic polyesters

Aliphatic polyesters are polymers, which contain the ester functional group along the main chain (Figure 1.9).

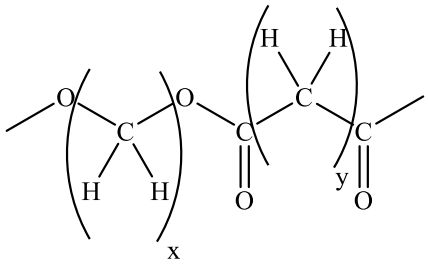

Figure 1.9. General structure of aliphatic polyesters.

They were synthesized for the first time in 1928 by the American chemist Wallace Carothers and his research group at DuPont, who started building up polymers by reacting small organic molecules through well-known reactions (for example, by combining dicarboxylic acids with diols or diamines) to form long macromolecular chains [Carothers, 1931]. From that time onwards, systematic studies to understand the formation and the properties of aliphatic polycondensated polyesters were carried out. These investigations led to determination of the "Carothers equation", which relates the conversion degree of functional groups with the average degree of polymerization of the resulting polyester. Further studies conducted by the American chemist Paul Flory improved the knowledge about the kinetics of polyesterification and polyester molar mass distribution. At the beginning, only low molecular weight materials (4000 g/mol), with poor thermal properties and high sensitivity to humidity were obtained; this caused a strong delay in the development of this class of polyesters. Recently, both academic and industrial research has focused its attention on them, thanks to their very good mechanical properties, biodegradability and biocompatibility. Moreover, great importance is given by the fact that some monomers, including dicarboxylic acids like adipic, succinic, sebacic, azelaic

acid and fatty acids, and diols like 1,3-propanediol, 1,4-butanediol, 1,3-butanediol, 1,10-decanediol can be obtained from renewable sources by fermentation of vegetable oils or sugars [Novamont, 2016; Ma et al., 2012; Wu et al., 2014; Zhu et al., 2013; Gomes et al., 2011; Díaz et al., 2014].

Nowadays, aliphatic polyesters are one of the most important classes of synthetic biodegradable polymers: pharmaceutics, medical and biomedical engineering (including drug delivery systems and functional materials in tissue engineering), soft and degradable packaging are just some of the fields in which these materials are intensively used.

Biodegradable aliphatic polyesters can be found in nature, synthesized by some types of microorganisms, like polyhydroxyalkanoates (PHAs), or can be obtained by chemical synthesis, like poly(butylene succinate) (PBS), poly(lactic acid) (PLA) and Poly(alkylene 1,4-cyclohexanedicarboxilate)s [Okada, 2002]:

- polyhydroxyalkanoates (PHAs) like poly(3-hydroxybutyrate) (P(3HB)), poly(3-hydroxyvalerate) (P(3HV)) and their copolymers poly(hydroxybutyrate-valerate) (PHBV), can be enzymatically produced from bacteria by feeding them with sugar or other nutrients such as alcohols, alkanes or alkenes (Figure 1.10). P(3HB), for example, shows properties comparable to those of polyethylene and polypropylene. Its brittleness and stiffness can be lowered through copolymerization with P(3HV), by choosing the proper microorganisms. Several companies (Meredian, Tianan Biologic Materials, PolyForm Canada, …) are producing PHAs by microbial fermentation, but their applications, for instance in the fields of agriculture, food services, packaging and biomedicine are still limited because of the high costs, related to the high raw material and processing costs, difficult extraction and purification procedures, small production volumes. Moreover, production of PHAs generates a large amount of biomass waste: about 5 kg of raw material is required to obtain only 1 kg of final product. [Kootstra et al., 2017].

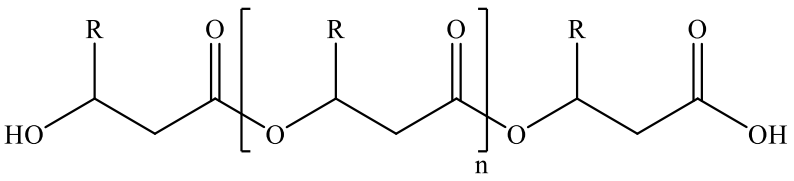

Figure 1.10. Chemical structure of PHAs.

- Poly(butylene succinate) (PBS), which is one of the most important aliphatic polyester (Figure 1.11) obtained by melt polycondensation of succinic acid SA (or dimethyl succinate DMS) and 1,4-butanediol, using titanium (IV) butoxide as catalyst.

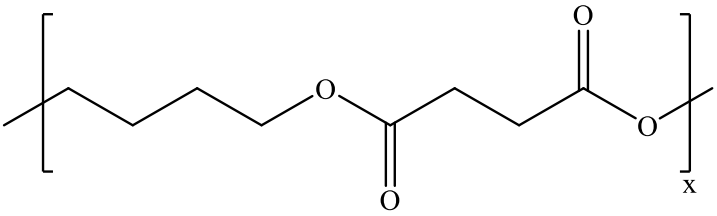

Figure 1.11. Chemical structure of PBS.

This material was synthesized for the first time in 1863 by the Portuguese Agostinho Vicente Lourençoche [Lourenço, 1863]. In the '30s, Carothers began to study succinic acid-based polyesters, obtaining PBS with a molecular weight significantly higher than that obtained up to then (around 5000g/mol), but still without the characteristics required for the market [Carothers, 1929]. Thanks to the use of new catalysts, together with the growing interest in bio-based polymers, the interest for this material grew again in the 1990s, when high molecular weight PBS was obtained: its good thermal and mechanical properties, comparable to those of LDPE and PP, ensured good workability and processability.

In 1993, Showa Denko [Showa Denko] put on the market the first bio-based PBS (Bionolle^{TM}), with a molecular weight of 40'000-100'000g/mol. This material found a wide range of applications including packaging and mulching films, envelopes and bottles, but also in electrical and aerospace engineering. Thanks to its biocompatibility, PBS finds also potential applications in biomedical field as implants, scaffolds for tissue engineering and drug delivery systems.

Nowadays, the principal producers of bio-based PBS are MCPP (Mitsubishi Chemical) [Mitsubishi Chemical], Showa Denko, with brand names BioPBS, GS PLA and Bionolle.

As regards monomers, the conventional production of SA is based on petrochemical products like n-butane or butadiene: first, butane is oxidized to produce maleic anhydride; then maleic anhydride undergoes catalytic hydrogenation to become succinic anhydride, which is further hydrogenated to obtain SA.

However, recent developments in glucose source fermentation and in purification technologies have made bio-based SA so economically attractive that bio-based production has surpassed the conventional one and the US department of energy has included SA among the first 12 value-added bio-based chemicals [Werpy et al., 2004]; the market of bio-based SA is predicted to reach over 699 million tons by 2020. Bio-based succinic acid is produced through fermentation processes, by yeasts and bacteria able to metabolize many C5 and C6 sugars as well as their derivatives, like lignocellulose. Despite fermentation processes require large volumes, longer reaction times, and only low yields are achieved, a decrease in production costs is expected in the short term. Regarding this point, BioAmber has already started the production of high-purity bio-SA from sugar beet and wheat, in France (2010) and in North America (2013), and new plants in Thailand, North America and Brazil, will be established [Domínguez de María, 2016]. Bio-based succinic acid is already produced also by Myriant [Myriant Corporation], from lignocellulose, by Revedia, starting from starch, through a fermentation process (Biosuccinium), and by BASF, in a joint venture with Corbion, by the action of micro-organism *Basfia succiniproducens*, using glycerol as substrate (Succinity).

Also 1,4-butanediol, which is conventionally petrochemically obtained from maleic anhydride, can be obtained from renewable sources for example by catalytic hydrogenation of bio-based SA. Regarding this point, BioAmber is producing BDO and THF green, while Novamont, in a joint venture with Genomatica, has created the first industrial plant in the EU for BDO production through fermentation [Bikiaris et al., 2008 (a); Howe-Grant M., 1991; Yield10 Bioscience; Ihn et al., 1995].

The success of PBS as thermoplastic material is strictly due to its properties. PBS is a semi-crystalline polymer (crystallinity degree around 35-45%), with a melting temperature of 110-130°C, one of the highest among poly(alkylene dicarboxylate)s [Yoo et al., 1999] and a glass transition temperature between -34 and -15°C [Zhihua et al., 2001]; melt crystallization is possible between 70 and 95°C. High molecular weight PBS synthesized without chain extenders shows a brittle behaviour, moderate stiffness (Young's modulus of about 300-500 MPa) [Xu et al., 2010; Gualandi et al., 2012 (a)], with very short elongation at break [Gigli et al., 2012 (a)]. The incorporation of urethane bonds through the use of isocyanates improves its elongation [Fabbri et al., 2014], up to

values comparable to those of polyolefins [Fujimaki, 1998]. Thanks to the possibility of being attacked by microorganisms and to the susceptibility even to abiotic degradation, bio-PBS has been proved to be fully compostable, according to the standard tests EN13432, US, BPI and OK-Compost.

- Poly(lactic acid) (PLA) is a thermoplastic and biodegradable polyester (Figure 1.12) which is obtained, mainly, through Ring Opening Polymerization (ROP), starting from lactide ring, the cyclic ester of lactic acid, and catalysed by heavy-metal-based catalysts (zinc and stannous oxides, zinc and tin chlorides or stannous octanoate). Another synthetic approach is Lactic acid condensation, in solution or in the melt, but this route is usually not preferred because of low molecular weight and brittleness of the polymers obtained [Lasprilla et al., 2012].

  The synthesis of polyesters from lactic acid was started by Carothers in 1932 and further developed by DuPont and Ethicon [Gross et al., 2002].

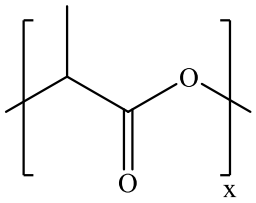

Figure 1.12. Chemical structure of PLA.

Thanks to its workability by injection moulding, extrusion, blowing and thermoforming, as well as its excellent biodegradability and biocompatibility, it was studied for the first time in 1971 as a potential material for controlled drug release. The extremely high production costs limited the applications of PLA only to biomedicine until the 1980s. Since then, the developments in process technology, together with a decreasing in the cost of biologically produced lactic acid, have led to the production of this kind of plastic also for other applications. One of the principal fields is still biomedicine, as a material for bioresorbable sutures, orthopedic fixation devices, temporary porous supports for the regeneration of tissues like bones, cartilages, tendons and nerves [Pawar et al., 2014]. Thanks to its good barrier performances, PLA is widely used also in food packaging to produce biodegradable cups, bottles and films. Other fields of application are agriculture (mulching and sawing films), gardening (pots that can be directly planted

in soil), automotive (light car parts) [Mazollier et al., 2003; Lammers et al., 2002] and buildings (non-flammable insulation).

Thanks to the growing interest on renewable sources, the microbial fermentative production of lactic acid has considerably increased. Bio-based Lactic acid can be obtained from the fermentation of sugars (dextrose, glucose and sucrose) present in maize flour, sugar beets, cellulose, lignin, wheat starch or potatoes. In order to limit the cost of raw materials, food and agro-industrial by-products or residues could be used as cheaper alternative, thanks to the action of selected microorganisms [Madhavan Nampoothiri et al., 2010]. Currently the total production capacity of PLA in the world is about 180,000 tonnes and the leading producers are the United States, Japan and Germany. The American company Nature Works is the world's largest PLA manufacturer (Ingeo), with an annual capacity of 140,000 tonnes. Other distributors are BASF, Corbion, SK Chemicals, Futerro, Synbra, Hisun, and the brand names are Purac, Ecovio, Luminy, EcoPlan, Futerro PLA and BioFoam, respectively.

PLA is also biodegradable by hydrolysis, recyclable and compostable (EN13432) [EN 13.432, 2005]. In the human body, at physiological temperature around 37 °C, it may be degraded in vivo in 2–3 years, while in composting conditions, where temperatures reached are up to 70 °C, times are much shorter [Vert, 2005]. Its sustainability and eco-friendly characteristics, together with the decreasing in production costs, will soon make PLA one of the most eye-catching biopolymer worldwide [Sangeetha et al., 2016].

Because of its chiral nature, Lactic acid exists in three different forms, L,L-LA, D,D-LA, and D,L-LA (*meso*) as well as a 50/50 mixture of L,L-LA and D,D-LA (*racemic lactide*), reported in Figure 1.13. Bio-based LA contains both D and L forms, but the L-form is predominant [Hamad et al., 2015].

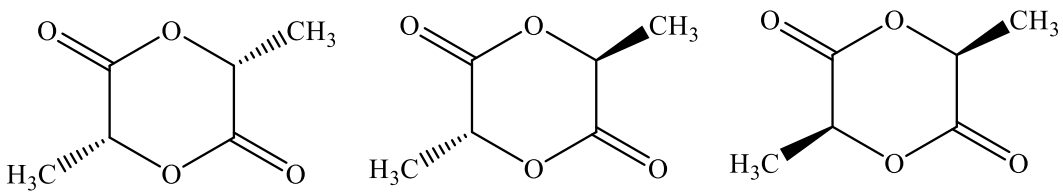

Figure 1.13. Chemical structures of LL-, meso- and DD-Lactides.

PLA material properties depend on many factors like the isomer type (D-, L-, DL-lactide), processing temperature and molecular weight. The stereochemical composition

has a strong effect upon the melting point and on the polymer crystallization ability [Chen et al., 2012]: PLLA crystallinity index is around 37%, glass transition temperature between 50 and 80 °C and melting temperature between 173 and 178 °C. The introduction of meso-lactide or D-lactide into PLLA reduces all these parameters apart from the glass transition temperature [Drumright et al., 2000]. As to mechanical properties, commercial PLA (i.e. 92% L-lactide, 8% meso-lactide), has a Young's modulus of 2.1 GPa and an elongation at break of 9%. After plasticization, the former decreases to 0.7 MPa and the latter rises to 200%. By varying the crystallinity degree of the polymer, it is also possible to modulate its degradation rate: the higher the crystallinity degree, the lower the biodegradability.

- Poly(alkylene 1,4-cyclohexanedicarboxylate)s are a very interesting class of aliphatic polyesters, characterized by the presence of a cyclohexane ring along the macromolecular chain. This ring increases the rigidity of the chains, as well as the thermal stability, which is even higher than that of their aromatic counterparts [Berti et al., 2008 (a); Berti et al., 2008 (b); Genovese et al., 2015], maintaining at the same time the biodegradability typical of aliphatic polyesters [Gigli et al., 2014 (a)]. Moreover, their good resistance to heat, light, and humidity make them particularly promising for packaging applications.

  This kind of polymers were studied since the early 1980s by Eastman Chemical Company, thanks to their high tensile strength, stiffness and impact properties.

  Even though 1,4-cyclohexane dicarboxylic acid is now obtained from non-renewable sources, it can be potentially obtained from bio-based terephthalic acid, starting from limonene and other terpenes [Berti et al., 2010]. Both *trans* and *cis* configurations of the aliphatic ring are possible (Figure 1.14) and stereochemistry strongly affects the final properties of the material: the *trans* stereoisomer is less flexible and more symmetrical than the *cis* one, favouring chain packing, and consequently the capacity of the polymer to crystallize [Berti et al., 2008 (a); Berti et al., 2008 (b)]. On the other hand, if the *trans* content is decreased, these properties are significantly reduced. According to a study on the influence of the *cis*/*trans* ratio on solid state properties, only polymers containing more than 70% of *trans*-cycles are able to crystallize, while polymers containing

considerable amounts of *cis*- stereoisomers (50-80%) are unable to organize themselves in an ordered state, remaining completely amorphous [Ihn et al., 1995].

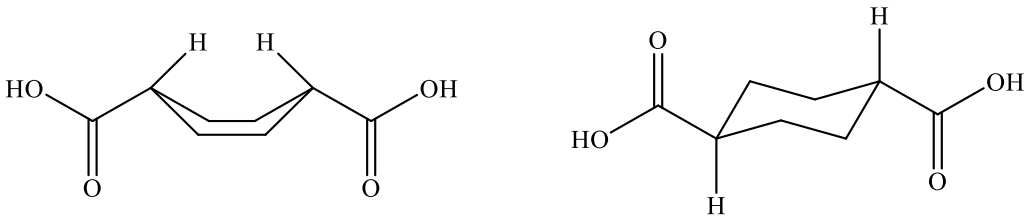

Figure 1.14. *cis*- and *trans*- configurations of 1,4-cyclohexanedycarboxylic acid.

Even though poly(alkylene 1,4-cyclohexanedicarboxylate)-based polymers have not been yet explored for industrial applications, recent studies [Guidotti et al., 2018 (a); Siracusa et al., 2018; Gigli et al., 2013 (a)] have shown interesting barrier properties to different gases and in some cases at different temperatures and humidity, which make them particularly promising for packaging applications.

1.5.2 Aromatic polyesters

Aromatic polyesters are characterized by the presence of one or more benzene rings along the main chain.

As it is well known, the use of aromatic polyesters, both in the forms of films and fibres, is preferred for those applications which require excellent physical-mechanical stability.

Among these, terephthalic polyesters (Figure 1.15) are the most produced; the main components of this family are:

- Poly(ethylene terephthalate) (PET), obtained through two-step melt polycondensation reactions between terephthalic acid (TPA) and ethylene glycol (EG), using Pb and Zn acetates or titanium alkoxides as catalysts [Marsh et al., 2007]. Fibres for clothing, bottles, containers, supports for electronics and many other items are produced with PET. Crystalline PET is also used as thermoplastic material for applications in the automotive, in the electric and electronic fields.
- Poly(propylene terephthalate) (PPT), obtained by two-step melt polycondensation as well, using propylene glycol (PG) instead of EG, and titanium alkoxides as catalysts. PPT fibres have proven to be significantly more performing than PET ones, in terms of

mechanical properties (i.e. fracture resistance). The fields of application of PPT are therefore different, as they include production of textile fibres, ropes for musical instruments, umbrellas, clothing, food packaging and artificial leather.

- Poly(butylene terephthalate) (PBT), obtained by polycondensation in the melt starting from TPA and 1,4-butanediol (BD) and using titanium alkoxides as catalysts. Thanks to its high resistance to chemical agents, good stability at high temperatures, good hardness and surface shine, this polymer has found its greatest application in the field of precision materials for electrical and electronic parts, for household and automotive parts.

During last years, aromatic polyesters based on 2,5-furandicarboxylic acid (FDCA) have been synthesized, as bio-based counterparts of terephthalic polymers [Sousa et al., 2015]. The only difference in their structure is the presence of furan ring instead of the benzene one (Figure 1.16).

FDCA has been polymerized with many different glycols [Papageorgiou et al., 2016] like ethylene glycol [Gomes et al., 2011; Matos et al., 2014; Codou et al., 2015; Avantium], 1,3-propanediol [Gomes et al., 2011] and 1,4-butanediol [Wu et al., 2014; Zhu et al., 2013; Ma et al., 2012; Gopalakrishnan et al., 2013; Soccio et al.,2016].

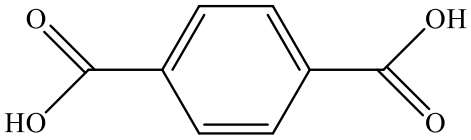

Figure 1.15. Chemical structure of terephthalic acid TFA.

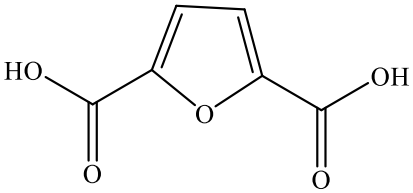

Figure 1.16. Chemical structure of 2,5-furandicarboxylic acid FDCA.

As regards the diacid part, FDCA can be obtained from renewable sources in many different ways, for example starting from cellulose or hemicellulose through a multistage process that includes bioconversion, dehydration and oxidation, in which a hexose and 5-

hydroxymetifurfural are important intermediates [Wu et al., 2012]. In order to obtain 5-hydroxymethylfurfural, glucose or fructose can also be dehydrated [Melo et al., 2014].

As regards the glycolic sub-units, ethanol from renewable sources was introduced on the market a few years ago: for example, Novepha [Novepha] produces from renewable sources ethylene glycol, 2,3-butanediol and propanediol. Moreover, the first plant for industrial scale production of bio-butanediol was started up in 2014 in Adria, by Novamont [Novamont e Genomatica alleati nel bioBDO, 2011].

The most important furan-based aromatic polyesters are:

- Poly(ethylene furanoate) (PEF), obtained by two-step melt polycondensation of 2,5-FDCA (or its dimethyl ester) and EG. High molecular weight PEF is one of the most interesting furan-based polymers, thanks to its properties, which are very similar or even better than those of PET. For this reason, many companies have focused their attention on this material: for example, Avantium, which is cooperating with Coca-Cola and other companies in order to replace PET bottles with bioplastic ones, is able to synthesize PEF by reacting a silanic dicarboxylic acid obtained from carbohydrates (that can be extracted from a wide range of biomasses such as sugar cane, agricultural residues or cereals) with bio-ethylene glycol, according to the patented "YXY" technology. The Coca-Cola Company has already presented, as a world premiere during Milan EXPO 2015, the first 100% bio-PEF bottle, entirely obtained from natural sugars contained in plants (PlantBottle™), like sugar cane and its processing waste.
- Poly(propylene furanoate) (PPF), obtained by polycondensation of 2,5-FDCA (or its dimethyl ester) and 1,3-propanediol (PD).
- Poly(butylene furanoate) PBF, obtained using the same procedure of PEF and PPF, but using BD as glycolic subunit. DMF is preferred to FDCA because of its higher purity, in order to avoid the darkening of the final polymer. Many different polymerization conditions and catalysts were used to find the best way to increase the molecular weight: through polycondensation, molecular weights of about 46000 Da were reached. PBF thermal and mechanical properties are very similar to PBT ones, while permeability values are better, even than those of the most common packaging materials (i.e. Nylon 6 and PET).

Another bio-based aromatic diacid that could potentially replace the terephthalic one is the 2,5-thiophene dicarboxylic acid (TFDCA). This monomer has a molecular structure, which is very similar to FDCA one: the only difference is the presence of a sulphur atom instead of the oxygen one in the aromatic ring (Figure 1.17).

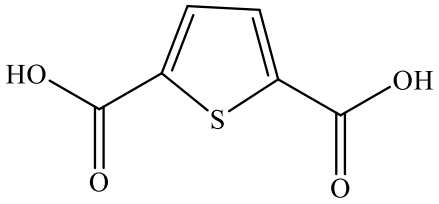

Figure 1.17. Chemical structure of TFDCA.

It is 100% bio-based, as it can be obtained from adipic acid through chlorination with thionyl chloride, as reported in Figure 1.18.

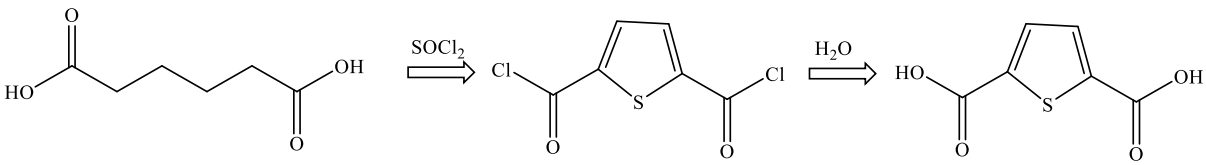

Figure 1.18. Synthetic procedure of TFDCA.

Moreover, by the resonance energy values of the terephthalic, furan and thiophene rings, which are reported in Figure 1.19 starting from the less to the most electronegative, TFDCA is likely to be more stable than FDCA.

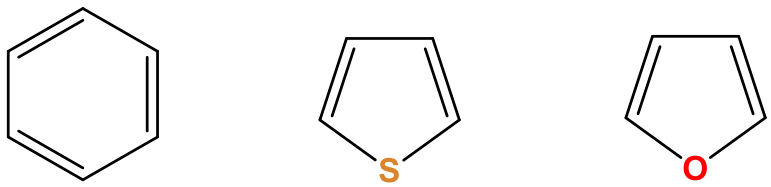

Benzene **Thiophene** **Furan**

E_{res} = 36 Kcal/mol E_{res} = 29 Kcal/mol E_{res} = 11 Kcal/mol

Figure 1.19. Resonance energies of terephthalic, furan and thiophene rings.

1.5.3 Synthesis

Polyesters are synthesized by polycondensation of difunctional monomers, like the self-condensation of hydroxy acids, diacids with diols, diacid chlorides with diols or by transesterification reactions of diesters and diols, or by ring-opening polymerization (ROP) of lactones and lactides [Nair et al., 2007].

The majority of biodegradable polyesters that are nowadays on the market are produced by both these methods. The first can be used for a wide range of diols and diacids, but it requires, in general, high temperature, long reaction time and removal of reaction by-products to obtain high molecular weight polymers. Another drawback is that the materials obtained do not have controlled chain lengths and present quite high polydispersity index (PDI). On the contrary, ring-opening polymerization, despite the limitation of monomers that can be used, allows the synthesis of higher molecular weight polymers under milder conditions and in shorter times.

Moreover, the growing interest on new enzymatic catalysed polymerization, an eco-friendly technique, which can realize high regiospecificity and stereospecificity, has led to the synthesis of polymers with controlled chain lengths, under milder conditions [Okada, 2002; Varma et al., 2005; Albertsson et al., 2008; Gross et al., 2010].

As an example, lipases can be used as catalysts in ring-opening polymerization of lactones and cyclic diesters, and in condensation polymerization of hydroxy acids and diacids with diols.

1.5.3.1 Polycondensation

Melt polycondensation is the most used synthetic technique for both aliphatic (i.e. PBA and PBS) and aromatic polyesters (poly(alkylene terephthalate)). Moreover, polycondensation is an alternative method for polylactic acid (PLA) industrial production.

There are two methods of polyesterification: homo-polycondensation of hydroxycarboxylic acids (Eqn. [1]) or hetero-polycondensation of a diol with a dicarboxylic acid (Eqn. [2]):

$$n\ HO\text{-}R\text{-}COOH \leftrightarrow HO\text{-}(RCOO)_n\text{-}H + (n\text{-}1)\ H_2O \quad \textbf{[1]}$$

$$n\ HO\text{-}R^1\text{-}OH + n\ HOOC\text{-}R^2\text{-}COOH \leftrightarrow HO\text{-}(R^1COOR^2COO)_n\text{-}H + (2n\text{-}1)\ H_2O \quad \textbf{[2]}$$

where R, R^1 and R^2 are alkylene groups. For the synthesis of high molar mass polymers, the condensation equilibrium constant (K_C) should be reasonably high. Generally, in the polycondensation of alcohols with carboxylic acids, K_C is not high enough (usually ≤ 10), and

in order to obtain sufficiently high degrees of polymerization (DP_n) the condensation side products, like water or methanol, have to be removed from the reaction environment [Carothers, 1936]. The number average degree of polymerization DP_n can be obtained from K_C according to the following equation:

$$DP_n = K_C^{0.5} + 1 \quad \textbf{[3]}$$

Since $K_C \approx 10$ for many condensation reactions between simple aliphatic alcohols and carboxylic acids, $DP_n \approx 4$ would result in the equilibrium polymerization. However:

$$DP_n = 1/(1 - p) \quad \textbf{[4]}$$

where p is the degree of conversion of the reactive groups [Carothers, 1936]. So, when K_C = 10, only 76% of hydroxyl and carboxylic group would react until an equilibrium is reached. In order to obtain polyesters with the required physical properties, $DP_n \geq 100$ is necessary; this means that the degree of conversion should be not less than 0.99 and $K_C \geq 10^4$. Values so high of K_C are usually obtained when acid chlorides (Schotten-Baumann reaction), acid anhydrides or activated carboxylic acids are used.

As already mentioned, by removing the low molar mass by-products of esterification from the reaction mixture, it is possible to shift the equilibrium towards high molar mass polyesters.

Eqn. [5], which is derived from Eqn. [3] by assuming $K_C >> 1$, provides a dependence of the degree of polymerization on the extent of removal of the by-products (q):

$$DP_n = (KC / q)^{0.5} \quad \textbf{[5]}$$

where $q = N_e/N_0$, i.e., the ratio of the concentration of the by-products at a given equilibrium to its hypothetical concentration resulting from reactive groups conversion degree related to the required DP_n. For instance, in order to prepare polyesters with $DP_n = 10^2$, the ratio KC/q must be higher than 10^4. If K_C = 10, then q should be lower than 10^{-3}. This means that only 0.1% of the by-products of its "normal" equilibrium concentration can remain in the reacting mixture. This is one of the practical limitations in the syntheses of many polyesters by polycondensation. Moreover, when high degrees of conversion are reached, the removal of low molar mass by-products, like water, is limited due to the high viscosity of the system.

Another factor that has to be taken into account is the stoichiometry of the substrates. Dependence of the number average degree of polymerization of the polyester formed in heteropolycondensation on the stoichiometric imbalance parameter r is given by the following equation:

$$DP_n = (1 + r) / (1 + r - 2p) \quad \textbf{[6]}$$

where $r = N_{OH}/N_{COOH}$ for $N_{OH} < N_{COOH}$ or N_{COOH}/N_{OH} for $N_{OH} > N_{COOH}$; N_{OH} and N_{COOH} are the concentrations of hydroxyl and carboxylic groups, respectively. Thus, for example at p = 0.99, and $DP_n = 100$ for the exactly equimolar reacting mixture (r = 1), if only 1.0 mol% of imbalance is introduced (r = 0.99), DP_n is reduced to the value of 67. Even if in the feed the 1:1 stoichiometry is ensured, one of the components can be partially lost during polycondensation, either because of volatilization, due to the high reaction temperature reached, or reactant losses by side reactions. In order to limit this problem, polycondensation based on transesterification was introduced; this technique is used, for example, for the large-scale production of poly(ethylene terephthalate).

The rate of polycondensation rarely agrees with simple kinetic expressions during the entire polycondensation process. Changes in the reaction mixture properties like viscosity or dielectric constant can affect the course of the reaction, even if the most fundamental assumption of equal reactivity of functional groups is respected. It is almost true indeed, because at high viscosities the "diffusion in" is slowed down, but this behaviour is compensated by equally slowing down of the "diffusion out" [Rabinovitch, 1937].

Expressions describing the molar mass distribution (or polymerization degree) of linear polyesters obtained by polycondensation have been explained for the first time by Flory in 1936. The number and weight fractions (n_i and w_i, respectively) of macromolecules having a degree of polymerization equal to i at a given degree of conversion p, is:

$$n_i = p^{i-1}(1 - p) \quad \textbf{[7]}$$

$$n_i = ip^{i-1}(1 - p)^2 \quad \textbf{[8]}$$

The number and weight average polymerization degrees (DP_n and DP_w, respectively) can be expressed according to the following equations:

$$DP_n = 1 / (1 - p) \quad \textbf{[9]}$$

$DP_w = (1 + p) / (1 - p)$ **[10]**

and the polydispersity index as:

$DP_w / DP_n = 1 + p = 2 - DP_n^{-1}$ **[11]**

Thus, for the conversion (p = 1) DP_w / DP_n = 2. The value of this parameter is particularly different in case of polyesters prepared by polycondensation or by ROP. In this latter case, as the kinetic control of the entire polymerization process is higher, the molar mass distribution is usually narrower and the ratio DP_w / DP_n is not much higher than 1.

Another point that must be considered is that polycondensation reactions can lead to the formation of a certain fraction of macrocyclic products: in polyesterification, two reactions that can potentially give cyclic molecules are back-biting and end-to-end condensation. However, for processes conducted in bulk and under reversibility governing conditions, cyclization can be considered as a side reaction of a secondary importance because critical concentrations of macrocycles (in terms of repeating units) are well below 1 g/l [Duda et al., 2002].

1.5.3.2 Ring opening polymerization

High molecular weight aliphatic polyesters with low polydispersity index can be easily prepared under mild conditions by ring-opening polymerization (ROP) starting from lactones and lactides of different ring-size, substituted or not by functional groups [Jérôme et al., 2008]. ROP is a "living" process, i.e. without any irreversible transfer and termination reactions, allowing a good control over the molecular parameters of polymeric chains (preventive determination of the molecular weight by the monomer-to-initiator molar ratio and a tight molecular weight distribution) and over the topology of the synthesized materials [Albertsson et al., 2002].

Lactones polymerization is usually carried out in bulk or in solution (THF, dioxane, toluene), emulsion, or dispersion. The temperature of bulk polymerization is in a range between 100 °C and 170 °C, while for solution polymerization lower temperatures are required, around 0 - 25 °C, in order to minimize side reactions like inter- and intramolecular transesterfication [Albertsson et al., 2002].

Most lactones polymerize through the action of catalysts or initiators. Depending on the nature of these last, ROP can proceed through different mechanisms: cationic, anionic (nucleophilic),

or coordination mechanism [Endo, 2009]. Common initiators used for the ROP of lactones are organometallic compounds, such as oxides, carboxylates, and alkoxides. The use of ionic initiators for the synthesis of polyesters cause unwanted inter- and intra-molecular transesterification reactions, which can lead to polymers with low molecular weight and broad molecular weight distribution. Many organometallic derivatives of metals, such as Al, Ca, Sn, Nd, Fe, Y, Yb, Sm, La, Ti, Zn, Zr and Mg, can effectively control the polymerization in contrast to their anionic counterpart [Jérôme et al., 2008]. Depending on the choice of the organometallics, ROP reactions can be carried out via two main polymerization mechanisms. Some of them work as catalysts and activate the monomer by complexation with the carbonyl group: in this case, polymerization is initiated by any nucleophile molecule (water or alcohol) present in the polymerization medium as impurities or added on purpose. In the second case, the organometallic itself is the initiator and the polymerization occurs through an 'insertion–coordination' mechanism. Metal alkoxides are common initiators, which first coordinate the monomer carbonyl, followed by the cleavage of the acyl–oxygen bond of the monomer and the insertion, at the same time, into the metal alkoxide bond. In Figure 1.20 an example of ROP of lactide is reported.

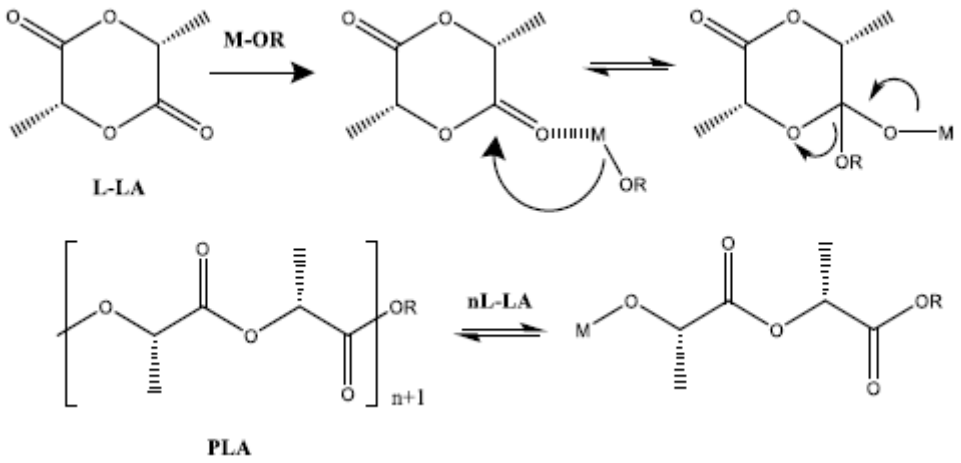

Figure 1.20. ROP of L-lactide.

For industrial applications, also in packaging, $Sn(Oct)_2$ is preferred due to the Food and Drug Administration approval. However, even if tolerated in food-related applications, it has to be avoided in materials used for biomedical applications. In a typical polymerization mechanism, $Sn(Oct)_2$ is converted into tin alkoxide, which is the actual initiator, by reactions with alcohols or other protic impurities.

$Sn(Oct)_2 + ROH \rightarrow Oct–Sn–OR + OctH$ **[12]**

$Oct–Sn–OR + ROH \rightarrow Sn(OR)_2 + OctH$ **[13]**

Therefore, the polymerization involves a coordination–insertion mechanism.

Thus again, the addition of a predetermined amount of alcohol to the polymerization medium is an effective way to control the molecular weight by the monomer/alcohol molar ratio. $Sn(Oct)_2$ is also efficient in copolymerization of various lactones.

As an example, industrial production of PLA (Ingeo) is carried out via ROP by Natureworks in North America, with a capacity of 140000 Tpa [Jérôme et al., 2008].

1.5.3.3 Chain extension

Chain extension will be extensively described in paragraph *1.6.2.2.1*.

1.5.4 Physical properties

The physical properties of both aliphatic and aromatic polyesters, like crystallinity degree, glass transition temperature and melting temperature, depend on many different factors such as the flexibility of the macromolecular chain, presence of polar groups, molecular mass, degree of branching and their orientation, etc. Generally, short-chain branches reduce the ability of crystallization of polymers while long-chain ones lower the melt viscosity and impart elongational viscosity with tension-stiffening behaviour [Albertsson et al., 2002]. Moreover, physical and mechanical properties of these materials can be tailored by blending and copolymerization or by changing the macromolecular architecture (e.g. hyper-branched polymers, star-shaped or dendrimers, etc.).

1.5.4.1 Thermal properties

Polymeric materials can be divided into thermoplastics and thermoset depending on their thermomechanical properties [Zheng et al., 2005]:

- Thermoplastics: polymers with a linear or branched structure, that can be repeatedly softened, moulded and hardened by heating and cooling without any negative effect on

the material's physical properties (i.e. saturated polyesters, polyamides, polycarbonates, etc). This is possible thanks to the presence of only secondary bonds with low thermal resistance within their chains, which can soften in a complete reversible way, without undergoing chemical transformations.

- Thermoset: polymers with high cross-linked structure that after heating and consequent hardening cannot be further processed or moulded (i.e. unsaturated polyesters, polyurethanes, resins, etc). This behaviour is due to the heat itself, which is directly responsible for the cross-linking of the material.

1.5.4.1.1 Thermal stability

Aromatic and aliphatic polyesters can undergo thermal degradation, especially at high temperatures involved in polycondensation reactions and in material processing. Heat is responsible for chemical modifications in polymeric chain (breaking of chemical bonds with the formation of volatile products) with consequent alteration of properties. For this reason, thermal stability evaluation is of great importance, in order to investigate the maximum temperature that a material can reach before it undergoes chemical degradation. Thermal degradation of polymers consists of two distinct reactions, which take place simultaneously in the reactor. One is a random bonding scission, which causes a decrease in the molecular weight of the raw polymer, and the other is a chain-end scission of C-C bonds, generating volatile products. The chain-end scission generally occurs when the backbone bonds are weaker than those of the side groups. It takes place at the gas-liquid interface in the reactor [Singh et al., 2008], starting from the end of the chain, with progressive release of monomeric units. This mechanism is also known as depolymerization reaction, which is opposite to the propagation step in addition polymerizations.

As to random bonding scissions, they may occur at any point along the polymer chain, even without the presence of any active site. β-scission is one of the most important examples of random degradation in polyesters, occurring when β-hydrogen atoms are available in the diol component [Sivasamy et al., 1992; Singh et al., 2008]. This bulk reaction [Zimmermann et al., 1973; Zimmermann et al., 1986; Chrissafis et al., 2005] consists in the extraction of a hydrogen atom bonded to the methylene in β position with respect to the carbonyl group, with the consequent breaking of the O-CH_2 bond. This random cleavage of ester bonds leads to the formation of terminal groups -COOH and a CH_2 = CH- (Figure 1.21):

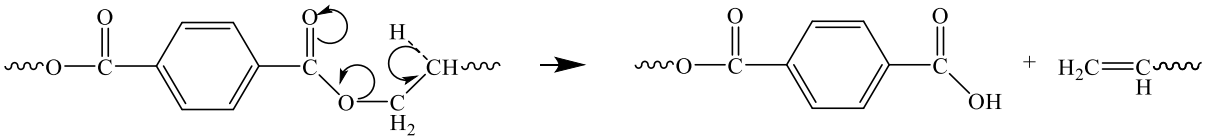

Figure 1.21. Polyesters β-scission reaction.

The tendency for chain scission is higher in polyesters obtained starting from monomers containing a higher number of methylene groups. This is true both for aromatic and aliphatic polyesters [Chrissafis et al., 2005]: for example, the degradation rates of PBT or PPT are higher than that of PET, as this last contains one or two methylene groups less and is more stable to decomposition. Similarly, poly(ethylene succinate) is more thermally stable than poly(butylene succinate).

Thermal degradation of polyesters yields a variety of products like CO_2 and H_2O but also formaldehyde, acetaldehyde, formic and acetic acid. The presence of acetaldehyde can lead to the formation of coloured by-products that darken the final polymer. Moreover, for applications in food packaging, acetaldehyde must be absent because of its high toxicity.

Thermal degradation can be investigated by thermogravimetric analysis, a technique which allows to determine mass loss during controlled heating. From a typical polymeric thermogram, reported in Figure 1.22, it is possible to see that main mass loss occurs in one stage, usually above 300°C. Sometimes it is possible to see also a small shoulder at lower temperatures, related to the presence of residual monomers, catalysts, low molecular weight oligomers that degrade at lower temperatures.

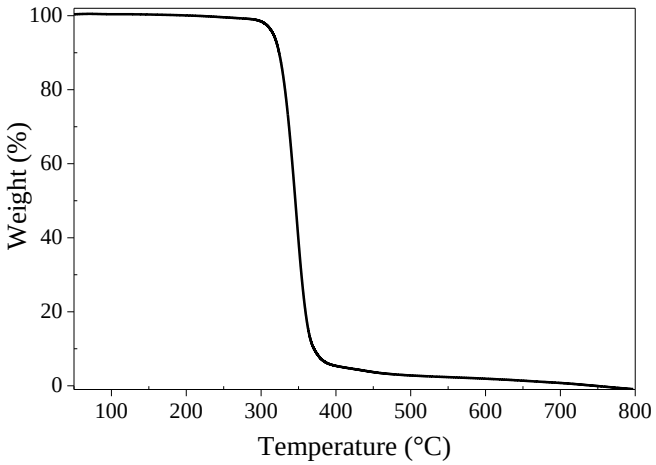

Figure 1.22. Typical polymeric thermogram.

Even though thermogravimetric analysis is for sure necessary for the study of chemical degradation mechanisms, it must be combined with other techniques, such as mass spectrometry or Fourier transform infrared spectrophotometry, in order to better understand the complex reactions that take place during heating.

1.5.4.1.2 Glass transition temperature and melting temperature

Polymers can be amorphous or semi-crystalline. In the first case, they are characterized by a random and disordered spatial arrangement of the chains and, when the temperature increases, they undergo a zero-order transition, called glass transition: the temperature at which it occurs is called glass transition temperature, T_g. Drastic macroscopic changes of many physical properties are observed. In particular polymers, from relatively fragile and rigid solids (below T_g) become rubbery or viscous liquids (above T_g). At molecular level, the glass transition is associated to cooperative motions involving long chain segments, which are due to the rotation of the chains around the single bonds between atoms.

Semi-crystalline polymers are characterized by the presence of a certain amount of 3-dimensional ordered structures. Unlike other materials, polymers are never 100% crystalline: the crystalline regions are in fact closely connected to disordered amorphous areas. Consequently, crystalline regions present many defects, and their fusion does not take place at a well-defined temperature (T_m), but in a range. In semi-crystalline polymers is present also a glass transition, which is related to the amorphous portion. In this case, however, crystallites behave as physical constraints to amorphous segments, causing a shift of T_g to higher temperatures than those of the same polymers but in a completely amorphous state. Some semi-crystalline polymers can be brought to an amorphous state by rapidly cooling them from the melt; this treatment, in fact, prevents the chains to rearrange in ordered domains. The presence of a certain degree of crystallinity involves a very drastic change in properties (density, transparency, mechanical response, etc.) with respect to the same material completely amorphous.

Chain symmetry and flexibility, as well as tacticity, are all factors that significantly influence the values of T_g and T_m. In particular, the higher the chain flexibility, the lower the T_g and T_m values. Chemical groups like -O-, -COO-, OCOO- and -(CH_2)- increase chain flexibility while the presence of polar groups, which favour intermolecular bonds, causes an increase of both T_g

and T_m. It is possible to increase stiffness also by incorporating in the main chain aromatic rings that prevent rotations around single bonds.

Thermoplastics polyesters have usually lower T_g values than thermoset ones. Aliphatic polyesters with x,y ≥ 2 (Figure 1.9) are characterized by a quite high crystallinity degree, glass transition temperature between –70 and –30°C, melting temperature usually ranging between 40 and 90°C (in most cases below 100°C). Usually, with a lower ratio between methylene and carboxylic groups in the polymer chain, higher melting temperatures are observed: for example, the T_m of poly(butylene adipate) is 47°C, while T_m of poly(butylene succinate) is 116°C [Soccio et al., 2012 (a); Gigli et al., 2016].

Aromatic polyesters present higher crystallinity degree and melting temperature than aliphatic ones. For example, terephthalic ones are semi-crystalline, with T_g usually above room temperature, which fall steadily by increasing alkylene group length. As to melting temperature, in the majority of cases it is well above 100°C and decreases alternately passing from an even number of alkyl units to an odd one: T_m of PET is 290 ° C, T_m of PPT is 237 ° C and T_m of PBT is 236 ° C [Jang et al., 1999; Kricheldorf et al., 1995; Žagar et al., 2004].

1.5.4.2 Mechanical properties

Polymers are viscoelastic materials, showing both an elastic and a plastic behaviour, depending on the kind and the intensity of the load applied. Elastic behaviour refers to materials that are able to return to their original shape after the application and the removal of a certain mechanical stress, while plastic one indicates materials that remain irreversibly deformed after stress removal. Mechanical properties of polymeric materials can be evaluated by analysing their behaviour in response to different kind of loads, both static and dynamic [Landel et al., 1993].

The most common are stress-strain measurements, in which the strain of a material (i.e. the change in sample length divided by the original length) in response to the application of a normal stress (i.e. the force applied to the system divided by the cross-sectional area) at a constant rate is evaluated. Through this kind of measurement, it is possible to determine:

- Young's modulus (also called elastic modulus) E, which is the slope of stress-strain curve in its initial linear part, corresponding to the elastic region;
- Stress and elongation at yielding, i.e. the point at which there is the passage from elastic region to plastic one;

- Stress and elongation at break, that is the point at which macroscopic fracture occurs.

Mechanical properties of polyesters, as well as those of polymers in general, depend on many factors, like molecular weight, crystallinity degree, thermal properties and molecular architecture. First, molecular weight must be sufficiently high in order to have acceptable mechanical properties. In addition, crystalline materials show a more rigid and brittle behaviour, with very low elongation at break (less than 10%), while, in case of lower crystallinity, higher elongation at break (even more than 500%) and lower elastic modulus can be observed. For example, elastic modulus of aromatic polyesters can reach values in the order of GPa, while for aliphatic polyesters this value could be at least one but also two order of magnitude lower (rubber Young's modulus is around 0.1MPa). As to the elastic modulus and the elongation at break, they are strictly dependent on the temperature at which measurements are performed, which is related to chain mobility: glassy materials are characterized by higher Young's modulus and lower elongation at break, vice-versa for materials in a rubbery state, where chains can move more easily [Van Krevelen et al., 2009; Ward et al., 2013]. Moreover, unlike the majority of polymers, which show yielding at a certain point of the stress-strain curve, some of them, like thermoplastic elastomers, do not show this phenomenon during stress-strain measurements: in this case, cyclic measurements can be performed. They consist in the application and the removal of a certain deformation for a determined number of times. Thanks to this kind of test the elastic return (which indicates the ability of a material to return to its initial shape after the removal of the stress) and the hysteresis area (which is a measure of the elastic energy lost after each cycle) can be determined.

1.5.4.3 Barrier properties

The evaluation of barrier properties is of primary importance for materials used in packaging applications, in particular when food is involved. Package should be able to control food products respiration, to supply a selective barrier to gases and water vapour, to maintain as long as possible a modified atmosphere when present, limiting, at the same time, the migration of lipids, and the possible release of food additives like flavour, colours, antioxidants and antimicrobial agents [Tharanathan, 2003]. In fact, oxygen inflow into the package can cause lipidic oxidation phenomena and changes in the colour of the food, while the variation of humidity can affect food freshness.

The term “high barrier” is usually applied in case of very low permeability of a material to low molecular weight species, like gases or organic compounds [Lagaron et al., 2004].

The transport of low molecular weight molecules through polymeric films depends on two different contributions, according to the solution-diffusion mechanism [Wijmans et al., 1995]. As to this model, molecules passage can be divided into three phases: 1) molecular adsorption, which consists in the dissolution of the penetrant in the surface exposed to the gas (upstream surface), 2) molecular diffusion, which occurs when the penetrant passes through the membrane under a concentration gradient, and 3) molecular desorption, which takes place when the penetrant returns in gas phase to the opposite side of the membrane (downstream surface). Thus, the steady state permeability of a certain penetrant P_1 is given by the following equation:

$$P_1 = \frac{J_{1,ss}}{p_1^u - p_1^d}\frac{l}{M_1} = < S_1 > \cdot < D_1 > \qquad \textbf{[14]}$$

Where $< S_1 >$ and $< D_1 >$, are the average solubility and diffusivity coefficients, respectively, $J_{1,ss}$ is the steady state diffusive mass flux of the penetrant, M_1 is the molecular mass of the gas, l is the polymeric membrane thickness, while p^u_1 and p^d_1 represent upstream and downstream penetrant partial pressures, respectively.

From the analysis of the transient permeation process, it is also possible to determine the average diffusion coefficient through the diffusional time lag (τ_L) method, according to the following equation:

$$\tau_L = \frac{l^2}{6 < D_1 >} \qquad \textbf{[15]}$$

The diffusion coefficient D represents the average ability of the permeant to move through the polymeric chains and is determined from Fick's first law of diffusion. This parameter is influenced by the size of the permeant molecules, and by free volume, crystallinity degree and stiffness of polymeric chains. Solubility coefficient S is defined, from Henry’s law, as the ratio between the equilibrium concentration of the dissolved penetrant in the polymer and its partial pressure in the gas phase. This value depends on the interactions between polymer and permeant, on the condensability of this latter and on the cohesive energy density of the polymer [Minelli et al., 2018].

High barrier performances are also the result of a very low fractional free volume and high intermolecular cohesion. According to the free volume theory, diffusing molecules can cross a polymeric volume jumping between thermally generated nanometric voids inside the polymer

matrix, called free volume elements (FVEs). Due to thermally induced random motions of the polymer chains, FVEs continuously form and disappear. Permeant molecules, if small enough, can jump into them, where they will remain until another chain motion occurs nearby. The total amount of voids in the amorphous portion of a polymer is called free volume [Duda et al., 1996]. In case of glassy polymers, the free volume can be modified by acting on the thermal history: if the polymer is quickly cooled, the formation of free volume is encouraged, vice-versa in case of slow cooling. Another way to change the amount of free volume is by acting on the chemical structure, through the addition or the removal of pending groups in the main chain: for example, the presence of polar groups with low specific volumes can reduce FVEs. At the same time chain packing is favoured thanks to the higher intermolecular interaction strength [Singh et al., 1998]. Chemical structure also defines the affinity between a potential permeant and the polymer matrix: low solubility will also result in low permeability, independently of whether the diffusion kinetics is favourable to permeant transport [Lagaron et al., 2004].

Crystallinity is another important parameter, which influences both solubility and diffusion. Crystalline regions, as they are denser, more compact and ordered than the amorphous ones, can preclude the penetrant adsorption by reducing its solubility. The presence of crystals in the polymeric matrix acts as a barrier to diffusion, increasing the length of the path that the permeant must follow. In some cases, also chain orientation, which is obtained by mechanical stretching at temperatures slightly lower than T_m, can affect permeability: polymeric crystals can be oriented in lamellar structures during deformation. This orientation lowers the diffusivity by increasing the path that the penetrant must perform. Furthermore, the stretching of semi-crystalline polymers can improve barrier properties through stress-induced crystallization and orientation of the amorphous portion [Weinkauf et al., 1990; Michaels et al., 1963].

In addition, transport phenomena can be very different depending on whether the permeation process occurs below or above the glass transition temperature of the polymer investigated. The general trend indicates that during the transition from a glassy to a rubbery state, an increase in free volume is recorded; this allows cooperative movements of large chain segments, thus favouring the permeability. However, correlations between T_g, relaxations in the rubbery state and permeant type are all factors that must be taken into account in the prediction of the overall effect.

Liquid crystalline polymers (also called mesomorphic) recently became very popular thanks to their highly oriented morphology resulting in higher mechanical strength [Chiou et al., 1987]

and barrier ability compared to those of semi-crystalline polymers. A possible explanation of this behaviour could be that the presence of a liquid crystalline order retards gas transport by acting like a three-dimensional impermeable crystal structure. Another hypothesis suggests that the efficient chain packing in the liquid crystalline phase is responsible for better hindering gas flow [Weinkauf et al., 1990].

1.6 Strategies to improve material final properties

At the beginning of last century, the great industrial progress led to the development of a wide range of different polymeric materials. Since 1970s, on the contrary, as most of the economically convenient monomers had already been exploited, polymer industry moved towards other directions: new homopolymers and copolymers based on already existing monomers were synthesized. As already said, copolymerization represents one of the best tools to tailor and improve the final properties of materials. However, acting on molecular structure is not always possible. For this reason, as most monomers cannot be easily copolymerized to gain intermediate properties, their polymers could be economically blended.

1.6.1 Blending

A polymer blend is obtained by mixing two or more polymers, in order to create a new material with different physical properties.

There is high commercial interest in polymer blends, as they can combine the attractive features of many materials into one, or improve poor characteristics of particular materials, including recycled ones. Moreover, it is a simple and cost-effective technique [Paul, 1989]. Polymer blends can be classified into homogeneous or heterogeneous, depending on their miscibility on a molecular level. Miscible blends, in which thermodynamic solubility occurs, are characterized by the presence of only one phase and a single glass transition temperature. Their properties range between those of the individual components and depend on blend composition. On the other hand, immiscible blends show phase separation, exhibiting T_g and/or T_m of each component.

The behaviour of the final material is strictly related to the properties of the individual components, but significantly depends also on the morphology of the blend itself and on the interfacial properties between its phases [George et al., 2013; Jiang et al., 1991].

It has to be noticed that only few polymer couples form miscible blends, while in most cases blends are immiscible, with poorer physical properties than those of their components. This problem is due to the lack of favourable interactions between phases and leads to poor interfacial adhesion, also in the solid state. Consequently, premature mechanical failure is the macroscopic effect. The more effective solution to this issue is the control of morphology through compatibilizing agents, which can improve blend performance by making blend components less immiscible. Compatibilizers are molecules containing both hydrophobic and hydrophilic parts; these parts can align along the interfaces between two phases, reducing their interfacial tension and increasing their compatibility. Higher compatibility results in better phase dispersion and stability against coalescence, together with improved mechanical performances [Chen et al., 1993].

1.6.1.1 Reactive blending

Reactive blending is a particular blending approach in which compatibilization is given by chemical reactions occurring during the mixing of the components in a molten state.

This technique can be carried out in the solid state, in solution or in the melt. This last way presents several advantages compared to the others: first, the absence of any solvent prevents from economic and environmental issues related to solvent removal, recovery, and losses. Moreover, melt processing reduces the probability of contamination of the final products. Chemical reactions involved must be able to occur in the melt at high temperatures. For this reason, thermal stability of both the reacting groups and the chemical bonds formed is another important limiting factor. As a consequence, only a few types of chemical reactions are commonly employed in reactive blending, which can be grouped into imidization, ring opening and amidation reactions, and interchange reactions between polycondensates. The most occurring interchange reactions in the case of polyesters are intermolecular alcoholysis, intermolecular acidolysis and esterolysis, which are of particular importance also at industrial level: they are used, for example, for the production of common plastics like PET.

Another important feature of reactive blending is the progressive evolution in the chemical structure of the so-obtained copolymers, from long block structures to random ones with the increase of the reaction time (Figure 1.23).

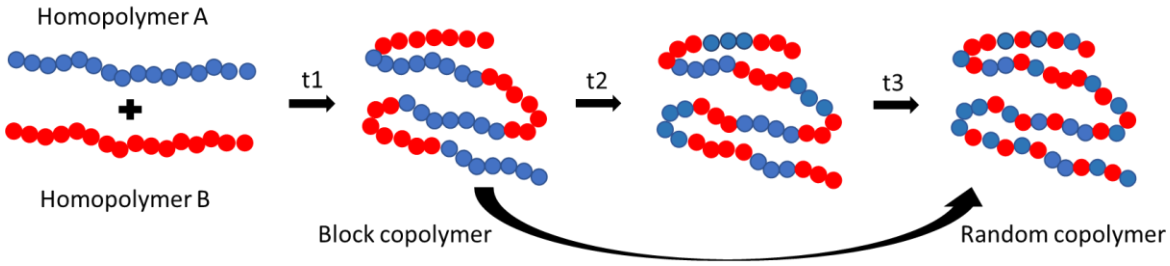

Figure 1.23. Evolution of polymer structure during reactive blending.

1.6.2 Copolymerization

The word "copolymer" indicates each macromolecule obtained from two or more different monomers. Copolymers can be divided in different categories, according to the relative arrangement of the monomers in the main chain. Considering a copolymer obtained by the combination of two different comonomeric sub-units, graphically represented by ◆ and ■, 4 categories can be distinguished:

- alternating copolymers, where ◆ and ■ units are regularly alternated:

- periodic copolymers, where ◆ and ■ units are arranged in repeating sequences:

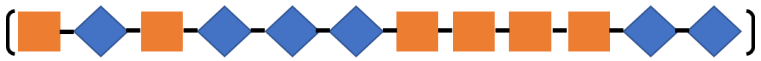

- statistical (or random) copolymers in which the distribution of comonomeric units follows Bernoullian statistics:

- block copolymers, where two or more homopolymeric subunits are linked by covalent bonds:

Copolymers can also be classified depending on the presence of branches in the structure. Linear copolymers are formed by a single main chain, while branched copolymers are characterized by the presence of one or more polymeric side chains linked to the main one.

Graft copolymers are a type of branched copolymers, in which homopolymeric side chains are structurally distinct from the main one, which is generally composed of a different homopolymer. The category of branched copolymers includes also star, brush and comb copolymers.

In order to better understand both structure and physical-chemical properties of a copolymer, it is important to take into account many different parameters, such as type and amount of repeating units, comonomeric sequences arrangement, molecular weight and its distribution, propagation and termination rate constants, presence of ramifications, cyclizations or cross-links.

Copolymerization is known to be the most effective way to improve properties of materials (like processability, mechanical performances, chemical resistance, biodegradability, etc) without altering those already satisfying for the intended use.

1.6.2.1 Random copolymers

For copolymers, as well as for homopolymers, thermal transition like T_g and T_m are of crucial importance. However, copolymers, being characterized by the presence of two or more different repeating units, can exhibit more crystalline and amorphous phases, related to different melting and glass transition processes.

T_g of amorphous random copolymers is usually a monotonic function of composition. The correlation between glass transition temperature and the comonomeric content can be expressed by Fox equation:

$$1/T_g = \omega_A/T_{g,A} + \omega_B/T_{g,B} \quad \textbf{[16]}$$

where ω_A and ω_B represent weight fractions of comonomeric units A and B, while $T_{g,A}$ and $T_{g,B}$ are the glass transition temperatures of the two parent homopolymers.

As to the crystallization ability, random copolymers containing crystallisable A and no crystallisable B comonomeric units can crystallize in two opposite ways. The first one consists in the formation of a two-phase system in which the crystalline phase composed of A units is in equilibrium with an amorphous phase containing both A units and non-crystallizable comonomer B units (comonomer exclusion). Otherwise, the copolymer can form a two-phase system in which the crystalline phase is a solid solution of A and B co-units; the comonomer B units produce defects in the crystalline A lattice and both phases have the same composition

(comonomer inclusion). Real copolymers generally exhibit a crystalline morphology intermediate to these two situations [Sanchez et al., 1973].

Comonomer exclusion in thermodynamic equilibrium was first described by Flory, in1947 [Flory, 1947]. According to his model, the upper bound of the copolymer melting temperature, (i.e. the T_m of crystals made of "infinitely long" homopolymeric sequences of A units) can be described as follows:

$$1/ T_m° – 1/ (T_m(X_B)) = (R / H_m°) \ln(1–X_B) \quad \textbf{[17]}$$

where $T_m°$ and $\Delta H_m°$ represent the equilibrium melting temperature and heat of fusion of 100% crystalline homopolymer, X_B is the concentration of B units in the polymer and R is the gas constant.

The main drawback of the model is the unrealistic assumption that these homopolymer sequences of infinite length build up unfolded crystals of the length of A sequences. This issue can be overcome, considering that homopolymer sequences of length ξ may only be included into crystals of lamellar thickness corresponding to that length. The melting point of infinitely long homopolymer sequences is then expressed by Baur's equation:

$$1/ T_m° – 1/ (T_m(X_B)) = (R / \Delta H_m°)[\ln(1 –X_B) –\langle\xi\rangle^{-1}] \quad \textbf{[18]}$$

where $\langle\xi\rangle = [2X_B(1–X_B)]^{-1}$ is the average length of homopolymer sequences in the melt.

Baur model, while incorporating finite crystal thickness and concomitant depression in the melting point fits experimental data much better than the Flory one [Baur, 1966; Helfland et al., 1973; Sanchez et al., 1973; Windle et al., 1985; Allegra et al., 1992; Yoshie et al., 1994; Wendling et al., 1998], even though it does not consider that the homopolymer sequences are invariably fixed in chains due to bond connectivity. Moreover, from experimental data is clear that comonomer exclusion alone in many cases cannot support the observed melting point depression. Therefore, comonomer inclusion must be considered in the melting point prediction. The case of comonomers B that are included as defects into crystals of A comonomer was investigated by Helfand and Lauritzen [Helfland et al., 1973] and later by Sanchez and Eby [Sanchez et al., 1973]. According to their model, T_m is then given by:

$$1/(T_m(X_B))–1/T_m°=(R/\Delta H_m°)\{(\varepsilon X_{CB})/(RT_m)+(1–X_{CB}) \ln[(1 –X_{CB})/(1–X_B)] + X_{CB}\ln(X_{CB} /X_B)\} \quad \textbf{[19]}$$

where X_{CB} is the concentration of B units in the co-crystal, and ε the free energy of defects. Starting from this equation, which is valid for any concentration X_{CB}, when $X_{CB} = X_B$, uniform inclusion takes place and Eqn. [19] reduces to:

$$T_m(X_B) = T_m^\circ \left[1 - \varepsilon X_B / \Delta H_m^\circ\right] \quad \textbf{[20]}$$

In the equilibrium state, the concentration X_{CB} is given by:

$$X_{CB}^{eq} = (X_B e^{-\varepsilon / RT}) / (1 - X_B + X_B e^{-\varepsilon / RT}) \quad \textbf{[21]}$$

and the equilibrium melting point is derived from Eqn. [19] as:

$$1/T_m^\circ - 1/(T_m(X_B)) = (R/\Delta H_m^\circ) \ln(1 - X_B + X_B e^{-\varepsilon / RT}) \quad \textbf{[22]}$$

This equation differs from the Flory equation (Eqn. [17]) only for the inclusion of the equilibrium fraction $X_B e^{-\varepsilon / RT}$ of repeating units B that are able to crystallize; in fact, in case of high defect free energies Eqn. [22] reduces to the Flory model. In addition, as this model underestimates the defect free energy and overestimates the melting temperatures for $\varepsilon \gg 0$, T_m derived by Eqn. [22] can be considered as an upper bound of the melting temperature. The behaviour when $\varepsilon \gg 0$ is the main limit of the Sanchez-Eby model: when ε is too high to allow co-crystallization, Eqn. [22] reduces to the Flory model (Eqn. [17]), but it should preferentially converge to the Baur model, (Eqn. [18]). The model proposed by Wendling and Suter [Wendling et al., 1998] converge to Eqn. [22] and Eqn. [18] in the limits of high and low defect free energies, respectively. According to this method, the melting temperature can be expressed as:

$$1/(T_m(X_B)) - 1/T_m^\circ = (R/\Delta H_m^\circ)\{(\varepsilon X_{CB})/(RT_m) + (1 - X_{CB}) \ln[(1 - X_{CB})/(1 - X_B)] + X_{CB} \ln(X_{CB}/X_B) + \langle \xi \rangle^{-1}\} \quad \textbf{[23]}$$

that, in case of comonomer inclusion, becomes:

$$1/T_m^\circ - 1/(T_m(X_B)) = (R/\Delta H_m^\circ)\{\ln(1 - X_B + X_B e^{-\varepsilon / RT}) - \langle \xi \rangle^{-1}\} \quad \textbf{[24]}$$

$$\text{where: } \langle \xi \rangle^{-1} = 2(X_B - X_B e^{-\varepsilon / RT})(1 - X_B + X_B e^{-\varepsilon / RT}) \quad \textbf{[25]}$$

Both the inclusion and exclusion models consider a depression of the crystalline melting point. For the inclusion model this depression is caused by a defective heat of fusion during

crystallization, whereas for the exclusion model it is caused by the fact that for crystallization, preferential ordering of the copolymer chains is required, which raises the entropy of fusion. However, careful crystallinity studies combined with calorimetric tests are needed to understand which model is more appropriate for a certain random copolymeric system.

1.6.2.2 Block copolymers

Block copolymers containing two different monomers A and B can present various architectures:

- linear di-block A-B;
- linear tri-block A-B-A;
- multiblock or segmented $(AB)_n$;
- star di-blocks $(AB)_nX$.

Moreover, when a third component is added, linear A-B-C, A-C-B, and B-A-C triblock copolymers can be prepared, and three-armed star ones too [Lodge et al, 2003].

Crystallization development in block copolymers is a complex mechanism, which depends on two competing self-organizing processes: microphase separation and crystallization. In general, di-block copolymers are characterized by the presence of an amorphous block together with a semicrystalline one, which both influence the T_g and T_m of the final material. Otherwise, when both blocks (or more than one within triblock polymers) can crystallize, the situation is more complicated. For example, when these copolymers are quenched from a microphase-separated melt into various temperatures below T_m of the corresponding blocks, various situations can be observed. When the melting temperatures of crystalline blocks are close enough, quenching can lead to a coincident crystallization of both blocks. Otherwise, when the melting temperatures are far from each other, one block can crystallize earlier in a specific morphology. This last can be affected by crystallization of the other block, depending on other parameters like segregation strength, crystallization temperature and molecular weight of the blocks [Müller et al., 2007].

The interest in this kind of materials is continuously growing, as their structure can overcome macroscopic phase separation [Hillmyer et al., 2014]. For example, styrenic A-B-A triblock copolymer is one of the most produced and least expensive class of block polymers available so far. They are characterized by glassy poly(styrene) end blocks (A) and rubbery central blocks (B) like poly(butadiene) or poly(isoprene). They show a thermoplastic elastomeric behaviour

thanks to the microphase separation of the styrene and isoprene segments, rather than any particularly ordered structure [Holden et al., 1996].

1.6.2.2.1 Chain extension

There are different ways to synthesize block copolymers. In the present research project high molecular weight block copolymeric systems were obtained through chain extension reactions between two hydroxyl-terminated subunits, both homopolymeric and copolymeric, usually obtained by polycondensation reactions.

As well known, polycondensates possess reactive end groups (OH, NH_2 or COOH), and a considerable number of fast reactions can be carried out with these groups. As to chain extenders, the most used are diphenyl carbonates, aliphatic and aromatic bisoxazolines, bisepoxides, diisocyanates, phosphites, caprolactam phosphite, bisketenimines, dianhydrides, oxazolinones and dicyanates. In particular, the use of diisocyanates has been deeply investigated [Shirahama et al., 2001; Cohn et al., 2006; Chen et al., 2011]. Moreover, by selecting number, chemical structure and composition, and relative amount of the hydroxyl-terminated comonomers, it is possible to synthesize a wide number of new materials with tailored properties, according to the final use.

Chain extension can be successfully used also to increase the molecular weight of aliphatic polyesters, improving their mechanical properties maintaining in the same time their biodegradability.

1.6.2.3 Aliphatic/aromatic copolymers

As known, the use of aromatic polyesters is preferred for those applications which require materials with excellent physical-mechanical stability, while biodegradability, which is peculiar of aliphatic polyesters, has favoured the use of these last as substitutes of traditional plastics, even if their mechanical performances are generally not particularly good [Tserki et al., 2006]. Copolyesters containing in their macromolecular chain both aliphatic and aromatic moieties are characterized by both excellent mechanical properties and good biodegradability. Thus, it is possible to overcome the peculiar problems of the two classes, providing a possible solution to pollution problems caused by the accumulation of plastic waste in the environment. The biodegradability of these polymers depends mainly on their chemical structure and, more in details, on the amount of hydrolysable ester bonds in the main chain, which is susceptible to

microbial attack. Other factors such as molecular weight, degree of crystallinity, stereoregularity and morphology also affect polymer biodegradation rate.

Many studies have been carried out to verify the actual biodegradability of these materials [Wenbiao et al., 2014; Shah et al., 2014], and it emerged that some species of thermophilic bacteria, (like *Thermomonospora fusca*, in conditions of high temperatures), as well as several microorganisms present in the soil (such as *R. bacteria. Depolimerans* and *Leptothrix*, at room temperature), are able to degrade these materials within a few weeks. As far as the degradation mechanism is concerned, the bacteria initially attack the aliphatic portion, which act as trigger for the degradation of the entire chain, until oligomers and then the starting monomers are obtained.

These aromatic-aliphatic copolyesters have been deeply investigated during the last few years, not only from the academic point of view but also at industrial level [Shah et al., 2014]. For example, introduction of phenyl side chains to poly(butylene succinate) (PBS) and poly(ethylene adipate) (PEA) was investigated [Jin et al., 2000]. Many studies on potential degradable aliphatic/aromatic copolyesters and blends prepared by poly(butylene terephthalate) (PBT) and aliphatic polyesters have been reported [Witt et al., 1995; Ki et al., 2000; Nagata et al., 2000; Witt et al., 1996; Kim et al., 1999; Lee et al., 1999; Kint et al., 2003]. Copolymerization between 2,5-furandicarboxylic acid or 2,5-thiophenedicarboxylic acid and adipic acid was also investigated [Wenbiao et al., 2014; Soccio et al., 2016].

The most important example of aliphatic/aromatic copolyester is represented by poly(butylene adipate-co-terephthalate) (PBAT), based on adipic acid, terephthalic acid and 1,4-butanediol, whose structure is shown in Figure 1.24. It is commercialized under different trade names, such as Ecoflex® by BASF [BASF], Easter Bio® from Eastman Chemical and Origo-Bi® from Novamont. This interesting material has properties similar to those of LDPE and has obtained both European (DIN EN 13432) and American (ASTM D 6400) certifications of biodegradability and compostability [Witt et al., 1996; Jacquel et al., 2015].

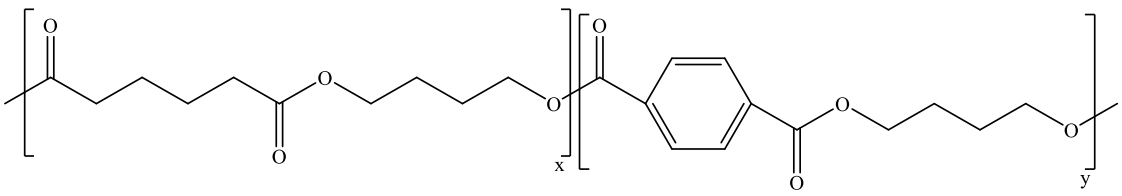

Figure 1.24. Chemical structure of poly(butylene adipate-*co*-terephthalate).

This material can also be mixed with other biodegradable polymers (such as starch products), to produce agricultural films. According to BASF Technical Bulletin, its compatibility with PLA, other polyesters and starch products is excellent. Ecoflex™ is used for compost bags for organic waste, agricultural and household films, coating materials for starch-based products (e.g., plates, cups) within the food industry, when high resistance to humidity and fat is needed. Ecovio™ is another commercial example of aromatic/aliphatic copolymer, made up partly of renewable raw materials. It is BASF Ecoflex™ combined with polylactic acid, which is obtained from sugars. Products made with Ecovio™ show high performances and durability, comparable to those of conventional plastics. Moreover, they can find applications as bags for organic waste, films in agriculture, compostable coffee capsules and as protecting aroma outer package.

1.7 Degradation processes

According to the standard requirements (ASTM D6400, ASTM D6866, ASTMD 7081, EN13432), the definition of biodegradability is the capability of a material to undergo decomposition into water, carbon dioxide, methane, inorganic compounds and biomass, whether by hydrolysis or by the enzymatic action of microorganisms [Bastioli, 2005].

Conventionally, materials are considered degradable or not in relation to effective degradation time: degradable materials are able to undergo degradation during their application, or immediately after it, whereas non-degradable ones need longer time to degrade than those of their effective application [Göpferich, 1996]. Polymer degradation consists in the scission of the main or side-chains, caused by thermal or mechanical activation, oxidation, hydrolysis, photolysis or radiolysis. As already mentioned, biodegradable polymers are also able to undergo degradation in biological environments by the enzymatic action of living cells or microorganisms (fungi, algae and bacteria). Soil, seas, rivers and lakes but also the human body are some examples of these environments. As to the solid ones, the two categories of polymers principally investigated in literature, and the only recognized by the norms and the market as biodegradable are:

- compostable materials, that degrade under composting conditions;
- materials that degrade in soil.

Biodegradation catalysed by microorganisms can occur in the presence (aerobic) or in absence (anaerobic) of oxygen, leading to the formation of carbon dioxide, water and new biomass through a three-steps mechanism: bio-deterioration (alteration of chemical and physical properties of the material), bio-fragmentation (polymeric chain breaking via enzymatic cleavage) and assimilation (uptake of molecules by microorganisms) and, in the end, mineralization (production of oxidized metabolites after degradation) [Pathak et al., 2017]. These processes can be described according to the following equations for aerobic (Eqn. [26]) and anaerobic (Eqn. [27]) processes, respectively:

$$C_{polymer} + O_2 \rightarrow CO_2 + H_2O + C_{residue} + C_{biomass} + salts \quad \textbf{[26]}$$

$$C_{polymer}\ CO_2 + CH_4 + H_2O + C_{residue} + C_{biomass} + salts \quad \textbf{[27]}$$

Where C represents Carbon atoms. If oxygen is present, aerobic biodegradation takes place and carbon dioxide is produced, whereas if no oxygen is involved, anaerobic degradation occurs and methane is produced instead of carbon dioxide [Leja et al., 2010].

Regarding polymers which can degrade in the human body, they should be more correctly defined as absorbable, resorbable or bioabsorbable, regardless of whether degradation occurs by enzymatic or chemical hydrolysis [Ikada et al., 2000]. Materials undergo degradation *in vivo* through a two-step mechanism, starting with chemical hydrolysis. This process is often considered autocatalytic, as chain scission leads to the formation of carboxylic end groups, which increase the acid environment and therefore accelerate the hydrolytic degradation rate. The second phase involves metabolic reactions: monomer fragments are converted into non-toxic products (i.e., lactic acid) which can be easily excreted from metabolism [Boland et al., 2016].

Degradation is affected by several factors, like matrix morphology, chemical and stereochemical structure, chain orientation, sequence disposition, molecular weight and its distribution, thermal properties, eventual presence of residual monomers, oligomers and other low molecular weight products, size, shape and porosity of the sample and degradation environment (i.e. humidity and oxygen %, presence of microorganisms or enzymes, pH and temperature) [Hakkarainen, 2002]. Crystallinity is the most important factor that affects degradation rate of solid polymers. Both enzymatic and non-enzymatic degradations proceed easier inside amorphous regions, which allow the diffusion of water and enzymes, than inside

crystalline regions, although crystals can be eventually degraded starting from the edges inward.

Polyesters are considered as biodegradable materials, thanks to the presence of ester bonds, which can be either hydrolysed or cleaved by enzymes, like lipases.

If this assumption is surely true for aliphatic polyesters, thanks to their potentially hydrolysable ester bonds and relatively short aliphatic chains, pure aromatic polyesters like PET or PBT are quite insensitive to any hydrolytic degradation at mild conditions, and enzymatic degradation is not particularly effective. This is probably due to less accessibility of ester bonds, due to steric hindrance of aromatic groups, for the lipases, which catalyse hydrolytic cleavage [Muller et al., 2006]. On the other hand, preliminary studies showed that some low molecular weight esters containing aromatic rings could be hydrolysed by lipases [Marten et al., 2003]. In addition, recently commercial low crystalline PET used to produce drink bottles could be depolymerized by the action of *Thermobifida fusca* at a very promising rate (17 µm/week at a temperature of 55°C, so that a 100 µm film would totally dissolve in 3 weeks) [Muller et al., 2005].

As already said, copolymers containing both aliphatic and aromatic sub-units represent a possible solution to biodegradability issues: the introduction of aliphatic moieties, in fact, can enhance both water uptake and hydrolytic chain scission. As an example, for copolyesters synthesized from adipic acid, terephthalic acid and 1,4-butanediol, amounts of about 50–60% of terephthalic acid was reported to be the upper limit for biodegradability [Muller et al., 2001]. Moreover, in the case of commercial copolyester Ecoflex®, the absence of accumulation of aromatic oligomers formed during depolymerization by composting process has been proven, and no ecotoxic effect resulted from these intermediates [Muller et al., 2001].

1.7.1 Hydrolytic degradation

Hydrolytic degradation is defined as scission of chemical bonds inside the polymer chain, by water uptake, to form oligomers and then monomers. During the first step, water attacks the water-labile bonds either by direct access to the material surface or by imbibition in the polymer matrix, followed by bond cleavage [Azevedo et al., 2004; Rydz et al., 2015]. In addition to neutral hydrolysis, which is the nucleophilic attack by H_2O, hydrolysis can be also catalysed by acid or basic environments or enzymes.

Therefore, in order to undergo degradation by the action of water, polymers must contain hydrolysable bonds like esters and orthoesters, anhydrides, ethers, amides, carbamides or ester amides [Lucas et al., 2008]. This kind of materials are considered as hydrophilic, as they can retain large amounts of water and can consequently degrade quite fast [Göpferich, 1996]. The type of bonds influences also the hydrolysis rate: orthoesters and anhydrides are the most reactive bonds, followed by amides and esters. Conversely, hydrophobic polymers, which cannot take up large quantities of water, are characterized by low degradation rates.

In addition, all degradable polymers can undergo surface (homogeneous) or bulk (heterogeneous) erosion: the preferred way depends on diffusivity of water inside the matrix, on the degradation rate of the functional groups inside the macromolecular chains and on the matrix dimensions (Figure 1.25) [Von Burkersroda et al., 2002].

Generally, bulk erosion takes place when water diffusion into the polymer is faster than the degradation of polymer bonds, whereas surface erosion occurs when the degradation of the polymer bonds is faster than water diffusion [Von Burkersroda et al., 2002].

Crystallinity degree, as well as hydrophilicity, play a relevant role in determining polymers degradability, as they significantly affect the surface accessibility. In fact, the crystalline regions hamper the accessibility of water and limit the degradation to the amorphous phase [Van der Zee, 1997].

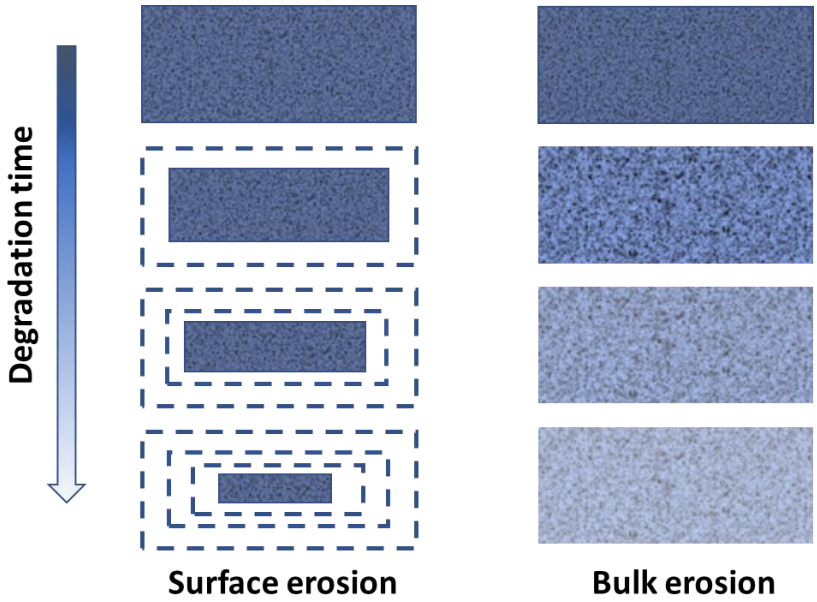

Figure 1.25. Changes of polymeric matrix during surface and bulk erosion.

The hydrolytic degradation of aliphatic polyesters occurs in bulk: the intrusion of water in polymeric bulk triggers the chemical degradation, leading to the formation of oligomers and monomers. From a macroscopic point of view, it is possible to distinguish two different phases. The first one consists in random cleavage of polymer chains with a concomitant decrease in molecular weight (while gravimetric weight losses are negligible), leading to a decrease in mechanical properties. During the last second stage of degradation, the molecular fragments are solubilized, disappearing with consequent loss in gravimetric weight [Grima et al., 2002].

1.7.2 Biodegradation in compost

Compostability is the ability of a material to undergo degradation when buried in a compost medium where moisture, aerobic environment and temperature are controlled. Nowadays there are many standard associations, which have defined worldwide standardized tests, aiming to assess "biodegradable" labels, like ISO and ASTM. For instance, ASTM D 6400 and ASTM D 6002-96 standards describe the requirements that a material should satisfy in order to be "compostable in municipal and industrial composting facilities". According to them, composting is defined as "a managed process that controls the biological decomposition and transformation of biodegradable materials into a humus-like substance called compost. The aerobic mesophilic and thermophilic degradation of organic matter make compost, the transformation of biologically decomposable material through a controlled process of biooxidation that proceeds through mesophilic and thermophilic phases results in the production of carbon dioxide, water, minerals and stabilized organic matter (compost or humus)". Therefore, in order to be compostable, a material should be not only biodegradable but has also to satisfy additional requirements such as [Rudnik, 2008]:

- conversion of the material (in powder, film or granular form) into carbon dioxide, water and biomass under micro-bacterial action;
- 90% of conversion into carbon dioxide and less than 10% of residual material with a size of 2 mm;
- same rate of biodegradation as other known compostable materials (leaves, grass, paper, etc…);
- time of biodegradation less than 180 days;
- absence of negative effects on the composting process;

- no-toxicity of the resulting compost.

In order to have the optimum biological activity in each stage of the process, compost must be of high quality. More in details, six parameters must be met [Compost Council of Canada]:

- balanced ratio of nutrients, consisting of dry carbonaceous materials, together with humid nitrogenous ones;
- adequate humidity %, coming from both nitrogenous materials, water supplied during the process and rainfall;
- porosity of the substrate, which must allow adequate air circulation;
- presence of air (at least 10-12%) necessary to microorganisms for the oxidation and metabolization of organic matter and supplied by both the porosity of the substrate and holes due to the presence of structuring materials like hood;
- proper temperature, which allows the development of micro-organisms as well as the elimination of those harmful for humans;
- variable pH, depending on the phase in which the process is located: during the initial oxidation process it should be around 9, reaching values of 7-7.5 at the end of the maturation phase.

According to ASTM standard, degradation of the waste in compost proceeds in three phases [Compost Council of Canada; Tuomela, 2002]:

1. Mesophilic phase: at the beginning, mesophilic bacteria and fungi degrade soluble organic matter compounds like monosaccharides, lipids and starch. Bacteria produce organic acids, and pH decreases to 5–5.5. Temperature rises spontaneously as exothermic degradation reactions release heat. Conversely, proteins degradation is related to the release of ammonia: for this reason, pH rises rapidly to 8–9. This phase can last from a few hours to some days.
2. Thermophilic phase: thermophilic phase starts when the temperature reaches 40ºC. The presence of thermophilic bacteria and fungi is observed, and the degradation rate increases. However, if temperature exceeds 55–60ºC, microbial activity and diversity rapidly decrease. After this heating, pH reaches a neutral level and then remains stable. The thermophilic phase can last from some days to several months.

3. Cooling and maturation phase: after the consumption of easily degradable carbon sources, compost starts cooling down, and then becomes stable. Mesophilic bacteria and fungi appear again (actinomycetes, some protists and many macro-organisms) even though most of the species are different from those of the mesophilic phase. From this point onwards, maturation starts. This phase is characterized by slow biological processes. Compost is then humified and becomes mature.

The duration of the different steps depends on the composition of the organic matter and the efficiency of the process, which can be checked through oxygen consumption [Rudnik, 2008]. Polymer degradation in compost can be evaluated by measurements of the molecular weight, which changes due to bond cleavage, or the gravimetric weight loss, which is due to depletion of low molecular weight species. Other parameters that can be useful to evaluate degradation are mechanical strength, degradation into monomers and monomers release. As to this last point, the Sturm Test can be particularly helpful to assess the ready biodegradability of materials [Sturm, 1973].

1.8 Fields of application

As already said, thanks to the abundance of monomers employed in polyester synthesis it is possible to prepare a wide range of materials possessing specific characteristics for many different applications. Moreover, polyesters can be processed by most conventional plastic processing techniques, like film extrusion, injection moulding, blow moulding and thermoforming. Two of the main sectors where these materials find application are biomedicine and packaging [Vroman et al., 2009]. In fact, thanks to their mechanical performance, biodegradability and biocompatibility, aliphatic polyesters are used, for example, for the fabrication of both medical (prosthesis, artificial skin, dental implants, vascular grafts, stents, bone screws and plates for temporary fracture fixation, porous structures for tissue engineering) [Diaz et al., 2014; Sokolsky-Papkov et al., 2007] and pharmacological devices (like controlled drug release systems for birth control and cancer therapy) [Catro et al., 2008]. Among other biomedical applications that are still at research level, polymer-based functions like targeting of receptors, promoting intracellular penetration of recalcitrant drugs and transfecting genes should be mentioned.

Apart from biomedicine, polyesters, both aromatic and aliphatic, find many applications in the environmental field: packaging, mulching and agricultural films, coatings for seeds, cigarette filters, cartridge and cartridge wax are only some example of this kind of applications [Vert, 2005]. In this field too, the use of biodegradable materials should be preferred, in order to avoid plastic accumulation issues.

Given the complexity and the range of applications in which polymeric biomaterials are currently used, there is not one polymeric system that could be considered the ideal one [Nair et al., 2007]. This underlines the need to dispose of a wide range of biodegradable materials that can match the specific requirements of each application.

1.8.1 Biomedical applications

Biomedicine is one of the most important field of application of polyesters. Among these materials, bioresorbable ones are of utmost interest, as their chains can be broken down in biological environment and excreted or resorbed without any surgical removal. Natural polymers like collagen, elastin, alginates, hyaluronic acid, albumin, chitin and fibrin were the first employed in this field, thanks to their intrinsic advantage of containing biological recognition sites. As natural polyesters are concerned with problems of purification, immunogenicity and contamination [Lutolf et al., 2005], from the 1960s, research started focusing in synthetic biomimetic and biodegradable polymers, such as poly(lactic acid), poly(glycolic acid), poly(lactic-co-glicolic acid), poly(ε-caprolactone) and their copolymers and polyhydroxyalkanoates. In the last years, as mentioned earlier, researchers focused their attention also on other materials, such as PBS and its copolymers.

For this kind of applications, biocompatibility represents a primary issue. There are many standardized tests developed by the U.S. Food and Drug Administration (FDA), the International Organization for Standardization (ISO) and the Japanese Ministry of Health and Welfare (JMHW), which assess all the requirements that a material should satisfy in order to be used in biomedical field.

Biocompatibility is tested both in vitro and in vivo. As to the first kind of tests, the most important are [Elisseeff et al., 2002]:

- cytotoxicity: cells are exposed directly to a polymeric surface (direct cytotoxicity), or indirectly by contact with polymeric by-products (indirect cytotoxicity), according to

the ISO10993-5. [UNI EN ISO 10993-5; Harmand, 1999]. After that, cell viability, proliferation and functionality must be verified;

- Cell viability: it is usually investigated by vital stains, like neutral red and tripan blue dyes. In particular, alive cells stain red, and the dead ones blue;
- Cell proliferation: it is usually checked by 3-[4-5-dimethylthiazol-2-yl]-2-5-diphenyl bromide tetrazolium bromide (MTT) and alamar blue methods. MTT is reduced to blue formazan crystals by the action of mitochondria, and then measured by spectrophotometric analysis [Smith et al., 1992]. Alamar is a nofluorescent blue which is reduced to fluorescent pink in viable cells. This method does not require cell destruction for the evaluation of proliferation.

In vivo compatibility evaluation is the following step to determine the compatibility of a material [ISO 1997]. According to ISO standards, short-term and long-term evaluations must be performed, and both local and systemic reactions should be investigated. These reactions include irritation, sensitization, hemocompatibility, carcinogenicity and genotoxicity. Short-term evaluations include subcutaneous implantation in rats, whose inflammatory response is evaluated at different time points (from 3 to 14 days), while potential systemic effects are analysed through blood, white cells and urine analyses and by determining the eventual presence of any polymeric by-products inside tissues or organs. It is important to say that all these in vivo experiments should accomplish ethical and legal rules, like the European Directive 86/609 – *Protection of Experimental Animals*, recently replaced by the Directive 2010/63 [Louhimies, 2002].

Biocompatibility, as well as mechanical properties (which have to be compatible to the implant site), hydrophilicity and biodegradation rate, can be tailored by acting on polymer chemistry, molecular weight, hydrophobicity/hydrophilicity ratio, surface charge, water adsorption and degradation mechanism.

1.8.1.1 Controlled drug release

One of the biggest challenges in the field of pharmacokinetics is to provide the therapeutic level of drug in a specific tissue during the entire length of treatment. Traditional delivery systems present an immediate release kinetics, without any control of the delivery process. As drug

adsorption is controlled only by the ability of human body to absorb these molecules, drug concentration in different tissues is characterized by an initial peak, sometimes almost reaching a toxic threshold, followed by a fast decrease to levels even below the effective therapeutic ones [Grassi et al.,2005; Langer et al., 1984].

In this framework, controlled drug delivery (CDD) is a widely investigated field, which aims to obtain constant concentration of therapeutic compounds in blood with minimum fluctuations, a predictable and reproducible release over a long period of time, optimized therapies and better patient compliance, protection of bioactive compounds with a short half-life, limiting in the same time side-effects, waste of drug and frequent dosing [Langer et al., 1998; Bajpai et al., 2008].

For all these reasons, it is not surprising that the market of controlled drug release has registered a continuous growth during the last few years: from studies carried out by Controlled Drug Release Society [Controlled Release Society], this market was about 171.8 billion of dollars 2016 and is predicted to reach almost 225.8 billion dollars by 2020 (Figure 1.26).

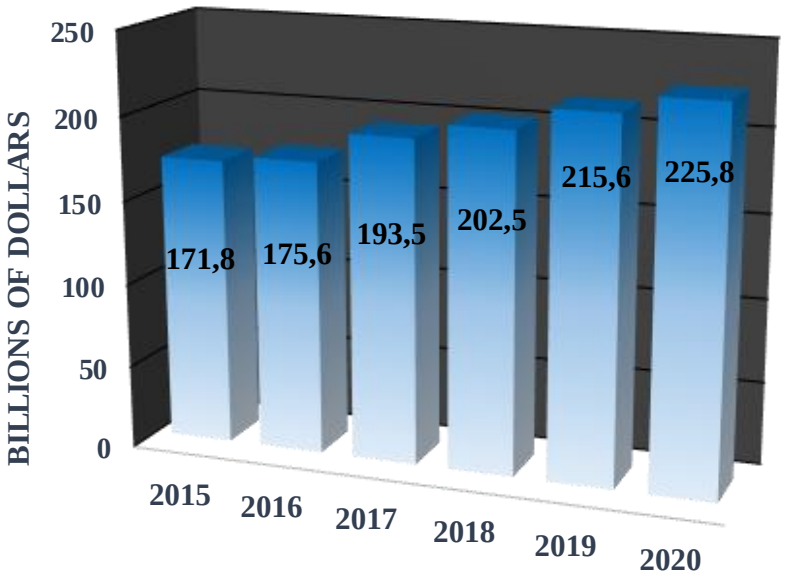

Figure 1.26. Global market of drug delivery systems (2015-2020).

(Source: Controlled Release Society 2018)

Modified drug delivery systems can cover many different release profiles (Figure 1.27):

1. delayed, but not constant release;
2. delayed for a finite “lag” time, followed by a constant rate release. These systems may be useful for the delivery of active agents during the night;

3. constant (or zero order) release: drugs are released at a constant rate so that their concentration in the blood stream remains constant at an optimal level of effectiveness;
4. delayed release followed by a tight pulse of drug. These systems may be useful both for nocturnal delivery and for the delivery of hormones, which usually requires pulsed rather than constant administrations;
5. multiple pulses release at specific timepoints.

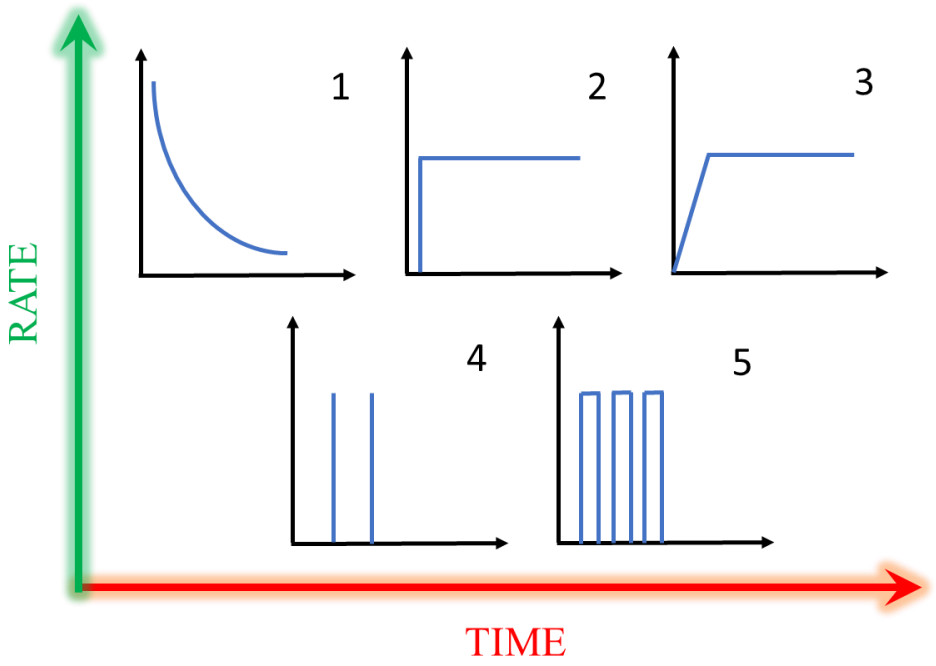

Figure 1.27. Different drug release profiles.

Drug delivery systems can be also classified according to the release mechanism:

- diffusion controlled systems: drugs diffuse through the polymer, which may then undergo biodegradation after exhaustion of the drug. There are two kinds of diffusion-controlled systems: reservoir (membrane) or matrix (monolithic) ones. The first are hollow devices, in which a drug core is encapsulated and surrounded by a polymeric membrane. Drug diffusion through the membrane is rate limiting and controls the overall release rate. The drug transport through the membrane usually follows a solution-diffusion mechanism at a constant rate, ensured by a saturated concentration of the drug inside the reservoir. In matrix systems, the drug is uniformly dispersed or dissolved. These devices are easier to formulate but present a first-order and

continuously decreasing release rate. This behaviour is due to the higher diffusion path length and the reduction of the surface area as the matrix release goes on.

- chemically controlled systems: in this case drug release usually takes place in the aqueous environment by either gradual biodegradation of a drug-containing polymeric system, biodegradation of unstable bonds through which the drug is coupled to the polymer, or both. In the former case, the polymer erodes thanks to the presence of hydrolytically or enzymatically labile bonds. As erosion, either in bulk or at the surface, occurs, the drug is released. In the latter approach, drug release is controlled by the rate of hydrolysis, which is responsible for the cleavage of chemical bonds between the drug and the polymer backbone;
- swelling controlled systems: this is the case of hydrogels, which consist of macromolecular chains cross-linked in a mesh structure, providing a matrix for drugs entrapment. When these hydrogels are placed at a temperature above their T_g and are in contact with a thermodynamically compatible solvent, polymeric chains relax [Shukla et al., 2003]. Swelling is the macroscopic result of this transition. Thus, external medium can enter inside the mesh and in the same time the dissolved drug diffuses through the swollen polymeric layer into the external environment;
- modulated release systems: in this case, drug release is controlled by external stimuli such as temperature, pH, electric or electromagnetic field, ionic strength, UV light, etc.

Aliphatic polymers, both natural and synthetic, are the most used materials for the fabrication of carriers with controlled drug delivery properties so far. Moreover, bioresorbability is a primary requirement that has to be satisfied, in order to avoid surgical removal after implantation [Jalil et al., 1990]. As to the synthetic polyesters, blends and copolymers of PLLA have been investigated, like poly(D,L-lactic acid) and poly(lactic-co-glycolic acid). The slow biodegradation rate of PLLA has limited the research on drug delivery systems based on this polyester alone [Zielhuis et al., 2007; Lensen et al., 2010]. For example, PDLLA has been commonly used as a drug delivery film for inorganic implants [Ulery et al., 2011], while PLGA has been used to deliver chemotherapeutics, proteins, anti-inflammatory drugs, vaccines, antibiotics, analgesics and siRNA [Ulery et al., 2011]. A commercially available drug delivery system based on injectable PLGA microspheres is Lupron Depot®, which is used for the treatment of endometriosis and prostatic cancer [Lofgren et al., 1995].

Also poly(caprolactone), due to its very low in vivo degradation rate and high drug permeability, has found applications as a long-term implant delivery device: Capronor® is a commercial contraceptive PCL product, which is able to release levonorgestrel in vivo for more than a year [Darney et al., 1989].

The shape of the drug carriers are usually nano-spheres, microspheres, beads, cylinders, and discs. Among these, micro- and nano-spheres, which are able to incorporate and release drugs through physical diffusion, followed by resorption of the polymeric material, are the most widely used. Such microspheres can be prepared with a simple and quite fast solvent-evaporation method [Ikada et al., 2000].

1.8.1.2 Tissue engineering

Disease, injury and trauma can cause damage and degeneration of human tissues. Conventional treatments are limited to transplanting tissue from one site to another into the same patient or from other individuals. These solutions, even though are clearly revolutionary, are related to several problems in terms of costs, discomfort for the patient, anatomical limits, eventual infections or rejections, and limited donors' availability. An alternative can be represented by tissue engineering, which aims to regenerate damaged tissues, instead of replacing them.

Just to give an idea about how regenerative medicine represents an important and continuously growing field, recent studies evidenced that the global market of tissue engineering was valued at 27 billion dollars in 2015 and is expected to increase from 32 billion in 2018 to 135 billion in 2024 (Figure 1.28) [BCC Research].

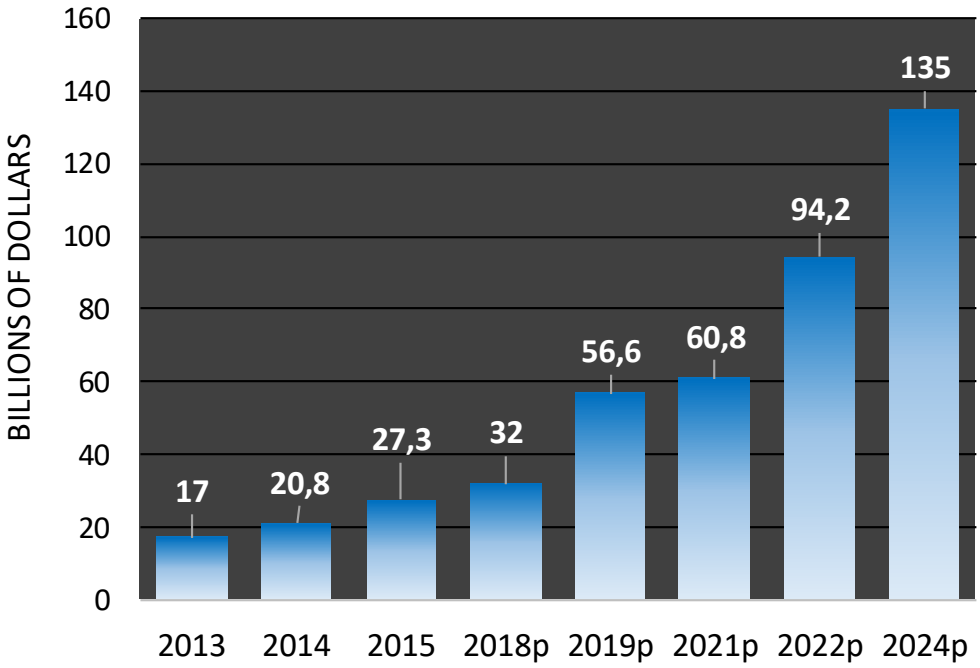

Figure 1.28. Global tissue engineering and regenerative medicine market 2013-2024.

(Source: BCC Research, 2016)

The term "tissue engineering" was officially defined in 1988, during the National Science Foundation workshop, as a multidisciplinary and innovative field in which polymer chemistry, chemical engineering, materials science and biology principles are applied in order to develop biological substitutes able to maintain, restore or improve tissue or organ function [Langer et al., 1993]. The so-called tissue engineering triad (Figure 1.29), on which regenerative processes are based, consists of:

- Cells, which can be obtained from the same patient (autologous), other patients (allogeneic) or other species (heterologous);
- Tissue inducing substances, like growth factors or genes involved in tissue formation;
- Three-dimensional matrices, called scaffolds, whose function is to provide a functional substrate for cell attachment, proliferation and even migration. Scaffolds should also support tissue development and maintain tissue shape, assuring in the same time both the diffusion of nutrients, oxygen and signal molecules, and the removal of metabolic waste [Owen et al., 2010].

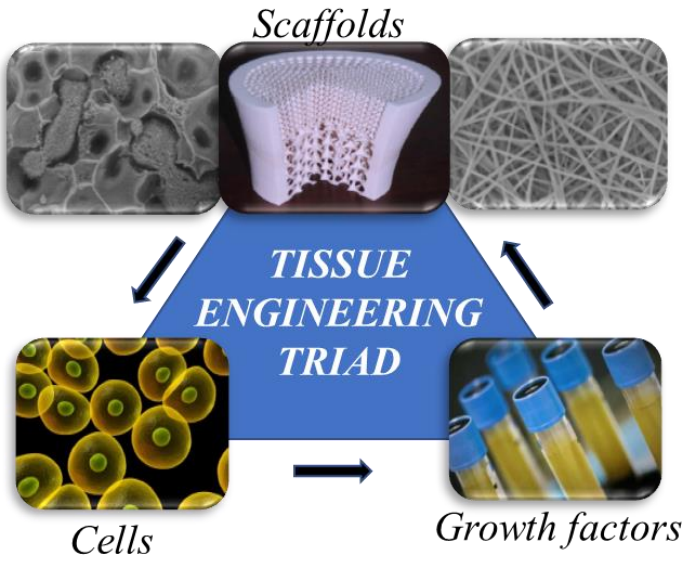

Figure 1.29. Tissue engineering triad.

From a practical point of view, scaffold implantation can occur in two ways: cellular and acellular methods. In the first, cells are seeded and proliferate on the scaffold outside the human body, in order to produce a tissue, which can be then implanted in the injured site. In the second case, scaffold is implanted directly on human body without any previous cell seeding; cells around the implant start entering the scaffold directly in vivo.

Regardless of the tissue type, as the ability of cells to recognize and react to changes in their environment is of primary importance in the development of physiological function in vitro as well as in vivo, it is necessary that materials used in tissue engineering should mimic the characteristics of extracellular matrix (ECM) naturally produced by cells. In addition, many requirements have to be considered, like:

- biocompatibility: cells should be able to adhere, grow, migrate and proliferate. Moreover, after implantation, the scaffold must not elicit any immune reaction, severe inflammatory response or rejection;
- biodegradability: scaffolds must be biodegradable, allowing cells to produce their own extracellular matrix [Babensee et al., 1998]. In addition, the degradation by-products should be no-toxic and metabolized by body without any interference;

- mechanical properties: ideally, the scaffold should have mechanical properties comparable to those of the implant site, from the time of implantation to the end of the remodelling process [Hutmacher, 2000];
- scaffold architecture: as already mentioned, an interconnected pore structure and high porosity are necessary to ensure cellular penetration, an adequate diffusion of nutrients to cells and their extra-cellular matrix and diffusion of waste products out of the scaffold. Moreover, pores should be large enough to allow cells migration into the structure, but not too much in order to permit efficient binding of a critical number of cells to the scaffold [Yannas et al. 1989; O'Brien et al., 2005];
- manufacturing technology: to become clinically and commercially available, scaffolds must be fabricated through cost-effective techniques, which allow an easy scale-up at industrial level.

Various approaches have been developed to obtain biomimetic three-dimensional scaffolds, like rapid prototyping, phase separation, stereolithography, selective laser sintering, fused deposition modelling, 3D printing and electrospinning. Among these, electrospinning is one of the most used to obtain continuous micro- and nanofibers [Jiang et al., 2004], with diameters ranging from tens of nanometers to some microns, comparable to those of fibrous components of ECM. According to this easy procedure, a polymeric solution is subjected to a high voltage, which can create a fine charged jet. The so charged polymer is then ejected onto an opposite charged collector, where it dries, forming thin fibres after solvent evaporation. Properties like fiber diameter, porosity and morphology can be controlled by acting on many different parameters, such as voltage, solution viscosity and conductivity and process temperature. For example, solution viscosity has been found to influence fiber diameter: the higher the viscosity, the larger the diameters [Reneker et al., 2000]. In addition, morphological changes can occur after variations in the distance between the syringe and the collector: increasing this distance or decreasing the electrical field make the bead density decrease [Reneker et al., 2000].

As to the polymeric materials used for applications in soft tissue engineering, PLLA has been extensively used for the fabrication of scaffolds for bone, cartilage, tendon, neural, and vascular regeneration [Ulery et al., 2011], alone or copolymerized with PDLLA, poly(lactide-*co*-glycolide) (PLGA), poly(ε-caprolactone), poly(ethylene glycol) (PEG), collagen, and chitosan [Ulery et al., 2011]. For example, PLGA shows great cell adhesion and proliferation properties.

Another interesting material is PHB, whose biocompatibility, good processability and degradability make it an excellent candidate for applications in long-term tissue engineering [Ulery et al., 2011].

PCL too, thanks to its good processability and mechanical flexibility has been used for the fabrication of scaffolds for the regeneration of bone, ligaments, cartilage, skin, nerves and vascular tissues [Ulery et al., 2011].

1.8.2 Food packaging applications

Packaging represents the largest field of application of plastics, covering alone almost 40% of the European demand [Plastics – the Facts 2017]. In addition, more than 30% of all packaging consumption is related to food [Smart Packaging Market Size & Share, Industry Report]. To date, petrochemical-based plastics, such as PET, polyethylene (PE), polypropylene (PP) and polystyrene (PS) have been extensively used as packaging materials because of their relatively low cost, good mechanical performance, good barrier behaviour to oxygen, carbon dioxide and aroma compounds, and so on [Siracusa et al., 2008]. In recent years, severe pollution problems related to their not complete recyclability and their accumulation in the environment have led to the design of new bio-based materials for food packaging, to replace their non-biodegradable counterparts [De Azeredo, 2009].

Among the applications of biodegradable polymers in this field, disposable cutlery, drinking and salad cups, plates, straws, stirrers, lids and cups, overwrap and lamination films, plates and containers for food dispensed at fast-foods should be mentioned.

Food, contrary to inanimate substances, has a limited shelf-life and specific properties. During its conservation, it can be subjected to alterations caused by enzymatic, chemical, and physical reactions, and it can be attacked by microorganisms such as bacteria and fungi. For this reason, packaging plays a key role in food conservation and preservation from microbiological and chemical contamination, ensuring at the same time the maintenance of structural, organoleptic and nutritional properties.

In order to satisfy all these requirements, food packages should have tailored mechanical, optical, and barrier properties, which depend on the structure of the polymeric packaging material. Materials must be tough and flexible enough to ensure their manipulation without any

food damage, and they should be able to control gas exchanges between food and environment [Siracusa, 2012].

Package should be designed also in relation to the specific food: for products whose physical and chemical deteriorations are related to moisture content, it is necessary to limit as much as possible water vapour diffusion. As to fresh vegetables and fruits, the main limits to their shelf-life are high respiration rate, acidification, loss in consistency and discoloration, high ethylene production, unpleasant flavours production and microbial attacks [Amanatidou et al., 2000; Barry-Ryan et al., 2000 (a); Barry-Ryan et al., 2000 (b); Sandhya, 2010]. In this case, it is necessary to reduce the rate of respiration by limiting O_2 passage, which is responsible for the oxidative breakdown of the complex substrates inside the product. In addition, oxygen concentration below 8% is necessary to reduce the production of ethylene [Russo et al., 2006]. Modern technologies include the so-called modified atmosphere packaging (MAP), active packaging, and smart packaging, designed to improve quality and safety [Hotchkiss, 1995]. Under controlled conditions, the atmosphere is modified in a way as natural as possible, and maintained during storage [Pasha et al., 2014]. MAP hinders deterioration processes, reduces food respiration, delays ripening, lowers ethylene production, retards consistency loss and reduces chlorophyll degradation by varying oxygen, nitrogen and carbon dioxide concentrations [Ohlsson et al., 2002; Farber et al., 2003; Xing et al., 2010].

In addition, it is appropriate to take into account the changes that the characteristics of plastics can undergo when in contact with food [Scott, 2000] and after temperature variations during storage [Conn et al., 1995] (usually ranging from -30 °C to 60 °C).

For all these reasons, only a limited number of biodegradable polymers have suitable properties for food packaging applications so far. Among these, the most important are [Liu, 2005]:

- starch-based polyesters: they currently dominate the market for biodegradable materials. Their applications include both film and rigid containers such as bowls, glasses plates, etc. These polymers show very low permeability to oxygen, but due to their hydrophilicity they cannot be used in particularly humid environments;
- cellulose-based polyesters: in this case, research focused on the development of cellulose derivatives, because of the poor mechanical properties of the cellulose itself. Cellulose acetate is one of the most promising and is used as a film for both fresh and cooked product packaging. However, these films have poor barrier properties to gases

and in humid environments they hydrolyse, with the consequent formation of acetic acid. For these reasons, their diffusion underwent a significant slowdown;

- poly(lactic acid): it presents good barrier and mechanical properties, comparable to those of PET and can be processed by injection or blow moulding. 70% of PLA produced is used both for tableware and for food packaging. It is also suitable for applications in contact with greases and oils, since it is not affected by them;
- polyhydroxyalkanoates: among this family of materials, the most used is PHB, thanks to its thermal properties and mechanical behaviour, which are similar to those of polypropylene (PP), even though it is more rigid and fragile. The low affirmation of PHB as packaging material is due to its low impact resistance and high production costs; however, thanks to its biodegradability, the development of PHB-based materials for fabrication of bottles, envelopes and films instead of PP will be surely considered in the next future.

1.8.2.1. Flexible food packaging

Flexible packaging represents a constantly growing sector, which is attracting increasing interest even at industrial level: according to the latest statistics, it is estimated that flexible packaging market, which in 2017 was 237 billion dollars, will reach values of more than 290 billion of dollars in 2023 [Mordor Intelligence, 2018].

Only last year, the total volume of packaging market amounted to about 3500 billion units sold (Figure 1.30), 67% of which consisted of plastics, both rigid (28%), but for the most part flexible (39%). Furthermore, this volume is expected to increase by 11% by 2021.

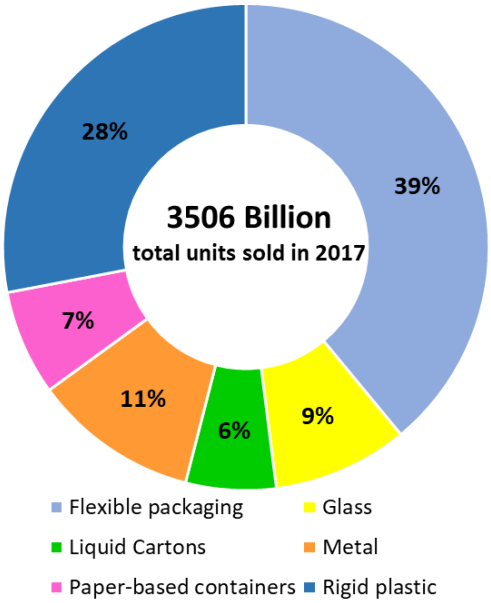

Figure 1.30. Global volume share of pack types, 2017.

(*Source: Euromonitor International*)

These numbers are not surprising. According to recent studies carried out by Flexible Packaging Europe, the substitution of all the packaging disposable on the market with flexible packaging, characterized by a lower density, and consequently lighter than the rigid one, would bring to a reduction of about 26 million tons of waste every year, as well as a reduction of 77% of the total amount recycled or landfilled. In addition, production costs and transport efficiency would be positively affected, maintaining the same functionality as rigid packaging. In fact, thin plastic films of only few microns of thickness can increase the shelf life of products, reducing at the same time energy consumption and greenhouse gas emissions. [Flexible Packaging: state of the industry report, 2017; Cooper, 2017].

Among the sectors in which flexible packaging is used, food market has registered the higher amounts, with over 20000 KTon every year (almost 80% of the total), followed by drinks, pet food, cosmetics, pharmaceutical products and tobacco. These values are expected to increase in the upcoming years [SmithersPira 2017].

As regards the composition of flexible packaging, Figure 1.31 shows that films represent a predominant slice with 46%, followed by synthetic resins (23%), and other minor components such as inks, paper, adhesives and foil. More in details, the principal plastics used to produce films are polyethylene (41%), polypropylene (28%), polyester (16%), Nylon (13%) and polystyrene (<1%).

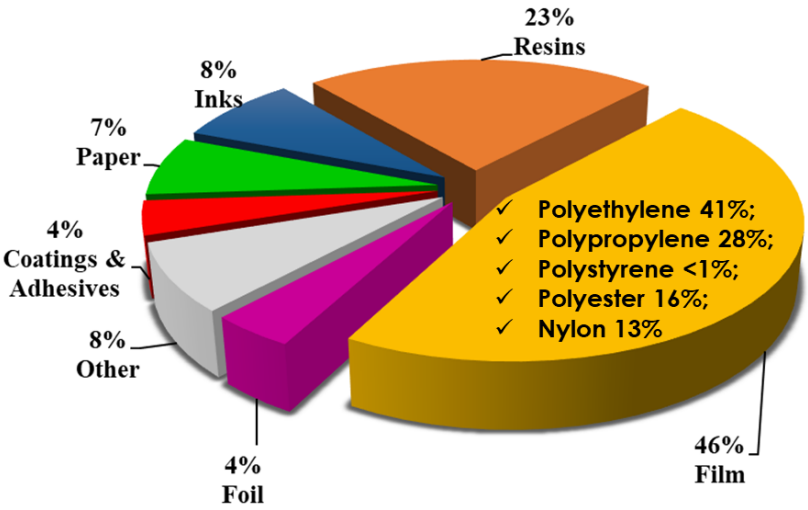

Figure 1.31. Composition of flexible packaging.

(Source: FPA 2016)

These materials can be recycled in many ways, including waste-to-energy, waste-to-fuel, waste-to-chemical and waste-to-monomer methods. However, the main drawback is the high recycling cost, taking also into account that recycling is not always possible in case of food packaging: if materials are contaminated by organic matter (grease, food residues, etc.) the only viable solutions are conversion, which is particularly expensive, and landfill.

For all these reasons, the use of biodegradable materials, such as bioplastics, should be favored.

2.AIM OF THE WORK

Biodegradable polyesters are attracting considerable attention for a wide range of applications, with a market continuously growing. Among the possible applications, flexible food packaging represents one of the most important fields. It is worth noticing that the 80% of the entire flexible packaging production is used in contact with food. In this scenario, biodegradable polyesters can represent a valid solution to issues related to accumulation of plastic waste in the environment, which is responsible for severe pollution problems, in the earth as well as in the oceans. Another alternative possible way to limit plastic accumulation could be recycling, through which plastics can be converted into energy, fuels, other chemicals or monomers. In 2016, for the first time, more plastic waste was recycled than landfilled [Plastics – the Facts 2017]. However, it has to be taken into account that recycling is not always possible, for example when packaging is contaminated by organic matter. In addition, as the recycling costs are generally high because of the presence, for example, of multilayer structures necessary to ensure high food safety, but also complicated to be separated, landfill is, unfortunately, most of the time the preferred choice. For all these reasons, the use of biodegradable and compostable materials should be preferred over conventional ones.

Another growing market of great importance in everyday life is that of health, in particular in fields such as regenerative medicine and pharmacology, with the fabrication of controlled drug delivery systems. In the former case, the corresponding market is predicted to reach 135 billion dollars by 2024. The use of 3-dimensional polymeric supports in order to favour cell and tissue regeneration can represent a valid alternative to conventional drug therapies or transplants, overcoming their drawbacks in terms of rejection and non-effectiveness, supporting at the same time the correct cell growth. This is of particular importance in cardiac tissue engineering, whose main problem is the irreversible loss of cardiac tissue due to heart failures or chronic diseases. In addition, if the materials used are able to hydrolyse in the human body without producing toxic products, it is possible to avoid the removal of the implant through surgery.

As to controlled drug release, it aims to avoid the side-effects related to conventional administration, ensuring a drug level in between the toxic and the effective ones during the entire therapy. The market of controlled drug delivery systems is predicted to reach almost 226 billion dollars by 2020.

Bioplastics, and in particular bio-polyesters, can represent a valid alternative for all these fields of applications, as they can satisfy at the same time the requirements of biodegradability,

biocompatibility with the environment where they are disposed and release of non-toxic degradation products, avoiding, in addition, the dependence on non-renewable sources.

To date, many aliphatic polyesters are already widely used for biomedical applications, while in the field of flexible food packaging also aromatic ones play a key role. More in details, Polylactic Acid (PLA) is already industrially produced and used for the fabrication of scaffolds as well as products for food-packaging [Pankaj et al., 2014]. This FDA approved material is characterized by high workability, biocompatibility and biodegradability, although the high rigidity does not make it suitable for applications in soft tissue engineering or flexible food packaging films. Another interesting aliphatic polyester, already used for packaging purposes thanks to its good mechanical properties and thermal stability, despite its high crystallinity degree, which is responsible for slow biodegradation rate and quite high rigidity [Papageorgiou et al., 2007], is poly(butylene succinate) (PBS). This material, recently FDA approved, turned out to be a potential candidate also in biomedicine, as widely described in literature [Gigli et al., 2016; Fabbri et al., 2018]. Among the aromatic polyesters, poly(ethylene furanoate), obtained from 2,5-furandicarboxylic acid, a fully bio-based building block, has recently attracted considerable attention as potential substitute of fossil-based PET. As to this point, Avantium, thanks to a close contact with Coca-Cola, is already planning the industrial production of PEF-bottles, with thermal, mechanical and barrier properties even better than those of PET. Although not yet on the market, poly(butylene 1,4-cyclohexanedicarboxylate) (PBCE) is another interesting bio-based aliphatic polyester, which is characterized by good thermal stability, interesting mechanical properties and also biodegradability [Berti et al., 2008 (b); Berti et al., 2010; Gigli et al., 2013 (a)].

Anyway, as already mentioned, these materials do not fulfil all the requirements needed for the applications of interest in the present Thesis. In this view, as it is well known, copolymerization represents a very efficient and useful tool to modify material properties, in order to get the most suitable ones for the specific applications. In this context, the present Thesis work aimed to demonstrate the high versatility of polyester class. In fact, through the researches carried out, we intended to show how, by using only one class of materials, it was possible to tailor *ad hoc* functional properties in relation to the intended use. On one side, the attention was focused on flexible food packaging, which is one of the most demanding in terms of plastic sources, on the other on soft tissue engineering and controlled drug release, as they represent the new frontier of biomedicine.

The research activity has been developed according to two different approaches. In one case, the chemical modification of polymers already available on the market was carried out with the aim of improving performances not optimal for the applications of interest, without detriment to those already satisfactory. In particular, thanks to copolymerization, it was possible to obtain highly biodegradable, more flexible and compostable materials, with good barrier performances, acting on the chemical structure and on the molecular architecture. As to the former, the effect of the length of glycolic subunit, of the presence and the length of ramification and of different heteroatoms (oxygen vs. sulfur), was investigated. On the other hand, the effect of molecular architecture, i.e. block vs. random distribution of comonomeric units, was evaluated. The molecular architecture will be controlled through different synthetic strategies: polycondensation allowed the synthesis of random copolymers, whereas through reactive blending it was possible to synthesize copolymers with different block length. Lastly, multiblock as well as triblock copolymers can be realized through chain extension, starting from prepolymers obtained by polycondensation, reactive blending or ring opening polymerization of L-lactide. It is worth noticing that all these techniques are solvent-free, simple and economic, and can be easily used for industrial scale-up.

The second research line of the present Thesis focused on the synthesis and characterization of new bio-based homopolymers and copolymers, to obtain new materials with a wide range of properties depending on the kind and the relative amount of the comonomeric units along the polymer chain as well as on the molecular architecture. In the following, a diagram reporting the different research activities carried out during the PhD is shown.

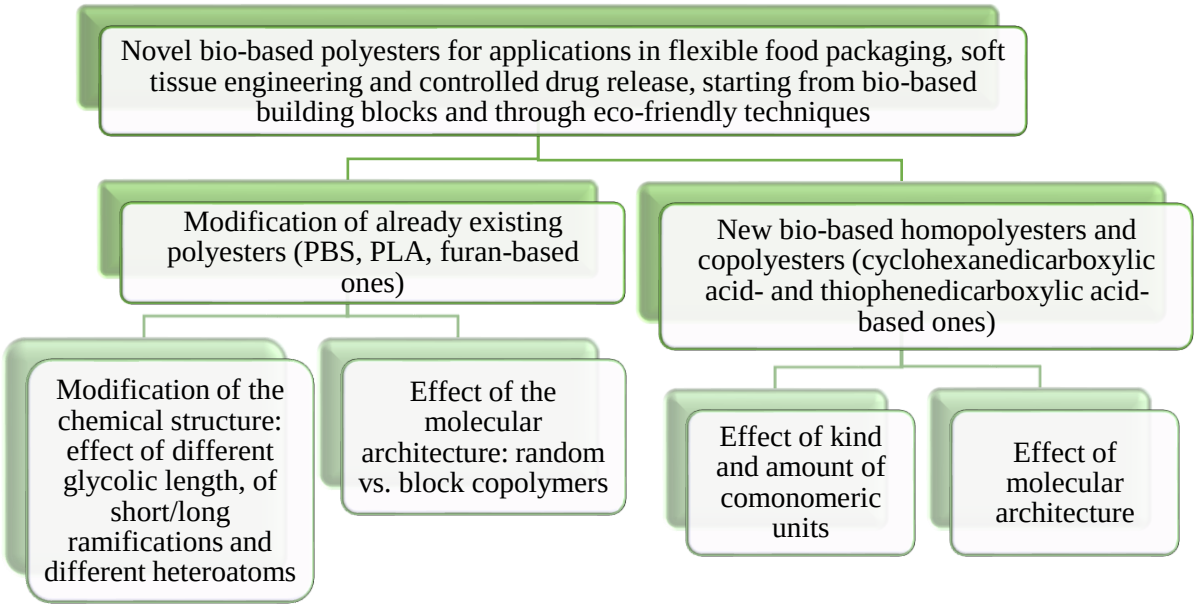

The whole Research activity consisted of the following steps:

- detailed bibliographic research to get the state of the art on the subject;
- synthesis of the new polyesters, through previous optimization of the reaction conditions;
- molecular, thermal, structural and mechanical characterization of the synthesized polymers;
- evaluation of the biodegradability under different environments and conditions.

In addition, in the case of flexible food packaging applications, barrier properties at different temperature and humidity conditions were checked, while for biomedicine, in case of soft tissue engineering, the fabrication of polymeric scaffolds was performed, and their biocompatibility tested. For controlled drug delivery applications, release profile studies of a model drug have been carried out.

The properties of the materials under study have been correlated to the chemical structure, to establish structure-property correlations, which are fundamental for an *ad-hoc* design of materials for specific applications.

3.MATERIALS AND METHODS

3.1 Materials

1,3-propanediol (1,3-PD), 1,4-butanediol (1,4- BD), 1,5-pentanediol (1,5-PeD), 1,6-hexanediol (1,6-HD), dimethylsuccinate (DMS), dimethyladipate (DMA), titanium tetrabutoxide ($Ti(OBu)_4$), titanium(IV) isopropoxide (TTIP), Sn(II)-2 ethylhexanoate ($Sn(Oct)_2$), and hexamethylene diisocyanate (HDI) were purchased from Sigma Aldrich (Milan, Italy). *Trans*-1,4-cyclohexanedicarboxylic acid (*Trans*-CHDA) containing 99% of *trans* isomer, 1,4-cyclohexanedicarboxylic acid (CHDA) containing a mixture of *cis*- and *trans*- isomers, triethylene glycol (TEG), neopentyl glycol (NPG), 2-butyl-2-ethyl propanediol (BEPD), 2,5-furandicarboxylic acid (FDCA), 2,5-thiophene dicarboxylic acid (TFDCA) and Dexamethasone (DXM) were purchased by TCI Europe (Zwijndrecht, Belgium). L-lactide (L-LAC, Chiral purity >99%) has been kindly provided by Purac (Amsterdam, The Netherlands) whereas Pripol 1009 has been kindly purchased by CRODA (Snaith, UK). All the used chemicals were reagent grade products and used without any further purification. In Figure 3.1 the chemical structures of the reagents employed in the syntheses are reported, while in Figure 3.2 those of catalysts and the chain extender are shown.

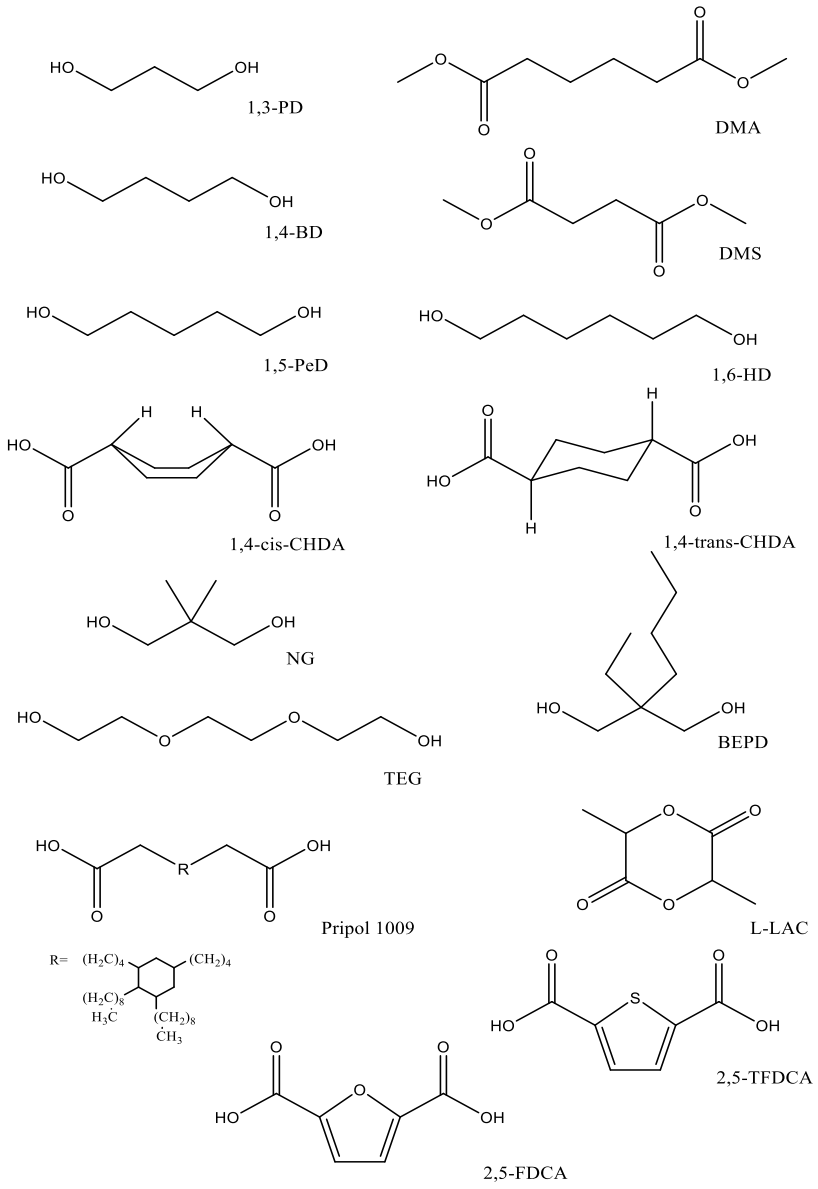

Figure 3.1. Chemical structures of the reagents.

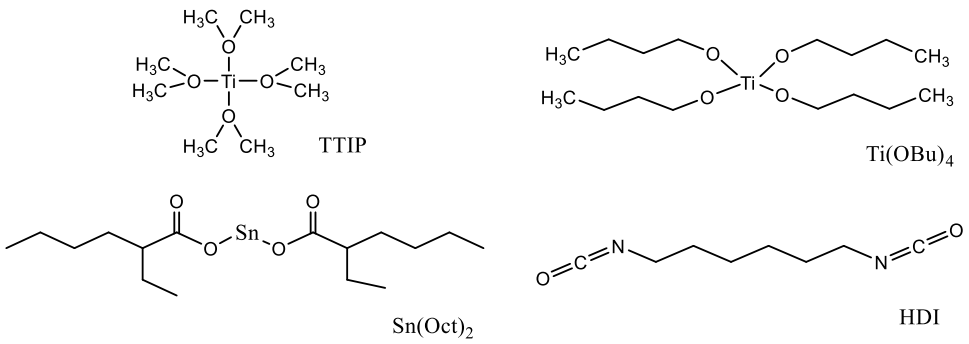

Figure 3.2. Chemical structures of the catalysts and the chain extender.

3.2 Synthetic strategies

In order to obtain the designed polymers, different synthetic strategies have been used:

- **Two-step melt polycondensation:** this approach has been employed to prepare homopolymers and random copolymers with both low (hydroxyl-terminated prepolymers) and high molecular weight (Figure 3.3).

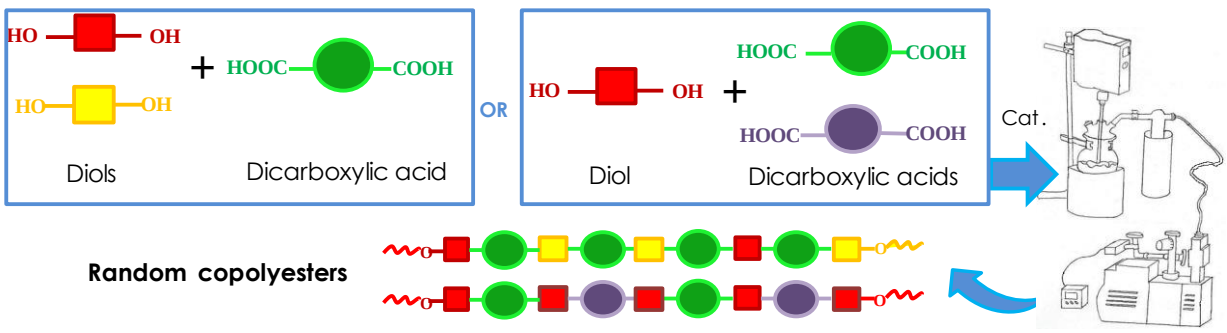

Figure 3.3. Schematic representation of polycondensation reactions.

- **Reactive blending:** this approach has been used to synthesize copolymers with different molecular structure. Starting from two molten parent homopolymers, just by varying the reaction time it was possible to obtain both block and random copolymers (Figure 3.4).

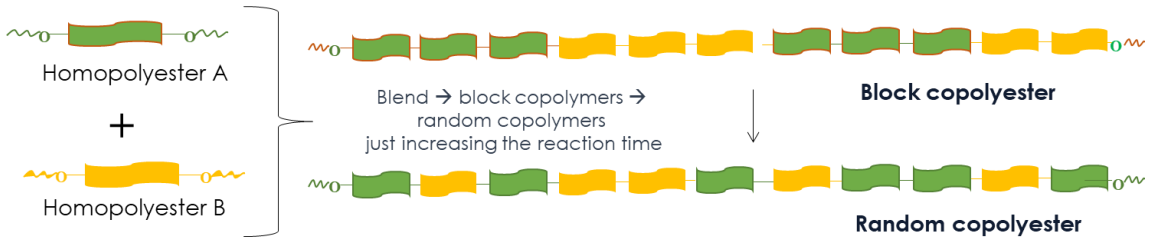

Figure 3.4. Schematic representation of reactive blending.

- **Ring opening polymerization (ROP)** of L-lactide: starting from hydroxyl-terminated prepolymers, used as initiators, and Sn(II)-2-ethylhexanoate as catalyst (100ppm/g polymer) it was possible to obtain Poly(lactic acid) based triblock copolymers (Figure 3.5). After ROP, these materials can also be chain extended, in order to obtain high molecular weight copolymers.

Figure 3.5. Schematic representation of ring opening polymerization reactions.

- **Chain extension**: this technique has been used to obtain triblock or multi-block copolyesters starting from OH-terminated prepolymers and hexamethylene diisocyanate (HDI) as chain extender (Figure 3.6).

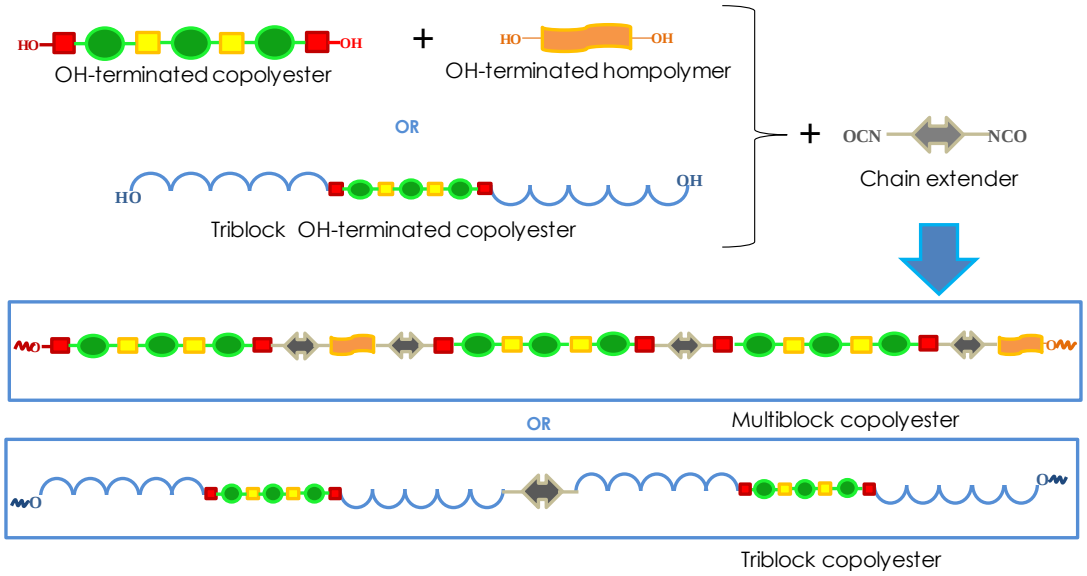

Figure 3.6. Schematic representation of chain extension reactions.

3.2.1 Polymers obtained by two-step melt polycondensation

3.2.1.1 Dimethyl ester synthesis

Prior to polycondensation reactions of some aromatic homopolymers, esterification of the diacids was carried out into a round-bottom flask containing the diacid and anhydrous methanol in large molar excess (1:30). The mixture was heated to 70°C under reflux up to complete dissolution. After cooling to room temperature, thionyl chloride (in the same molar amount as the hydroxyl end groups of the diacid) was added dropwise. Then, the so-obtained mixture was heated to 70°C and let to react for other 3 hours under reflux. During cooling, the dimethyl ester precipitated was filtered and washed with anhydrous methanol. The product was then recrystallized by dissolution in methanol at 60°C and after that quenched in ice bath.

3.2.1.2 Homopolymer synthesis

Homopolymers syntheses have been carried out in bulk, starting from the right monomers (diacids/dimethyl esters and diols) and catalysts (about 200 ppm of Ti/g of theoretical polymer), in a 250mL stirred glass reactor put in a termostatted bath. A 20% molar excess of diol with respect to the acid counterpart for high molecular weight aliphatic polyesters, 40% for hydroxyl-terminated prepolymers and 80% for aromatic polyesters was used. In this latter case, the high excess of diol was due to its role also as solvent, to favour the melting of the aromatic acid.

In the first stage, under pure nitrogen flow, the temperature was raised to 140-190°C (lower temperatures were used for aromatic polyesters, while for aliphatic ones higher temperatures were employed) and maintained there until the 90% of the theoretical amount of methanol was distilled off (about 2 hours for aliphatic polyesters and four for aromatic ones). Curiously, in the case of aromatic polyesters milder process conditions were employed. This was due to the necessity to avoid the degradation of the aromatic ring and unwanted side reactions. During the second stage, the temperature was raised up to 200-230°C (for aromatic and aliphatic polyesters, respectively) and in the same time a gradual vacuum was applied (until about 0,1mbar), in order to facilitate the removal of glycol in excess and to promote the transesterification reactions. In case of high molecular weight polymers, the synthesis was carried out until a constant torque was measured. For the hydroxyl-terminated prepolymers, the reaction was stopped when the polymeric fluid reached a quite high viscosity, and the torque values were about 2-3 N * cm. Reagents and operating conditions employed for the syntheses of high molecular weight homopolymers are reported in Table 3.1, while their chemical structures are collected in Figure 3.7.

Table 3.1. Reagents and operating conditions employed for high molecular weight homopolymer syntheses.

Polymer	Dicarboxylic acid/ester	Glycol	$T_{1^{st}}$ stage (°C)	$T_{2^{nd}}$ stage (°C)
Poly(butylene succinate) (PBS)	DMS	1,4-BD	180	230
Poly(butylene adipate) (PBA)	DMA	1,4-BD	170	210
Poly(butylene cyclohexanedicarboxylate) (PBCE)	1,4-CHDA	1,4-BD	180	220
Poly(propylene 2,5-furanoate) (PPF)	2,5-FDCA	1,3-PD	180	220
Poly(butylene 2,5-furanoate) (PBF)	2,5-FDCA	1,4-BD	170	220
Poly(pentamethylene 2,5-furanoate) (PPeF)	2,5-FDCA	1,5-PeD	170	220
Poly(hexamethylene 2,5-furanoate) (PHF)	2,5-FDCA	1,6-HD	170	220
Poly(propylene 2,5-thiophenate) (PPTF)	2,5-TFDCA	1,3-PD	170	200
Poly(butylene 2,5-thiophenate) (PBTF)	2,5-TFDCA	1,4-BD	140	200

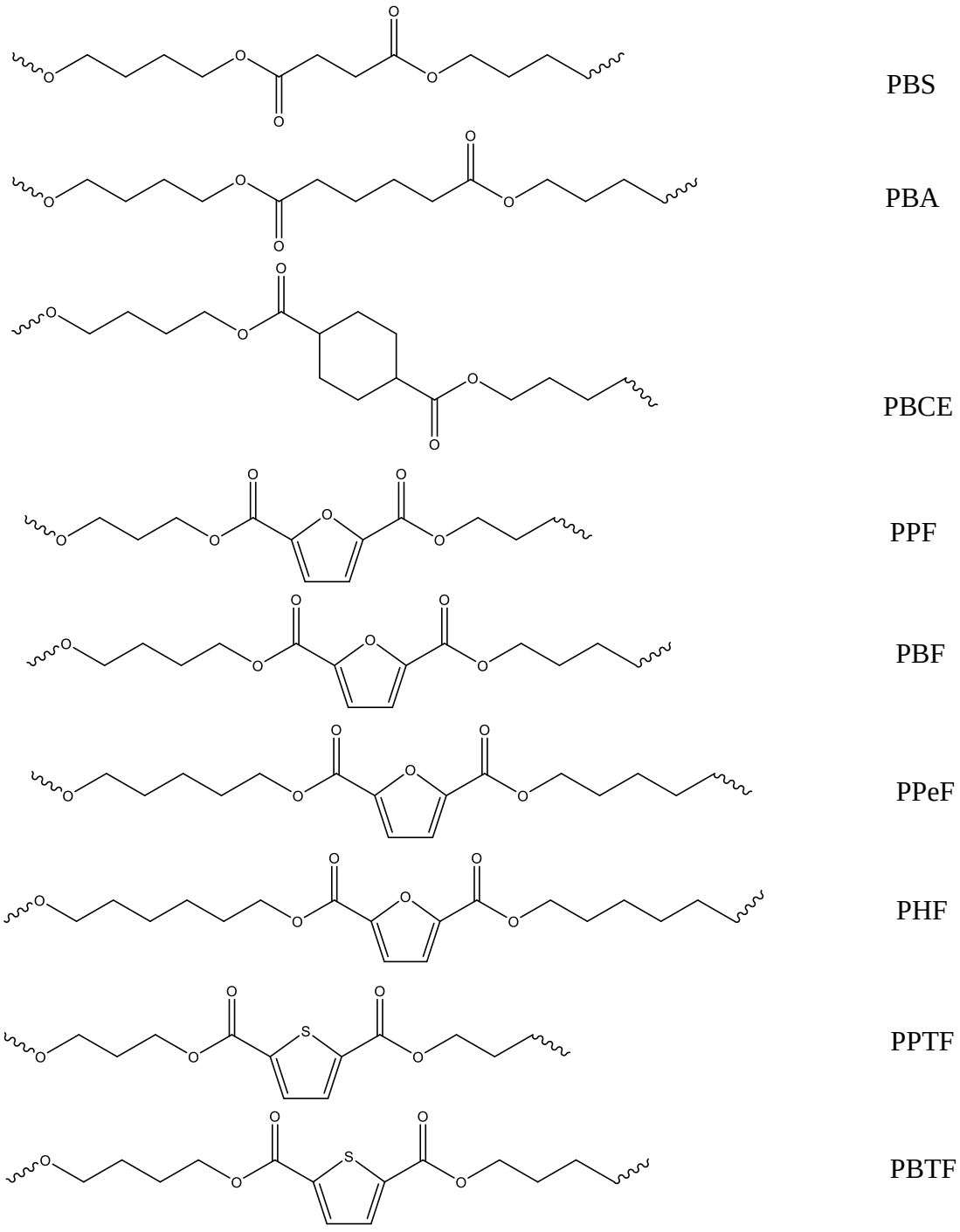

Figure 3.7. Chemical structure of the synthesised homopolymers.

Reagents and operating conditions employed for the syntheses of hydroxyl-terminated homopolymers are reported in Table 3.2, while their chemical structures are reported in Figure 3.8.

Table 3.2. Reagents and operating conditions employed for hydroxyl-terminated homopolymer syntheses.

Polymer	Dicarboxylic acid/ester	Glycol	T1st stage (°C)	T2nd stage (°C)
Poly(butylene succinate) (PBS-OH)	DMS	1,4-BD	190	230
Poly(triethylene glycol succinate) (PTES-OH)	DMS	TEG	190	230
Poly(hexamethylene 2,5-furanoate) (PHF-OH)	2,5-FDCA	1,6-HD	180	220
Poly(triethylene glycol 2,5-furanoate) (PTEF-OH)	2,5-FDCA	TEG	180	220

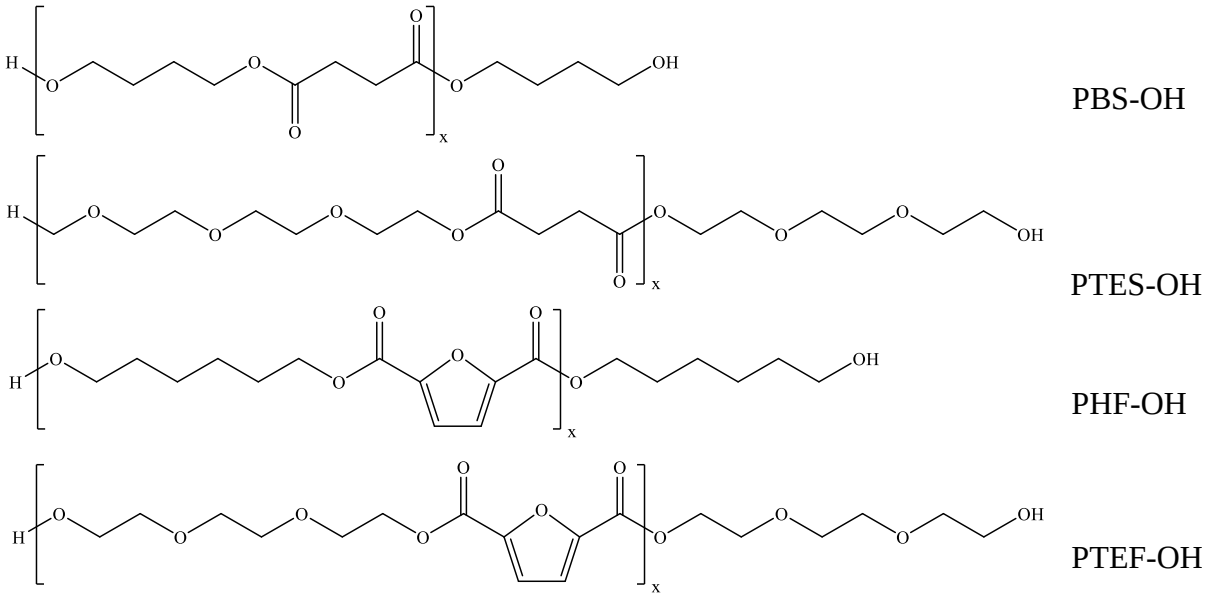

Figure 3.8. Chemical structure of the synthesised hydroxyl-terminated homopolymers.

3.2.1.3 Copolymer synthesis

Random copolymers syntheses have been carried out in bulk, according to the procedure above mentioned for the homopolymers. Depending on the copolymeric system, and in order to obtain

copolymers with different compositions, different ratios of the two diols or dicarboxylic acids/dimethyl esters have been used.

Seven different classes of random high molecular weight copolymers have been synthesized:

- Poly(butylene/triethylene glycol succinate), P(BS_xTES_y);
- Poly(butylene adipate/2,5-thiophenate), P(BA_xBTF_y);
- Poly(butylene/2-butyl-2ethyl propanediol succinate), P(BS_xBEPS_y);
- Poly(butylene/neopentyl glycol succinate), P(BS_xNS_y);
- Poly(butylene/2-butyl-2ethyl propanediol cyclohexanedicarboxylate), P(BCE_xBEPCE_y);
- Poly(butylene/neopentyl glycol cyclohexanedicarboxylate), P(BCE_xNCE_y);
- Poly(butylene succinate/Pripol), P($BS_xBPripol_y$);

In all cases, x and y represent the mol% of the two comonomeric units. In Table 3.3 the reagents and the conditions used for the syntheses are reported, while the structures of the so obtained copolymers are reported in Figure 3.9.

Table 3.3. Reagents and operating conditions employed for copolymer syntheses.

Polymeric system	**Dicarboxylic acid/ester**	**Glycol**	**$T_{1^{st}stage}$ (°C)**	**$T_{2^{nd}stage}$ (°C)**
	1/2	**1/2**		
P(BS_xTES_y)	DMS	1,4-BD/TEG	180	230
P(BA_xBTF_y)	DMA/2,5-TFDCA	1,4-BD	170	210
P(BS_xBEPS_y)	DMS	1,4-BD/BEPD	180	230
P(BS_xNS_y)	DMS	1,4-BD/NG	180	230
P(BCE_xBEPCE_y)	1,4-CHDA	1,4-BD/BEPD	180	220
P(BCE_xNCE_y)	1,4-CHDA	1,4-BD/NG	180	220
P($BS_xBPripol_y$)	SA/Pripol 1009	1,4-BD	190	230

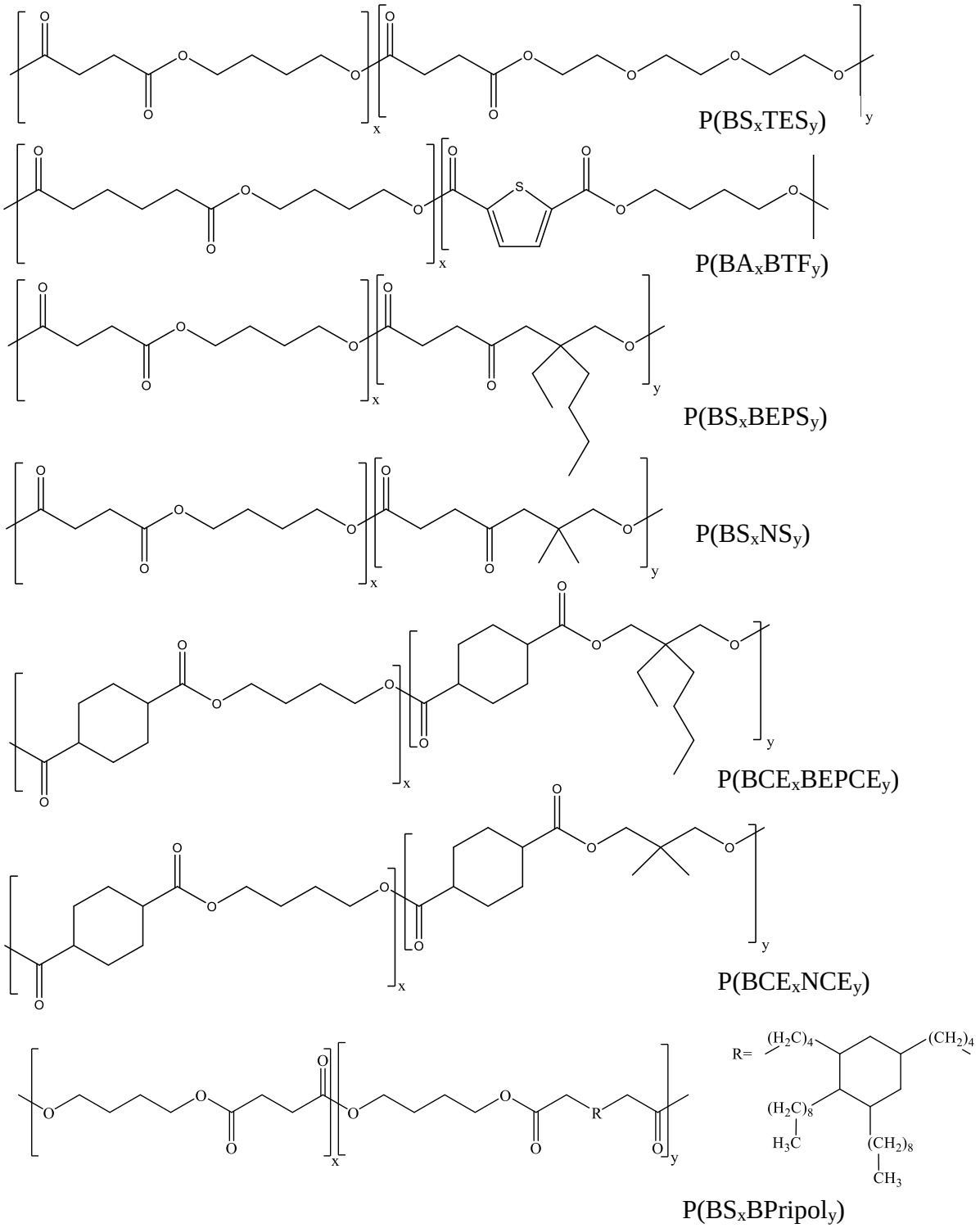

Figure 3.9. Chemical structure of the high molecular weight random copolymers.

Two different classes of random hydroxyl-terminated copolymers have been synthesized, according to the procedure above described for the homopolymers:

- Poly(butylene/neopentyl glycol succinate), P(BS_xNS_y)-OH;
- Poly(butylene succinate/Pripol), P($BS_xBPripol_y$)-OH;

In Table 3.4 the reagents and the conditions used for the syntheses are listed, while the chemical structures of the hydroxyl-terminated copolymers are reported in Figure 3.10.

Table 3.4. Reagents and operating conditions employed for hydroxyl-terminated random copolymers syntheses.

Copolymer	Dicarboxylic acid/ester	Glycol	$T_{1^{st}stage}$ (°C)	$T_{2^{nd}stage}$ (°C)
	1/2	1/2		
P(BS_xNS_y)-OH	DMS	1,4-BD/NG	190	230
P($BS_xBPripol_y$)-OH	DMS/Pripol009	1,4-BD	190	230

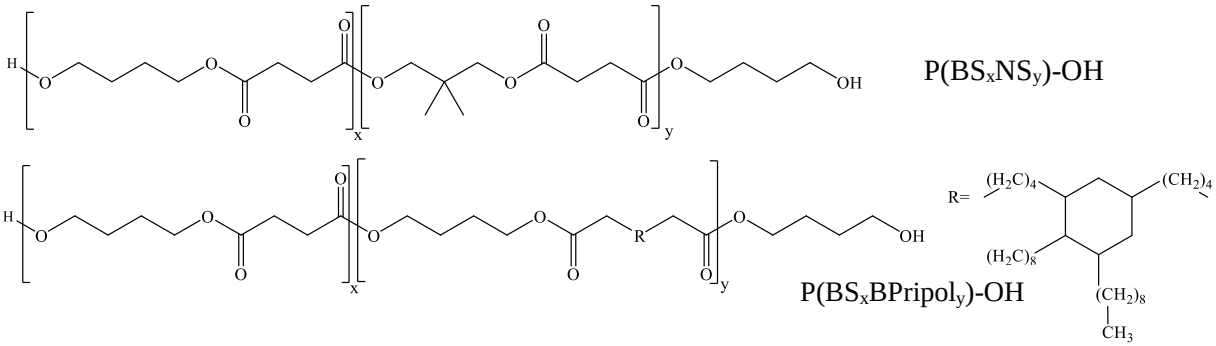

Figure 3.10. Chemical structure of the hydroxyl-terminated random copolymers.

3.2.2 Polymers obtained by reactive blending

Different multiblock copolyesters P(BS_mTES_n)-OH, characterized by different block length, were obtained through reactive blending, starting from hydroxyl-terminated poly(butylene succinate) (PBS-OH) and poly(triethylene glycol succinate) (PTES-OH). These parent homopolymers were melt mixed for different times in an equimolar ratio, in a 250 mL glass

reactor under pure nitrogen flow. The temperature was kept at 240°C and the stirring rate was about 100rpm. Copolymer formation was catalysed by the residual catalyst, $Ti(OBu)_4$, present in the two parent homopolymers; m and n represent the block length. In Figure 3.11 the chemical structure of the so obtained copolymers is reported.

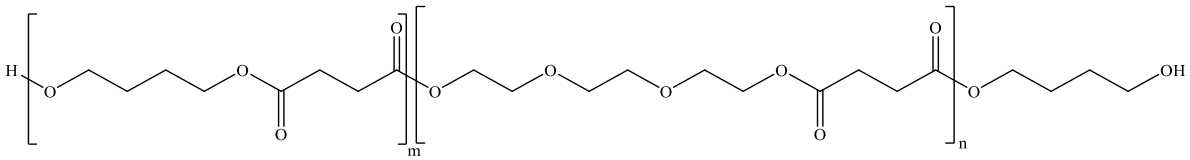

$P(BS_mTES_n)$-OH

Figure 3.11. Chemical structure of the copolymers obtained by reactive blending.

3.2.3 Block copolymers by ROP

Ring opening polymerization (ROP) was employed in order to obtain triblock copolyesters ABA, where L-lactide represents the *hard block* A, and B is usually a central *soft block*. Two different copolymeric $P(BS_mTES_n)$-OH A blocks have been considered (m and n indicate the block length): $P(BS_{13}TES_{12})$-OH and $P(BS_2TES_2)$-OH, previously obtained by reactive blending. Purified $P(BS_mTES_n)$-OH prepolymer was charged in a 250ml glass reactor, heated at 170°C and held in pure nitrogen atmosphere until it was completely molten. After that, the desired amount of L-Lactide was added, together with the catalyst Sn(II)-2-ethylhexanoate (100ppm/g of polymer). During this phase, which lasts about 3 hours, the ring opening polymerization (ROP) of L-Lactide by OH terminal groups of the A block takes place, with the formation of the triblock copolymers $PLLAP(BS_{13}TES_{12})$ and $PLLAP(BS_2TES_2)$. In order to increase their molecular weight, these were then chain extended, using hexamethylene diisocyanate (HDI) as chain extender. An equimolar amount of HDI with respect to OH groups (determined by ^{1}H-NMR) was used. Isocyanate groups of HDI react with the hydroxyl terminals of PLLA, thus leading to a sudden increase in torque value. After the addiction of HDI, the reaction has been carried out for about 2 hours, until a constant torque value was registered. Chain extension of PLLA was also considered for sake of comparison. The chemical structures of the so obtained high molecular weight triblock copolymers are reported in Figure 3.12.

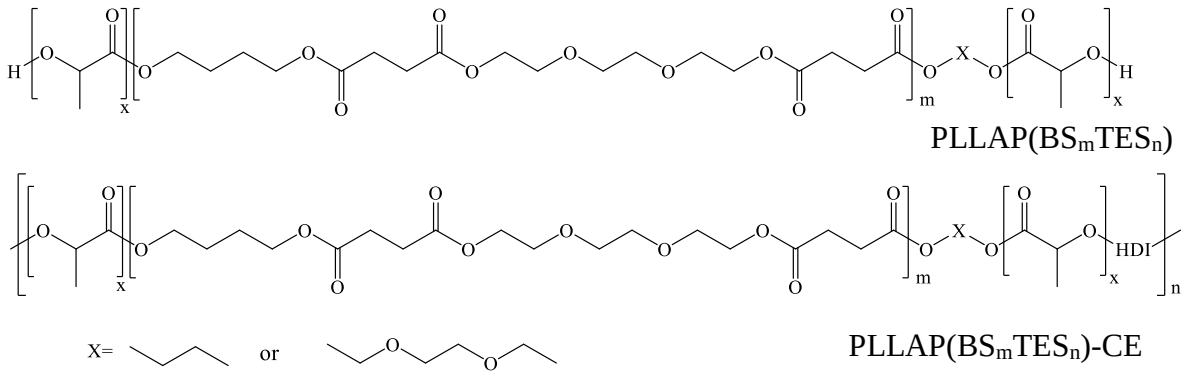

Figure 3.12. Chemical structure of the high molecular weight triblock copolymers obtained by ROP and chain extension.

3.2.4 Multiblock homo- and copolymers by chain extension

Multiblock copolymers were obtained by chain extending hydroxyl terminated prepolymers in different amounts. The prepolymers were put in a 250 ml glass reactor under constant stirring of 100 rpm and heated at 170°C, under pure nitrogen flow. When the mixture was completely molten, HDI was added, in equimolar amount with respect to the OH groups of the two prepolymers. The reaction was carried out until a constant torque was measured (about 30 minutes). The chemical structure of multiblock copolymers obtained is reported in Figure 3.13.

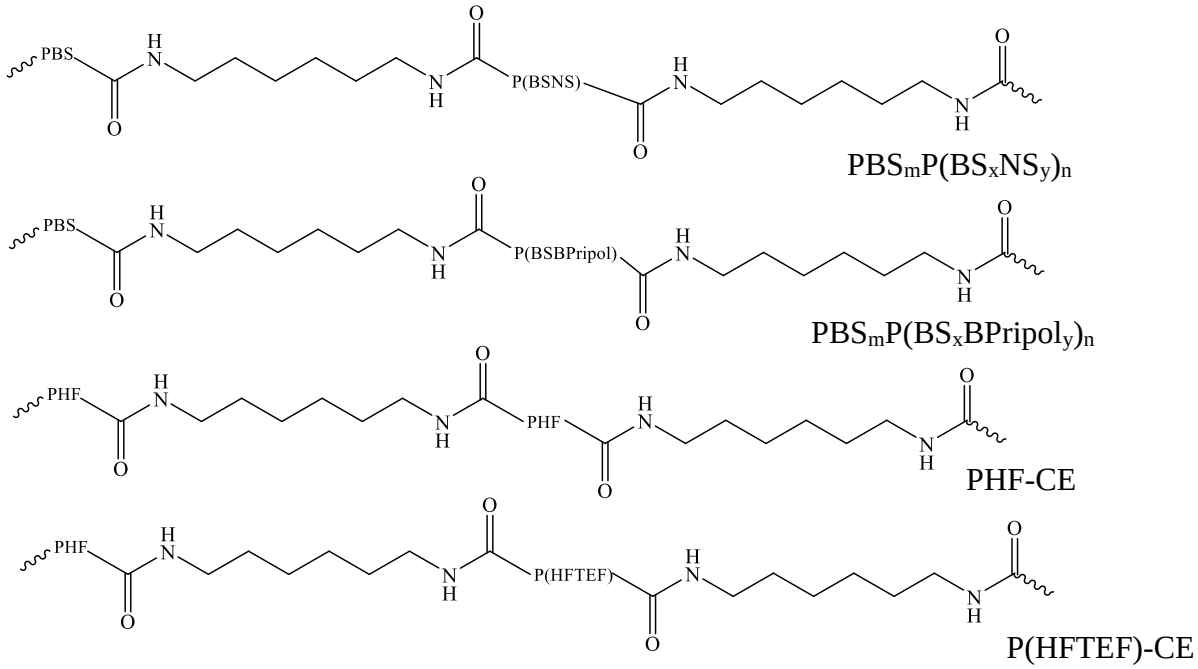

Figure 3.13. Chemical structure of the multiblock copolymers obtained by chain extension.

3.3 Molecular characterization

3.3.1 Nuclear Magnetic Resonance (NMR)

Nuclear Magnetic Resonance spectroscopy is one of the principal techniques used to investigate the chemical structure of molecules. Polymer structures and actual copolymer compositions were determined by means of ^{1}H-NMR, while ^{13}C-NMR was used to evaluate the distribution of comonomeric units along the polymeric chain (molecular architecture).

Aliphatic polyesters were dissolved in deuterated chloroform, containing 0.03 vol.% tetramethylsilane (TMS) as an internal standard, whereas aromatic ones were dissolved in a mixture of 70% v/v deuterated chloroform and deuterated trifluoroacetic acid. A Varian Inova 400 MHz instrument was employed for the measurements. ^{1}H-NMR spectra were recorded at room temperature, and the polymer concentration of the solutions was 0.5 wt% (relaxation delay of 1 s, acquisition time of 1 s and up to 64 repetitions). ^{13}C-NMR spectra were obtained using 5 wt% solutions and a full decoupling mode with a NOE effect (relaxation delay of 2 s, acquisition time of 1 s and up to 512 repetitions).

The arrangement of the comonomeric units in the copolymeric chain may be deduced by the degree of randomness, b, which has been determined by means of ^{1}H-NMR and ^{13}C-NMR. In particular, for physical blends the value of b is close to 0, for random copolymers is equal to 1, for block copolymers is comprised between 0 and 1, while in case of copolymers with an alternate structure the value of b is equal to 2.

The value of b was calculated taking into account the resonance peaks of the carbon atoms of the common subunits between the comonomeric units (X and Y), and it can be expressed as:

$$b = P_{X-Y} + P_{Y-X} \quad \textbf{[28]}$$

where P_{X-Y} is the probability of finding a X unit next to an Y one and P_{Y-X} is the probability of finding a Y unit next to a X one, respectively. Those probabilities can be expressed as follows:

$$P_{X-Y} = (I_{X-Y} + I_{Y-X})/2 \,/\, ((I_{X-Y} + I_{Y-X})/2 + I_{X-X}) \quad \textbf{[29]}$$

$$P_{Y-X} = (I_{Y-X} + I_{X-Y})/2 \,/\, ((I_{Y-X} + I_{X-Y})/2 + I_{Y-Y}) \quad \textbf{[30]}$$

where I_{X-Y}, I_{Y-X}, I_{X-X}, I_{Y-Y} represent the integrated intensities of the resonance signals of X-Y, Y-X, X-X, Y-Y sequences, respectively. Moreover, the average length of the sequences of the two different comonomeric units can be defined as:

$L_X = 1/P_{X-Y}$ **[31]**

$L_Y = 1/P_{Y-X}$ **[32]**

In the case of block copolymers, the degree of polymerization of hydroxyl-terminated prepolymers (DP), which is the number of repeating units present in each chain, has been calculated from the normalized areas of protons of central glycol (I_{Int}) and protons of terminal glycol (I_{Ext}) as follows:

$DP = [I_{Int} / I_{Ext}] * 2 + 1$ **[33]**

The polymer molecular weight (M_n) was then calculated according to the following equation:

$M_n = DP * W_{ru} + W_{glycol}$ **[34]**

Where W_{ru} and W_{glycol} are the molecular weights of the repeating unit and the glycol, respectively.

3.3.2 Gel Permeation Chromatography (GPC)

The molecular weights of the polymers under investigation were obtained by means of gel-permeation chromatography (GPC) at 30°C using a 1100 HPLC system (Agilent Technologies) equipped with PLgel 5-mm MiniMIX-C column. In case of aliphatic polyesters refractive index was employed as detector and chloroform was used as eluent, while for aromatic polyesters UV index was used as detector and a chloroform/hexafluoro-2-propanol (95:5 v/v) was used as eluent. In all cases, 0.3 mL/min flow and sample concentrations of about 2 mg/mL were adopted. Calibration curve was obtained using polystyrene standards in the range of 800 – 100000 g/mol.

3.3.3 Intrinsic viscosity measurements

Intrinsic viscosity (η) measurements were performed using a clearly washed Ubbelohde type viscosimeter 31 13/Ic (diameter 0.84 mm) at 30 °C in a mixture phenol/1,1,2,2-tetrachloroethane (60/40 w/w). The flow time measurements were made with an equipped

stopwatch. The solutions of the samples were prepared starting from precise amounts of polymers (0.16 g) and adding the volume of as-prepared mixture of solvents so that the final solution concentration was 0.8 g/dl. The samples were maintained at 90 °C until their complete dissolution, then cooled to room temperature and filtered. The measurements were repeated five times to make sure the accuracy of the results. The intrinsic viscosity (η) was obtained according to the following equation:

$$\eta = \frac{ln\frac{t}{t_0}}{c} \quad \textbf{[35]}$$

where t_0 is the efflux time of the solvent (s), t is the efflux time of the mixture polymer + solvent and c is the polymer concentration (g/dl).

3.4 Sample processing

3.4.1 Film by compression moulding

Thin polymeric films of about 100μm thickness were obtained by compression moulding, using a Carver laboratory press. The materials were put between two Teflon sheets, heated at a temperature 40°C higher than their melting temperature and kept for two minutes at a pressure of 5 tons/m^2. Then the films were cooled to room temperature in press using tap water. Prior to further tests, films were stored at room temperature for at least two weeks, in order to reach equilibrium crystallinity.

3.4.2 Scaffold fabrication

Some of the synthesized polymers were subjected to electrospinning in order to realize scaffolds for applications in tissue engineering. Electrospun mats were fabricated in laboratories of Consiglio Nazionale delle Ricerche (CNR) of Bologna, thanks to the scientific collaboration with Dr. Annalisa Aluigi. Four copolymers have been taken into account:

- P($BS_{70}NS_{30}$) random copolymer;
- P(BSBPripol) random copolymer;
- PBSP(BSNS) block copolymer;
- PBSP(BSBPripol) block copolymer.

All copolymers were dissolved in hexafluoro-2-propanol at a concentration of 15% (w/v). 3D-scaffolds were produced by means of a handmade electrospinning apparatus, comprised of a high-voltage power supply (SVH150, Alintel Power Electronics, Italia), a syringe pump (KDS200, KD Scientific Inc., USA), a glass syringe, a stainless steel blunt-ended needle (inner diameter = 0.84 mm) connected with the power supply electrode and a grounded aluminum plate-type collector. Polymer solution was dispensed to the needle, which was placed horizontally on the collecting plate. Electrospun scaffolds were produced at RT and a relative humidity of 40% ± 5%. More in details, the polymeric solutions were dispensed at a constant rate of 0.05 mL/min, the distance between the needle and the collector was 15 cm, and the voltage applied was +20 kV. After 45 minutes, 7 cm x 7 cm random nanofiber-mats were obtained. Electrospun materials were kept under vacuum over P_2O_5 at RT overnight in order to remove residual solvent.

3.5 Thermal characterization

3.5.1 Differential Scanning Calorimetry (DSC)

Calorimetric measurements were carried out using a Perkin Elmer DSC6 (Waltham, MA, USA) calibrated with high purity standards (indium and cyclohexane). In the typical setup, the external block temperature control is set at −70 °C. Weighed samples of about 10 mg were encapsulated in aluminum pans and heated to about 40 °C above fusion temperature at a rate of 20 °C/min (first scan), held there for 5 min, and then rapidly quenched (100 °C/min) to −70 °C. Finally, they were reheated to a temperature well above the melting at a heating rate of 20 °C/min (second scan). For some samples, thermal annealing was performed at different temperatures: this procedure consists in holding each sample for 10 min at the indicated temperature, followed by quenching and a temperature scan (20 °C/min). For other specific thermal treatments, described afterwards in the text, different heating rates were also used.

The glass-transition temperature (T_g) was taken as the midpoint of the heat capacity increment Δc_p associated to the glass-to-rubber transition. The crystallization temperature (T_c) and the melting temperature (T_m) were determined as the peak values of the exothermal and endothermal phenomena in the DSC curve, respectively. The specific heat increment Δc_p, associated with the glass transition of the amorphous phase, was calculated from the vertical distance between the two extrapolated baselines at the glass transition temperature. The heat of

crystallization (ΔH_c) and the heat of fusion (ΔH_m) were calculated considering the total areas of the DSC exothermic and endothermic peaks, respectively. In order to determine the crystallization rate under non-isothermal conditions, some samples were heated at 20°C/min to about 40°C above fusion temperature, kept there for 3 minutes and then cooled at 5°C/min. The temperature corresponding to the peak value in the DSC cooling-curve (T_{cc}) is related to the crystallization rate.

3.5.2 Thermogravimetric Analysis (TGA)

Thermogravimetric analysis (TGA) was carried out under nitrogen atmosphere using a Perkin Elmer (Waltham, MA, USA) TGA7 apparatus (gas flow: 40 mL/min). Weighed samples of about 5 mg were loaded on a sample pan and heated at 10 °C/min from 40°C up to 800 °C. $T_{5\%}$ was determined as the temperature corresponding to the 5% of mass loss, T_{onset} as the temperature at which degradation starts, while the temperature of maximum weight loss (T_{max}) has been calculated as the minimum value of the thermogram derivative.

3.6 Wide-angle X-Ray diffraction (WAXS)

X-ray diffraction patterns (XRD) of polymeric powders, films and scaffolds were performed in the wide angles region by means of a PANalytical X'PertPro diffractometer equipped with a fast solid state X'Celerator detector (Almelo, the Nederlands). The radiation was supplied by a copper target (λ = 0.1548 Å) and data were acquired in the 5-60° 2θ interval, by collecting 100 s at each 0.10° step. For some samples, in situ XRD analysis was performed by using an Anton Paar TTK-450 (Graz, Austria) sample stage at different temperatures, which will be described more in details below in the text. The index of crystallinity (X_c) was calculated from the X-ray diffraction profiles by the ratio between the crystalline diffraction area (A_c) and the entire area of the diffraction profile (A_t):

$$X_c = A_c/A_t \quad \textbf{[36]}$$

The crystalline diffraction area was obtained by subtracting the amorphous halo from the total area of the diffraction profile. The incoherent scattering was also taken into account. For some

copolymeric systems, the unit cell parameters were calculated by whole pattern fitting using Powder Cell 2.3 for Windows.

3.7 Surface wettability

Static contact angle measurements were performed on polymer films by using a KSV CAM101 instrument (Helsinki, Finland) at ambient conditions by recording the side profiles of deionized water drops for image analysis. At least eight drops were observed on different areas for each film and contact angles were reported as the average value ± standard deviation. Each drop was deposited on the films by placing it in contact with the polymeric surface using the syringe needle and then withdrawing this last. The data were recorded after 5 second from the deposition of the drop on the surface. For some block copolymers the data were recorded also after 1 minute from the deposition, in order to check any variations in the drop shape and in the contact angle value.

3.8 Mechanical characterization: tensile test

The tensile testing of the polymers was performed using a Zwick Roell Texture machine (Ulm, Germany), equipped with rubber grip and a 500 N load cell, controlled by computer and an Instron 4465 tensile testing machine (Norwood, MA, USA), equipped with a rubber grip and a 100 N load cell. A pre-load of 1 MPa with a 5 mm/min speed was used. Rectangular films and scaffolds (5 mm wide and about 0.1 mm thick) with a gauge length of 20 mm were employed and different crosshead speeds were adopted (10, 20 and 50mm/min). Load-displacement curves were obtained and converted to stress-strain curves. Tensile elastic modulus was determined from the initial linear slope of the so-obtained stress-strain curve. At least five replicate specimens were tested for each sample and the results were provided as the average value ± standard deviation. Cyclic loading was performed under the same experimental conditions. More in details, film and scaffold samples were strained up to 50-100% and then 25 cycles were carried out.

3.9 Hydrolytic degradation tests

Hydrolytic degradation studies were carried out in triplicate on rectangular polymeric films and scaffolds (5 x 35 mm, about 0.1 mm thick). First, all the samples were dried over P_2O_5 under vacuum at room temperature to constant weight, then weighed to obtain the sample initial mass. After that, they were immersed in phosphate buffered solution (0.1 M, pH = 7.4) and incubated in a SW22 Julabo shaking water bath at 37°C and 50 rpm. The buffer solution was periodically changed to keep the pH constant during the entire experiment. At different time intervals, triplicate sacrificial specimens of each sample were repeatedly washed with deionized water and dried over P_2O_5 under vacuum for 2 days to constant weight. The mass loss was determined gravimetrically by comparing the residual weight with the initial value, while the residual molecular weight was determined by GPC analysis. Moreover, for block copolymers the chemical composition after degradation was evaluated by means of NMR spectroscopy, while the residual crystallinity degree was calculated by means of DSC analysis.

3.10 Micro and nanoparticles preparation

Both empty and Dexamethasone (DXM) containing micro (MPs) and nanoparticles (NPs) have been prepared by oil-in-water miniemulsion process. The organic phase formed by 50 mg and 100 mg (in case of nano and microparticles respectively) of polymer dissolved in 5mL of chloroform, has been added to 10 mL of SDS 0.3 wt% aqueous solution. In the case of DXM containing particles, 1,25 mg of drug was put in addition to the so obtained mixture. The emulsion of the organic phase in the aqueous one has been obtained by mechanical stirring at room temperature for 30 min. Afterwards, chloroform was evaporated keeping the system under stirring for 50 minutes. The final dispersion has been centrifuged (1000 rpm, 3 min, 0 °C) and in case of nanoparticles, the precipitated material has been removed to guarantee a lower NPs size polydispersity. For the same reason, in case of microparticles the supernatant has been removed, and the precipitated material kept.

3.11 Particles characterization

The determination of the MP hydrodynamic diameter was carried out by means of optical microscopy employing a Carl Zeiss Axioskop 2 optical polarizing microscope equipped with a video camera and connected to a computer. 10 µl drops containing microparticles were placed between a coverslip and a slide and then observed at room temperature. The software allowed images acquisition and determination of hydrodynamic diameter of the microparticles. The determination of NP hydrodynamic diameter distributions was carried out by means of dynamic light scattering (DLS) measurements employing a Malvern Nano ZS instrument with a 633 nm laser diode. Samples were put in disposable polystyrene cuvettes of 1 cm optical path length using water as solvent. The width of DLS hydrodynamic diameter distribution is indicated by PDI (polydispersion index). In the case of a monomodal distribution (Gaussian) calculated by cumulant analysis, PDI can be expressed as follows:

$$PDI = (\sigma/Z_{avg})^2 \quad \textbf{[37]}$$

where σ is the width of the distribution and Z_{avg} is the average diameter of the particle population, respectively.

The so obtained particles were also thermally characterized by DSC measurements.

3.12 Drug release experiments

DXM-loaded micro and nanoparticles were suspended in deionized water and placed in a dialysis cellulose membrane bag, with a molecular weight cut-off of 12400. The membrane was then immersed in phosphate buffered solution (0.1M, pH = 7.4) and incubated in a SW22 Julabo shaking water bath at 37 °C and 50 rpm. At predetermined time intervals, phosphate buffer aliquots (1.5 ml) were collected, replaced with the same amount of fresh buffered solution, and DXM release was monitored by measuring UV absorbance at 235 nm with a Cary 1E (Varian) spectrophotometer. The values were then converted to DXM concentrations through a calibration curve obtained in the same buffer. Entrapment efficiency can be calculated as follows:

$$\text{Entrapment efficiency (\%)} = \frac{\text{weight of drug in particles}}{\text{weight of drug fed initially}} * 100 \quad \textbf{[38]}$$

The drug amount inside the particles was determined by preparing them as described above, solving them in chloroform and by measuring UV absorbance at 235nm of the so obtained solution.

3.13 Biocompatibility studies

3.13.1 Biocompatibility studies on P(BSxTESy) copolymeric system

The following biocompatibility studies were performed in the laboratories of Health Sciences and Technologies - Interdepartmental Center for Industrial Research (HST-ICIR) of the University of Bologna, thanks to the scientific cooperation with Prof. Emanuele Domenico Giordano and Dr. Marco Govoni.

3.13.1.1 Indirect cytotoxicity

Indirect cytotoxicity evaluations of PBS homopolymer and P(BS_mTES_n) copolymers were performed in accordance with the ISO10993-5 international standard for biological evaluation of medical devices [Gualandi et al., 2012 (b)]. Embryonic rat cardiac H9c2 cells [obtained from the European Collection of Cell Cultures (ECACC)] [Govoni et al., 2010] were seeded in a 12-well culture plate (2.5 X 104 cells/well) in standard Dulbecco's modified Eagle's medium (DMEM) supplemented with 10% heat inactivated fetal bovine serum (FBS), 2mM of L-glutamine, and 100 U/mL of penicillin/streptomycin, at 37 °C in a humidified atmosphere containing 5% CO_2 to allow their attachment and were quantified by resazurin (i.e. PrestoBlue®) fluorescence assay (Life Technologies, Monza, Italy). After 24 h, the culture medium was discarded and replaced by polymer-extract media. The cells were then incubated for 48 h, and after that PrestoBlue® assay was performed again for cytotoxicity screening.

The PrestoBlue® fluorescence (E_x/E_m = 540/590 nm) was read in a Tecan Infinite 200 multilabel multiplate reader (Tecan Italia S.r.l.). Three separate experiments (n=3), two replicates each, were performed. The signal obtained from cells cultured in DMEM was used as negative control, while a cytotoxic response, used as positive control, was obtained by adding 1 mM H_2O_2 for 120 min to cells and readings 48 h after cell seeding.

Fluorescence values were calculated and reported as the average value ± standard deviation, and the one-way ANOVA with Tukey's as post-test was used to evaluate statistical differences between samples.

3.13.1.2 Cell adhesion and proliferation

Cell adhesion and proliferation were assessed in accordance with ISO10993-5 [Gualandi et al., 2012 (c)]. Cell viability was quantified at day 1, 3 and 7 with the PrestoBlue® fluorescence assay. Control signal was acquired from H9c2 cells cultured on standard polystyrene substrates (Sarstedt, Numbrecht, Germany). Three separate experiments, two replicates each, were performed. Fluorescence values were expressed as average value ± standard deviation. Comparison between groups was performed using the one-way ANOVA with Tukey's as post-test and differences were considered significant for $P < 0.05$.

3.13.1.3 RNA isolation and gene expression profile

Total RNA was extracted from H9c2 seeded on polymers, using TRIzol® reagent (Life Technologies, Monza, Italy) and chloroform [Pasini et al., 2013]. For each sample, 400 ng of total RNA was reverse-transcribed using the iScript® cDNA synthesis kit (Bio-Rad, Milan, Italy). Gene expression analysis was performed in a CFX ConnectTM Real-Time PCR Detection System (Bio-Rad), using the SsoAdvancedTM Universal SYBR® Green Supermix (Bio-Rad). Myosin heavy chain (MHC) sense and antisense primers, used for DNA amplification by RT-quantitative polymerase chain reaction (qPCR) were 50-TGGCACCGTGGACTACAATA-30 and 50-TACAGGTGCATCAGCTCCAG-30, respectively (TIB MOLBIO CBA, Genua, Italy); glyceraldehyde-3-phosphate dehydrogenase (GAPDH) sense and antisense primers were 50-CCTCCTCATTGACCTCAACTAC-30 and 50-CATGGTGGTGAAGACGCCAG-30, respectively (TIB MOLBIO CBA, Genua, Italy).
Amplification was performed in a 20mL final volume, including 5mL of complementary DNA as template [DeWinter, 2013]. Specificity of the obtained products was addressed, performing a melting curve analysis. Two separate experiments, two replicates each, were performed and data were normalized to GAPDH expression (reference gene) since the mRNA transcript for this gene was equivalently expressed among the samples. Fold-changes in gene expression were determined by the 2-DDCq method and are presented relative to levels in H9c2 cultured on

PBS homopolymer. Comparison between groups was performed using unpaired Student's t-test and differences were considered significant at $P < 0.05$ [Govoni et al., 2017].

3.13.2 Biocompatibility studies on block/random PBS-based copolymeric system

The following biocompatibility studies were performed in the Translational Cardiomyology Laboratory, Department of Development and Regeneration of the Katholieke Universiteit Leuven (KUL), thanks to the scientific cooperation with Prof. Dr. Maurilio Sampaolesi and Dr. Robin Duelen.

3.13.2.1 Human Induced Pluripotent Stem cells (iPSCs) culture on scaffolds

Commercially available integration-free human iPSC line (Thermo Fisher Scientific), generated using cord blood-derived $CD34^+$ progenitors with seven episomally expressed factors (OCT4, SOX2, KLF4, c-MYC, NANOG, LIN28 and SV40 T) were cultured and maintained feeder-free (Geltrex™ LDEV-Free, hESC-Qualified, Reduced Growth Factor Basement Membrane Matrix) in Essential 8™ medium (both from Thermo Fisher Scientific) under normoxic conditions (37°C, 5% CO_2) in a 6-well culture plate. Every 4 to 6 days of proliferation, cells were passaged non-enzymatically in colonies using EDTA (Thermo Fisher Scientific) (1:15 split ratio). In parallel, iPSCs were also seeded on nanofibrous copolymeric scaffolds, which were previously cut and mounted on CellCrown inserts (Merck), in a 12-well culture plate in Essential 8™ medium. Two different culturing conditions were adopted: in the first case iPSCs were seeded directly on scaffolds, while in the latter a thin coating layer was applied before the seeding. As a control, iPSCs were cultured without scaffolds on a thin coating layer. After 6 days, total RNA from cells seeded on scaffolds was collected. Cells were also fixed for immunostaining for protein analysis.

3.13.2.2 Human Induced Pluripotent Stem cells (iPSCs) cardiac differentiation on scaffolds

Human iPSCs were differentiated into functional cardiomyocytes, according to a monolayer-based protocol (Figure 3.14), taken from Life Technologies [PSC Cardiomyocyte Differentiation Kit Prototype]. Before inducing cardiac differentiation, iPSCs were cultured using a thin coating layer (GFR Matrigel) in Essential 8™ medium (both from Thermo Fisher Scientific) under hypoxic conditions (37°C, 5% CO_2, 5% O_2) in a 6-well culture plate (split

ratio of 1:15) for 3-4 days, until they reached a confluence between 65 to 85% in a 6-well culture plate (favoured by the presence of the coating). At day 0 of differentiation, cells were placed under normoxic conditions and differentiated towards the mesodermal lineage, using a chemically defined medium consisting of RPMI 1640 (Thermo Fisher Scientific), supplemented with 5 to 7 μM CHIR99021 (GSK3β inhibitor; Axon Medchem) for 48 h (Cardiomyocyte Differentiation Medium A). At day 2, the mesodermal cells were fed with basal medium containing 4 μM IWR-1 (Wnt inhibitor; Merck) for 48 h (Cardiomyocyte Differentiation Medium B). From day 4 onwards, medium was changed every two days with Cardiomyocyte Maintenance Medium.

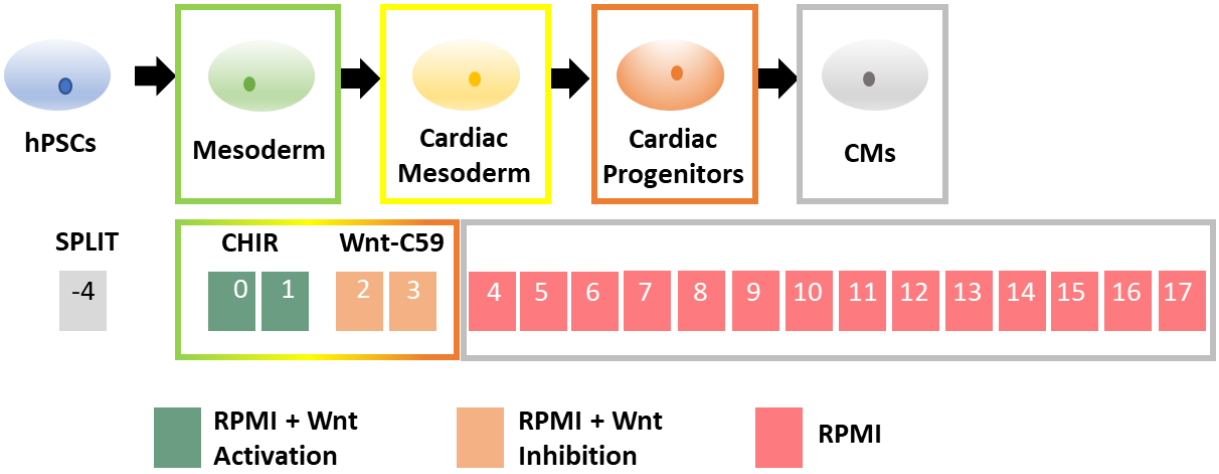

Figure 3.14. Schematic representation of the monolayer-based cardiac differentiation protocol.

The same cardiac differentiation method was applied for iPSCs seeded on scaffolds in a 12-well culture plate; in this case the initial seeding density was lower (1:20). Contracting cardiomyocytes appeared at day 8 or 9. At different time points (day 0, 2, 4, 8, 15) RNA samples from cells grown on scaffolds were collected, together with RNA from cells under normal culturing conditions. Moreover, after 6 days of differentiation, cells were fixed for immunostaining analysis.

3.13.2.3 Quantitative Real-Time PCR (qRT-PCR)

Total RNA from human iPSCs seeded on scaffolds, as well as from cells under normal culturing conditions, was extracted using the PureLink RNA Mini Kit (Thermo Fisher Scientific) and treated with the DNA-Free Kit (Thermo Fisher Scientific) to obtain highly pure RNA. 250-500 ng RNA was reverse transcribed into cDNA with Superscript III Reverse Transcriptase First-

Strand Synthesis SuperMix (Thermo Fisher Scientific). Quantitative real-time PCR was performed with the Platinum SYBR Green QPCR SuperMix-UDG (Thermo Fisher Scientific), using ViiA7 Real-Time PCR instrument (Applied Biosystems). The oligonucleotide primer sequences are reported in Table 3.5 (from IDT). A 10-fold dilution series ranging from 10^{-3} to 10^{-8} of 50 ng/µL human genomic DNA was used to evaluate the primer efficiency. Relative expression values were obtained by normalizing Ct values of the analysed genes to Ct values of the housekeeping genes *GAPDH, RPL13a* and *HPRT*.

All data were collected from three independent experiment, were analysed using GraphPad Prism and were reported as mean value ± standard deviation. Differences between groups were examined for statistical significance using ANOVA test. Significance of the differences versus control was indicated as follows: $P < 0.05$: *, $P < 0.01$: ** and $P < 0.001$: ***.

Table 3.5. Primer sequences used in Real-Time QPCR analysis.

Gene	Primer	Primer sequences 5'>3'
ANKRD	Forward	GTGTAGCACCAGATCCATCG
	Reverse	TCAACGCCAAAGACAGAGAAG
BRACH	Forward	ACCCAGTTCATAGCGGTGAC
	Reverse	AAGCTTTTGCAAATGGATTG
c-MYC	Forward	TCCTCGGATTCTCTGCTCTCCT
	Reverse	AGAAGGTGATCCAGACTCTGACCT
cMyHC (MYH6)	Forward	GCCCTTTGACATTCGCACTG
	Reverse	CGGGACAAAATCTTGGCTTTGA
CTGF	Forward	GCTCGGTATGTCTTCATGCTG
	Reverse	GAAGCTGACCTGGAAGAGAAC
CYR61	Forward	GGGATTTCTTGGTCTTGCTG
	Reverse	CCAATGACAACCCTGAGTGC
GAPDH	Forward	TCAAGAAGGTGGTGAAGCAGG
	Reverse	ACCAGGAAATGAGCTTGACAAA
GATA4	Forward	CGACACCCCAATCTCGATATG
	Reverse	GTTGCACAGATAGTGACCCGT
GDF-3	Forward	ACACCTGTGCCAGACTAAGATGCT
	Reverse	TGACGGTGGCAGAGGTTCTTACAA
HPRT	Forward	TGACACTGGCAAAACAATGCA
	Reverse	GGTCCTTTTCACCAGCAAGCT
hTERT	Forward	GAACATGCGTCGCAAACTCTTTGG
	Reverse	CAGCACACATGCGTGAAACCTGTA
KLF4	Forward	CGGACATCAACGACGTGAG
	Reverse	GACGCCTTCAGCACGAACT
LATS2	Forward	CCCATCTTGCTGATGTACTCC

	Reverse	AGCTGCAGAAGTGAACCG
NANOG	Forward	TGGCCGAAGAATAGCAATGGTGTG
	Reverse	TTCCAGGTCTGGTTGCTCCACATT
NKX2.5	Forward	ACCTCAACAGCTCCCTGACTCT
	Reverse	ATAATCGCCGCCACAAACTCTCC
OCT4	Forward	CGAGCAATTTGCCAAGCTCCTGAA
	Reverse	GCCGCAGCTTACACATGTTCTTGA
REX1	Forward	TGGAGGAATACCTGGCATTGACCT
	Reverse	AGCGATTGCGCTCAGACTGTCATA
RPL13a	Forward	CCTGGAGGAGAAGAGGAAAGAGA
	Reverse	TTGAGGACCTCTGTGTATTTGTCAA
SOX2	Forward	GAGAGACAAGTAGAGGAGCAGTT
	Reverse	TGGCGAACCATCTCTGTGGT
STK3	Forward	GTTCTGGCTTTCTGAATGTTGG
	Reverse	GACCTCTGGATTGTTATGGAGT
STK4	Forward	TCTTGCCAAAGCTGTTGATCT
	Reverse	CAATGCAGAGGATGAGGAAGAG
TAZ	Forward	ATTCATCGCCTTCCTAGGGT
	Reverse	GGCTGGGAGATGACCTTCAC
TNNT2	Forward	ACAGAGCGGAAAAGTGGGAAG
	Reverse	TCGTTGATCCTGTTTCGGAGA
YAP	Forward	ACGTTCATCTGGGACAGCAT
	Reverse	GTTGGGAGATGGCAAAGACA
α3	Forward	TGTGGCTTGGAGTGACTGTG
	Reverse	TCATTGCCTCGCACGTAGC
α6	Forward	ATGCACGCGGATCGAGTTT
	Reverse	TTCCTGCTTCGTATTAACATGCT
α7	Forward	CAGCGAGTGGACCAGATCC
	Reverse	CCAAAGAGGAGGTAGTGGCTATC
β3	Forward	GTGACCTGAAGGAGAATCTGC
	Reverse	CCGGAGTGCAATCCTCTGG
β4	Forward	GCTTCACACCTATTTCCCTGTC
	Reverse	GACCCAGTCCTCGTCTTCTG

3.13.2.4 Immunofluorescence staining

Human iPSC-seeded copolymeric scaffolds were prepared for immunofluorescence to evaluate cell morphology, proliferation and pluripotency. Briefly, the samples were washed with PBS, then fixed with 4% paraformaldehyde (PFA; Polysciences) for 20 minutes at 4°C and permeabilized in PBS (Thermo Fisher Scientific) containing 0.2% Triton X-100 (Merck) and 1% bovine serum albumin (BSA; Merck) for 30 minutes. Blocking was performed with 10%

donkey serum (Merck) for 30 minutes. Cells were incubated overnight at 4°C with the primary antibodies, followed by their Alexa Fluor 488-, and 594-conjugated secondary antibodies (Thermo Fisher Scientific; 4 μg/mL). The primary antibodies used to see pluripotency proteins were goat OCT4 (Santa Cruz SC-8626; 5 μg/mL) and rabbit NANOG (Thermo Scientific PA1-097X; 10 μg/mL), while those used to stain cardiomyocytes were mouse ACTN2 (Abcam EA-53; 5 μg/mL) and goat NKX-2.5 (Santa Cruz Biotechnology A-16; 5 μg/mL). Nuclei were stained with Hoechst (33342, Thermo Fisher Scientific; 1:10000) for 1 minute. Analyses were performed using a ZEISS LSM800 confocal microscope (from ZEISS) and an Eclipse Ti Microscope and NIS-Elements AR 4.11 Software (from Nikon).

3.13.3 Biocompatibility studies on PLLAP(BSTES) copolymeric system

The following biocompatibility studies were performed in the laboratories of Human Anatomy of the Department of Health Science, University of Piemonte Orientale, thanks to the scientific cooperation with Prof. Francesca Boccafoschi.

3.13.3.1 Human endothelial cells culture

Human endothelial cells, EA. hy926 (ATCC® CRL-2922™) were cultured in high-glucose Dulbecco's modified Eagle's medium (DMEM) additioned with 10% fetal bovine serum (FBS) and penicillin (100U/ml), streptomycin (100mg/ml), and glutamine (2mM; all from Euroclone, Italy) at 37°C in humid 5% CO_2 atmosphere. Cells ($2*10^4$ / cm^2) were cultured on controls (polystyrene wells for MTS assay or glass coverslip for phalloidin staining) and on PLLA and PLLAP(BSTES)2 films for 1, 3 and 7 days of culture. Tests were performed in triplicate.

3.13.3.2 Viability assay (MTS)

Cell viability has been measured using a colorimetric method (CellTiter 96® Aqueous Non-Radioactive Cell Proliferation Assay — Promega, Italy). The CellTiter 96® AQueous Assay is composed of solutions of a novel tetrazolium compound [3-(4,5-dimethylthiazol-2-yl)-5-(3-carboxymethoxyphenyl)-2-(4- sulfophenyl)-2H-tetrazolium, inner salt; MTS] and an electron coupling reagent phenazine methosulphate (PMS). MTS is bioreduced by cells into a formazan product that is soluble in culture medium. The absorbance of the formazan product at 490 nm can be measured directly in 96-well assay plates. The conversion of MTS into the aqueous

soluble formazan product is accomplished by dehydrogenase enzymes found in metabolically active cells. The quantity of formazan product as measured by the amount of 490 nm absorbance is directly proportional to the number of living cells. Briefly, at each time point (1, 3 and 7 days of culture) cell culture medium was removed, and MTS solution was added into each assay-plate; after 4h incubation of cells with MTS solution, the UV–vis absorbance of the solution at 490 nm was measured. Polystyrene wells were used as control.

3.13.3.3 Cell morphology: phalloidin staining

Cell morphology on the control as well as on PLLA and PLLAP(BSTES)2 films was observed through fluorescent microscopy (Leica Microsystems DM2500) at 10X magnification. At 1, 3 and 6 days, cells were fixed in formaldehyde 4% for 60 min at room temperature. After rinsing, phalloidin – tetramethylrhodamine (TRITC) conjugated (Sigma, Italy) was incubated for 45 min at 37 °C in the dark. For nuclear staining, 4',6-diamidino-2-phenylindole (DAPI) was used.

3.14 Composting studies

The biodegradation experiments on some copolymeric systems have been carried out at 58.0 ± 0.1 °C. Compost was supplied by HerAmbiente S.p.A. (Bologna, Italy) and had the following composition (as declared by HerAmbiente): organic carbon: 22.08% of the dry solid, humic and fulvic carbon: 13.44% of the dry solid, C/N ratio: 12.97, pH: 8.15 and salinity: 2.88 dS/m. Film specimens of about 20 × 20 mm were employed. Each sample was placed in a 100 mL bottle in between two layers of compost (20 g each). On top of the upper layer, 10 mL of deionized water were added.

3.14.1 Weight loss analyses

Prior to degradation experiments, each sample was weighed to obtain the initial mass. At determined timepoints triplicate specimens were collected, gently washed under stirring with an ethanol aqueous solution (70% vol) and then with a SDS aqueous solution (2% vol), and finally dried over P_2O_5 under vacuum for 2 days to constant weight prior to further characterization. The weight loss was then calculated using the following equation:

$((m_i - m_f) / m_i) * 100$ **[39]**

where m_f and m_i are the final and the initial sample weight, respectively.

3.14.2 Scanning electron microscopy (SEM)

Surface microstructure of the degraded samples was analysed by scanning electron microscopy (SEM) on gold sputtered films glued with carbon tape on aluminium stabs on a desktop Phenom microscope (Amsterdam, The Netherlands).

3.15 Gas permeability studies

Barrier properties evaluation of the polymers investigated has been conducted in the labs of Agri-food Science and Technology Department, University of Bologna, thanks to the scientific cooperation with Prof. Valentina Siracusa.

Permeability tests were performed by a manometric method using a Permeance Testing Device, type GDP-C (Brugger Feinmechanik GmbH), in accordance to ASTM 1434-82, DIN 53 536 in compliance with ISO/DIS 15 105-1 and to Gas Permeability Testing Manual of the instrument. The equipment consists of two chambers between which the film is placed. After a preliminary high vacuum desorption of the system, the upper chamber was filled with the gas used for the test (CO_2, O_2 or N_2) at ambient pressure. A pressure transducer, set in the lower chamber, recorded the increasing of gas pressure as a function of time. The gas transmission rate (GTR, expressed as cm^3 cm m^{-2} d^{-1} bar^{-1}) defined as the value of the film permeability to gas, was determined considering the pressure increase in relation to time and volume of the device.
All the measurements have been carried out using food grade O_2, CO_2 and N_2 at 23°C, with a relative humidity (RH) of 0%, and a gas stream of 100 cm^3/min. The area of the film samples was 78.5 cm^2 (standard measurement area). In some cases, permeability was checked also at different temperatures (5, 10, 15, 35, 38, 40, 45 and 50 °C) and different RH (85% at 23 °C and 95% at 38 °C).

Experiments were performed at least in triplicate and results are provided as the average ± standard deviation. Sample temperature was set by an external thermostat HAAKE-Circulator DC10-K15 type (Thermo Fisher Scientific, Waltham, MA, USA).

4.RESULTS AND DISCUSSION

4.1 Bio-based aromatic polyesters containing different glycolic length subunit as potential candidates for food packaging

The challenges surrounding plastic waste treatment are complex as well as urgent: these issues are particularly serious in the case of plastic waste from food packaging. In fact, in this case recycling is particularly limited, due to the multi-layered structures, and because of the organic contamination with food. Therefore, viable and long-term solutions are necessary to address this growing environmental concern. In this framework, taking also into account that petroleum is a non-renewable source, whose reserves are constantly decreasing, the major issue of packaging research is the development and the promotion of "bio-plastics". Within this wide class of materials, polyesters from 2,5-furandicarboxylic acid (FDCA) represent an interesting family: in particular, poly(ethylene 2,5-furanoate) (PEF) represents a valid bio-based alternative to traditional PET with its considerably enhanced barrier performance as well as attractive thermal and mechanical properties. The aim of the present study is to devote attention to a family of fully bio-based polyesters obtained by combining FDCA with diols characterized by different number of $–CH_2–$ groups. The so-obtained materials have been characterized from the molecular, thermal and mechanical point of view and compared with PEF. Barrier properties to O_2 and CO_2 gases have been also investigated for potential applications in food packaging. Specifically, objective of this research is to evaluate the effect of glycol subunit length to address the impact on material final properties.

4.1.1 Synthesis and molecular characterization

All the polymers under investigation were successfully synthesized by two-step melt polycondensation technique, according to the procedure reported in Paragraph 3.2.1.2 using $Ti(OBu)_4$ and TTIP as catalysts and starting from the dimethyl ester. This last was prepared and purified according to the procedure described in Paragraph 3.2.1.1. The molecular weights (M_n) and the polydispersity indexes (D) are listed in Table 4.1. As it can be seen, all the materials show a reasonably high molecular weight and quite low polydispersity, thus confirming the good control over the polymerization process. The materials were also characterized from the molecular point of view by means of ^{1}H-NMR. All the spectra were consistent with the expected structure, as no other additional peaks were present. More in detail, in case of PBF, the methylene protons of the glycolic subunit (4H, m) and (4H, t) were located at δ 2.0 ppm and δ

4.5 ppm, respectively, while the singlet of the diacid subunit was located at δ 7.4 ppm. As to PPeF spectrum, the methylene protons of the glycolic subunit (2H, m), (4H, m) and (4H, t) were located at δ 1.55 ppm, δ 1.82 ppm and δ 4.35 ppm, respectively, while the singlet of the diacid subunit was located at δ 7.2 ppm. As to PPF and PHF spectra, see Figure 4.16A and Figure 4.22A, respectively.

Table 4.1. Molecular characterization data of the homopolymers under study obtained by GPC analysis.

Polymer	M_n (g/mol)	D
PPF	30000	2.3
PBF	27300	2.3
PPeF	29600	2.4
PHF	28900	2.3

4.1.2 Thermal characterization

The thermal stability was evaluated by thermogravimetric analysis under pure nitrogen atmosphere. In Table 4.2, the temperatures corresponding to initial decomposition (T_{id}) and to maximum degradation rate (T_{max}) are listed. From the analysis of these data, it is possible to see that all the polyesters under investigation are high thermally stable, with T_{id} above 380 °C, apart from PPF, which is characterized by lower thermal stability (T_{id} = 360 °C). As known, in polymers containing 1,3-propanediol, β-scission reactions are favored [Soccio et al., 2009 (b)]. Moreover, PBF, PPeF and PHF are characterized by the presence of lower amount of both furan rings and ester groups for chain length unit with respect to PPF.

As to the calorimetric analyses, they were carried out on compression molded films, after three weeks of storage at room temperature, in order to uniform the thermal history of the samples. According to the data listed in Table 4.2, for the homopolymers containing glycols with an even number of CH_2 groups, the typical behavior of semicrystalline materials has been found, with a glass transition phenomenon followed by an endothermic melting peak at higher temperature. On the other hand, homopolymers containing glycols with an odd number of CH_2 groups turned out to be amorphous: more in details, PPF is characterized by the presence, after the T_g endothermic step, of an exothermic peak followed by an endothermic one at higher temperature,

with $\Delta H_c = \Delta H_m$, while PPeF shows only the endothermic baseline deviation related to glass-to-rubber transition.

As it can be seen from Table 4.2, T_g values regularly decrease as the glycol sub-unit length is increased, as a consequence of the higher mobility given by longer flexible diols. In addition, in case of polyester containing longer glycolic subunits, the number of stiff aromatic rings for each chain unit is lower.

The melting phenomenon follows the well-known odd/even trend, showing higher T_m and ΔH_m values for the polyesters containing an even number of methylene groups. This effect can be ascribed to the reduction of symmetry that leads to less perfect crystals (lower T_m) and hinders the crystallization capability (lower ΔH_m). This last feature is suppressed in PPeF, that shows just the T_g phenomenon.

Table 4.2. Thermal characterization data of the homopolymers under study obtained by TGA and DSC analyses.

Polymer	T_{id} °C	T_{max} °C	I scan						II scan					
			T_g °C	ΔC_p J/g°C	T_c °C	ΔH_c J/g	T_m °C	ΔH_m J/g	T_g °C	ΔC_p J/g°C	T_c °C	ΔH_c J/g	T_m °C	ΔH_m J/g
PEF*	391	404	82	-	-	-	219	48	83	0.395	185	1	214	1
PPF	360	387	52	0.361	119	7	169	7	52	0.359	-	-	-	-
PBF	382	404	n.d.	-	-	-	170	41	39	0.366	109	33	169	33
PPeF	392	414	17	0.221	-	-	-	-	15	0.350	-	-	-	-
PHF	384	404	n.d.	-	-	-	145	43	9	0.359	56	33	143	39

*[Burgess et al., 2015]

In Figure 4.1 T_g and T_m are plotted as a function of the glycolic subunit length for the materials under investigation and for terephthalic counterparts, added for sake of comparison. By comparing the different glass transition temperatures, regardless the different crystallinity degree, it is possible to notice that both the systems present the same behavior, i.e. T_g regularly decreases as the glycol sub-unit length is increased. In addition, at the same length of the glycol sub-unit, $T_{g,benzene} < T_{g,furan}$, because of the different ring aromaticity/polarity ratio, although the differences are less pronounced as the glycol length is increased. In particular, the higher T_g of furan-based materials can be ascribed to the smaller angles between the furan ring and the ester group, which hinder ring flipping. Another reason could be found in the higher polarity of this kind of ring, which favours inter-chain interactions. As to the melting temperatures, furan-based

samples present lower values than those of their terephthalic counterparts, being however characterized by the same trend. A different balance of the main structural parameters (symmetry, ring aromaticity/polarity ratio, inter-chain interactions and chain flexibility) in the two families has to be the reason of a less effective crystal packing in furan-based polyesters.

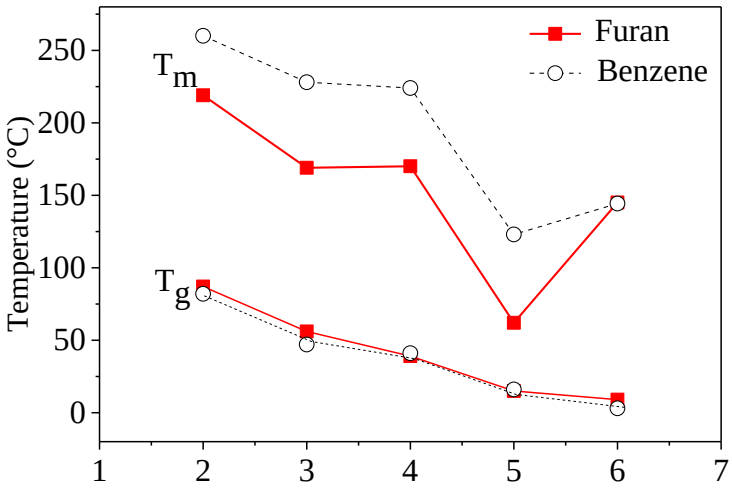

Figure 4.1. T_g and T_m trends as a function of glycolic subunit length for the materials under investigation compared to those of terephthalic ones (PPeF T_m: powder from solvent casting).

4.1.3 Mechanical characterization

Determination of mechanical properties of materials is of crucial importance to evaluate their suitability for specific applications. To evaluate the mechanical response of the polymers synthesized, tensile tests were carried out. Stress-strain measurements were performed on rectangular samples (50 x 5 x 0.3 mm) by measuring the variation of stress as a function of the strain applied. The tensile testing data (elastic modulus E, stress at break σ_B and strain at break ε_B), are summarized in Table 4.3 and shown in Figure 4.2.

Many factors affect the mechanical behavior of polymers. In particular, chain flexibility (i.e. T_g value) and crystallinity degree (ΔH_m) play a key role in the determination of mechanical response.

As a general trend, elastic modulus E and stress at break σ_b decrease, whereas elongation at break ε increases with the glycol sub-unit length.

More in detail, PBF shows similar values of elastic modulus and stress at break, and higher elongation at break with respect to PPF. This behavior can be considered as the result of two opposite factors: PPF is amorphous with higher T_g than PBF which, in turn, is semicrystalline.

As to PHF, its lower values of E and σ_B and higher ε_B with respect to PPF and PBF, can be explained taking into account that although semicrystalline, it is in its rubbery state at room temperature. Among this family of materials, PPeF is the most performing, with the lowest values of E (almost 2.5 orders of magnitude lower with respect to PPF and PBF) and σ_B (1.5 orders of magnitude lower), together with an outstanding elongation at break ε_B, of more than 1700%. This interesting behavior can be explained on the basis of its amorphous state as well as its T_g below room temperature. Surprisingly, it has to be noticed that it was possible to obtain a free-standing PPeF film by compression molding, although this material, as already said, is completely amorphous and at room temperature is in the rubbery state, being its T_g of 15 °C. Lastly, it has to be emphasized that liquid crystal polymers represent the most performant barrier materials nowadays, demonstrating that the 2D-ordered phase is the one that mostly determines the exceptional barrier properties, even more than 3D-crystalline phase.

Table 4.3. Mechanical characterization data obtained by stress-strain measurements.

Polymer	E (MPa)	σ_b (MPa)	ε% (MPa)
PPF	1363±158	31±3	3±1
PBF	1131±160	37±3	3.6±0.3
PPeF	2.30±0.4	0.6±0.1	1762±203
PHF	906±34	22±1	42±4

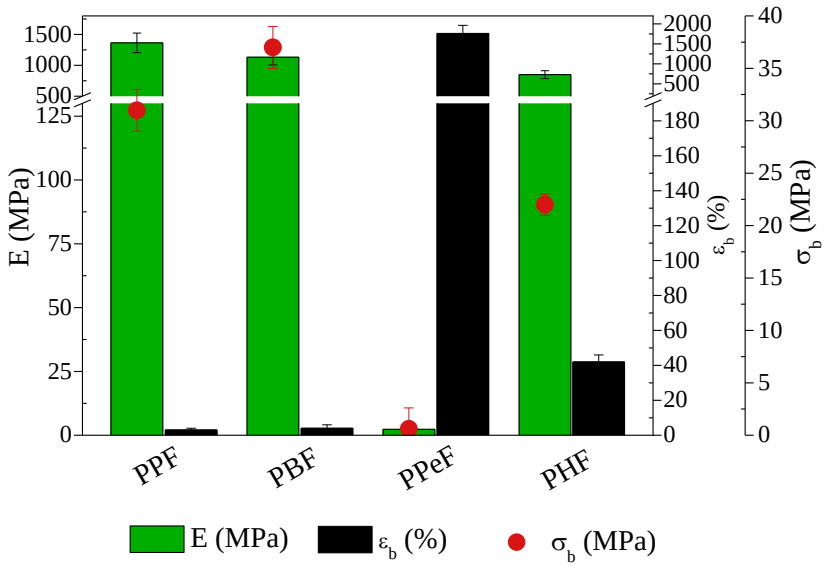

Figure 4.2. Mechanical characterization values for the materials investigated obtained by stress-strain measurements.

4.1.4 Gas permeability studies

Gas barrier behaviour of furan-based polymers was investigated at 23 °C using dry O_2 and CO_2 gases, to check the performance of the materials for potential applications in food packaging. The Gas Transmission Rate (GTR) values, which are an index of permeability through the polymeric matrix, are listed in Table 4.4 and shown in Figure 4.3. In Table 4.4 the GTR values to oxygen and carbon dioxide of PET and its furan-based counterpart PEF are also reported for comparison purposes, as well as BIF ratios values.

As it can be clearly seen, all the polymers synthesized in the present study show excellent barrier ability, even better than that of PEF [Burgess et al., 2014; Burgess et al., 2015], both to O_2 and CO_2. As one can see, GTR values follow an even/odd trend, being the odd CH_2 number containing polymers more performing than the even CH_2 number containing ones. As concerns PEF, PBF and PHF, GTR increases with the glycol subunit length for both gases, whereas for PPF and PPeF an opposite trend was evidenced: $GTR_{PPeF} < GTR_{PPF}$.

An opposite trend was also registered for CO_2/O_2 permselectivity ratio: it increases with the glycol length for PPF and PPeF, whereas it is reduced for PHF with respect to PBF. Considering all the samples, however, CO_2/O_2 permselectivity ratio increases with glycol subunit length, due to a reduced macromolecular polar character, with consequent decrement of CO_2 solubility in the polymer matrix.

As these materials show outstanding barrier performances, the presence of a 2D-ordered phase can be hypothesized. This assumption is supported by previous studies [Burgess et al., 2014 (b); Guidotti et al., 2018 (b); (c); Araujo et al., 2018], which already showed some examples, including furan moieties as mesogenic groups among the wide family of main chain mesogenic-containing polymer liquid crystals (PLCs).

In this view, in addition to disordered amorphous region, two kinds of ordered phases (2D and 3D ones) have to be considered. It is reasonable that, the development of one of them occurs at the expense of the other, i.e., the less 3D-crystalline samples could contain higher amount of 2D-ordered phase. As a matter of fact, the most performing PPF and PPeF, which are amorphous, could be able to rearrange in mesophase regions more than PBF and PHF, which are semicrystalline. Synchroton measurements have been recently carried out to corroborate this hypothesis in collaboration with a group of physic of matter of CSIC of Madrid. The data acquired are going to be analysed and will be object of a future paper.

Table 4.4. Gas transmission rate (GTR) and BIF data for the polyesters under study, at 23 °C, using O_2 and CO_2 as dry gas test., compared to those of PET and PEF.

Polymer	GTR O_2	GTR CO_2	BIF O_2	BIF CO_2
PET **	0.3630	1.37	1	1
PEF *	0.0702	0.171	5	8
PPF	0.0224	0.0288	16	48
PBF	0.10	0.19	4	7
PPeF	0.0013	0.0015	279	913
PHF	0.19	0.5	2	3

**[Hu et al., 2005]

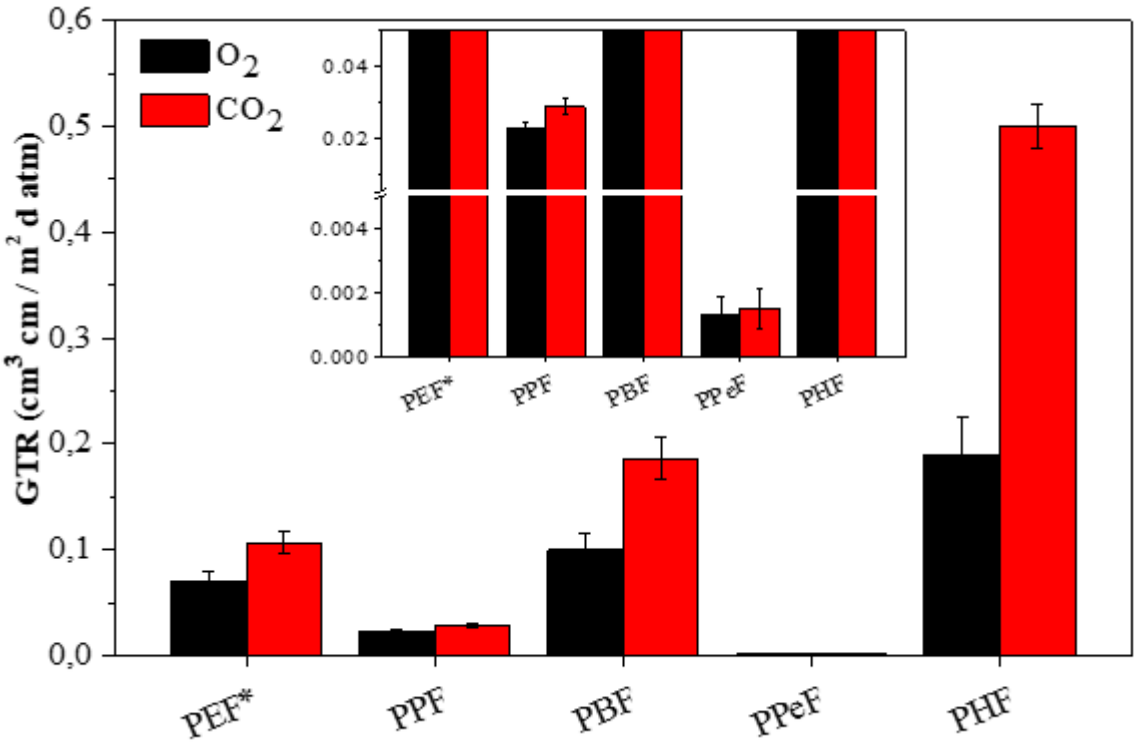

Figure 4.3. GTR values of O_2 and CO_2 through polymeric films (T=23 °C) compared to those of PEF.

4.1.5 Conclusions

Novel fully bio-based polyesters containing furan ring and glycol sub-unit of different length have been successfully prepared. After the synthesis, a simple two-step melt polycondensation,

the obtained materials were characterized from the molecular, thermal and mechanical point of view. In addition, gas barrier tests were carried out to check their potential application in the field of sustainable food packaging as a valid bio-based alternative to traditional PET.

From the results obtained, it is clear that the polymer final properties can be simply tuned by playing on glycol sub-unit length.

From the calorimetric data, it can be seen that T_g values decrease as the glycol subunit length is increased. On the other hand, T_m and ΔH_m values show an even/odd trend, similarly to their terephthalic counterpart.

From studies on mechanical properties, it emerges that simply by changing glycol sub-unit length is possible to get rigid as well as very flexible materials, all characterized however by very good thermal stability, crucial characteristic during material processing.

Interestingly, these materials are characterized by excellent barrier performance, preserving at the same time good mechanical properties. The reason of this behaviour, which is typical of polymer liquid crystals (PLCs) can be found in the presence of 2D-ordered domains, the so-called mesophase, whose formation seems to be favoured in the less crystalline samples.

In conclusion, all the polymers under investigation can be considered smart bioplastics for sustainable and green food packaging applications, which range from flexible to rigid packages.

4.2 Novel 2,5-thiophenedycarboxylic acid-based material: ordered structures and their impact on functional properties.

In response to urgent issues related to the research of new high-performance bioplastics to replace the traditional ones, based on fossil and non-renewable sources, a new bio-based aromatic polyester, poly(butylene 2,5-thiophenedicarboxylate), PBTF was successfully synthesized. PBTF was obtained starting from 2,5-thiophene dicarboxylic acid as well as its dimethyl ester, and then the two samples were characterized from the molecular, thermal, structural and mechanical point of view. PBTF gas permeability was also investigated to different gases and at different temperatures, below and above its glass transition temperature. Its gas barrier behavior was then compared with that of other already widely used polyesters, like PET and PEF.

From the results obtained from calorimetric and diffractometric studies, it was possible to hypothesize the presence of a no-induced 2D-ordered phase, called *meso*-phase, responsible for its outstanding barrier performances. From the comparison of the two PBTF samples, the one obtained by the diacid, the other starting from the dimethyl ester, it was evicted that different ordered structures developed. Such ordered structures had a strong impact on the functional properties (mechanical and barrier ones). The observed different functional properties are the result of a different crystallinity degree and amount of mesophase. In addition, the absence of any crystallinity in PBTF sample obtained from dimethyl ester, allowed for a significant improvement of barrier behavior, because of a reduced amount of dislocations, thus leading to a more tortuous path through the polymeric matrix. Furthermore, PBTF polymorphism was unveiled.

The simple synthetic strategy, combined with the exceptional functional properties, open new scenarios within the world of sustainable packaging polyesters.

4.2.1 Synthesis and molecular characterization

PBTF was successfully synthesized by two-step melt polycondensation technique, according to the procedure reported in Paragraph 3.2.1.2 using $Ti(OBu)_4$ and TTIP as catalysts and starting from 2,5-thiophenedicarboxylic acid (TFDCA) ($PBTF_{Acid}$), or from its dimethyl ester, dimethyl thiophenedicarboxylate (DMTFDC) (h_PBTF). DMTFDC was previously synthesized and purified, according to the procedure described in Paragraph 3.2.1.1. In this latter case, in order

to check the effect of molecular weight on functional properties, also a low molecular weight PBTF was synthesized (l_PBTF), simply by stopping polycondensation reaction earlier during the second polymerization stage. The as obtained PBTFs appeared as lightyellow solid materials, while the purified samples looked like white floccules. The chemical structure was checked by ^{1}H-NMR. The spectra (Figure 4.4) did not reveal any impurities and confirmed the expected structure, which is the same for all PBTF samples. The molecular weights M_n and the polydispersity indexes D, obtained by GPC analysis, are listed in Table 4.5. As it can be seen, $PBTF_{Acid}$ and h_PBTF showed reasonably high and comparable molecular weights and narrow polydispersity, thus confirming that the synthetic strategy adopted allowed a good control over the polymerization. Furthermore, l_PBTF was characterized by a molecular weight three-time lower with respect to h_PBTF (Table 4.5).

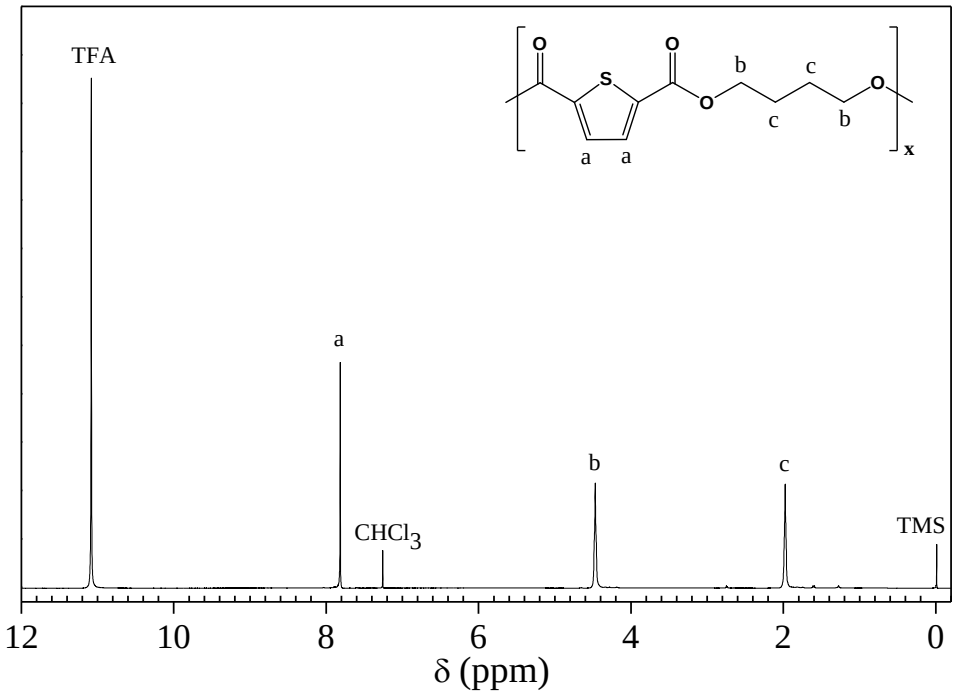

Figure 4.4. ^{1}H-NMR spectrum of PBTF obtained by ^{1}H-NMR.

4.2.2 Thermal characterization

The thermal stability was investigated by TGA under pure nitrogen flux. The temperatures corresponding to the beginning of degradation (T_{onset}) and to the maximum weight loss rate (T_{max}) are collected in Table 4.5. Both high molecular weight PBTF samples display high thermal stability, as the degradation process starts above 390°C. Weight loss occurs in one step

and no residual mass was detected at 750 °C. In addition, no effect of the monomer used, diacid or dimethyl ester was observed (Table 4.5). On the other hand, low M_n PBTF (l_PBTF) showed a slightly lower thermal resistance, confirming the influence of molecular weight on thermal degradation of polyesters [Chrissafis et al., 2006].

Table 4.5. Molecular weight and thermogravimetric data obtained by GPC and TGA, respectively.

Sample	M_n (g/mol)	D	T_{onset} (°C)	T_{max} (°C)
l_PBTF	14400	1.7	367	391
h_PBTF	39600	1.6	391	410
$PBTF_{Acid}$	41400	1.6	391	411

The main thermal transition of polymeric powders (P) and of films (F) obtained by compression molding, are shown in Figure 4.5 and listed in Table 4.6. Only high molecular weight samples were studied in form of powder and film, as the film obtained by low molecular weight PBTF was too brittle for further functional properties evaluation.

The first DSC scan turned out to be dependent on molecular weight, starting raw materials and polymer processing. As to powder samples, both appeared to be semicrystalline, probably because of solvent-induced crystallization due to purification process [Lotti et al., 2016], with a melting endothermic peak at about 150°C (Figure 4.5A). Looking into more detail the DSC traces, one can see that the endotherm of l_PBTF_P is located at higher temperature and is narrower, in agreement with the formation of a more perfect and uniform crystalline phase.

Table 4.6. Calorimetric data (I and II scan) obtained by DSC analysis.

Sample	I scan								II scan			
	$T_{m,I}$ °C	$\Delta H_{m,I}$ J/g	T_{cc} °C	ΔH_{cc} J/g	T_m °C	ΔH_m J/g	T_g °C	ΔC_p J/°C g	T_{cc} °C	ΔH_{cc} J/g	T_m °C	ΔH_m J/g
l_PBTF_P	-	-	-	-	152	27	24	0.320	83	7	152	23
h_PBTF_P	-	-	-	-	147	33	25	0.320	93	23	147	23
h_PBTF_F	-	-	87	28	148	28	24	0.291	88	27	148	27
$PBTF_{Acid}$_F	51	4	-	-	150	30	25	0.287	89	28	150	28

On the contrary, a broader melting peak can be noticed for the high molecular weight PBTF, thus indicating a wider distribution of crystal size and perfection.

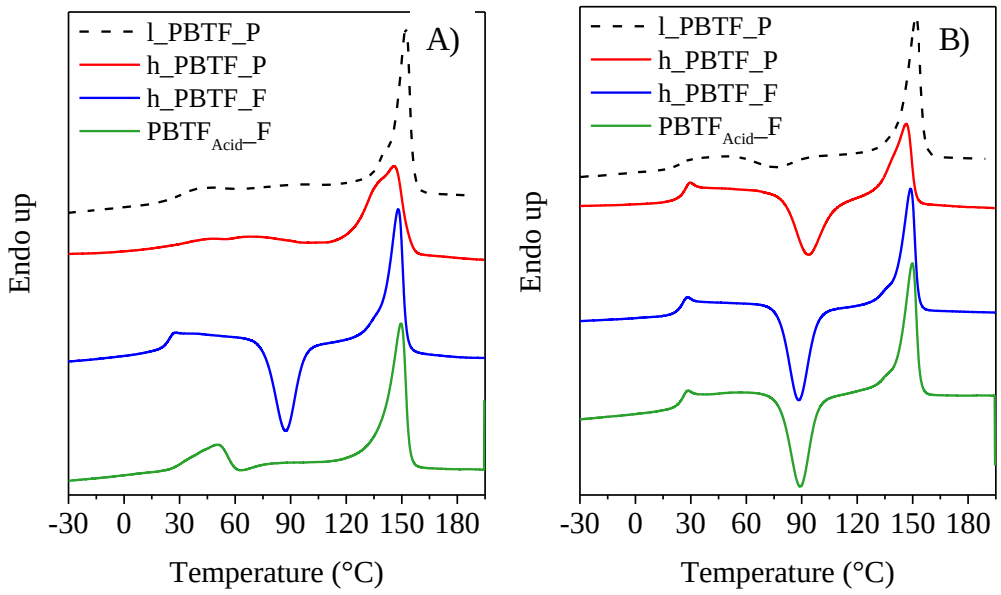

Figure 4.5. DSC traces of l_PBTF_P, h_PBTF_P, h_PBTF_F and $PBTF_{Acid}$_F: A) I scan and B) II scan after melt quenching.

Focusing the attention on the films, it can be seen that the compression molding process completely depressed the crystallization of h_PBTF_F, since its DSC trace shows an exothermic crystallization peak during heating, whose intensity is comparable to that of melting one at higher temperature ($\Delta H_{cc} = \Delta H_m$). Conversely, the film of PBTF prepared from TFDCA ($PBTF_{Acid}$_F) displays a semicrystalline nature, with the presence of a low endothermic peak

(around 50°C), followed by an intense melting phenomenon at higher temperature. In this case, the filming procedure did not significantly affect the crystallization capability of $PBTF_{Acid}$_F. This evidence can be ascribed to the different raw materials employed in the synthesis: it is presumable, indeed, that TFDCA esterification helped removing impurities that act as nucleating agents, thus favoring $PBTF_{Acid}$_F crystallization after molding.

Although not visible in the first calorimetric scan, the presence of the low endothermic peak at around 50°C in the h_PBTF_F sample cannot be excluded, as the crystallization phenomenon might have hidden this less pronounced transition.

As to the II calorimetric scan (Figure 4.5B), carried out after rapid cooling from the molten state, all the samples under investigation show a comparable behavior. More in details, an endothermal baseline shift, related to the glass to rubber transition can be noticed, followed by a cold crystallization peak and a melting endotherm at higher temperatures. In all cases, except for l_PBTF_P, the enthalpy of crystallization is comparable to that of melting ($\Delta H_{cc} = \Delta H_m$), proving that the quenching procedure was effective and able to suppress the crystallization ability of the samples. On the other hand, l_PBTF displayed a partially crystalline nature, as a result of a faster crystallization rate. This behavior is due to the easier folding of shorter macromolecular chains present in this sample during the rapid cooling from the melt.

In order to better understand the nature of the low temperature endothermic peak present in $PBTF_{Acid}$_F sample, annealing treatments were performed (at 65 °C, 100 °C, 130 °C and 145 °C, respectively), and the corresponding traces are shown in Figure 4.6A. It is interesting to notice that after annealing, this peak shifts to higher temperature, while the position of the melting peak at higher temperature was not affected by thermal treatment. In addition, the higher the annealing temperature, the sharper the peak and the more pronounced its temperature shift: from 51°C to 78 °C, 109 °C and 140°C, respectively, suggesting an improvement of its associated phase. Moreover, after annealing, the baseline deviation associated to glass transition became fully visible (Figure 4.6A), thus allowing for the detection of T_g, which is around 30 °C. The calorimetric trace related to the highest annealing temperature (145 °C) is characterized by the presence of only one endothermic phenomenon at higher temperature with respect to the most intense peak of the other annealed samples. This evidence can be due to whether an improvement of the crystalline phase corresponding to the endothermic peak located at 150°C or to the development of a new ordered phase.

The effect of the heating rate on the two endothermic peaks was also evaluated, and the corresponding DSC traces are shown in Figure 4.6B. As it can be seen, the position of the first endothermic peak is deeply affected by the scanning rate, whereas the peak at higher temperature is not influenced. As it is well known, melting phenomena are first order transitions, which do not depend on the heating rate. Conversely, the dependence on the scanning rate indicates a second order transition, such as glass to rubber transition or isotropization of 2D-ordered phases, i.e. meso-phase. The presence of meso-phase has been already evidenced for other polyesters, such as PET [Ran et al., 2002; Keum et al., 2003] and polylactide [Stoclet et al., 2010; Lv et al., 2011], although in these cases it develops after straining and/or thermal treatment.

In addition, the reversibility of this transition was also verified, by subjecting $PBTF_{Acid}$ film to the following thermal treatment: heating steps to 65, 100, and 130°C, each followed by quenching to -40°C and heating to the subsequent temperature of 100, 130, and 180°C, respectively (Figure 4.6C). According to this kind of treatment, the low endothermic peak should disappear if associated to a first order transition. Conversely, it is still evident, with progressive shift towards higher temperatures after each cycle, thus confirming the reversible nature of this transition.

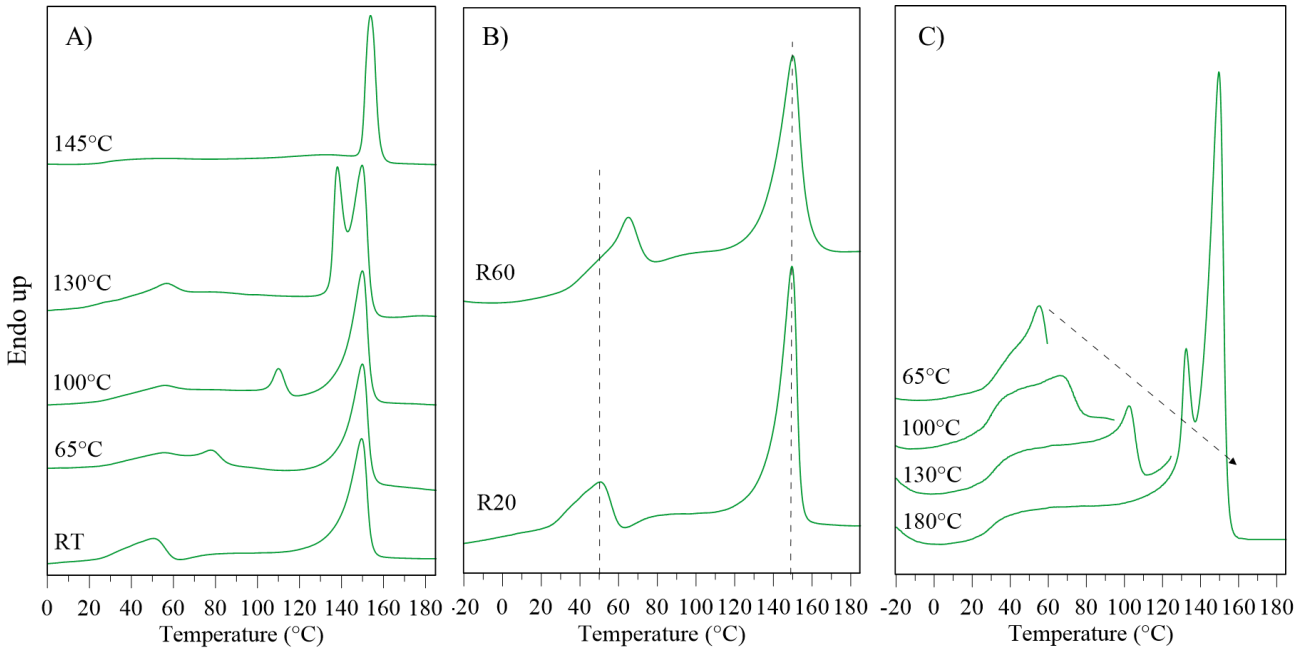

Figure 4.6. DSC curves of $PBTF_{Acid}$_F: (A) untreated and annealed (10 min at the indicated temperatures) film; B) different heating rates (20 and 60°C/min, dotted lines represent eye guides); C) consecutive heating steps to 65, 100, 130 and 180°C.

4.2.3 Structural characterization

To shed light on the complex thermal behavior, WAXS analysis was carried out on the PBTF samples under study. Any possible influence of molecular weight, starting raw materials and processing on the development of ordered phases was also evaluated.

The X-ray diffraction (XRD) patterns of l_PBTF_P, h_PBTF_P, h_PBTF_F and $PBTF_{Acid}$_F are shown in Figure 4.7, together with the profile of a fully developed α-PBTF phase, which will be described more in details later.

Apart from h_PBTF_F, which shows a pattern typical of a fully amorphous materials, according to DSC trace (Figure 4.5A), all other samples display some peaks ascribable to crystalline domains.

As to $PBTF_{Acid}$_F, XRD pattern displays few, broad peaks of low intensity overlapped with a bell-shape intense background. The two most intense peaks are located at 2θ = 22.9 and 24.7° (d= 3.88, 3.60 Å), while other less intense peaks are located at 2θ = 8.7, 15.1, 17.1° (d= 10.1, 5.8, 5.1 Å). To improve this not clear diffractometric pattern, PBTF film was subjected to tensile tests (hereinafter referred to as fiber), as it is known that stretching is an efficient tool to induce crystallization and, consequently, to obtain a more perfect crystalline phase. XRD pattern of $PBTF_{Acid}$ fiber (Figure 4.7A-a) did not look like that of a typical 3D crystalline phase, being characterized by two partially overlapped broad reflections, located at 16.7 and 24.2° (d= 5.3, 3.7 Å). This kind of profile is typical of a roughly 2D-ordered phase, hereafter called meso-PBTF. By comparing film and fiber diffraction profiles (Figure 4.7A) it is possible to hypothesize the simultaneous presence of a meso-phase and a crystalline one in $PBTF_{Acid}$_F, the former being the majority fraction. In addition, it seems that the mechanical treatment favors the formation of the meso-phase over the crystalline one.

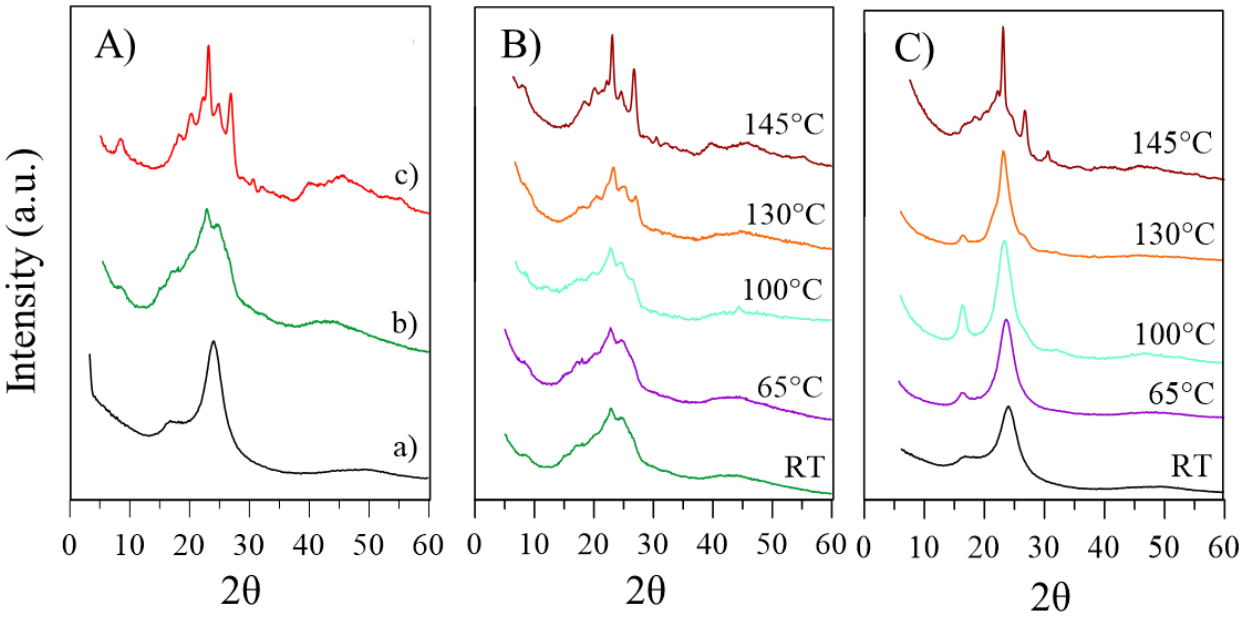

Figure 4.7. XRD patterns of $PBTF_{Acid}$: (A) from bottom to top, fiber (a), film (b), well crystallized sample (c) obtained by slow cooling from the melt; XRD scans performed at RT on untreated and annealed (10 min at the indicated temperatures) film (B) and fiber (C).

The presence of meso-PBTF in the film is supported also by DSC measurements carried out on the fiber. This last has been subjected to the same thermal treatments previously described for the film: $PBTF_{Acid}$ fiber shows indeed an analogous thermal behavior with respect to film [Guidotti et al., 2018 (c)].

This evidence seems to prove that the second order low-temperature endothermic peak, present in both PBTF fiber and film, is due to the meso-phase showed in WAXS analysis. To verify this hypothesis, annealed $PBTF_{Acid}$ films and fibers were subjected to X-ray diffraction analysis, and the corresponding XRD patterns are shown in Figure 4.7B and Figure 4.7C, respectively. As to XRD profiles of $PBTF_{Acid}$ annealed film, they show a progressive improvement of the ordered phase: the higher the annealing temperature, the higher the sharpness, the definition and the intensity of the peaks located at $2\theta = 23.1$ and 26.9° (d = 3.84 and 3.31 Å). Moreover, several additional reflections at $2\theta = 8.4$, 18.2, 20.2, 22.2 and 24.8° (d = 10.5, 4.87, 4.39, 3.99, 3.60 Å) become evident (Figure 4.7B).

The XRD profiles of annealed $PBTF_{Acid}$ fibers show a similar trend (Figure 4.7C). In this case meso-phase becomes more perfect as the annealing temperature is increased (up to 100 °C), as the two peaks at $2\theta = 16.7$ and 24.2° become sharper and more intense.

On the other hand, a decrease of the signal at 2θ = 16.7°, related to the meso-phase, as well as the appearance of a shoulder at 2θ = 26.6°, ascribable to the crystal phase, can be seen when the annealing temperature is of 130°C. Finally, at the last annealing temperature (145 °C) $PBTF_{Acid}$ fiber shows a typical semicrystalline polymer profile, with the two main sharp peaks at 2θ = 23.1 and 26.7°. These two peaks are visible also in the XRD pattern of a well crystallized sample of PBTF, obtained by slow cooling from the melt (Figure 4.7A-c). The XRD profile of such sample is characterized by two main peaks at 2θ = 23.1 and 26.8° (d = 3.84 and 3.32 Å) and several less intense reflections at 2θ = 8.4, 18.2, 20.2, 22.2 and 24.8° (d = 10.5, 4.87, 4.39, 3.99, 3.60 Å). Hereinafter this phase will be referred to as α-PBTF.

As it can be seen from Figure 4.8, l_PBTF_P and h_PBTF_P XRD profiles are completely different from that of α-PBTF. More in details, the profile of l_PBTF_P is characterized by main peaks at 2θ = 15.6°, 21.1° and 24.9° (d = 5.7, 4.2 and 3.6 Å) together with some others less intense at 2θ = 9.25°, 19.2°, and 31.3° (d = 9.5, 4.6, and 2.9 Å, respectively).

This phase was defined as β-PBTF. On the other hand, the XRD pattern of h_PBTF_P is characterized by three peaks at 2θ = 13.9°, 16.2° and 24.8° (d = 6.3, 5.4 and 3.6 Å) together with other two less intense at 2θ = 8.2° and 21.2° (d = 10.8 and 4.2 Å).

Since this profile is not overlapping with the above reported ones, the presence of a further crystal form, hereafter referred to as γ-PBTF, can be hypothesized.

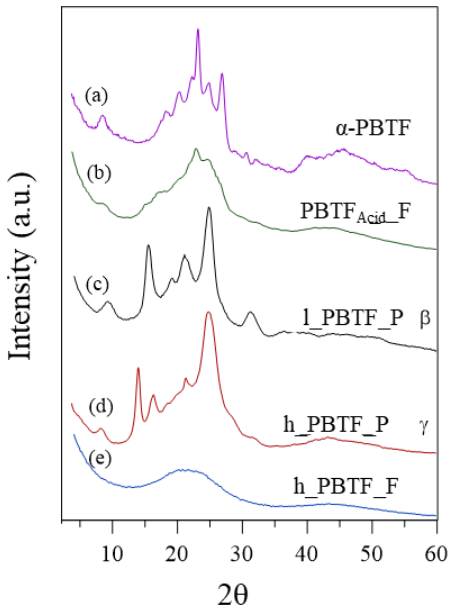

Figure 4.8. XRD patterns of PBTF polymorphs: a) fully developed α-PBTF, b) $PBTF_{Acid}$_F, c) l_PBTF_P (β-PBTF), d) h_PBTF_P (γ-PBTF) and e) h_PBTF_F.

The thermal stability of α-PBTF, β-PBTF and γ-PBTF was checked by subjecting the samples to a thermal treatment resembling I and II DSC scans (Figure 4.9).

As to α-PBTF (Figure 4.9A), a significant enhancement of peak intensities occurs as temperature is increased, up to melting. Since it is possible to see an evolution of the patterns towards the profile typical of α crystal phase, it is possible to state that the low intensity and broad reflections present in the untreated $PBTF_{Acid}$ film can be ascribed to this phase. After melt quenching, during the II scan, the sample, initially amorphous, starts crystallizing and arranging in the α-PBTF lattice.

As to β-PBTF phase, it maintains its stability up to 120°C (Figure 4.9B). When further heated to a temperature close to melting, a partial transformation in α-PBTF can be seen. The further heating of the melt quenched sample induces the crystallization of α-PBTF phase.

A similar behavior was detected for γ-PBTF (Figure 4.9C), since during the first scan, the typical peaks of γ-PBTF remain stable up to 120°C, and then decrease in intensity when higher temperatures are reached. At 140°C, two peaks located at $2\theta = 23.1°$ and 26.9° appear, confirming the complete shift to α-PBTF phase. In this case too II scan favors the partial crystallization of α-PBTF. According to all these results, it is clear that α-PBTF is the more thermodynamically stable among all PBTF crystalline phases.

The same temperature scans have been carried out also on PBTF fiber. From the results obtained, it is possible to say that up to 100°C (Figure 4.10) meso-phase peaks become sharper and more intense as the temperature is increased, then from 140°C a small worsening occurred. At 145°C, which is very close to the melting point, a significant change in the XRD pattern occurs, with a shift toward a profile which can be ascribed to a low crystalline α-PBTF.

α-PBTF is also the profile obtained subjecting amorphous h_PBTF_F to the same thermal treatment. Furthermore, its mechanical elongation reveals the presence of mesophase, as well as in $PBTF_{Acid}$_F.

According to these results, PBTF represents a clear example of how macromolecular chains can arrange in the solid state to produce many different polymorphs characterized by different properties. The profiles of these three different PBTF crystalline phases are very different and easily detectable.

However, although the shape of an XRD pattern is strictly related to the solid-state structure, the profile deconvolution necessary for the identification of parameters like unit cell

dimensions, symmetry and atom positions is quite difficult, especially if, as in this case, the fiber diagram is not available.

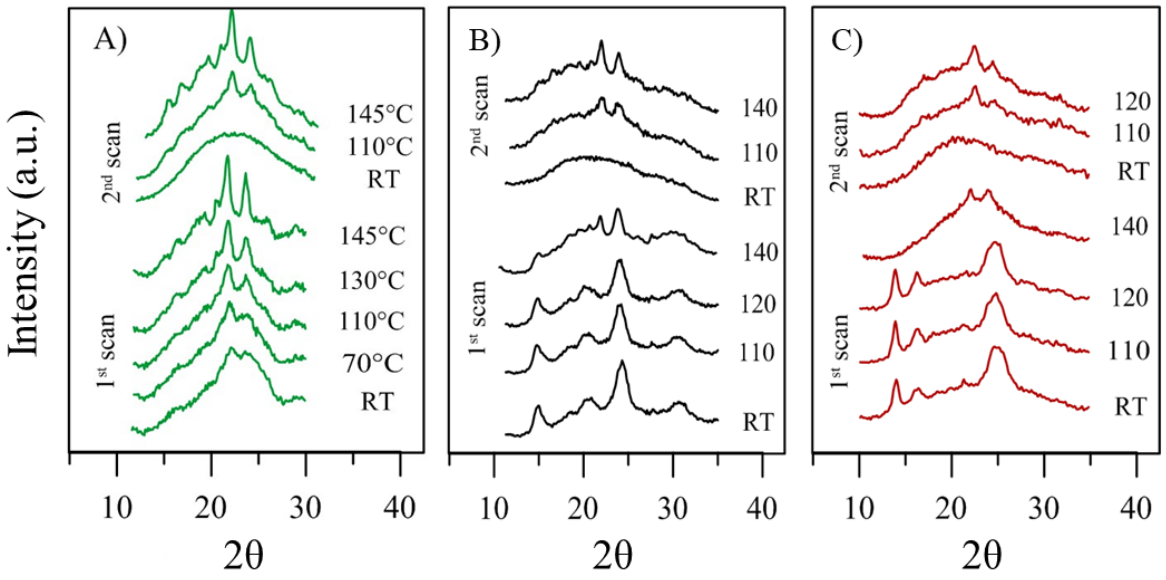

Figure 4.9. *In situ* XRD for A) $PBTF_{Acid}$_F, B) l_PBTF_P (β-PBTF) and C) h_PBTF_P (γ-PBTF) (I scan and II scan after quenching from the melt).

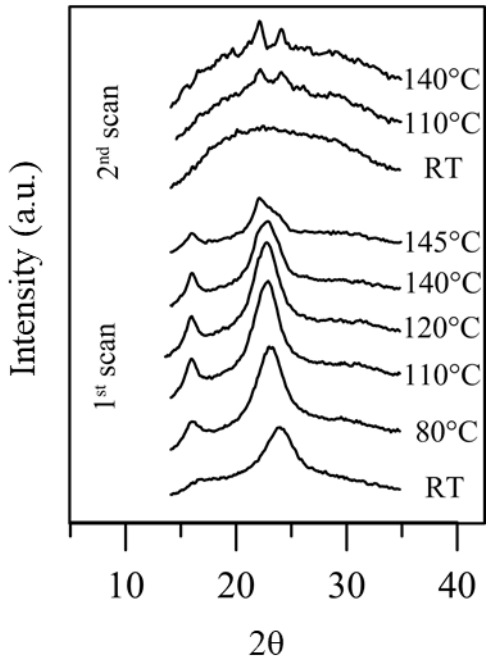

Figure 4.10. *In situ* XRD for $PBTF_{Acid}$ fiber (I scan and II scan after quenching from the melt).

A possible strategy to solve this problem is the search of some analogies with patterns of other polymers characterized by comparable chemical backbone. In this scenario, β-PBTF was compared with poly(butylene furanoate) PBF and poly(butylene terephthalate) PBT (Figure 4.11).

A good match between β-PBTF and α-PBT was found, since three couple of peaks present in α-PBT profile can be merged in single peaks within the β-PBTF pattern.

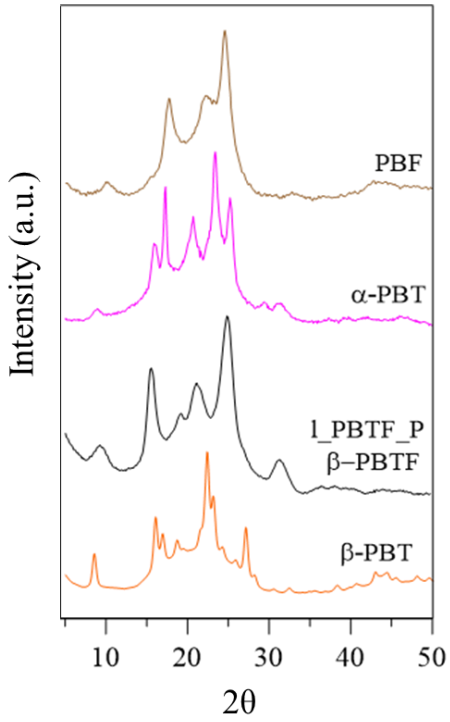

Figure 4.11. XRD patterns of PBF, α-PBT, β-PBTF (l_PBTF_P sample) and β-PBT (calculated).

A Rietveld refinement was performed by using a disordered chain where the sulfur atoms of the thiophene rings statistically assume one of the two possible orientations. Of course, it was assumed that β-PBTF crystal fraction could be structurally isomorphous to α-PBT and it was taken into account the intrinsic lower symmetry of PBTF, because of the presence of a sulfur atom inside the aromatic ring, with respect to PBT. Considered all this, a good agreement between observed and calculated data was found. The results obtained are shown in Figure 4.12 with refined unit cell a = 4.56Å, b = 6.59Å, c = 11.21Å, α = 98.5°, β = 111.6°, γ = 116.0°.

However, the same approach could not be used for α-PBTF and γ-PBTF, because of lack of similarities with known profiles of other polymers.

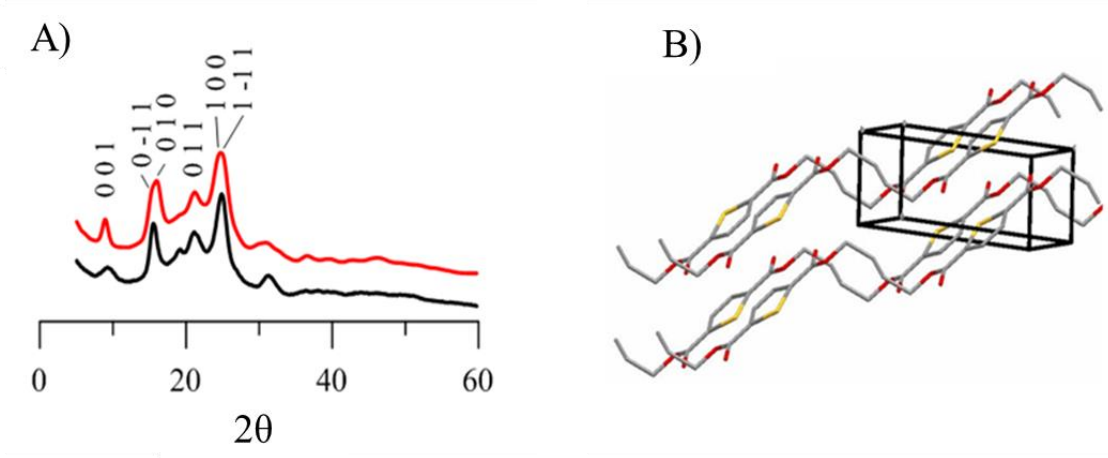

Figure 4.12. Structural study of β-PBTF: A) comparison between the XRD pattern of PBTF powder sample (black) and calculated (red) from crystal data obtained by structure refinement; B) a sketch of the structure (atom codes: C=grey, S=yellow, O=red).

4.2.4 Mechanical characterization

The influence of the different monomers (diacid vs. dimethyl ester) employed for the synthesis of PBTF on mechanical properties was investigated by comparing h_PBTF_F performances with those of $PBTF_{Acid}$_F, measured under the same conditions.

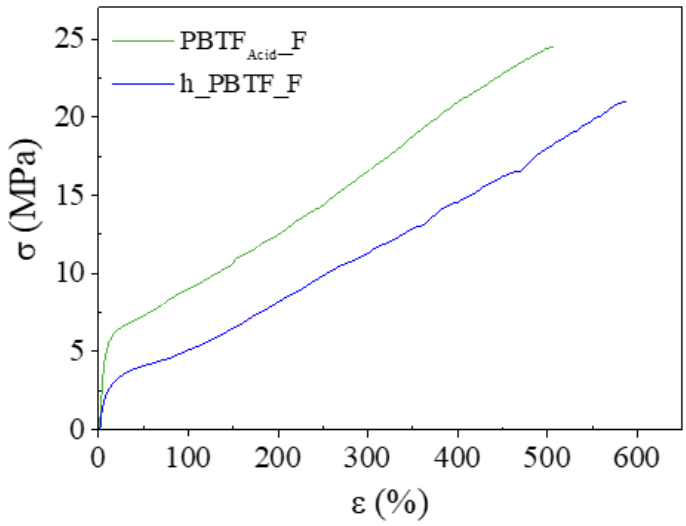

Figure 4.13. Stress-strain curves of h-PBTF and PBTF films.

The results obtained are reported in Figure 4.13. The two samples h_PBTF_F and $PBTF_{Acid}$_F show a similar elongation at break ε_b, being 580 ± 60 and 555 ± 50, respectively. On the

contrary, a reduction of 50% of the elastic modulus E and of 20% of the stress at break σ_b of h_PBTF_F with respect to $PBTF_{Acid}$_F can be observed (47 ± 3 *vs.* 89 ± 7 MPa and 19.4 ± 2.0 *vs.* 24.5 ± 0.5 MPa, respectively). This behavior can be explained as due to the different crystallinity degree of the two samples (Table 4.6), being $PBTF_{Acid}$_F characterized by a significant presence of crystalline domains, while in h_PBTF_F no crystallinity was detected. In addition, both the mesophase and the temperature at which tensile tests were carried out can be responsible for the high elongation at break as well as their good stress at break. In particular, the measurements were performed at room temperature, which is around T_g, meaning that the samples are not in a fully glassy state.

In addition, since no yield was recorded, it is possible to say that PBTF shows thermoplastic elastomeric behavior, making this polyester particularly interesting for applications in flexible packaging. This mechanical response of PBTF is quite peculiar, in particular if compared to that of some furan-based materials like PEF and PBF. Indeed, PBF shows both yield and higher elastic modulus, above 800 MPa [Soccio et al., 2016 M.; Zhou et al., 2014; Wu et al., 2012; Zhu et al., 2013]. Very high elastic modulus, together with brittle fracture, were evidenced for PEF, too [Jiang et al., 2012; Siracusa, 2012].

4.2.5 Gas permeability studies

According to literature [Robertson, 2013], gas permeability is affected by many factors, like the molecular structure and symmetry, chain stiffness, degree of order, crystallinity and glass transition temperature. Gas transmission through a polymer matrix is also dependent on the tortuosity of the path, which in turn is related to the amount of impermeable crystalline domains. Taking into account all these factors, the influence of the different monomers (diacid vs. dimethyl ester) employed for the synthesis of PBTF on gas barrier properties was investigated by comparing h_PBTF_F performances with those of $PBTF_{Acid}$_F under the same conditions. From the GTR values, it was possible to see a significant reduction of both O_2 and CO_2 permeability for h_PBTF_F with respect to $PBTF_{Acid}$_F. The performance improvement is more pronounced for CO_2 gas, with about 7.5× lowering (0.0042 vs. 0.032), while O_2 GTR was reduced from 0.019 to 0.0030 in h_PBTF_F with respect to $PBTF_{Acid}$_F (about 6.3x lowering). Again, these results can be explained taking into account the presence, in these samples, of mesophase. In fact, as it is well known, ordered structures, like crystalline or mesophase ones,

are impenetrable to most gases, thanks to their high chain packing, while amorphous regions are considerably more permeable [Hedenqvist, 2012].

Consequently, the improvement of the barrier performances observed for h_PBTF_F compared to those $PBTF_{Acid}$_F can be explained with the presence of mesophase in h_PBTF_F too.

In addition, it can be also hypothesized that the presence of crystalline domains in $PBTF_{Acid}$_F limits the mesophase formation, as already reported in the literature for propene/ethylene copolymers [Cavallo et al., 2010]. The complete absence of crystallinity in h_PBTF_F favor the development of a higher amount of highly packed 2D-ordered structures, thus leading to a lower gas permeability [Hedenqvist, 2012]. More in details, for $PBTF_{Acid}$_F the number of domain boundaries is high because of the simultaneous presence of both crystalline and mesophase domains, while a lower content of disclinations can be hypothesized for h_PBTF_F, in which crystalline phase was not detected. The lower amount of disclinations is responsible for a more tortuous crossing path for both gases.

The effect of temperature on the gas transmission rate values was investigated for $PBTF_{Acid}$_F sample. More in details, GTR measurements were carried out for O_2, CO_2 and N_2 gases at 5, 10, 15, 23, 35, 40 and 45 °C, respectively. All the values obtained are listed in Table 4.7 and shown in Figure 4.14A. As expected, GTR is affected by temperature, increasing as the temperature is risen. In particular, starting from 23 °C, which is also near the T_g of $PBTF_{Acid}$ (i.e. 25°C), a sudden and considerable increase of the permeability was recorded for the temperatures above T_g. Conversely, a lower dependence on the temperature was observed in the ranges 5-15°C and 35-45°C. The lower GTR values in the range 5-15°C can be explained considering that below T_g, the chain segments have a limited mobility, with a reduced free volume. Consequently, gas molecules must pass through a more tortuous path to diffuse through the polymeric membrane.

However, it must be noticed that PBTF gas barrier performances are very good in the entire range of temperatures, both below and above T_g. This interesting result can be ascribed again to the presence, together with the crystalline phase, of the meso-phase, which is responsible for a denser packing of the macromolecular chains and acts as an additional obstacle to gas molecules diffusion.

Table 4.7. GTR values of N_2, O_2 and CO_2 in the range 5-55°C and perm-selectivity ratios for $PBTF_{Acid}$ film (film thickness = 166 µm).

Temperature	GTR (cm^3 cm m^{-2} d^{-1} bar^{-1})			Perm-selectivity		
(°C)	O_2	N_2	CO_2	CO_2/O_2	CO_2/N_2	N_2/O_2
5	$0.016 \pm 13E^{-5}$	$0.016 \pm 8E^{-5}$	$0.023 \pm 8E^{-5}$	1.4	1.4	1.0
10	$0.017 \pm 8E^{-5}$	$0.017 \pm 8E^{-5}$	$0.024 \pm 13E^{-5}$	1.4	1.4	1.0
15	$0.018 \pm 2E^{-5}$	$0.018 \pm 2E^{-5}$	$0.024 \pm 3E^{-5}$	1.3	1.3	1.0
23	$0.025 \pm 10E^{-5}$	$0.023 \pm 3E^{-5}$	$0.032 \pm 10E^{-5}$	1.3	1.4	1.0
35	$0.035 \pm 13E^{-5}$	$0.028 \pm 7E^{-5}$	$0.036 \pm 13E^{-5}$	1.0	1.3	0.8
40	$0.036 \pm 55E^{-5}$	$0.029 \pm 7E^{-5}$	$0.036 \pm 18E^{-5}$	1.0	1.2	0.8
45	$0.036 \pm 13E^{-5}$	$0.029 \pm 7E^{-5}$	$0.037 \pm 13E^{-5}$	1.0	1.3	0.8

As to perm-selectivity ratios (Table 4.7), they turned out to be dependent on the measuring temperature, thus confirming the dependence of this parameter not only on the chemical structure of the material, but also on the temperature at which the measurement is carried out. [Siracusa et al., 2017].

In addition, by comparing $PBTF_{Acid}$ barrier properties with those of other bio-based polyesters and traditional polyesters already widely used for packaging applications, it is possible to notice that permeabilities to oxygen and carbon dioxide are well below those of PLA, PEF and amorphous PET and comparable to those of PPF.

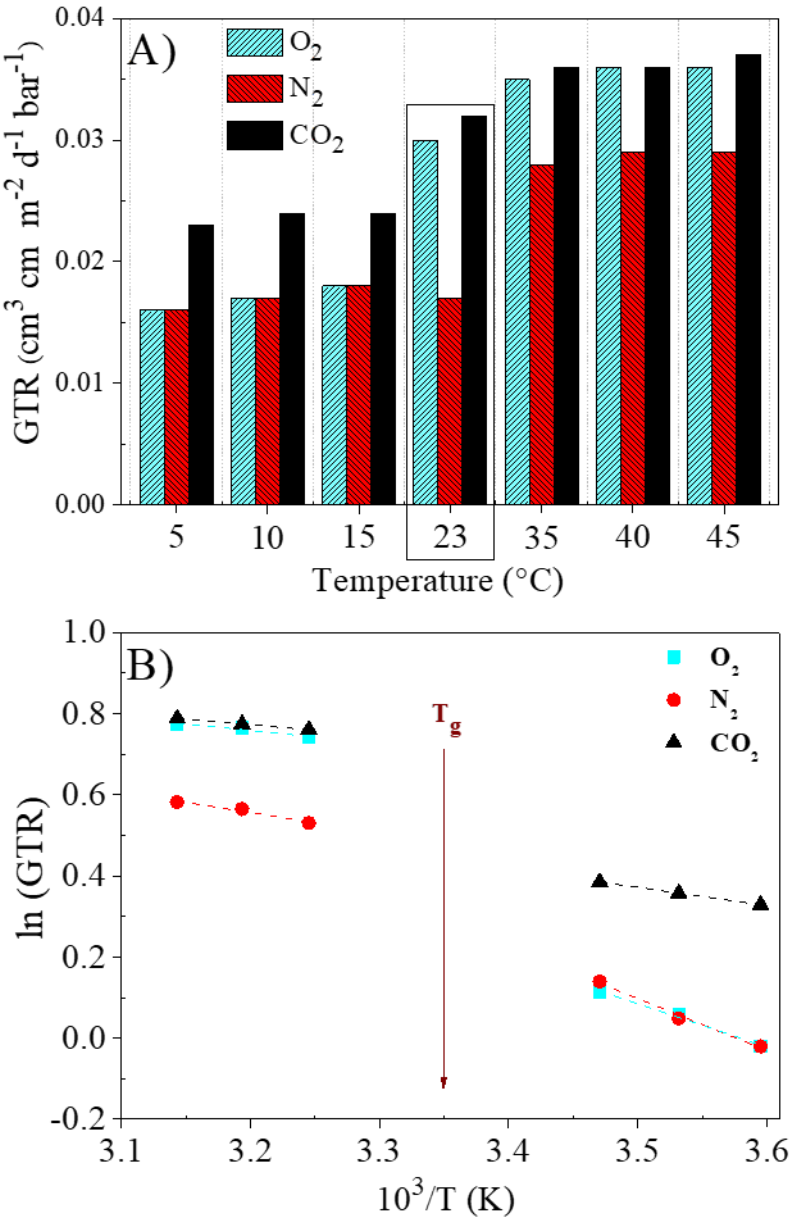

Figure 4.14. Gas transmission rate (A) and Arrhenius plot of GTR (B) in the range 5-45°C for CO_2, O_2, and N_2.

For temperatures at which no thermal transitions in polymers (i.e. glass to rubber transition) or in the permeants (i.e. boiling point) occur, the dependence of permeation on the temperature can be described by the Arrhenius model [Komatsuka et al., 2009]. More in details, a linear dependence of the logarithm of a transport parameter to the reciprocal of the absolute temperature 1/T can be expressed as follows:

$$P = P_0^{-Ep/RT} \quad \textbf{[40]}$$

where P is the gas permeability (GTR), P_0 a pre-exponential factor of permeation, E_p the activation energy for permeation and R the gas constant.

Since gas permeability changes across $PBTF_{Acid}$ T_g, it can be supposed that E_p will be higher at temperatures above T_g than below T_g [Komatsuka et al., 2009]. Therefore, E_p was calculated in both the temperatures ranges 5-15°C (below T_g) and 35-45°C (above T_g), and the relative Arrhenius plot is shown in Figure 4.14B. The activation energy values were calculated through a linear fitting of the experimental data (dashed lines) and listed in Table 4.8. As it can be seen, the experimental data well fit the theoretical behavior for all the gases analyzed, thus proving a good correlation between permeability and temperature.

Table 4.8. Activation energy of the gas transmission rate process for O_2, N_2 and CO_2, with the relative R^2 coefficient (in brackets).

Temperature range (°C)	**E_p (KJ/mol)**		
	O_2	**N_2**	**CO_2**
5 - 15	8.91 (0.98)	10.65 (0.98)	3.73 (0.99)
35 - 45	2.68 (0.89)	4.21 (0.93)	2.25 (0.99)

For all the gases considered, E_p values change with the temperature range considered, below or above T_g, according to different trends. More in details, E_p trends for O_2 and N_2 are quite similar, since a higher E_p is recorded below T_g, whereas in the range 35-45°C a lower dependence of GTR on the temperature can be seen (i.e. lower E_p). Conversely, in case of CO_2, E_p appeared to be independent on being above or below T_g.

Moreover, E_p value is deeply affected by the permeant size, increasing with the decrease of the permeant size, according to the order already observed in literature: $CO_2 < O_2 < N_2$ [Fu et al., 2015]. Anyway, above T_g, the effect of permeant size on the activation energy for the three gases is less remarkable, probably because of the enhanced mobility of the macromolecular chains which favors gas flow.

4.2.6 Conclusions

Both low and high molecular weight bio-based poly(butylene 2,5-thiophene dicarboxylate) PBTF was successfully synthesized through melt polycondensation, starting from diacid or its dimethyl ester.

Molecular weight, kind of starting raw materials and processing (purified powder or compression-molded film) were found to deeply affect the structural behavior in terms of nature and amount of crystalline domains. Low molecular weight macromolecules easily folded, while esterification of TFDCA, by removing the impurities that can act as nucleating agents during crystallization, prevents crystallization process. In addition, the presence of three different polymorphs, namely α-PBTF, β-PBTF and γ-PBTF, in addition to the presence of 2D-ordered domains were detected. It was proven that α-PBTF is the most thermodynamically stable crystal phase. Thanks to the similarities with α-PBT, it was possible to refine the crystal structure of β-PBTF.

More interestingly, PBTF shows peculiar mechanical properties, with its high elongation at break and complete absence of yield, together with outstanding barrier properties, even better than those of PEF, which is considered one of the most successful biopolyesters.

As to the exceptional barrier performances, these have been explained on the basis of the peculiar structural PBTF arrangement that allows the formation of the 2D-ordered phase, i.e. meso-phase, and of 3D-crystalline domains. Both together cause a dense chains packing, thus hindering gas flow.

Most importantly, it was demonstrated that by selecting a different starting material, i.e. TFDCA or DMTFDC, it was possible to deeply change the mechanical and gas permeability behavior of PBTF, playing on the different amount of crystalline domains. These last not only influence E and σ_B values but have also a key role in determining the content of mesophase that, as already said, is responsible for the outstanding gas barrier performance of this polyester. Indeed, the absence of any crystallinity maximize the amount of mesophase, leading to a considerable reduction of both oxygen and carbon dioxide transmission.

In conclusion, the winning combination of excellent tensile and gas barrier properties make PBTF a very promising candidate for sustainable flexible packaging applications.

4.3 Effect of different aromatic ring on gas barrier behaviour: Poly(propylene 2,5-thiophenedicarboxylate) *vs.* Poly(propylene 2,5-furandicarboxylate)

Recently, both academic and industrial interest is focused on the development of high gas barrier bioplastics to substitute the traditional fossil-based ones. In this view, a new bio-based aromatic polyester, poly(propylene 2,5-thiophenedicarboxylate) (PPTF), has been prepared and compared to its furan-based counterpart (PPF). Both the materials were synthesized through two-step melt polycondensation, and were characterized from the molecular, thermal, mechanical and structural points of view. Gas permeability behaviour to oxygen, carbon dioxide and nitrogen at 23°C was evaluated, to check the potential applications of these bio-based plastics in the field of packaging. Both the polyesters under investigation are characterized by superior gas barrier performances in respect to PEF and PET. As to CO_2 gas test, gas transmission rate was measured also at different temperatures. In addition, the permeability at different relative humidity was checked for both biopolyesters, the thiophene-containing one showing better performances than its furan-containing counterpart. More in details, the permeability of PPF sample got worse with respect to PPTF one with the increasing of humidity, because of the more polar nature of furan ring. In addition, the different polarity of the aromatic ring had an impact on the crystallization capability, which in turn affects mechanical and barrier performances.

The simple synthetic strategy adopted, as well as the exceptional barrier properties make these new bio-based materials potential alternatives in the world of sustainable packaging materials.

4.3.1 Synthesis, molecular and surface characterization

Poly(propylene 2,5-thiophenedicarboxylate) PPTF and Poly(propylene 2,5-furandicarboxylate) PPF were successfully synthesized through two-step melt polycondensation, according to the procedure reported in Paragraph 3.2.1.2, using $Ti(OBu)_4$ and TTIP as catalysts.

The as-prepared samples appeared as light yellow hard solid materials, whereas the purified ones were white floccules.

The new polymers are characterized by the same glycolic subunit, differing however for the diacid one, which contains furan ring in the case of PPF, thiophene one in PPTF. These two aromatic five-membered rings show different resonance energies, being of 6.2 Kcal/mol for furan and 29.1 Kcal/mol for thiophene, respectively. Resonance stabilization of heteroaromatic

rings depends in turns on several factors, and results in different molecular properties. As to the ability of one of the heteroatom's non-bonding electron pairs to participate in the aromatic π-system, oxygen, which is highly electronegative, more difficulty shares its non-bonding electron pair than sulfur. Consequently, because of the higher electronegativity of oxygen, the furan ring is the less aromatic. In addition, electronegativity of the heteroatoms is responsible for a dipolar moment on the ring, directly proportional to the heteroatom electronegativity (Figure 4.15).

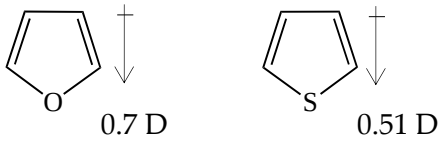

Figure 4.15. Dipole moment vector of furan and thiophene rings.

The molecular weights (M_n) and the polydispersity indexes (D) of PPTF and PPF, obtained by GPC analysis, are listed in Table 4.9. As it can be seen, both the materials show a reasonably high molecular weight and quite narrow polydispersity, thus confirming the good control over the polymerization process. The homopolymers were also characterized by means of ^{1}H-NMR spectroscopy. Both the spectra, shown in Figure 4.16, were consistent with the expected structure, as no other additional peak can be detected.

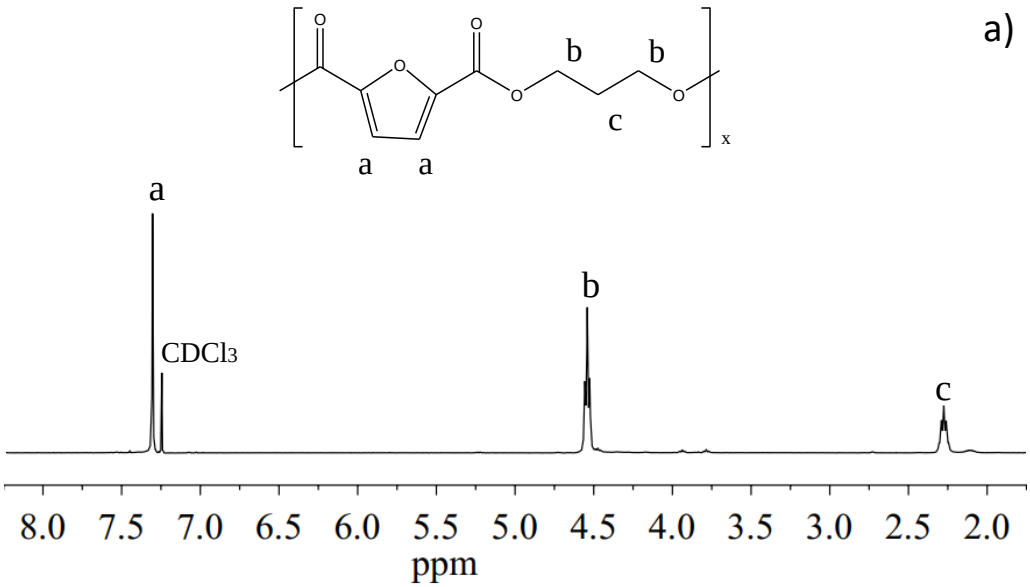

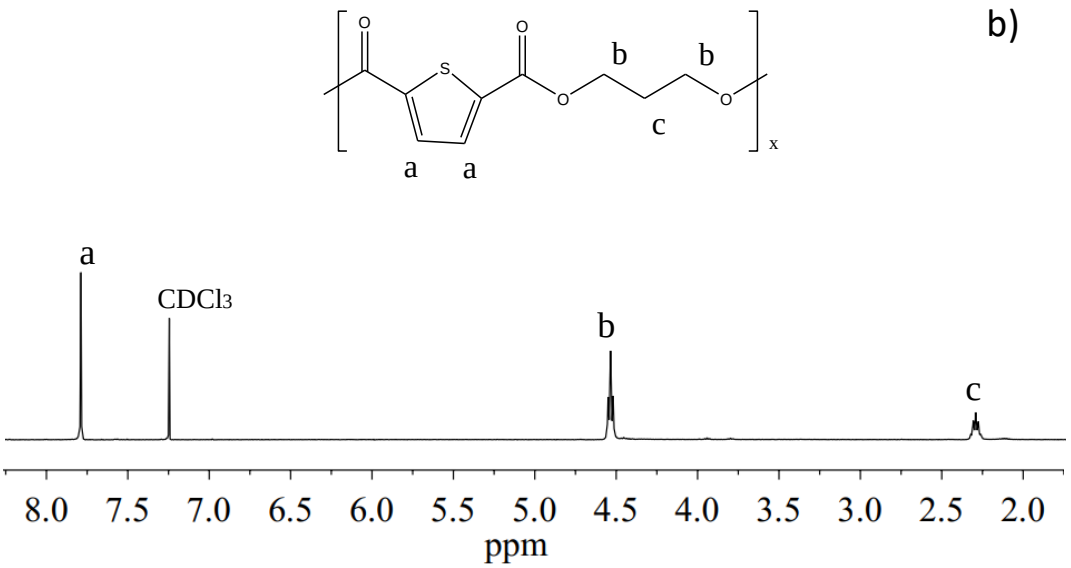

Figure 4.16. ^{1}H-NMR spectrum of: a) PPF; b) PPTF with resonance assignments.

According to WCA data listed in Table 4.9, PPF film is more hydrophilic than PPTF, as expected on the basis of its higher dipole moment.

4.3.2. Thermal characterization

The thermal stability of the polymers under study, as previously done for other materials investigated in the present Thesis, was evaluated by thermogravimetric analysis (TGA). The temperatures corresponding to the beginning of degradation T_{onset} and to the maximum weight loss rate T_{max} are listed in Table 4.9, while thermograms together with their corresponding derivatives are shown in Figure 4.17: both the materials show good thermal stability, as the degradation process occurs at 800 °C. The degradation process happened in one step, and at the end a residual weight of 6% was observed. By comparing the two samples, PPTF turned out to be more thermally stable than PPF. The reason of this evidence can be found whether in the higher resonance energy, in p to d π-back bonding or in the lack of ring strain due to the longer C-S bond in case of PPTF.

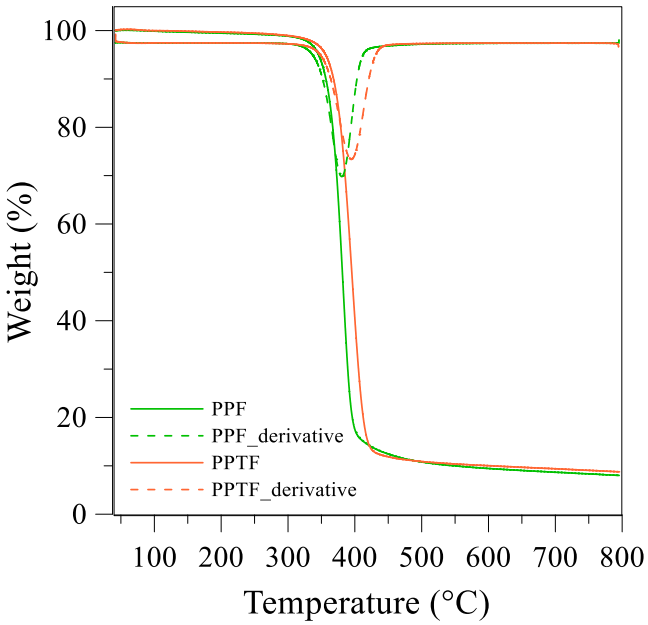

Figure 4.17. Thermogravimetric curve (solid line) and corresponding derivative (dashed line) under nitrogen flow for PPF and PPTF.

Calorimetric analysis was carried out on PPF and PPTF samples, in the forms of powders (PPF_P and PPTF_P) and films (PPF_F and PPTF_F). The relative thermal transition temperatures are collected in Table 4.9, while DSC curves are shown in Figure 4.18.

According to the data reported in the Table 4.9, it can be seen that the two powders show identical phase behaviour, being both samples semicrystalline, although PPF is able to crystallize during heating once T_g is exceeded ($\Delta H_{cc} < \Delta H_m$). PPTF is characterized by a higher crystallinity degree, thus indicating a higher crystallizing ability with respect to PPF.

As to the glass to rubber transition, both T_g values are located above room temperature. Moreover, T_g, of PPF is higher than that of PPTF, despite this latter is characterized by a higher crystallinity degree. This evidence can be due to stronger interchain interactions within PPF macromolecular chains, as a consequence of the higher electronegativity of oxygen atoms. By comparing powders to films, it can be noticed that the T_gs of the powders are higher than those of the corresponding films, which is reasonable considering their higher crystallinity, due to solvent-induced crystallization.

By comparing the melting temperatures of the two samples, the higher T_m of PPTF with respect to PPF can be ascribed to a more perfect crystalline phase, due to the higher mobility of

polymeric chains as well as the higher aromaticity of thiophene ring, which enhance chain folding.

After quenching from the melt, the two polyesters, regardless of whether they are in the form of film or powder, showed a different phase behaviour. PPF is indeed completely amorphous, being the corresponding DSC trace characterized only by the baseline deviation related to the glass transition phenomenon, while PPTF is semicrystalline, as the corresponding DSC trace shows the glass transition phenomenon followed by a cold crystallization exothermic peak and an endothermic melting peak at higher temperature. As the heat of crystallization is lower than the heat of fusion, PPTF cannot be quenched in a completely amorphous state by rapid cooling, under the experimental conditions adopted. This behaviour can be considered as a proof of the higher crystallizing capability of PPTF with respect to PPF. As to the glass transition temperature of II calorimetric scan, they are in line with those of the I scan (T_g of PPTF lower than that of PPF).

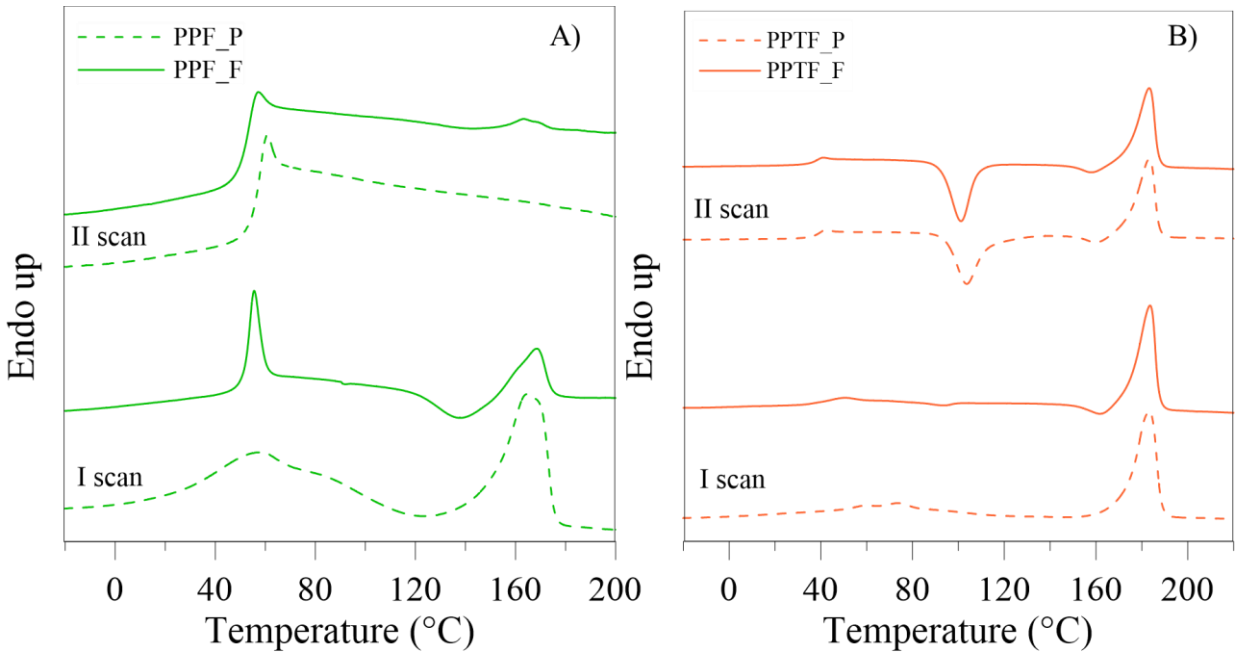

Figure 4.18. Calorimetric traces of: A) PPF and B) PPTF powder and film (20 °C/min): 1st scan and 2nd scan after melt quenching.

Table 4.9. Molecular, thermal and mechanical characterization data of PPF and PPTF.

	PPF		**PPTF**	
MOLECULAR CHARACTERIZATION				
M_n (g/mol)	30000		26300	
D	2.3		2.3	
WCA (°)	90 ± 3		94 ± 3	
THERMAL CHARACTERIZATION				
Thermogravimetric analysis				
T_{onset} (°C)	360		373	
T_{max} (°C)	387		396	
Differential scanning calorimetry				
1st scan				
	powder	***film***	***powder***	***film***
T_m (°C)	165	169	183	184
ΔH_m (J/g)	26	7	39	37
T_g (°C)	56	52	45	40
ΔC_p (J/g°C)	0.278	0.361	0,128	0.229
T_c (°C)	119	138	-	161
ΔH_{cc} (J/g)	7	7	-	3
2nd scan				
	powder	***film***	***powder***	***film***
T_m (°C)	-	-	183	183
ΔH_m (J/g)	-	-	34	36
T_g (°C)	52	52	39	38
ΔC_p (J/g°C)	0,361	0,359	0.315	0.227
T_c (°C)	-	-	104	101
ΔH_{cc} (J/g)	-	-	30	31
MECHANICAL CHARACTERIZATION				
E (MPa)	1363 ±158		1419±165	
σ_B (MPa)	31 ± 3		12±4	
$\varepsilon_{B\ (\%)}$	3 ± 1		2±0.5	
GAS PERMEABILITY CHARACTERIZATION AT 23°C RH 0%				
O_2-GTR	$0.0224\pm3E^{-6}$		$0.0202\pm14E^{-5}$	
CO_2-GTR	$0.0288\pm3E^{-6}$		$0.0243\pm13E^{-5}$	
N_2-GTR	$0.0157\pm6E^{-5}$		$0.0120\pm2E^{-5}$	

4.3.3. Structural characterization

The crystal phases of PPF and PPTF samples were analysed by means of X-ray diffraction (XRD) technique. The diffractometric patterns are shown in Figure 4.19. PPTF powder showed most evident peaks at 2θ = 9.2°, 16.3°, 17.9°, 22.5°, 24.1°, 26.6° (d= 9.6, 5.4, 4.9, 3.9, 3.7, 3.3 Å, respectively) and crystallinity index X_c of 46 (±3) %. PPTF film showed the main reflections at 2θ = 9.3°, 16.3°, 23.3°, 25.6° (d = 9.5, 5.4, 3.8, 3.5 Å) and crystallinity index X_c of 43 (±3) %. The position and shape of the reflections of the two samples in form of powder and film are so different to suggest the presence of two different crystalline phases. For this reason, hereinafter the crystalline phase of the powder will be indicated as α-PPTF, whereas that of film as β-PPTF. As to PPF polymer, the film immediately after moulding shows a very poor crystallinity (X_c = 3(±2) %). After an annealing treatment (45 minutes at 110°C), a considerable increase in crystallinity (X_c = 31(±3) %) can be noticed. Moreover, the WAXS pattern becomes very similar to that of PPF powder (X_c = 37(±3) %). PPF powder and PPF film therefore develop the same crystalline phase, characterized by main reflections located at 2θ = 10.2°, 16.4°, 19.1°, 22.6°,25.0°, 28.6° (corresponding to d = 8.7, 5.4, 4.6, 3.9, 3.6, 3.1 Å, respectively).

From the comparison between PPF and PPTF, it can be evicted that the former sample is characterized by a lower crystallinity degree, in agreement with calorimetric data.

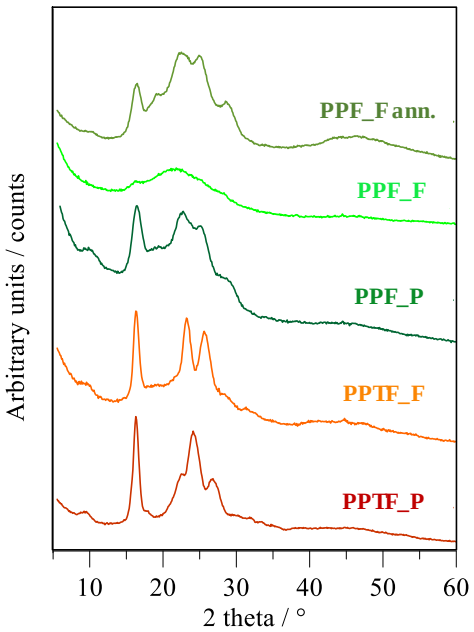

Figure 4.19. X-ray diffraction profiles of PPTF and PPF in form of both powder and film, and PPF film after annealing for 45 min. at 110°C.

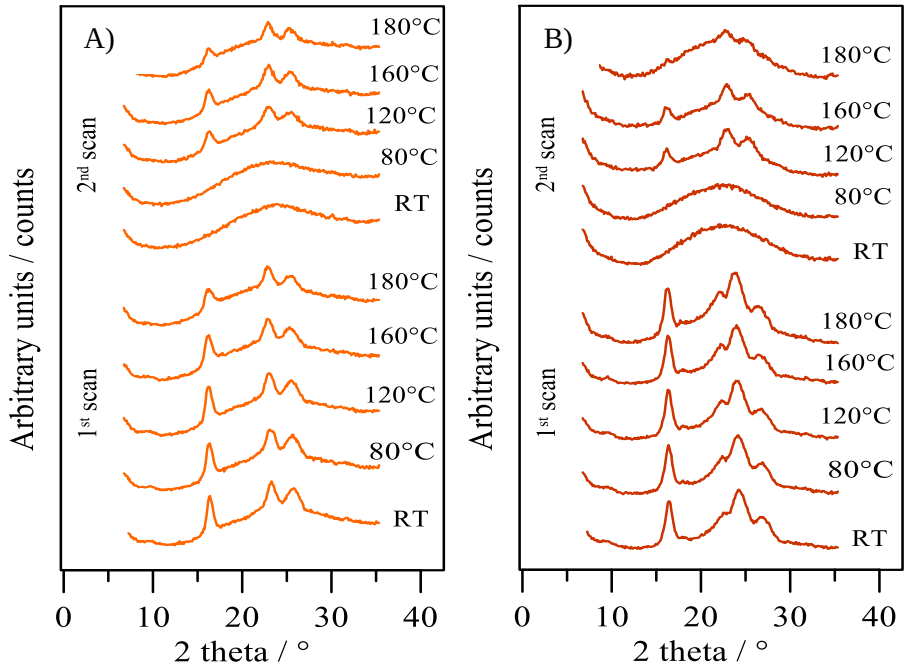

Figure 4.20. XRD patterns collected in situ at the indicated temperatures for PPTF in the form of A) film and B) powder.

In order to investigate the thermal stability of the two different crystal phases of PPTF present in the powder and in the film, *in situ* XRD measurements were performed. As it can be seen in Figure 4.20, during 1st scan both samples show their own crystal phase up to melting point, without any phase transformation by solid-solid transition. Conversely, during 2nd scan, after quenching from the molten state, the powder sample (Figure 4.20B) shows the crystalline profile characteristic of the β-form, thus suggesting that β crystalline phase could be the more stable.

4.3.4. Mechanical characterization

Tensile measurements have been performed on both PPF and PPTF films to test the suitability of these materials for the intended use. The values of elastic modulus E, stress at break σ_b and elongation at break ε_b are collected in Table 4.9.

As it can be seen, PPTF is characterized by a slightly higher elastic modulus with respect to PPF (1419±165 MPa vs. 1363 ±158 MPa). This evidence can be explained considering the

crystalline phase present in this sample. On the contrary, the stress at break of PPF is 2.5 times higher than that of PPTF (31 ± 3 MPa vs. 12±4 MPa), as a consequence of its higher T_g value. As to the elongation at break, it turned out to be very similar for the two samples under investigation. No significant effect of kind of ring on the mechanical properties has been thus evidenced. Lastly, PPF and PPTF showed similar characteristics, in terms of elastic modulus and brittle fracture, to those of PEF.

4.3.5. Gas permeability studies

Gas barrier performances of PPF and PPTF were evaluated at 23 °C using dry N_2, O_2 and CO_2 gases, to check the performance of the materials for potential applications in food packaging. The GTR values normalized for the sample thickness are listed in Table 4.9. According to the values obtained, it is clear that both the polymers under investigation are characterized by outstanding barrier performances, better than those of PEF [Burgess et al., 2014; Burgess et al., 2015] and comparable to those of PBTF [Guidotti et al., 2018 (c)].

The excellent barrier properties of the family of furan-based polyesters are supported by both structural and dynamical studies, which show that the furan moiety is capable to hinder the ring flipping [Burgess et al., 2014 (b)] as well as to limit the sub-glass local dynamics [Genovese et al., 2018]. The gas flow is limited also because of the establishment of C-H···O interactions among adjacent segments of the polymeric chain. As described in literature for PEF [Araujo et al., 2018], the intensity of these interactions is higher when FDCA subunits are in the *syn* conformation. It is plausible that the glycol methylene groups number can affect the *syn*/*anti* conformation ratio: in particular, the presence of an additional CH_2 group in the PPF glycol subunit with respect to PEF one, could promote the *syn* conformation of FDCA, thus increasing the amount of C-H···O interactions and improving the barrier properties of PPF.

Moreover, according to the experimental data, for both PPF and PPTF samples, CO_2 turned out to be more permeable than O_2 and N_2, as already observed for other similar materials previously investigated [Genovese et al., 2014; Guidotti et al., 2017], as a consequence of the lower diffusivity and higher solubility as the permeant size is decreased (CO_2 molecular diameter = 3.4 Å, O_2 molecular diameter = 3.1 Å and N_2 molecular diameter = 2.0 Å, respectively) [Robertson, 2013]. Nevertheless, the GTR values to oxygen and carbon dioxide were not so different, similarly to PEF [Burgess et al., 2015], since the polar nature of furan and thiophene

units is responsible for a high affinity (i.e. solubility) between CO_2 molecules and polymeric matrix.

As to the differences in barrier performances between PPF and PPTF, these can be explained taking into account that PPTF film is semicrystalline whereas PPF one is amorphous. As it is well known [Jamshidian et al., 2012], crystallinity, chain polarity and flexibility, molecular weight and its distribution are all factors that can affect barrier behaviour. In this case, the action of crystallinity is particularly important, since it limits chain mobility, thus hampering gas diffusion and permeation. Generally, as polymeric crystals are impenetrable to gas molecules, high-crystalline polymers are high barrier materials.

4.3.5.1 Activation energy

As it is well known from literature, permeability is influenced by temperature according to an Arrhenius-type equation [Siracusa, 2012; Schmid et al., 2015], which shows how GTR exponentially increases as the temperature is increased. Activation energy (E_a) is a measure of the energy amount needed to start the permeation process. By plotting the Ln GTR as a function of the reciprocal temperature 1/T (in K), a linear trend can be obtained. The activation energy can be calculated from the value of the slope ($-E_a/R$) of the Arrhenius line, where R is the gas constant.

In the present study, the activation energy for CO_2 gas test was evaluated, being 32 KJ/mol and 20 KJ/mol for PPF and PPTF, respectively ($R^2 = 0.9$, for both samples). The higher activation energy of PPF can be ascribed to the higher polarity of furan ring compared to thiophene one, which is responsible for a higher affinity of CO_2 molecule.

Lastly, it is worth noticing that the values calculated for the polymers under study are of the same order of magnitude as PEF value (23.7 KJ/mol) [Burgess et al., 2015].

4.3.5.2 Influence of relative humidity on the gas transmission rate

The effect of both RH and temperature on the gas transmission values was evaluated, in order to explore the possible application of these new materials in different environmental conditions (i.e. temperate and tropical climates). In Figure 4.21, the GTR values with RH of 85% at 23 °C and of 90% at 38°C, respectively, are shown. These conditions were chosen to mimic the standard and the tropical ambient, respectively, in agreement with the *Gas Permeability Testing Manual* [Gas Permeability Testing Manual, 2008].

The results obtained evidence (Figure 4.21) that the GTR values of both PPTF and PPF films increase as RH is increased, as already reported in literature for other polymers [Schmid et al., 2015; Vandewijngaarden et al., 2014; Hedenqvist, 2012]. The water vapor molecules that cross the polymer matrix can acts as plasticizer, leading to an increase of polymer free volume and, consequently, to an increment of permeability [Vandewijngaarden et al., 2014]. This behaviour is more evident in case of N_2 and O_2. The less pronounced effect for CO_2, is probably due to the higher affinity (solubility) of this gas with both polymeric membranes. It must be noticed that both furan and thiophene rings are polar moieties and CO_2 molecules are characterized by an induced dipole moment.

In Table 4.10 the GTR increment, expressed as percent with respect to the value determined at 23°C and 38 °C and 0% RH, is shown for both polymers. At 23°C, the major increments of GTR is recorded for PPF, probably because of the higher plasticizer effect of water. Indeed, PPF chains are characterized by higher polarity, with respect to those of PPTF, as evidenced by the higher dipole moment of the furan ring. Conversely, PPTF film shows excellent resistance to humidity.

An opposite trend was registered at 38°C since this temperature is very close to PPTF glass transition temperature. At this temperature, indeed, macromolecular cooperative motions occur, with a considerable raise of free volume, and therefore of frequency of gas diffusive jumps.

Table 4.10. GTR increment, expressed as percentage, at 23°C and 85% of RH and at 38°C and 90% of RH.

	PPF		**PPTF**	
Gas	***23°C, 85%RH***	***38°C, 90% RH***	***23°C, 85%RH***	***38°C, 90% RH***
N_2	+ 123	+75	+109	+167
O_2	+77	+60	+3	+96
CO_2	+23	+15	+17	+30

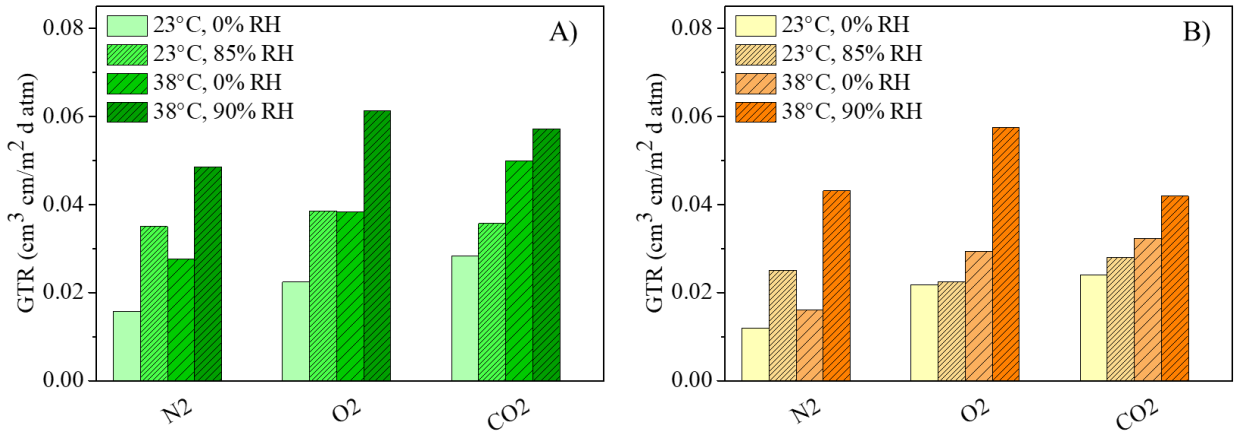

Figure 4.21. GTR values at 23 and 38 °C 0% RH, at 23°C and 85% RH, at 38°C and 95% RH for A) PPF and B) PPTF.

4.3.6 Conclusions

Two 100% bio-based aromatic polyesters were synthesized by two step melt polycondensation, a solvent-free and simple synthetic technique which can be easily scaled up at industrial level. The two materials under investigation present the same glycolic subunit, but they differ in the diacid one: PPF is characterized by the presence of furan ring, whereas PPTF contains thiophene one. More in details, thiophene ring is characterized by higher resonance energy, and lower dipole moment with respect to furan ring. These features are responsible for different solid-state properties, being PPTF more thermally stable, characterized by a lower T_g and by higher crystallizing ability with respect to PPF. The different hetero-aromatic five membered rings affect also the barrier behaviour, although both samples turned out to be outstanding in terms of permeability performances (being even superior to those of PEF). However, the measurements carried out at different RH highlighted that the gas transmission increases as RH is increased, with a more pronounced increment in case of PPF at 23°C, due to a stronger plasticizer effect of water because of the higher polarity of furan ring compared to thiophene one. An opposite result was obtained at 38°C: in this case, PPTF turned out to be less performant than PPF, as the temperature of 38°C, which simulates tropical atmosphere, is close to PPTF's T_g, and consequently a considerable increment of free volume occurs.

In conclusion, both the biopolyesters herein presented, PPF and PPTF can be considered excellent candidates for applications in sustainable packaging, PPF being preferable in areas with a tropical climate, PPTF in temperate regions.

4.4 New multi-block 2,5-furandicarboxylic acid-based copolymer containing PEG-like sequences for sustainable flexible packaging

A novel bio-based multi-block poly(ester urethane) P(HFTEF)-CE containing 2,5-furandicarboxylic acid along its macromolecular chain was synthesized through chain extension of two hydroxy-terminated prepolymers, poly(hexamethylene furanoate) PEF-OH and poly(tryethylene furanoate) PTEF-OH, for possible applications in the field of flexible food packaging. Homopolymer PEF-CE was also synthesized for sake of comparison. Molecular, thermal and structural analyses evidenced that copolymerization had a strong impact on solid-state as well as on functional properties. In particular, the molecular architecture plays a key role in determining a faster degradation rate, an improvement in flexibility and gas permeability. Indeed, the alternation of the two different prepolymeric units, one "hard" (PEF-OH), the other "soft" (PTEF-OH), permitted to obtain a tenacious material with a high melting temperature (due to the high crystallinity degree of the hard segment), characterized by a low elastic modulus and an improved elongation at break (thanks to the presence of the soft segment).

In order to evaluate the potentiality of these new materials for applications in the field of sustainable flexible packaging, gas permeability behaviour to oxygen, carbon dioxide and nitrogen at 23°C was evaluated. Both the polyesters under investigation are characterized by gas barrier performances comparable to those of PEF and PET.

4.4.1 Synthesis, molecular and surface characterization

OH-terminated Poly(hexamethylene furanoate) PHF-OH and poly(triethylene furanoate) PTEF-OH were synthesized by two-step melt polycondensation, according to the procedure described in paragraph 3.2.1.2, using $Ti(OBu)_4$ as catalyst. The chemical structure, as well as the actual composition and the average molecular weight of the hydroxyl-terminated prepolymers, were determined by ^{1}H-NMR spectroscopy.

In Figure 4.22A and Figure 4.22B, the ^{1}H-NMR spectra of PHF-OH and PTEF-OH are reported, respectively, together with the peaks attribution. Both the spectra were consistent to the expected structure, thus allowing the exclusion of any side reactions during the polymerization. At lower fields, the peaks related to the aromatic furan ring can be detected: the a’ protons at δ 7.20 ppm of PHF-OH and the a’’ protons at δ 7.24 ppm of PTEF-OH. In the region in between

δ 1.48 and δ 4.35 ppm, the signals attributable to the glycol subunit can be observed. At higher δ values, the peaks of the methylene groups in α position to the ester oxygen can be found: b at δ 4.33 ppm in case of PHF-OH and e at δ 4.50 ppm for PTEF-OH, respectively. The remaining protons related to glycol subunit are located at higher fields. More in details, the c and d protons of the hexanediol moiety can be detected at δ 1.78 and δ 1.48 ppm, while the f and g protons of triethylene subunit are located at δ 3.70 and δ 3.80 ppm. In addition, the less intense signals ascribable to the methylene protons in α position to the terminal hydroxyl groups are also present: b' at δ 3.68 ppm and e' at δ 3.60 ppm, for PHF-OH and PTEF-OH, respectively.

From the ^{1}H-NMR spectra, it was possible also to calculate the degree of polymerization (DP) and the average molecular weight (M_n) for both the prepolymers. As to DP, it was calculated from the relative areas of b protons of central hexanediol (I_b) and b' protons of terminal hexanediol ($I_{b'}$) for PHF-OH, whereas the relative areas of e protons of central triethylene glycol (I_e) and e' protons of terminal triethylene glycol ($I_{e'}$) were used for PTEF-OH, applying Eqn. [33].

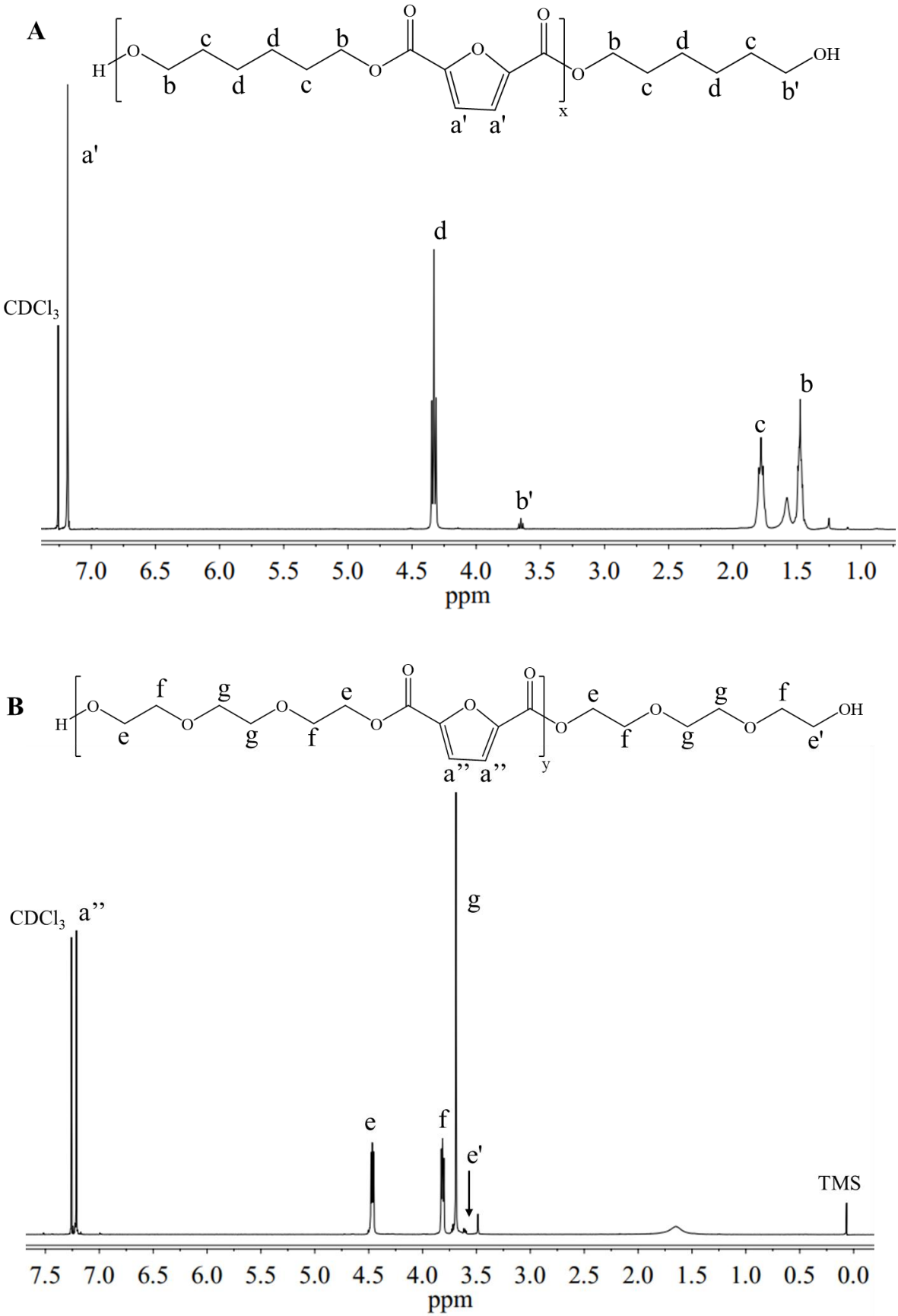

Figure 4.22. ^{1}H-NMR spectrum of **A**) PHF-OH and **B**) PTEF-OH prepolymers with peaks assignment.

The so-obtained DP (23.3 for PHF-OH and 17.4 for PTEF-OH), was used to calculate the average molecular weight (M_n) according to Eqn. [34]. The M_n values calculated by ^{1}H-NMR analysis were 5668 g/mol and 4860 g/mol for PHF-OH and PTEF-OH, respectively.

In the ^{1}H-NMR spectrum of P(HFTEF)-CE copolymer, the presence of three less intense peaks, ascribable to the chain extender HDI, can be noticed, beside the resonance peaks of both the hydroxyl-terminated prepolymers. The signal of the z methylene groups in α position to the nitrogen atom at δ 3.10 ppm (4H, t) and the peaks of the w and y protons at δ 1.20 ppm (8H, m) were evidenced.

In addition, actual composition of P(HFTEF)-CE multiblock copolymer was calculated from the relative areas of the b and e peaks, corresponding to the hexamethylene and triethylene subunits, respectively (Table 4.11). The actual weight composition was very close to the feed one (HF: 54.4 wt%; TEF: 45.5 wt%).

The amount of chain extender HDI inside the polymer chain was estimated from the z peak intensity with respect to b signal integral for PHF-CE, while to the sum of b and e peaks intensities, for P(HFTEF)-CE. For both the chain extended high molecular weight polymers, the HDI amount was about 3%.

Table 4.11. Molecular, structural and surface characterization data.

Polymer	HF (mol %)	HF (wt%)	η (dl/g)	X_c (%)	WCA (°)
PHF-CE	100	100	1.43	50±2	109±1
P(HFTEF)-CE	57.5	54.4	1.52	21±3	100±2

Intrinsic viscosity measurements were carried out on both the multiblock polymers, PHF-CE and P(HFTEF)-CE, according to the procedure reported in Paragraph 3.3.3. As reported in Table 4.11, the η values are high and comparable, thus proving the optimization of the synthetic process.

Water contact angle measurements were performed in order to check the polymer wettability. The WCA values are listed in Table 4.11, while in Figure 4.23 images of two drops on the polymeric films are shown. These results highlight that the introduction of two ether oxygen atoms along the glycol subunit is responsible for a reduction of WCA of about 10°, thus proving the higher hydrophilicity and wettability of P(HFTEF)-CE copolymer with respect to PHF-CE homopolymer.

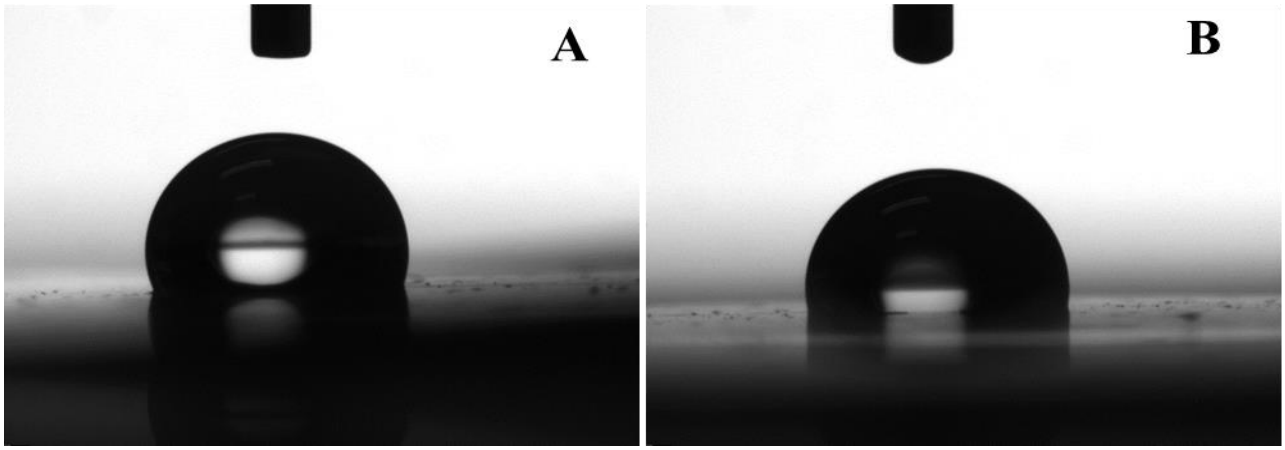

Figure 4.23. WCA images for A) PHF-CE and B) P(HFTEF)-CE.

4.4.2 Thermal and structural characterization

Thermogravimetric analysis (TGA) under pure nitrogen atmosphere was performed to determine the thermal decomposition temperature of the materials under study. More in details, the temperatures corresponding to the 5% of weight loss ($T_{5\%}$) and to the highest degradation rate (T_{max}) are listed in Table 4.12. These data are of particular importance since their knowledge allows material processing, avoiding potential problems related to thermal degradation processes.

TGA curves are shown in Figure 4.24. From the results obtained, it is possible to say that both the materials are characterized by an excellent thermal stability, being $T_{5\%}$ above 300 °C for both the polyesters. In addition, according to the $T_{5\%}$ values, the introduction of the triethylene subunit inside the macromolecular chain makes the thermal degradation starting at lower temperature. This result suggests that at the first stage the degradation process mainly involves ether oxygen atoms, which are not present in HF segments. Conversely, at higher temperatures, particularly around T_{max}, no significant differences between the two samples can be detected, being T_{max} the same for both PHF-CE and P(HFTEF)-CE (407 °C). This result indicates that at this stage degradation involves subunits which are present in both the repeating units, probably the ester groups -COOR-. Last, for both the materials a 100% weight loss takes place even in nitrogen inert atmosphere.

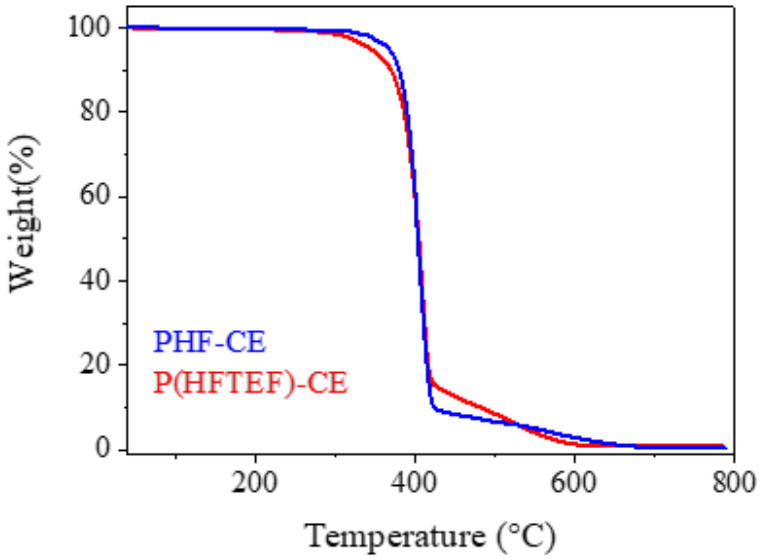

Figure 4.24. TGA curves of PHF-CE and P(HFTEF)-CE obtained under N_2 atmosphere.

Calorimetric analysis on compression moulded films was carried out after 30 days of permanence at room temperature. This time is necessary to standardize the thermal history of the materials under investigation, as their glass transition temperature is below room temperature. In Table 4.12, the calorimetric data of I and II scans for all the samples are listed, while Figure 4.25 shows the calorimetric traces of I and II scan of the chain extended films, PHF-CE and P(HFTEF)-CE, together with the I scan curve of the same films subjected to mechanical stretching.

As it can be seen from the data listed in Table 4.12, both hydroxyl-terminated prepolymers PHF-OH and PTEF-OH are semicrystalline in the first scan, with an endothermic baseline deviation related to T_g (equal to 20 and 11 °C, respectively) and an endothermic peak at higher temperature due to the melting of the crystalline phase. The T_m values are 147 °C (ΔH_m = 51 J/g) and 76 °C (ΔH_m = 35 J/g), for PHF-OH and PTEF-OH, respectively. The introduction of two ether oxygen atoms within the glycolic subunit is responsible for a decrease in the chain stiffness (i.e. T_g decreases) as well as in the crystallization ability, being both T_m and ΔH_m reduced. This last trend is also confirmed by the II calorimetric scan, since PHF-OH cannot be blocked in the amorphous state by quenching from the melt (being characterized by the presence of both the glass to rubber transition and the melting phenomena), while PTEF-OH was successfully quenched (it shows only the step of the glass transition).

Table 4.12. Thermal characterization data obtained by TGA and DSC analyses.

Polymer	$T_{5\%}$ °C	T_{max} °C	I SCAN				II SCAN					
			T_g °C	Δc_p J/g*°C	T_m °C	ΔH_m J/g	T_g °C	Δc_p J/g*°C	T_c °C	ΔH_c J/g	T_m °C	ΔH_m J/g
PHF-OH			20	0.165	54 147	5 51	18	0.122	-	-	145	40
PTEF-OH			11	0.243	76	35	9	0.550	-	-	-	-
PHF-CE	360	407	19	0.084	55 140	3 44	18	0.155	-	-	141	38
P(HFTEF)-CE	330	407	7	0.364	54 135	3 20	13	0.416	63	7	136	17
PHF-CE*			20	0.127	48 141	3 49	18	0.198	-	-	140	35
P(HFTEF)-CE*			8	0.267	47 138	2 30	13	0.318	-	-	136	16

*film after mechanical stretching

As to the multiblock copolymers, also in this case, the I scan calorimetric curves (Figure 4.25B) are typical of semicrystalline materials, showing in addition to the endothermic baseline deviation related to the glass transition, two melting endotherms at higher temperature. In addition, the chain extended homopolymer PHF-CE does not present remarkable changes with respect to its relative prepolymer PHF-OH. Conversely, copolymerization deeply affects the crystallization ability of the TEF segments, which is suppressed in the multiblock copolymer: in fact, the I scan DSC curve of P(HFTEF)-CE copolymer does not show any endothermic peak due to the melting of the PTEF crystals, being, on the contrary, very similar to that of PHF-CE. Moreover, it must be highlighted that the T_m values of both the chain extended polyesters, for the two melting phenomena at 55 and 140 °C, are very similar, thus confirming the multi-block nature of the copolymer.

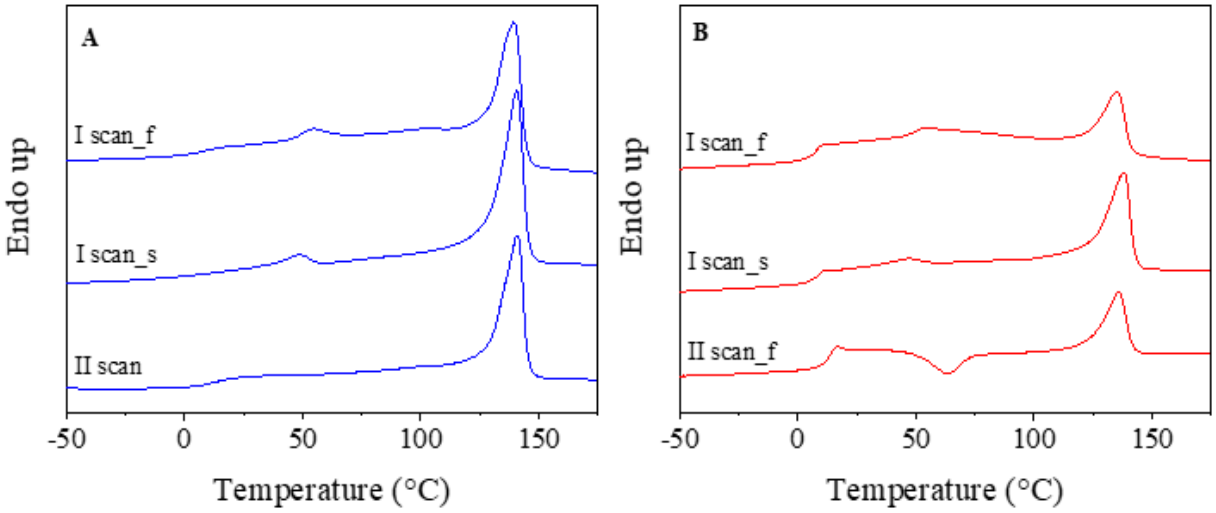

Figure 4.25. Calorimetric curves of **A**) PHF-CE and **B**) P(HFTEF)-CE multiblock polymers: I and II scan of the as moulded film (f) and the I scan of the film after mechanical stretching (s).

However, the copolymerization effect is clear if the associated heat (ΔH_m) is considered, in particular in the case of the endothermic phenomenon at higher temperature, which is decreased from 44 J/g in PHF-CE to 20 J/g in P(HFTEF)-CE. This drop can be ascribed to both the reduction of the crystallisable HF moieties and to the presence of the TEF co-units, which hamper the folding of the HF segments and, therefore, limit the formation of crystals. It is also interesting to notice that the value of ΔH_m related to the endothermic phenomenon at 55 °C does not change by copolymerization, being 3 J/g for both the materials. According to this result, it seems that this peak is not dependent on the kind of glycolic subunit (hexamethylene *vs* triethylene glycol).

In order to study the thermal transitions of the samples in a complete amorphous state, a second calorimetric scan was performed after quenching from the melt. In fact, as it is well known, a semicrystalline material generally shows a different behaviour with respect to the same material but in a complete amorphous state. Although conflicting results are reported in the literature [Minakov et al., 2004], it is commonly accepted that crystallinity acts as physical cross-links, causing an increase in T_g values.

For this purpose, II calorimetric scans on the samples quenched from the melt were performed, the corresponding traces being shown in Figure 4.25. As expected, while the II scan curve of PHF-CE homopolymer is quite similar to the I scan one, II scan trace of P(HFTEF)-CE multiblock copolymer considerably changes after melt quenching. More in details, in addition

to the step of the glass transition at 13 °C and the melting peak at 136 °C, P(HFTEF)-CE shows a crystallization exotherm halfway between T_g and T_m (T_c = 63 °C). This peak indicates that after T_g the polymer chains are capable to organize themselves in ordered crystalline structures, which melt at a higher temperature. However, since $\Delta H_m > \Delta H_c$, it can be assessed that not even P(HFTEF)-CE could be totally quenched under the experimental conditions applied.

Although both the chain extended materials show a semicrystalline behaviour, by comparing their different T_{gS} it is possible to notice that the introduction of triethylene subunit allows for an increase in chain mobility. Indeed, the T_g of the copolymer is comprised between those of the two prepolymers ($T_{g\ PTEF\text{-}OH} < T_{g\ P(HFTEF)\text{-}CE} < T_{g\ PHF\text{-}OH}$).

As to the film subjected to mechanical stretching, from the data collected in Table 4.12 and the DSC curves shown in Figure 4.25, it can be noticed that mechanical treatment does not substantially affect the thermal transitions in the case of homopolymer, while it is responsible for a slight increase in melting enthalpy (ΔH_m) for the copolymer, thus indicating a further crystallization of the polymeric chains, due to stretching.

In order to better understand the nature of the crystalline phase in the multiblock materials and to investigate the origin of endotherms evidenced by DSC, diffractometric wide-angle X-ray scattering analysis (WAXS) was performed.

The diffraction profiles of both the films and the stretched fibers of PHF-CE and P(HFTEF)-CE block polyesters are shown in Figure 4.26. The film profiles are characteristics of semicrystalline materials, containing some well-defined reflections, typical of the ordered portion of the material, overlapped with a bell-shaped baseline, related to the fraction of amorphous material. As it can be noticed, the patterns of the two films show a very similar profile, thus indicating the presence of the same type of crystalline structure in both the materials, i.e. the crystalline lattice of PHF. Nevertheless, the ratio between crystalline portion and the bell related to the amorphous fraction considerably changes in the multiblock copolymer with respect to the homopolymer. More in details, as it can be seen by the crystallinity degree (X_c) values calculated from the WAXS analysis and listed in Table 4.11, X_c remarkably decreases after copolymerization. This behaviour agrees with the decrease of the melting enthalpy (ΔH_m) related to the peak at the highest temperature (≈ 140 °C), evidenced by DSC analysis. In this framework, the lowest endothermic peak in the calorimetric traces (≈ 50 °C) could be due to the melting of crystals with the same lattice, but with a lower degree of perfection, although this hypothesis does not explain the reason why the enthalpy related to this

process is not affected by copolymerization (Table 4.12). In order to clarify this point, WAXS analysis was also carried out on the films previously subjected to mechanical stretching. According to the profiles shown in Figure 4.26, both WAXS spectra of the homopolymer and the copolymer subjected to stretching significantly change with respect to the initial samples, showing two well defined and quite large peaks at 2θ = 16° and 24 °, respectively. This result suggests the presence of 2D-ordered regions, generally referred to as mesophase. As shown in the present Thesis and in some recently published papers, the presence of mesogenic aliphatic (cyclohexane) and aromatic (furan and thiophene) rings can give rise to this kind of ordered structures [Guidotti et al., 2018 (a); (b); (c); (d)]. The presence of these domains, which can be detected in the DSC traces as a small endothermic peak in the temperature range between T_g and T_m, are responsible for WAXS spectra similar to those obtained by stretching the multi-block polymers under investigation. It has to be underlined that the formation of this 2D-ordered phase is not induced by stretching: the DSC traces of the samples both before and after mechanical stretching show the same endothermic peak around 50 °C, ascribed to the isotropization of the mesophase. The different diffractometric profile of the film after stretching can be due, on the contrary, to the orientation of the mesophase regions already present in the film obtained by compression moulding.

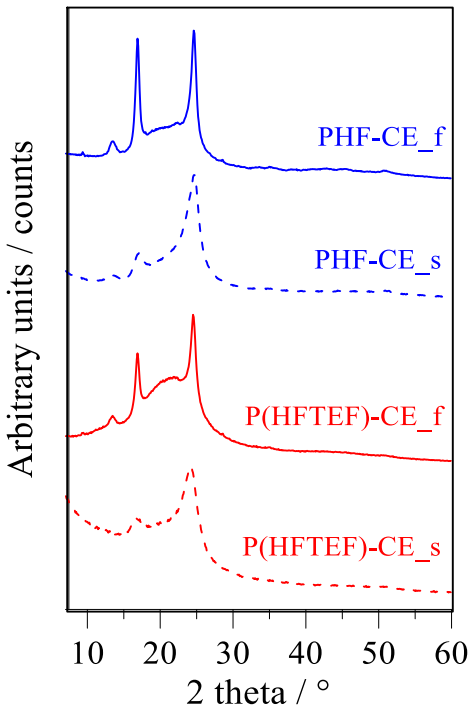

Figure 4.26. WAXS patterns of PHF-CE and P(HFTEF)-CE: compression moulded films (f) and stretched films (s).

4.4.3 Mechanical characterization

The mechanical properties of the materials under investigation were measured on thin rectangular films (5 X 50 mm) with useful section length of 20 mm and thickness of about 100 μm. Stress-strain tests were carried out at constant speed by measuring the variation of stress as a function of the deformation applied.

The values of elastic modulus (E), stress at break (σ_B) and elongation (ε_B) at break are listed in Table 4.13, while the relative stress-strain curves are shown in Figure 4.27.

Both the samples under investigation are characterized by a T_g value lower than room temperature, which gives elasticity to the polymeric chains, and a certain amount of crystalline phase, although in very different percentages, which confers stiffness to the material.

Table 4.13. Mechanical characterization data: elastic modulus (E), tensile stress (σ_B) and percentage elongation at break (ε_B).

Polymer	E (MPa)	σ_B (MPa)	ε_B (%)
PHF-CE	738±34	32±3	180±41
P(HFTEF)-CE	215±12	26±2	704±65

It is well known that the mechanical performances are strictly related to many factors, like the amount of crystalline phase and chain flexibility, which differently affect the final properties. The former factor is responsible for an increasing of the elastic modulus and a decreasing of the elongation at break, while the latter is directly proportional to the elongation at break and inversely proportional to the elastic modulus.

Copolymerization with flexible PEG-like co-units is responsible for a remarkable variation of the mechanical properties. More in details, the elongation at break is significantly improved, reaching values of 700% in the case of P(HFTEF)-CE with respect to 200% in the case of PHF-CE. It has to be noticed that the elongation at break of PHF-CE is anyway quite high, due to the presence of the chain extender HDI, which acts as a joint. As to the elastic modulus, it is considerably reduced in the case of the copolymer with respect to the homopolymer, being almost four times lower. On the contrary, no significant differences can be detected in the tensile stress values.

It has to be noticed that in both cases a certain yield is present, at a stress of 30 MPa in the case of the homopolymer, and of 8 MPa for the copolymer.

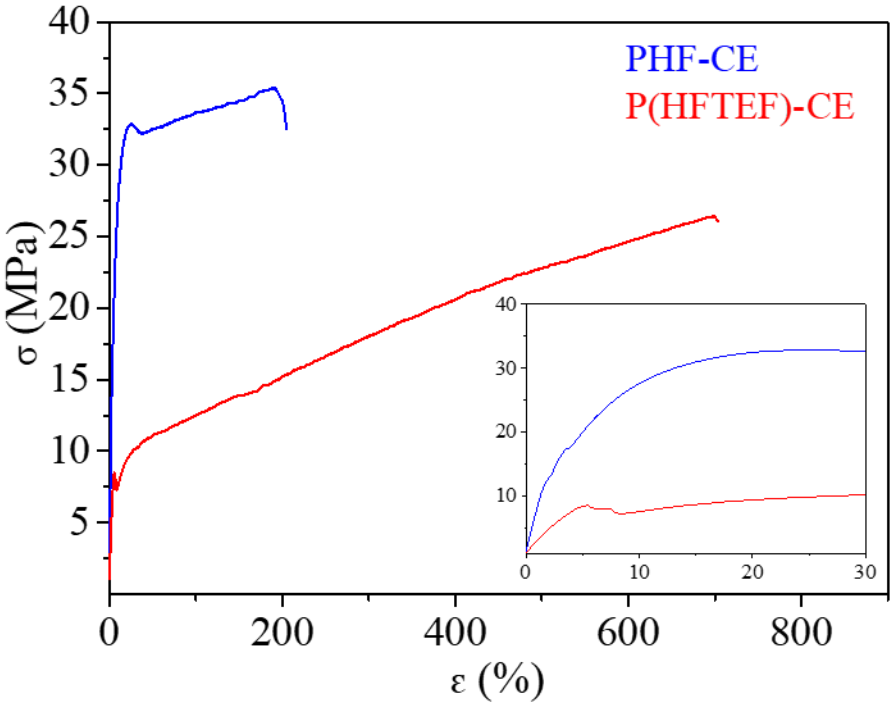

Figure 4.27. Stress-strain curves of the multiblock polymers PHF-CE and P(HFTEF)-CE. In the insertion: magnification of low stress-strain region.

4.4.4 Gas permeability studies

Gas permeability tests on polymeric films were carried out at 23 °C to pure nitrogen, oxygen and carbon dioxide. The permeability values, expressed as Gas Transmission Rate (GTR), are listed in Table 4.14 and shown in Figure 4.28.

In Figure 4.28, the GTR values to O_2 and CO_2 of commercial polymers already used as flexible food packaging materials are reported for sake of comparison, together with other high-performance bio-based polyesters.

Table 4.14. Gas transmission rates (GTR) of PHF-CE and P(HTEF)-CE to different gases.

Poymer	**GTR CO_2** $cm^3cm\ m^{-2}\ day^{-1}\ atm^{-1}$	**GTR O_2** $cm^3cm\ m^{-2}\ day^{-1}\ atm^{-1}$	**GTR N_2** $cm^3cm\ m^{-2}\ day^{-1}\ atm^{-1}$
PHF-CE	0.889	0.237	0.023
P(HFTEF)-CE	0.510	0.190	0.008

From the results obtained, it is clear that copolymerization improves barrier performances for all the three gases tested. This result is particularly interesting taking into account that copolymer film is much less crystalline than homopolymer one (Table 4.11). Therefore, this low permeability cannot be ascribed to the higher crystallinity degree. In addition, the improvement of barrier properties cannot be even correlated to a more rigid amorphous phase (i.e. lower free volume), since the copolymer shows a lower T_g value, due to the higher chain mobility given by the PEG-like triethylene subunits. As already reported in the literature, the excellent barrier properties of furan-based polymers can be ascribed to the hindering of ring flipping [Burgess et al., 2014 (b)], as well as to the limited local movements below T_g [Genovese et al., 2018] and to the establishment of C-H···O interactions between adjacent polymeric chain segments [Araujo et al., 2018]. In addition to the above-mentioned reasons, the results obtained can be ascribed to the presence of the mesophase. This kind of 2D-ordered structure, which determines a very high chain packing that hampers gas flow, gives to the material a behaviour similar to that of liquid-crystalline polymers, characterized by outstanding barrier properties. The presence of mesophase in the polymers under study was demonstrated by both calorimetric and diffractometric analyses (Figure 4.25 and Figure 4.26). In this framework, the lower GTR values of the copolymer shows that in this sample, since the amount of crystalline phase is lower, the polymeric chains can give rise to a higher fraction of mesophase, which is more performing in terms of gas barrier ability with respect to 3D crystalline phase. In addition, ether oxygen atoms in the TEF segments are responsible for an increase in C-H···O interactions between adjacent polymeric chain segments.

Moreover, as can be evicted from the experimental data, for both the samples under study, CO_2 is more permeable than O_2 and N_2, as observed for other similar polymers previously investigated [Genovese et al., 2014; Guidotti et al., 2017], due to diffusivity drop and solubility increment with the decreasing of permeant size (carbon dioxide molecular diameter = 3.4 Å, oxygen molecular diameter = 3.1 Å and nitrogen molecular diameter = 2.0 Å, respectively) [Robertson, 2013].

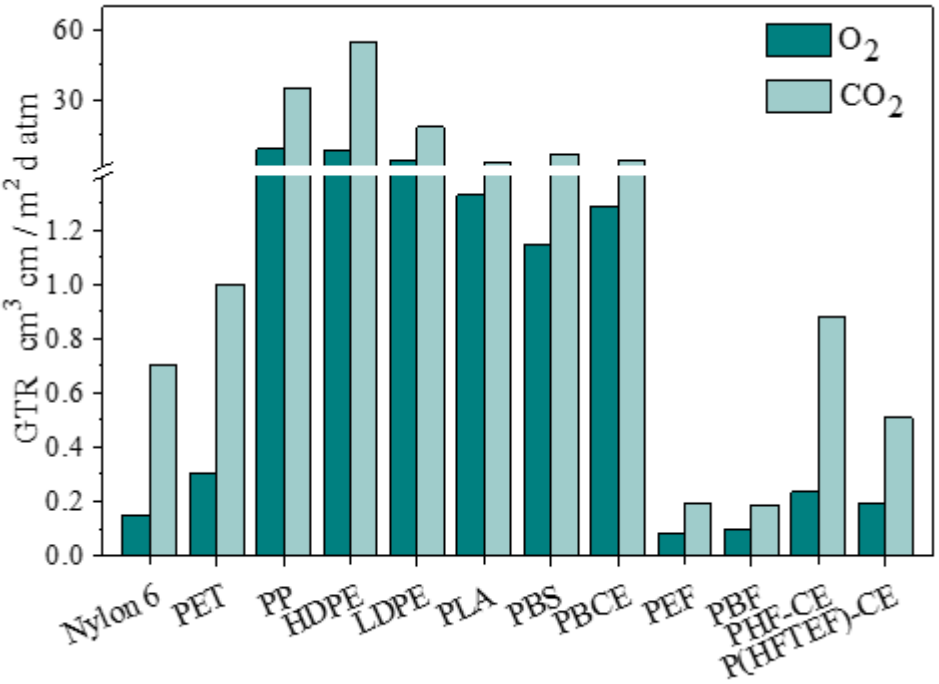

Figure 4.28. GTR values to O_2 and CO_2 of PHF-CE and P(HTEF)-CE and other commercial and lab synthesized polymers.

It is interesting to note that the GTR_{CO_2}/GTR_{O_2} ratio is lower in the case of the copolymer: the result can be explained on the basis of the greater polarity of P(HFTEF)-CE polymer chains, as a consequence of the introduction of ether oxygen atoms, which favour the solubility of the carbon dioxide molecules in the polymer matrix.

In Figure 4.28 GTR values to O_2 and CO_2 for PHF-CE and P(HFTEF)-CE, together with those of commercial polymers already widely used as flexible food packaging materials and others lab-synthesized considered potential candidates for this application, are reported. Barrier properties of both PHF-CE and P(HFTEF)-CE are comparable or even better than those of the commercial materials considered. As to the comparison to the other furan-based polyesters like PEF and PBF, the materials object of this study turned out to be slightly worse in terms of GTR. This result can be ascribed to the decrease of the furan rings content by volume units, and consequently of the mesogenic groups in PHF-CE and in P(HFTEF)-CE, thus reducing the mesophase portion. Nevertheless, taking into account the mechanical improvement, especially the increasing of flexibility obtained in the case of the multiblock copolymer, this latter can still be considered as an excellent candidate for the production of flexible food packaging.

4.4.5 Composting studies

To check whether the materials under study can be considered good candidates for biodegradable and sustainable packaging, biodegradability in compost of PHF-CE and P(HTEF)-CE was evaluated, according to the conditions described in Paragraph 3.14. In Figure 4.29 the percentage weight loss of the samples calculated at different incubation times (30, 75 and 105 days) is shown, together with residual composition and degree of crystallinity of the partially degraded block copolymer. As it can be seen from the data collected, while the gravimetric weight loss is negligible for the homopolymer (3% after 105 days of incubation), on the contrary, it progressively increases reaching 40% after 105 days for the copolymer.

This result confirms that copolymerization of PHF homopolymer, through the introduction of PEG-like segments, improves its functional properties also in terms of compostability. As to the composition variation (Figure 4.29), the amount of TEF co-units, which are entirely contained in the amorphous areas of the copolymeric material, progressively decreases, thus causing also an increase in the crystalline/amorphous phase ratio: as a matter of fact, X_c increases with the incubation time. An explanation of this behaviour can be the lower crystallinity and hydrophobicity of P(HFTEF)-CE with respect to PHF-CE, which favour microbial attack.

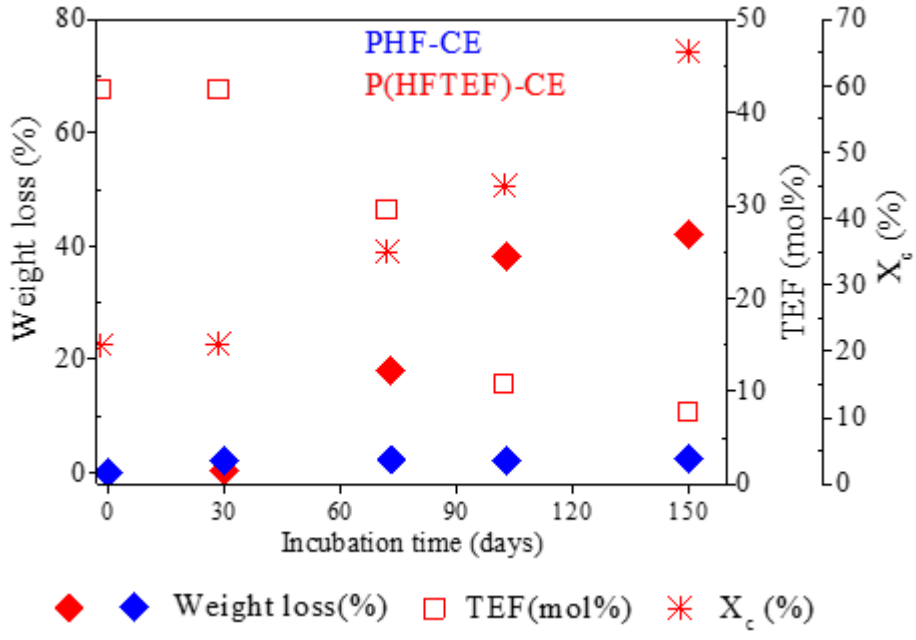

Figure 4.29. Percentage weight loss (left axis), molar percentage of TEF co-units and degree of crystallinity (right axes) as a function of incubation time.

Composting effectiveness was also evaluated both at macroscopic and at microscopic level by surface analysis. In the first case, as it can be seen from Figure 4.30, homopolymer films do not present significant changes after 105 days of incubation, whereas copolymeric samples are characterized by many differences, in terms of both consistency and colour. These last become indeed darker and more fragile with the incubation time.

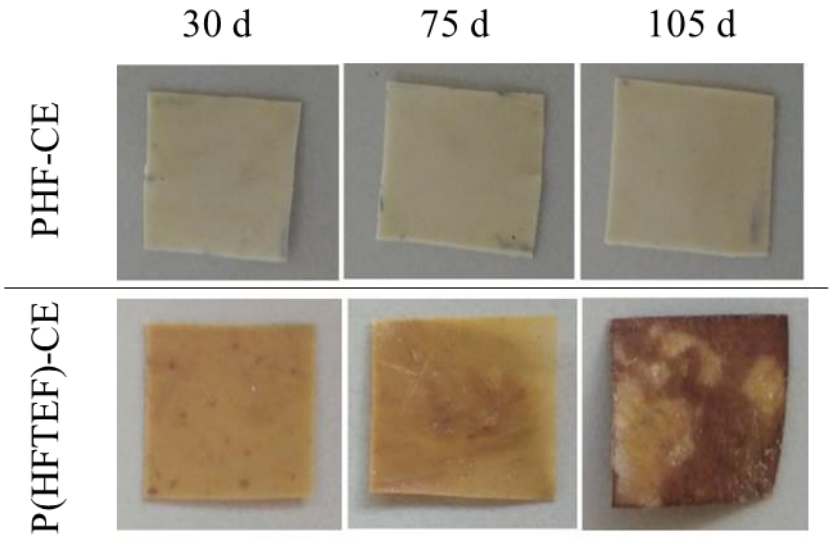

Figure 4.30. Images of PHF-CE and P(HFTEF)-CE films at different incubation times.

At microscopic level, scanning electron microscopy (SEM) analysis was performed. As it can be observed from Figure 4.31, despite the almost negligible weight loss, the surface of PHF-CE film presents different points of attack by microorganisms, thus indicating that, even though at slower rate, the degradation process occurs also in the homopolymer. In the case of P(HTEF)-CE, in agreement with both weight loss results and macroscopic analysis, a considerable loss of material can be detected as a consequence of the microbial attack, which is extended to the entire surface.

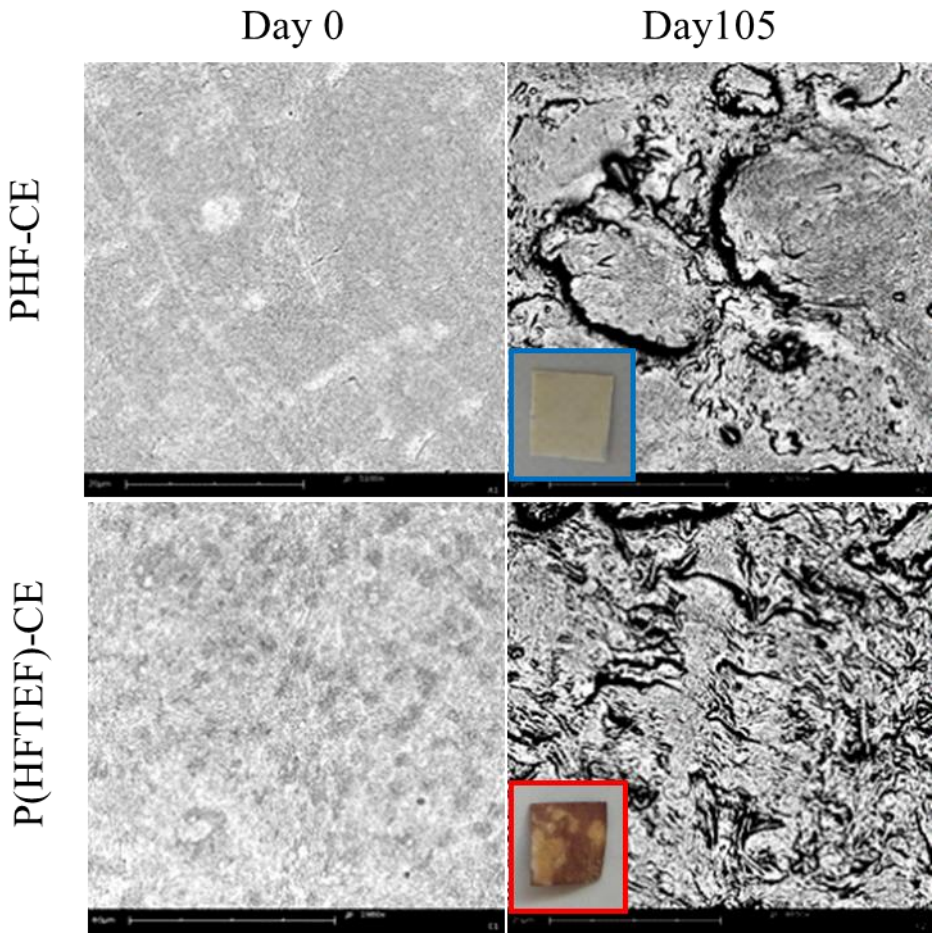

Figure 4.31. SEM images of PHF-CE and P(HFTEF)-CE: as moulded films (left panels) and films incubated in compost for 105 days (right panels).

4.4.6 Conclusions

A new bio-based multi-block copolyester urethane P(HFTEF)-CE was obtained by chain extension of a crystalline *hard* block, such as poly(hexamethylene furanoate) (PHF-OH), and a flexible *soft* block, like poly(triethylene furanote) (PTEF-OH). The block homopolymer PHF-CE was also successfully synthesized for sake of comparison.

Thanks to copolymerization it was possible to obtain a material with elastomeric properties (i.e. low elastic modulus and high elongation at break), characterized at the same time by a high melting temperature and good thermal stability.

This new material turned out to be compostable, thanks to the introduction, along its macromolecular chain, of ether oxygen atoms, which are responsible for a decrease in the crystallinity and an increase in the hydrophilicity.

As to gas barrier ability, the polymers under investigation showed better barrier performances than those of most of the polymers on the market (i.e. polyolefins, PET, Nylon, PLA and PBS), being less performant only with respect to PEF which, however, is not suitable for flexible packaging application due to its high rigidity.

To conclude, it is possible to say that the aim of this research was completely addressed: both the mechanical properties and the biodegradation rate were significantly improved compared to those of PEF, maintaining at the same time excellent barrier properties.

In addition, the copolymerization strategy used to obtain P(HFTEF)-CE, which is simple and solvent-free, allowed to improve the unsatisfactory properties of the parent homopolymer PHF-CE, without negatively affecting the already good ones.

4.5 Novel bio-based aliphatic/aromatic random copolymers of poly(butylene 2,5-thiophenedicarboxylate) for food packaging applications

A new class of bio-based aromatic/aliphatic copolyesters of poly(butylene 2,5-thiophenedicarboxylate) (PBTF) was successfully synthesized through the introduction in the main PBTF chain of aliphatic co-units based on adipic acid. Random copolymers with different molar composition of aromatic and aliphatic co-units were obtained by two step melt polycondensation and characterized from the molecular, structural, thermal and mechanical point of view. DSC and WAXS analysis clearly showed the presence, inside these copolymers, of a peculiar microstructure with a bidimensional order, called mesophase, which significantly affect also mechanical properties of the obtained materials.

As the aim of this study was to enhance the biodegradability of PBTF parent homopolymer, compostability studies were carried out. The results obtained showed that biodegradation rate increased with the increase of aliphatic co-unit amounts, which are responsible for an easier access to the ester bonds for the enzymes involved in chain depolymerization. Lastly, gas permeability tests were performed. The values measured showed that barrier behavior was strictly dependent on copolymer composition. More in details, copolymers rich in BTF co-units showed permeability values to oxygen and carbon dioxide comparable to those of poly(ethylene furanoate). By increasing the BA co-units amount, an increase in permeability value was registered, remaining however competitive with respect to polyolefines and polylactic acid.

4.5.1 Synthesis and molecular characterization

PBTF homopolymer and P(BAxBTFy) random copolymers have been synthetized following the procedure described in Paragraphs 3.2.1.2 and 3.2.1.3, respectively. At room temperature, and after the purification process, all the synthesized polyesters appeared as semicrystalline light yellow powders. The samples are listed in Table 4.15, which also collects the molecular characterization data obtained by means of ^{1}H-NMR (actual chemical composition, degree of randomness, length of both BTF and BA segments) and GPC analysis (molecular weight and polydispersity index).

Table 4.15. Molecular characterization data obtained by ^{1}H-NMR analysis and GPC.

Polymer	M_n	D	%BA	b	L_{BA}	L_{BTF}
PBA	32600	2.4	100	-	-	-
P(BA90BTF10)	28300	2.7	85	1.01	6.9	1.2
P(BA70BTF30)	27700	2.6	67	1.04	2.5	1.6
P(BA50BTF50)	24600	2.5	48	1.01	2.1	1.9
P(BA30BTF70)	21300	2.5	26	0.98	1.4	3.8
P(BA10BTF90)	23900	2.6	11	1.04	1.1	9.1
PBTF *	26500	2.5	0	-	-	-

*[Guidotti et al., 2018 (c)]

The two homopolymers PBTF and PBA and the P(BAxBTFy) copolymers show relatively high and comparable molecular weights. In addition, from the ^{1}H-NMR analysis the awaited structures were confirmed, thus excluding the occurrence of any side-reaction during polymerization. As an example, in Figure 4.32A, ^{1}H-NMR spectrum of P(BA70BTF30) copolymer with resonance assignments is reported. In particular, aromatic protons of thiophene subunit (a signal) can be seen at δ 7.73 ppm, while d methylene protons related to the aliphatic adipic subunit are located at δ 2.32 ppm. From the relative areas of a and d signals actual copolymeric composition can be calculated, which turned out to be very close to the feed one, thus indicating a similar reactivity of the two diacids.

Because of to the high temperatures involved in polycondensation reactions and the use of $Ti(OBu)_4$ as catalyst, copolymers characterized by a random distribution of the comonomeric units can be expected [Allen et al., 1989; Soccio et al., 2010].

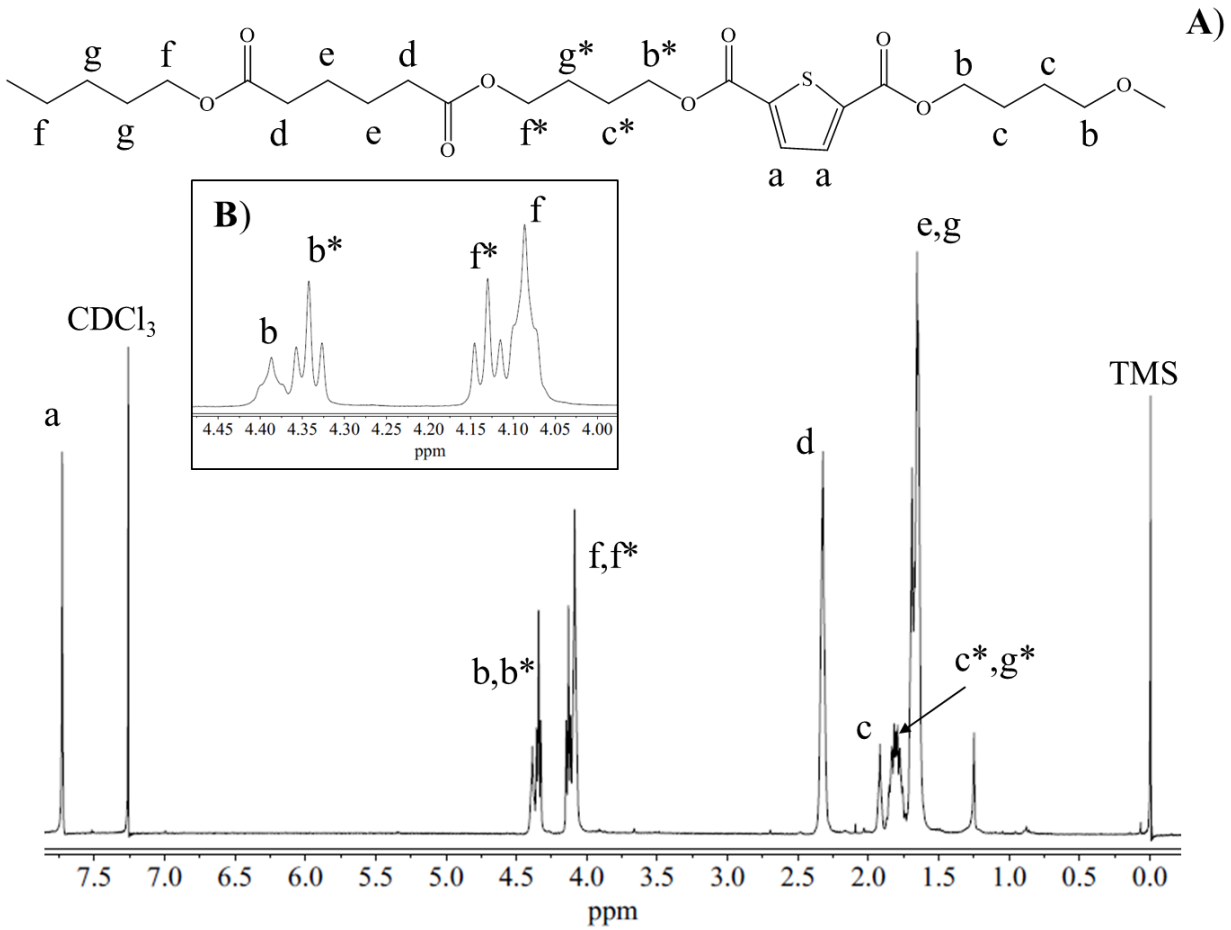

Figure 4.32. **A**) ^{1}H-NMR spectrum of P(BA70BTF30) copolymer with resonance assignments; **B**) magnification of the δ 3.9 ppm – δ 4.5 ppm region.

Also the molecular architecture of the P(BAxBTFy) copolymers was checked by ^{1}H-NMR. In Figure 4.32B a magnification of the chemical shift region between δ 3.9 ppm – δ 4.5 ppm is reported. It is possible to notice that two additional peaks are present, which can be attributed to the b* and f* methylene protons of butanediol subunits in between BA-BTF heterosequences. These peaks are shifted with respect to those of f protons and b protons related to butanediol subunits in between BA-BA and BTF-BTF homosequences, respectively. The arrangement of the comonomeric units was then deduced by the degree of randomness b.

For the calculation of b Eqn. [28] has been used, where $P_{X\text{-}Y}$ ($P_{BA\text{-}BTF}$) and $P_{Y\text{-}X}$ ($P_{BTF\text{-}BA}$) are the probabilities of finding a BA unit next to a BTF one and the probability of finding a BTF unit next to a BA one, respectively. In turn, the two probabilities can be calculated according to Eqn. [29] and Eqn. [30], where $I_{X\text{-}Y}$ ($I_{BA\text{-}BTF}$), $I_{Y\text{-}X}$ ($I_{BTF\text{-}BA}$), $I_{X\text{-}X}$ ($I_{BA\text{-}BA}$) and $I_{Y\text{-}Y}$ ($I_{BTF\text{-}BTF}$) are

the integrated intensities of the resonance signals of BA-BTF, BTF-BA, BA-BA and BTF-BTF sequences, respectively.

According to the values listed in Table 4.15, b turned out to be close to 1 in all cases, confirming the random structure of the synthesized materials.

In addition, in Table 4.15 the average length values of the BA and BTF sequences, L_{BA} and L_{BTF}, respectively, are also reported. These lengths have been calculated according to Eqn. [31] and Eqn. [32]. As expected, the higher the mol % of BTF co-unit, the longer the BTF sequences.

4.5.2. Thermal and structural characterization

Thermogravimetric analysis (TGA) was carried out on all the synthesized materials to evaluate their thermal stability. More in details, the temperature corresponding to the onset of the weight loss (T_{onset}) and that corresponding to the maximum weight loss rate (T_{max}) are listed in Table 4.16, while in Figure 4.33 thermogravimetric curves are shown.

As it can be seen, thermal decomposition takes place in one step. All the samples are characterized by a good thermal stability, being T_{onset} above 325°C, even though some differences related to chemical composition can be highlighted. More in details, PBTF shows the highest thermal stability, probably thanks to its aromatic structure, while PBA the lowest.

The thermal stability of the copolymers is a function of the molar composition, regularly increasing with the increase of BTF co-unit amount. The char residue, i.e. the residue at the end of TGA analysis, changes according to the composition too: PBTF is characterized by the highest residual char, PBA by the lowest, while also in this case the copolymers are placed in between the two parent homopolymers, as the residual char increases according to the presence of higher amounts of BTF co-units.

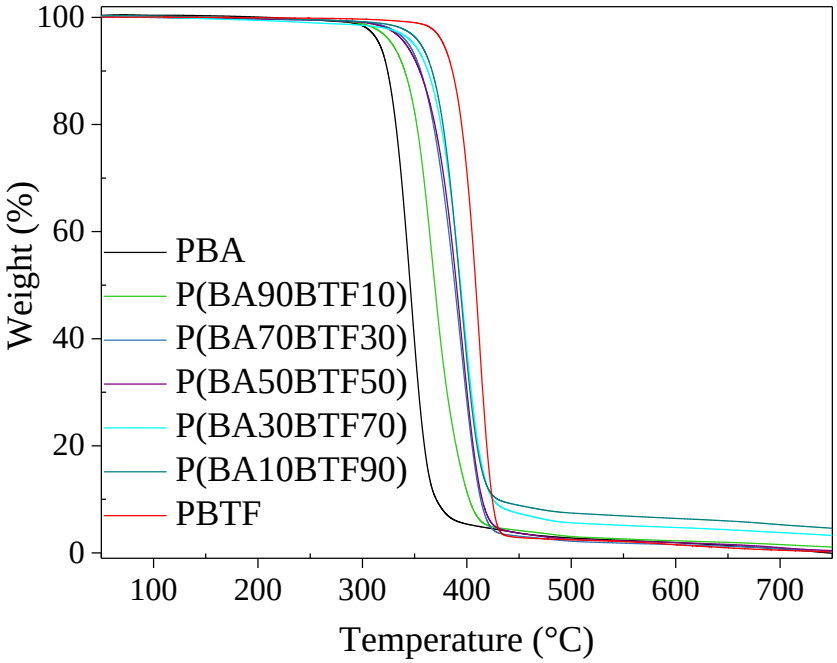

Figure 4.33. TGA curves of PBA, PBTF and P(BAxBTFy) copolymers (N_2, 10 °C/min).

Table 4.16. Calorimetric data obtained from TGA and DSC (I scan and crystallization temperature upon cooling from the melt) of PBA, PBTF, and P(BAxBTFy) copolymers.

Polymer	T_{onset} °C	T_{max} °C	I Scan						II Scan
			T_g °C	ΔCp J/g °C	$T_{m,II}$ °C	$\Delta H_{m,II}$ J/g	$T_{m,I}$ °C	$\Delta H_{m,I}$ J/g	T_c °C
PBA	327	350	-57	0.04	/	/	60	65	31
P(BA90BTF10)	348	368	-48	0.12	/	/	52	54	21
P(BA70BTF30)	361	395	-39	0.37	50	3	40	11	-
P(BA50BTF50)	366	396	-23	0.34	52	24	96	1	-
P(BA30BTF70)	372	398	-5	0.17	52	8	115	20	51
P(BA10BTF90)	373	395	14	0.19	54	9	141	29	85
PBTF *	391	411	n.d.	n.d.	52	4	150	30	113

Prior to further characterization, polymeric films obtained by compression molding were stored at room temperature for two months, to uniform their thermal history and reach equilibrium crystallinity.

The DSC curves of all the samples under investigation are shown in Figure 4.34A while their relative data of I scan are listed in Table 4.16.

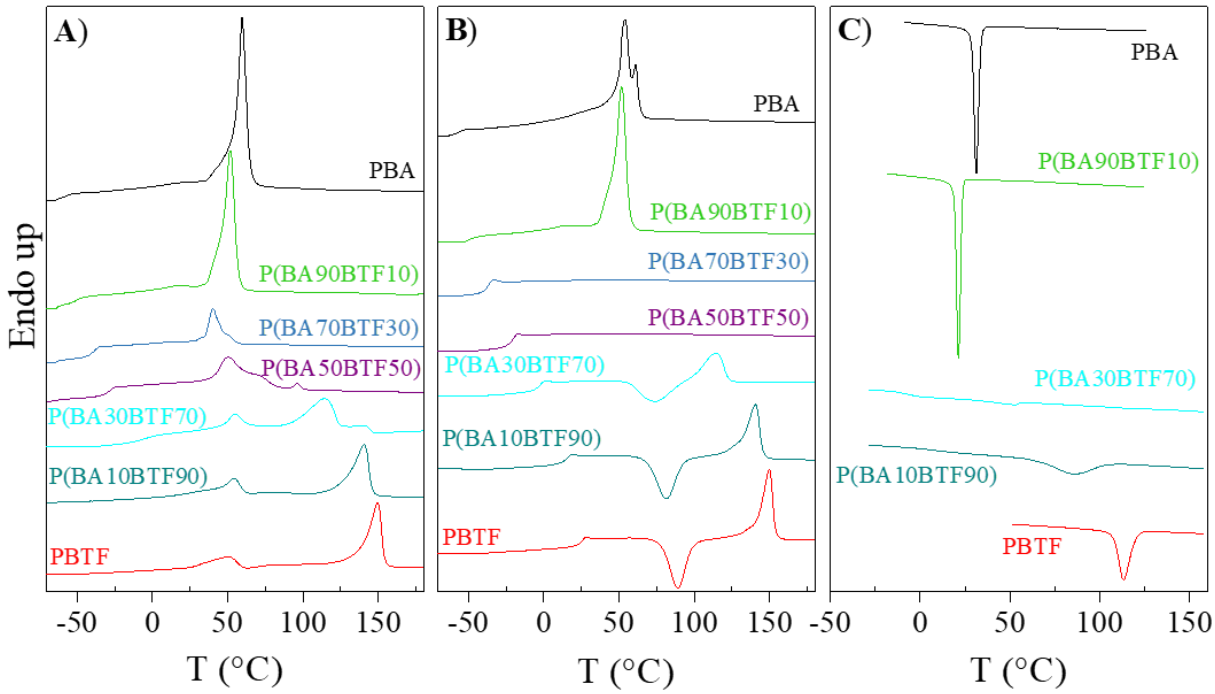

Figure 4.34. DSC curves of PBA, PBTF and P(BAxBTFy) copolymers. **A**) I scan; **B**) II scan after melt quenching; **C**) cooling from the melt at 5 °C/min.

During the first scan, all the polymers under investigation show the same phase behaviour: in fact, they are all semicrystalline, with an endothermic baseline variation associated to the glass to rubber transition, followed by an endothermic peak at higher temperature related to the melting of the crystalline portion. As regards the temperatures at which these transitions occur, they are significantly different for the two homopolymers, as aromatic PBTF is characterized by T_g and T_m significantly higher than those of aliphatic PBA (Table 4.16). The effect of copolymerization is evident both on T_g and T_m values. More in details, a progressive lowering of T_g can be observed with the increase of the amount of BA co-units, which are responsible for a higher mobility of the macromolecular chains (lower T_g values).

On the other hand, the melting behavior seems to be less clear. As a matter of fact, PBA, P(BA90BTF10) and P(BA70BTF30) show a single melting endotherm which shifts to lower temperatures as the BTF co-unit amount increases. Conversely, PBTF and the copolymers with a molar BTF fraction higher than 0.5 are characterized by the presence of two different

endothermic peaks, the first one composition-dependent, the second one located at about 52 °C independently of copolymer composition (Figure 4.34A). This interesting trend is reported also in Figure 4.35, in which the endothermic peak temperature is plotted as a function of the molar composition.

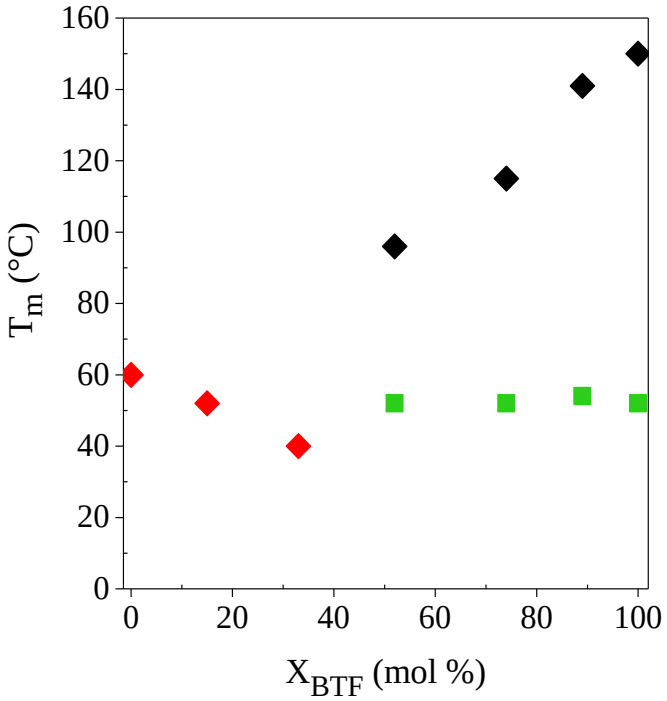

Figure 4.35. Temperature of endothermic peaks as a function of the molar copolymer composition.

The behaviour of the composition-dependent peak is typical of random copolymers in which both comonomeric units can crystallize, regardless whether the comonomeric unit present in lower amount is rejected or included in the crystalline phase of the other co-unit (red and black diamonds in Figure 4.35). Moreover, the peak intensity is dependent on the amount of the crystallisable co-unit, regularly decreasing (i.e. lower ΔH_m) as the content of the other comonomer added to PBA or PBTF chains is increased. (Table 4.16).

In order to investigate the nature of the crystalline phase present in all the samples under study and to understand better the origin of the low constant temperature endotherm, X-ray diffraction analysis (WAXS) was carried out. The diffraction patterns of both the homopolymers and the copolymers are shown in Figure 4.36.

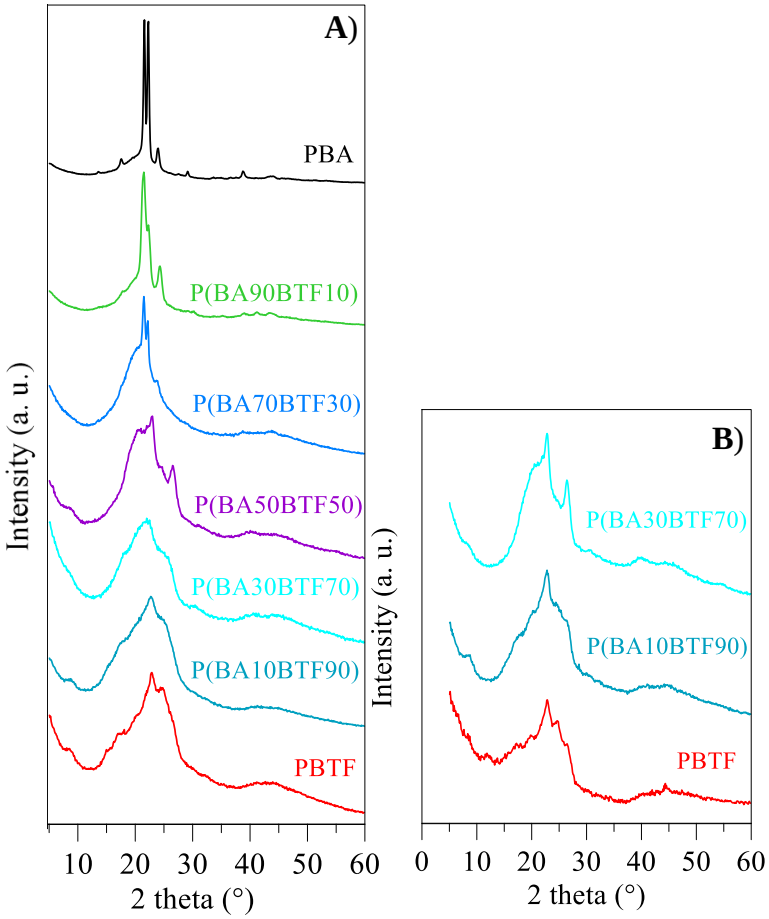

Figure 4.36. **A**) WAXS profiles of PBA, PBTF and P(BAxBTFy) copolymers recorded at RT; **B**) patterns of annealed samples.

All the profiles are typical of semicrystalline materials, containing some well-defined reflections, corresponding to ordered portion of the material, over a bell-shape baseline, due to the presence of amorphous regions. As to PBA homopolymer, its profile shows three sharp and intense peaks at 21.59°, 22.27° and 23.96° (2θ), which correspond to d = 4.10 Å, 3.99 Å and 3.71 Å, respectively. This kind of pattern is typical of the 110, 020, 021 reflections of PBA α-phase [Yang et al., 2010].

Conversely, PBTF diffraction pattern is less defined, containing low and broad peaks over an intense bell-shape baseline, corresponding to α-PBTF crystalline phase already reported [Guidotti et al., 2018 (c)]. More in details, the two peaks located at 2θ 22.9° and 24.7° (d = 3.88, 3.60 Å) are the most intense, whereas those at 8.7, 15.1, 17.1° (d = 10.1, 5.8, 5.1 Å) are less intense. The introduction of BTF co-units along the PBA main chain is responsible of a progressive lowering of crystallinity degree in P(BA90BTF10) and P(BA70BTF30) samples

(Figure 4.36A). Anyway, in both cases, only the α-PBA phase was detected. The diffraction profile significantly changes with a further increase of BTF mol%, being characterized by only broad reflections of low intensity. To better evidence the presence of α-PBTF phase in PBTF-richer copolymers, annealing treatments have been carried out and the relative patterns are shown in Figure 4.36B. As it can be seen, only two main peaks are clearly visible, probably due to the development of a crystalline phase isomorphic with α-PBTF.

As from WAXS analysis it was not possible to clearly understand the kind of crystallyne phase developed in P(BAxBTFy) copolymeric system, P(BA30BTF70), which can be considered representative of the richest PBTF copolymers' family, was subjected to deeper calorimetric studies (Figure 4.37).

It should be noticed that both the parent homopolymers are characterized by polymorphism and copolymerization can induce the formation of a further polymorphic phase.

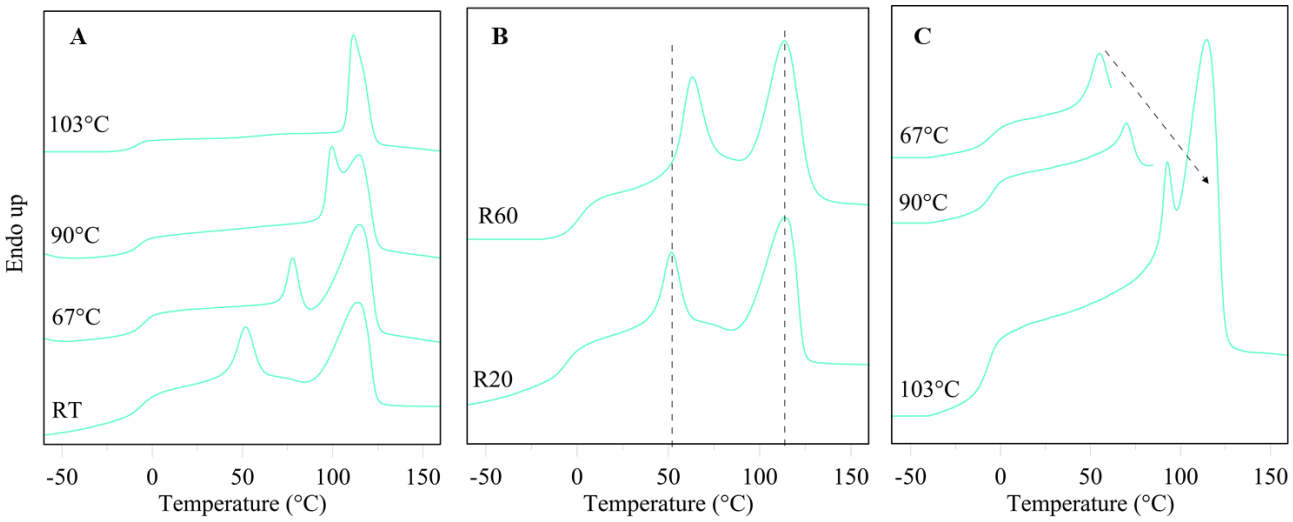

Figure 4.37. DSC studies on P(BA30BTF70): **A**) curves (20°C/min) after annealing at 67, 90, and 103°C for 10 minutes and of untreated film; **B**) curves at different heating rates (20 - 60°C/min); **C**) traces of consecutive heating steps to 67, 90, and 103°C (20°C/min).

After annealing treatments at different temperatures (Figure 4.37A), a shift of the low temperature endothermic peak II to higher temperature is registered, whereas peak I was not affected by the thermal treatment. More in detail, by increasing the annealing temperature, the peak becomes sharper and the temperature shift is more evident, up to its complete disappearance, when the annealing temperature is of 103°C. This behaviour can be due to an improvement of its associated phase. The effect of the heating rate on the position of the two

endotherms was also investigated (Figure 4.37B). Peak I remains unchanged, whereas peak II is significantly displaced to higher temperatures as the heating rate is increased, thus suggesting that only peak I is related to a first order transition (i.e. melting of crystalline domains). On the other hand, as already seen for PBTF homopolymer [Guidotti et al., 2018 (c)], the reversibility of peak II can be ascribed to the presence of uninduced meso-phase. To confirm this hypothesis also for PBTF rich copolymers, P(BA30BTF70) sample was subjected to the following thermal treatment (Figure 4.37C): heating scan to 67, 90 and 103°C, each followed by quenching to -60°C and subsequent heating to the next higher temperature (i.e. 90 and 103°C, respectively). After these sequential calorimetric studies, peak II is shifted to higher temperatures but is still present, unlike what is supposed to be for a I order transition.

After annealing treatment at 67, 90 and 103°C for 10 minutes on P(BA30BTF70) copolymer, also WAXS patterns were recorded (Figure 4.38). A considerable improvement of the pattern can be observed as the annealing temperature is increased. As previously reported in the present Thesis, meso-phase can be induced also by stretching [Ran et al., 2002; Lv et al., 2013]. In this view, X-ray pattern of P(BA30BTF70) after mechanical elongation tests was acquired. Interestingly, the so-obtained profile is typical of a meso-phase, thus suggesting that stretching favour the formation of a 2D-ordered phase over a crystalline one (Figure 4.38A). The same behaviour had been already observed for PBTF homopolymer [Guidotti et al., 2018 (c)].

In addition, from the comparison between the diffraction profiles obtained from the films before and after tensile stretching (Figure 4.38A), the simultaneous presence of both crystalline and meso-phase can be evicted. Anyway, the heat of fusion value associated with meso-phase indicates that this phase is very small as compared to traditional 3D one, due to the peculiar features of these domains.

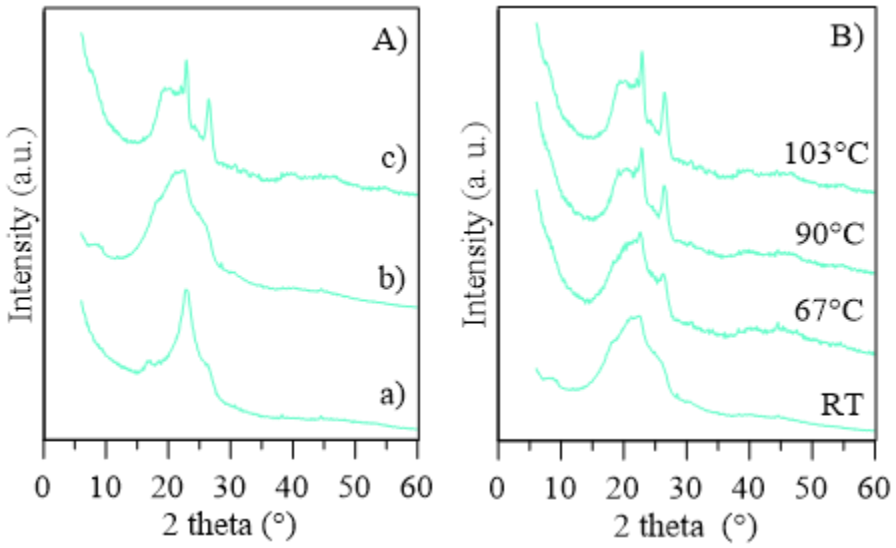

Figure 4.38. WAXS patterns of P(BA30BTF70). **A**) from bottom to top: a) film after tensile tests; b) untreated film; c) crystallized sample after annealing; **B**) XRD pattern performed at RT on samples annealed in DSC for 10 min at the indicated temperatures.

Moreover, the meso-phase content changes as a function of the copolymer composition. More in detail, according to the data collected in Table 4.16, PBTF contains the lowest content of meso-phase, P(BA10BTF90) and P(BA30BTF70) a higher and comparable amount, while P(BA50BTF50) shows the highest content.

As it is well known, the half-time of primary crystallization in isothermal experiments is related to the temperature of the maximum of the crystallization peaks in non-isothermal conditions (T_c) [Legras et al., 1986; Fabbri et al., 2016]. For this reason, all the samples under investigation have been subjected to non-isothermal treatment by cooling from the melt at a controlled rate, to verify that in the copolymers the crystallization ability decreases as the co-units amount is increased.

In Figure 4.34C the exothermic crystallization peaks are shown, while the corresponding data are collected in Table 4.16. As expected, for BA-rich samples, T_c decreases as the BTF co-units content is increased. Similarly, for BTF-rich ones, this value decreases as the BA co-unit amount increases. Moreover, both P(BA70BTF30) and P(BA50BTF50) cannot crystallize under the experimental conditions adopted and not even at slower cooling rate (1°C/min). The results obtained confirm that the regularity of the polymeric chain, which is reduced in P(BAxBTFy) copolymers by the introduction of comonomeric units, strongly affects the perfection of the final crystalline phase as well as the crystallization rate.

The effect of copolymerization on the amorphous phase was more deeply investigated by subjecting the samples to a rapid cooling from the melt (quenching). As known, if the cooling rate is faster than crystallization one, it is possible to prevent this latter, thus allowing for a better detection of glass-to-rubber transition.

From DSC curves after melt quenching shown in Figure 4.34B, it is possible to discriminate three different behaviours. PBA and P(BA90BTF10) do not show any significant difference from the I scan, being characterized by a glass transition step followed by a melting endothermic peak, while P(BA30BTF70) and P(BA50BTF50) samples are completely amorphous, as they show only a broad baseline deviation associated to the glass transition. Lastly, BTF-rich copolymers P(BA30BTF70), P(BA10BTF90), as well as PBTF homopolymer, display a glass transition step followed by an exothermic crystallization peak and, at higher temperatures, a melting endotherm. In this latter case, once T_g is exceeded, the macromolecular chains acquire sufficient energy and mobility and are able to crystallize during heating. Moreover, as $\Delta H_c = \Delta H_m$, also these samples are completely amorphous after melt quenching.

As to glass-to-rubber transition in the II DSC scan, T_g is influenced by the molar composition, as it increases when the BTF co-unit content is increased. Moreover, all the copolymers show a single glass transition temperature, whose values are located in between those of the two parent homopolymers (Figure 4.34B).

Among the several equations reported in the literature used to describe the effect of random copolymerization on the T_g of the final materials, the Fox equation is the most used [Eisenberg, 1984]. In Figure 4.39 the II scan T_g values as a function of the BTF co-unit weight fraction (W_{BTF}) are reported. The green curve indicates the trend of T_g according to the Fox equation:

$$1/T_g = W_A/T_{gA} + W_B/T_{gB} \quad \textbf{[41]}$$

where T_{gA} and T_{gB} are the glass transition temperatures of the pure homopolymers PBA and PBTF, while W_A and W_B represent the corresponding weight fractions.

As it can be seen, even though, according to the Fox's equation, T_g values increase is directly proportional to the BTF co-unit amount, the experimental data obtained are lower than the theoretical ones. This behaviour is not surprising since Fox equation does not consider neither the chemical structure nor the polymeric chain mobility [Vannini et al., 2005; Berti et al., 2004; Soccio et al., 2008]. In this framework, Gordon Taylor's equation can be used to overcome these limitations:

$$T_g = (T_{gA} * W_A + T_{gB} * W_B) / (W_A + k * W_B) \quad \textbf{[42]}$$

As it can be seen, this equation contains an additional correction parameter k with respect to the Fox's equation. In this case, the value of k = 2 allows for a good interpolation of the experimental data. The trend of T_g values according to the Gordon Taylor's equation is shown by the red curve (Figure 4.39).

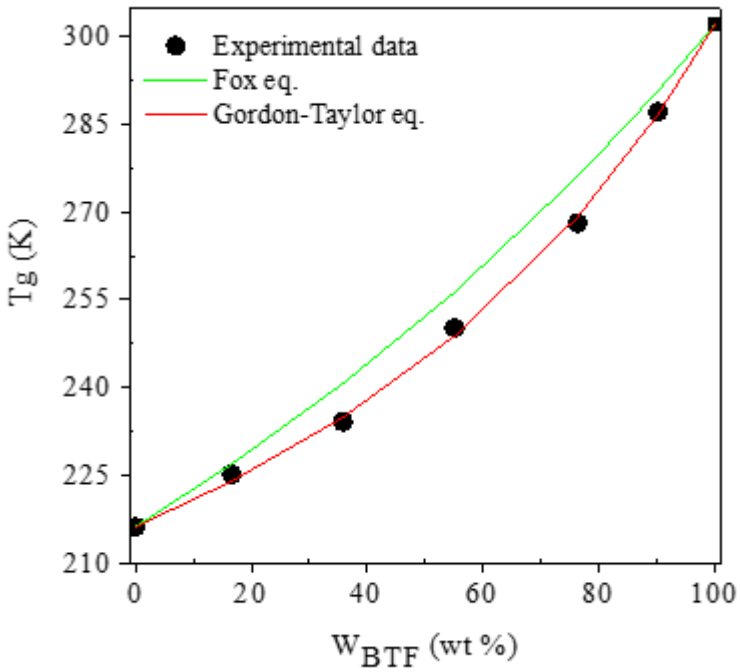

Figure 4.39. T_g values for P(BAxBTFy) copolymers as a function of weight BTF composition, with theoretical trends predicted by both Gordon-Taylor eqn. (red line) and by Fox eqn. (green line).

4.5.3 Mechanical characterization

Mechanical properties of P(BAxBTFy) copolymeric system, were investigated through tensile tests. In Table 4.17 the corresponding mechanical data are reported: elastic modulus (E), stress and deformation at yield (σ_y and ε_y, respectively) and stress and deformation at break (σ_b and ε_b, respectively).

According to the data reported in Table 4.17, the mechanical behaviour is quite complex, as it depends both on chain flexibility (given by the BA aliphatic co-units), and on the presence of three different ordered phases, named α-PBA, which is evident in PBA and PBA-rich

copolymers, α-PBTF and meso-phase, whose presence was detected in PBTF and PBTF-rich copolymers, respectively.

As a general trend, elastic modulus E is directly proportional to crystallinity degree. This behaviour is clear if the elastic modulus of the two homopolymers is compared: E_{PBA} is about 3 times higher than E_{PBTF}, because of the higher amount of crystal phase (Table 4.16), whose effect is predominant with respect to the higher rigidity of the PBTF repeating unit.

In addition, the presence of meso-phase significantly affects the mechanical response of the samples, causing an increase of elastic modulus in the materials with comparable crystallinity amount, as it can be seen in the case of PBTF and P(BA10BTF90). When meso-phase content is comparable, as the case of P(BA10BTF90) and P(BA30BTF70), then crystallinity degree plays again a predominant role.

Table 4.17. Mechanical characterization data (elastic modulus E, stress and deformation at yield σ_y and ε_y, respectively, and stress and deformation at break σ_b and ε_b, respectively), obtained by tensile tests.

Polymer	E (MPa)	σ_y (MPa)	ε_y (%)	σ_b (MPa)	ε_b (%)
PBA	287 ± 20	18.2 ± 0.8	12.2 ± 0.7	43.7 ± 3.6	1190 ± 62
P(BA90BTF10)	186 ± 10	12.7 ± 0.2	14.0 ± 0.8	12.0 ± 2.5	1352 ± 153
P(BA70BTF30)	176 ± 4	/	/	1.2 ± 0.4	271 ± 15
P(BA50BTF50)	53.3 ± 3	/	/	5.4 ± 1.1	72 ± 7
P(BA30BTF70)	181 ± 12	14.7 ± 0.4	23.0 ± 1.1	7.8 ± 0.5	122 ± 20
P(BA10BTF90)	543 ± 24	25.4 ± 0.4	17.5 ± 0.6	14.0 ± 1.5	207 ± 14
PBTF *	89 ± 7	/	/	24.5 ± 0.5	555 ± 50

Stress at break σ_b is related to the amount of crystalline phase too, as it decreases with the increase of the co-unit amount for both PBA- and PBTF-rich copolymers.

As regards the elongation at break ε_b values, they decrease as the presence of a 2D-ordered phase increases, probably because these domains hinder the stretching of the macromolecular chains.

4.5.4 Composting studies

The compostability of PBA, PBTF and P(BAxBTFy) copolymers was monitored by incubation studies in compost, in order to check if these materials can represent valid alternatives as biodegradable packaging films. Specimens were collected at specific timepoints (17, 33, 54, 73 days), and their gravimetric weight loss was calculated. In Figure 4.40A the weight loss % as a function of incubation time is shown.

As it can be seen, the degradation rate is strictly related to the molar composition: PBTF and P(BA10BTF90) weight loss is negligible, whereas all the other samples show an opposite behavior, being appreciably degraded. In addition, as it can be seen from Figure 4.40B, all the materials underwent significant fragmentation, apart from PBTF homopolymer. In particular, PBA and P(BA90BTF10) samples totally disappeared after 73 days of incubation, showing a weight loss of 100%. As to the other copolymers, P(BA70BTF30), P(BA50BTF50) and P(BA30BTF70), weight loss is directly proportional to the BA co-units amount.

This behavior can be attributed to the different chain mobility, which is related to the difference between the T_m of the polymers under study and the composting temperature (58 °C). In turn, the T_m significantly affects the amount of crystalline domains: for example, the operating temperature is within the melting endothermic peak of PBA-rich samples. Consequently, both high chain mobility and low crystallinity, with respect to those present at room temperature should be expected. Both these factors allow a higher accessibility of the ester bonds to the depolymerizing enzymes, thus increasing the degradation rate. It has also to be considered that amorphous regions are more easily degraded than more packed crystalline ones [Gigli et al., 2012 (a)].

SEM analysis was carried out on samples after 73 days of incubation to check the microscopic morphology of the films after degradation. Not degraded samples were also observed for sake of comparison. As an example, the micrographs of PBTF, P(BA30BTF70), P(BA50BTF50) and P(BA70BTF30) copolymers before and after incubation are shown in Figure 4.41. Non-incubated films present a homogeneous and quite smooth surface, while after 73 days the surfaces considerably changed: on one hand, PBTF surface can be considered as unaltered, on the other hand holes, channels and cracks can be clearly seen on copolymeric surfaces, more intense as the BA co-unit amount increases, according to the weight loss results (Figure 4.40A).

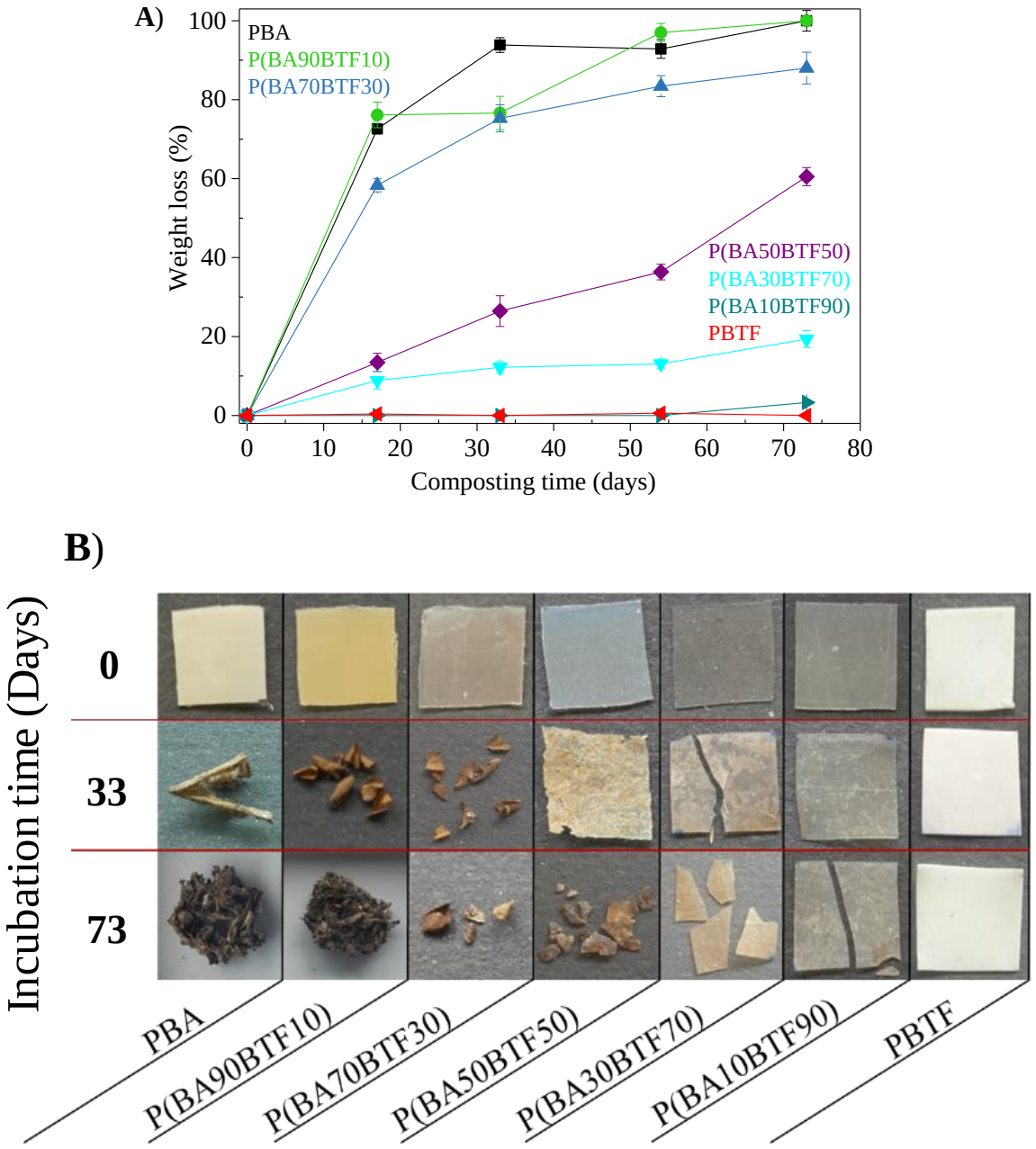

Figure 4.40. **A**) gravimetric weight loss as a function of composting time; **B**) visual observations of partially degraded films at three different composting time (0, 33 and 73 days).

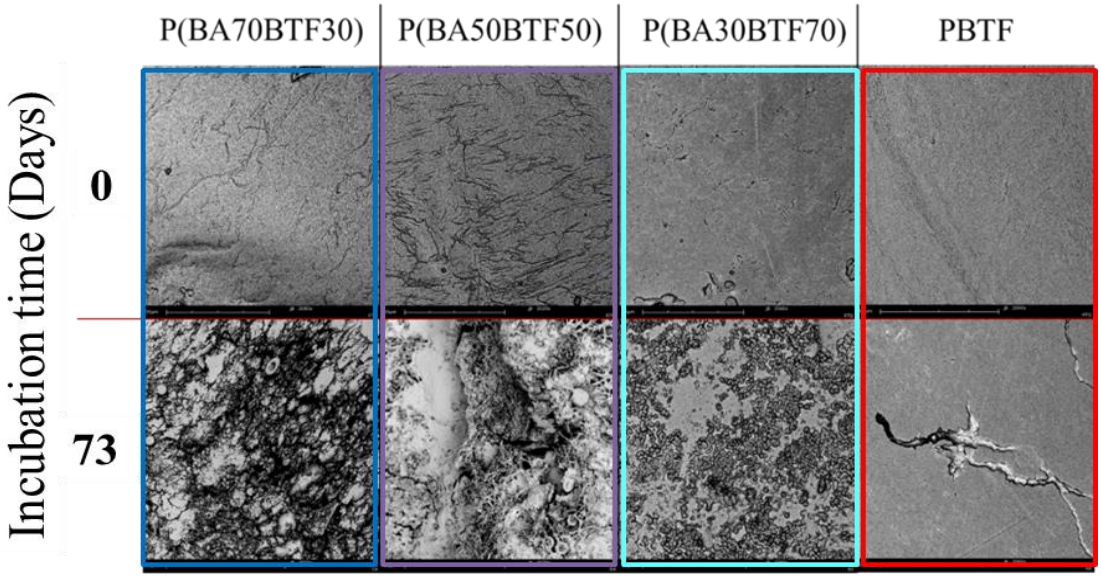

Figure 4.41. SEM micrographs (2000x magnification) of degraded films as a function of composting time.

4.5.5 Gas permeability studies

O_2 and CO_2 gas permeability (expressed as GTR values) for the P(BAxBTFy) copolymeric system is shown in Figure 4.42. As already reported in the present Thesis and in the literature, PBTF is characterized by excellent gas barrier properties, even better than those of PEF, thanks to the presence of meso-phase [Guidotti et al., 2018 (c)]. As to the copolymers, their performances are strictly related to the amount of BA comonomeric units: the higher the BA mol%, the higher the gas permeability.

It is well known that permeability is a very complex phenomenon, affected by both gas parameters, such as size and polarity, and by material features, like glass transition temperature, crystallinity degree, presence of cross-linking and chain stiffness [Robertson, 2013]. Intuitively, the more tortuous the path through the macromolecular chains, the lower the GTR values.

Even though higher amounts of meso-phase are supposed to lead to an improvement of barrier performances, other parameters move in the opposite direction, enhancing the GTR. More in detail, both glass transition temperature and content of crystalline domains decrease with the increase of the BA co-unit amount. At 23°C, the temperature at which the permeability tests were carried out, PBTF is in the glassy state, whereas all copolymers are in the rubbery one (i.e.

higher chain flexibility) and, except for P(BA90BTF10), they all display a ΔH_m related to the melting of the 3D crystals lower than that of their parent homopolymers. In addition, the long aliphatic sequences present in the copolymers may negatively affect the high packing ability of PBTF, causing higher interplanar distances and thus facilitating the gas flow through the polymeric matrix.

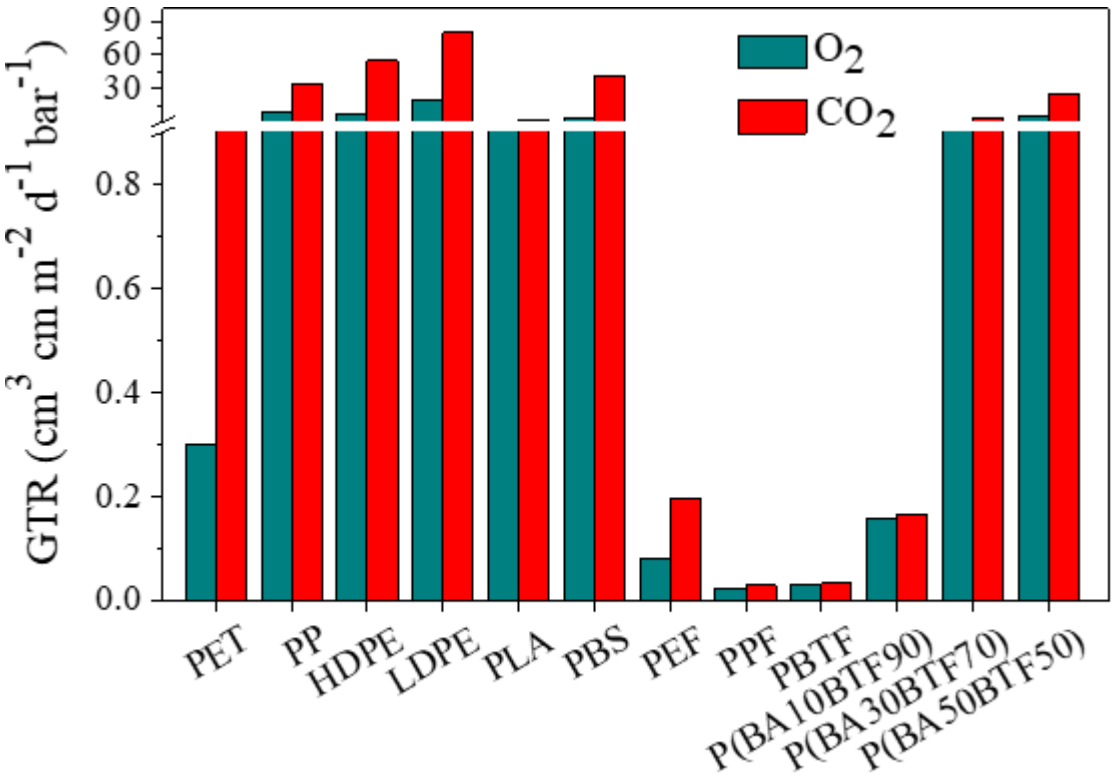

Figure 4.42. O_2 and CO_2 GTR values of PBTF and P(BAxBTFy) copolymers compared to those of other fossil-based plastics and biopolymers [Guidotti et al., 2018 (b), (c); Mensitieri et al., 2011; Siracusa et al., 2015; Burgess et al., 2014; Burgess et al., 2015].

The results obtained look of particular interest if compared to the values of other fossil-based plastics and biopolymers widely used for packaging applications (Figure 4.42). Gas barrier ability of P(BA10BTF90) is comparable to that of PEF, while P(BA30BTF70) and P(BA50BTF50) show permeability values similar to those of polyolefines and poly(lactic acid).

4.5.6 Conclusions

Novel high molecular weight bio-based poly(butylene adipate/2,5-thiophene dicarboxylate) P(BAxBTFy) random copolymers were successfully synthesized through 2-step melt polycondensation technique.

In particular, thanks to calorimetric and WAXS analyses, it was possible to demonstrate for the first time the presence of uninduced meso-phase in random copolyesters, thanks to the particular ability of BTF sequences capable of organizing themselves both in 2D as well as in 3D ordered domains.

Meso-phase was found to positively affect the barrier properties, as it hinders the gas molecules flow, and the elastic modulus, since an increase of chain stiffness took place. Conversely, a worsening effect on the elongation at break was observed as the meso-phase content is increased, because of the limited stretching ability of these domains.

In addition, by acting on the content of flexible aliphatic sequences inside the copolymers, it was possible to modulate both solid-state properties and biodegradation rate. Therefore, copolymerization with adipic acid turned out to be a simple and effective strategy to enhance PBTF homopolymer compostability, as well as to tailor its performances, based on the intended application.

4.6 Novel Poly(butylene 1,4-cyclohexane dicarboxylate) random copolymers containing aliphatic side chains for flexible food packaging applications.

Novel bio-based poly(butylene 1,4-cyclohexane dicarboxylate) random copolymers with different composition were designed for sustainable and flexible packaging applications. On one side, the linear butylene moiety has been substituted by glycol subunits with alkyl pendant groups of different length: neopentyl glycol (NG) in one case, 2-butyl-2-ethyl propanediol (BEPD) in the other case. On the other side, copolymers with different cis/trans isomer ratio of cyclohexane rings were obtained. All the samples were characterized from the molecular, thermal, diffractometric and mechanical point of view. Barrier performances tests to gases like O_2, CO_2, and N_2 were also carried out. Even though the presence of side alkyl groups did not alter thermal stability, it deeply influenced the formation of ordered phases, which affect functional properties like mechanical response and barrier performance. More in details, the copolymers are characterized by improved flexibility and barrier properties with respect to both the homopolymer and other polymers already employed for flexible packaging applications. The most pronounced improvements were obtained in the case of copolymers containing higher co-unit amounts and with cyclohexane rings in *trans* configuration.

4.6.1 Synthesis and molecular characterization

PBCE homopolymer, P(BCExBEPCEy), P($BCE_{65}BEPCE_{35}$)-ct, and P($BCE_{70}NCE_{30}$) random copolymers have been synthetized following the procedure described in Paragraphs 3.2.1.2 and 3.2.1.3 respectively. At room temperature, all the synthesized polyesters appeared as semicrystalline light yellow solids. The samples are listed in Table 4.18, which also collects the molecular characterization data obtained by means of ^{1}H-NMR and ^{13}C-NMR spectroscopy and by GPC analysis.

Table 4.18. Molecular characterization data of PBCE, P(BCE_xBEPCE_y) and P($BCE_{80}NCE_{20}$) random copolymers.

Polymer	BCE mol% feed	BCE mol% ^{1}H-NMR	BCE wt% ^{1}H-NMR	*cis* mol% ^{1}H-NMR	b ^{13}C-NMR	M_n g/mol GPC	D GPC
PBCE	100	100	100	2	-	44300	2.3
P($BCE_{85}BEPCE_{15}$)	85	85	81	2	1.01	45700	2.3
P($BCE_{65}BEPCE_{35}$)	65	65	59	3	1.01	45900	2.5
P($BCE_{50}BEPCE_{50}$)	50	51	45	3	0.98	46600	2.2
P($BCE_{80}NCE_{20}$)	80	80	79	2	0.99	46300	2.2
P($BCE_{65}BEPCE_{35}$)-ct	70	69	63	30	0.98	49300	2.2

According to the data collected in Table 4.18, all the samples are characterized by high and comparable molecular weights, thus proving that no significant thermal degradation reactions occurred during the synthesis.

As to ^{1}H-NMR and ^{13}C-NMR analyses, they were carried out to confirm the chemical structure, calculate the actual composition and the degree of randomness b. In Figure 4.43 the ^{1}H-NMR spectrum of P($BCE_{65}BEPCE_{35}$) with the resonance assignments is shown as an example.

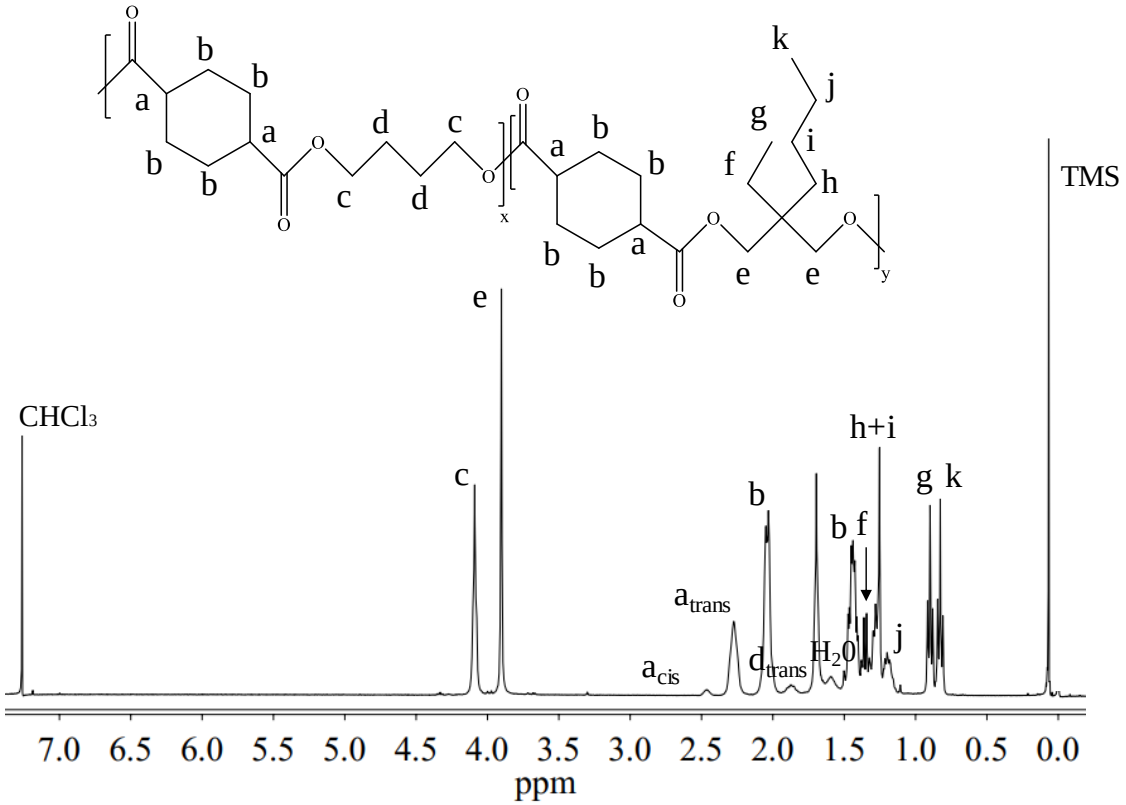

Figure 4.43. ^{1}H-NMR spectrum of P($BCE_{65}BEPCE_{35}$) with resonance assignments.

Since no additional peaks are present in the spectrum, the chemical structure of the copolymeric material is confirmed. For $P(BCE_xBEPCE_y)$ random copolymers the composition was determined taking into account the relative area of the resonance peak of the c protons corresponding to the butylene subunit, located at δ 4.11 ppm, and the area of the signal at δ 3.90 ppm of the e protons of the butyl-ethyl propylene moiety (Figure 4.43). For $P(BCE_{80}NCE_{20})$, to calculate the actual composition the signal of neopentyl subunit at δ 3.85 ppm was used. For all the copolymers under investigation the actual composition is close to the feed one (Table 4.18), confirming the good control obtained during the synthesis. ^{13}C-NMR spectroscopy was used to evaluate the degree of randomness b. In Figure 4.44, for example, the ^{13}C-NMR spectrum of $P(BCE_{65}BEPCE_{35})$ is shown, together with the peaks attribution and the magnification of the region between δ 176.50 and δ 174 ppm, where the signals due to the ester group carbons are located. In this region, the signals related to the ester carbons at δ 175.38 and δ 175.13 ppm, corresponding to the B-CE-B (w carbons) and BEP-CE-BEP (z carbons) triads, can be noticed, together with two additional peaks. These last correspond to the B-CE-BEP and BEP-CE-B (x and y carbons) triads, consequent to transesterification reactions.

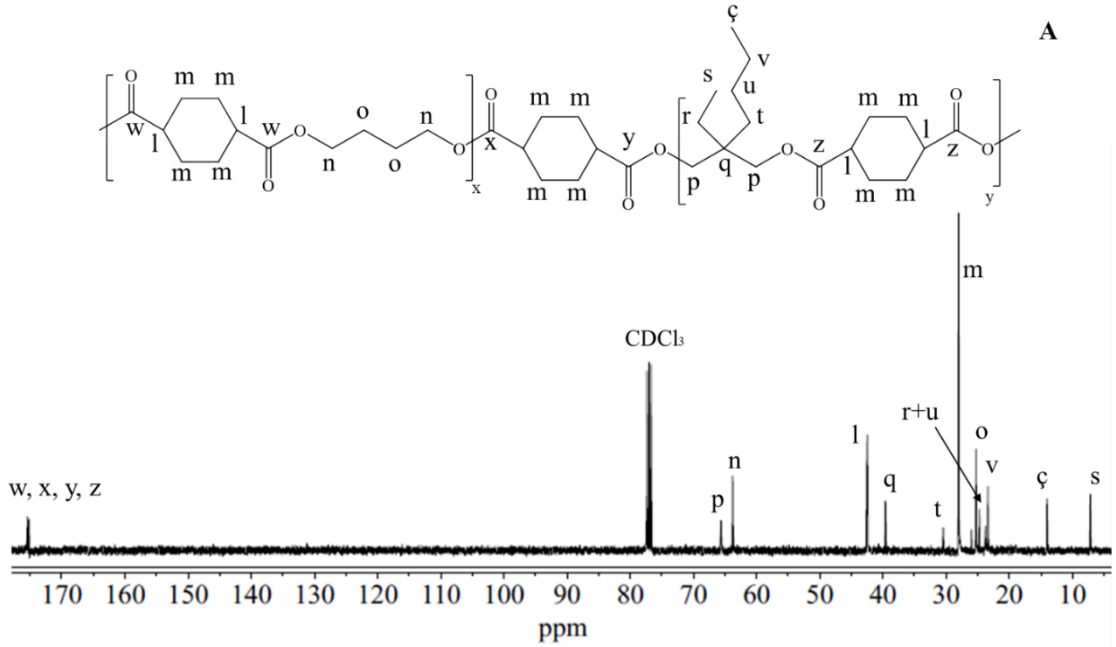

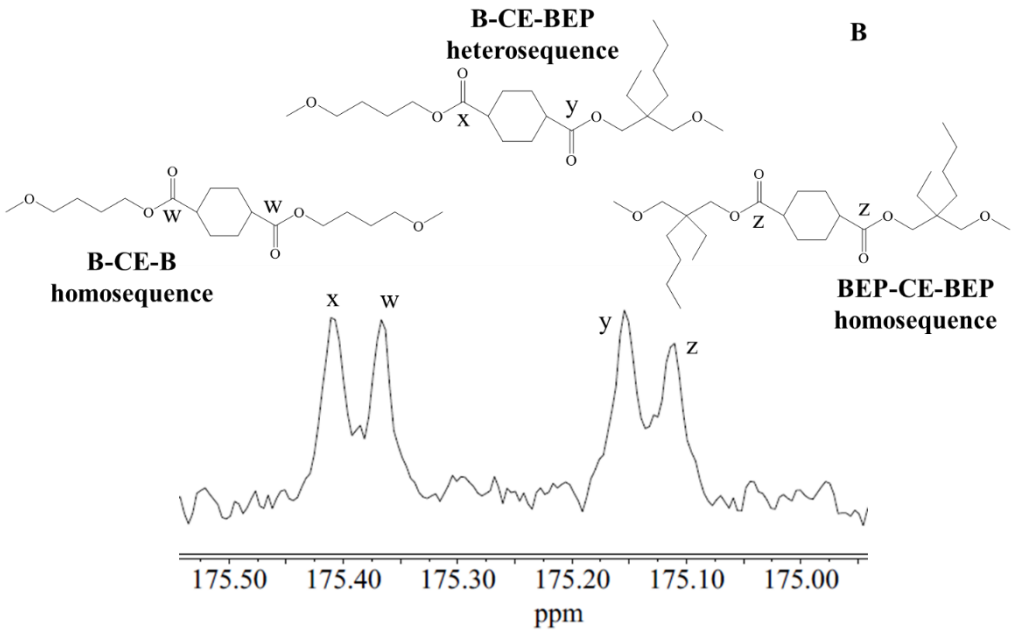

Figure 4.44. A) ^{13}C-NMR spectrum of P(BCE$_{65}$BEPCE$_{35}$) with resonance assignments; **B)** magnification of ^{13}C-NMR spectrum in the region between δ 176.50 ppm and δ 174 ppm, together with the schematic representation of B-CE-B, B-CE-BEP, and BEP-CE-BEP triads.

As to the degree of randomness b, in the present work it was calculated from the intensities of the w, z, x, and y peaks, according to Eqn. [28], where P_{X-Y} (P_{B-BEP}) and P_{Y-X} (P_{BEP-B}) are the probability of finding a B unit close to a BEP one and the probability of finding a BEP unit next to a B one, respectively. These two parameters can be obtained from Eqn. [29] and Eqn. [30], where I_{X-Y}, I_{Y-X}, I_{X-X} and I_{Y-Y} represent I_x, I_y, I_w and I_z, respectively (Figure 4.44B).

As expected, due to the high reaction temperature and catalyst employed, all the copolymers resulted characterized by a random distribution of comonomeric units (b calculated equal to 1).

4.6.2 Thermal characterization

The thermal stability of all the samples was analysed by thermogravimetric analysis under nitrogen flow. Thermogravimetric curves are shown in Figure 4.45, while the temperatures of 5% weight loss ($T_{5\%}$) and maximum weight loss rate (T_{max}) are listed in Table 4.19. For all the copolymers under investigation, the weight loss is 100% and takes place in one step. All the samples analysed show very good thermal stability, as weight loss starts above 380 °C. In addition, in the copolymers both $T_{5\%}$ and T_{max} increase with respect to those of PBCE, proving

that thermal degradation occurs at higher temperatures. The increment in thermal stability is related to copolymer composition, being higher the higher the amount of co-unit. This behaviour may be probably ascribed to the presence of ramifications on the carbon in the β position with respect to the ester oxygen, which hamper β-scission processes.

The thermal data of the samples under study obtained by DSC analysis are listed in Table 4.19, while the relative calorimetric curves are reported in Figure 4.46.

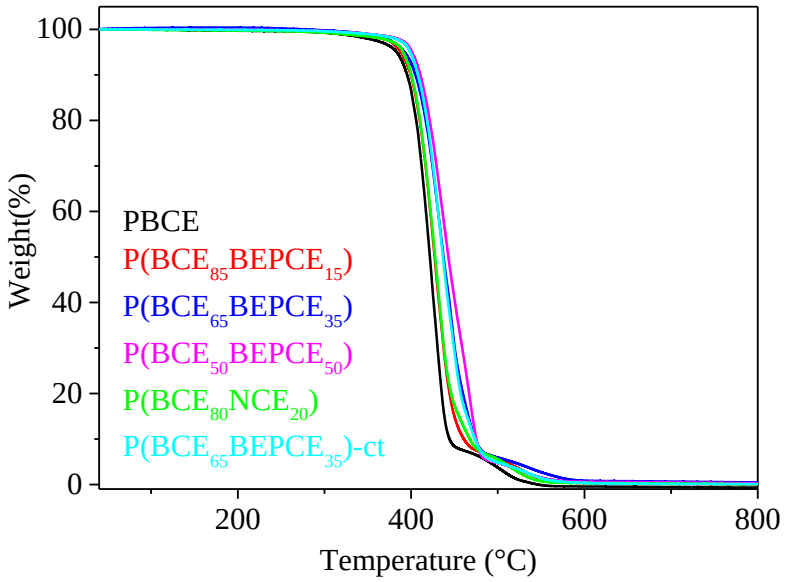

Figure 4.45. TGA traces of PBCE homopolymer, P(BCE$_x$BEPCE$_y$), P(BCE$_{65}$BEPCE$_{35}$)-ct and P(BCE$_{80}$NCE$_{20}$) random copolymers.

Table 4.19. Thermal characterization data of PBCE, P(BCE$_x$BEPCE$_y$), P(BCE$_{65}$BEPCE$_{35}$)-ct and P(BCE$_{80}$NCE$_{20}$) random copolymers, obtained by TGA and DSC.

Polymer	$T_{5\%}$ °C	T_{max} °C	I SCAN						II SCAN					
			T_g °C	Δc_p J/g·°C	T_I °C	ΔH_I J/g	T_{II} °C	ΔH_{II} J/g	T_g °C	Δc_p J/g·°C	T_{cc} °C	ΔH_{cc} J/g	T_{II} °C	ΔH_{II} J/g
PBCE	381	426	10	0.099	51	1	166	30	8	0.120	-	-	167	30
P(BCE$_{85}$BEPCE$_{15}$)	389	428	7	0.128	49	2	140	23	6	0.258	40	19	135	21
P(BCE$_{65}$BEPCE$_{35}$)	393	432	10	0.171	50	12	85	6	8	0.210	-	-	-	-
P(BCE$_{50}$BEPCE$_{50}$)	400	437	10	0.332	-	-	-	-	11	0.328	-	-	-	-
P(BCE$_{80}$NCE$_{20}$)	390	428	15	0.246	49	2	130	19	11	0.298	51	17	130	19
P(BCE$_{65}$BEPCE$_{35}$)-ct	394	433	0.3	0.268	50	13	-	-	0.5	0.363	-	-	-	-

According to the molecular characterization data (Table 4.18), any influence of molecular weight on the glass transition and melting temperature of the synthesized polymers can be excluded, as all the samples are characterized by high and comparable M_n.

As shown in Figure 4.46A, all the copolymers, except for P($BCE_{50}BEPCE_{50}$), are semicrystalline, being the corresponding DSC curves characterized by the presence of an endothermic baseline deviation related to the glass to rubber transition, followed by endothermic peaks at higher temperatures related to the melting of ordered crystalline portions. Conversely, P($BCE_{50}BEPCE_{50}$) copolymer shows only the glass-to-rubber transition at 11 °C.

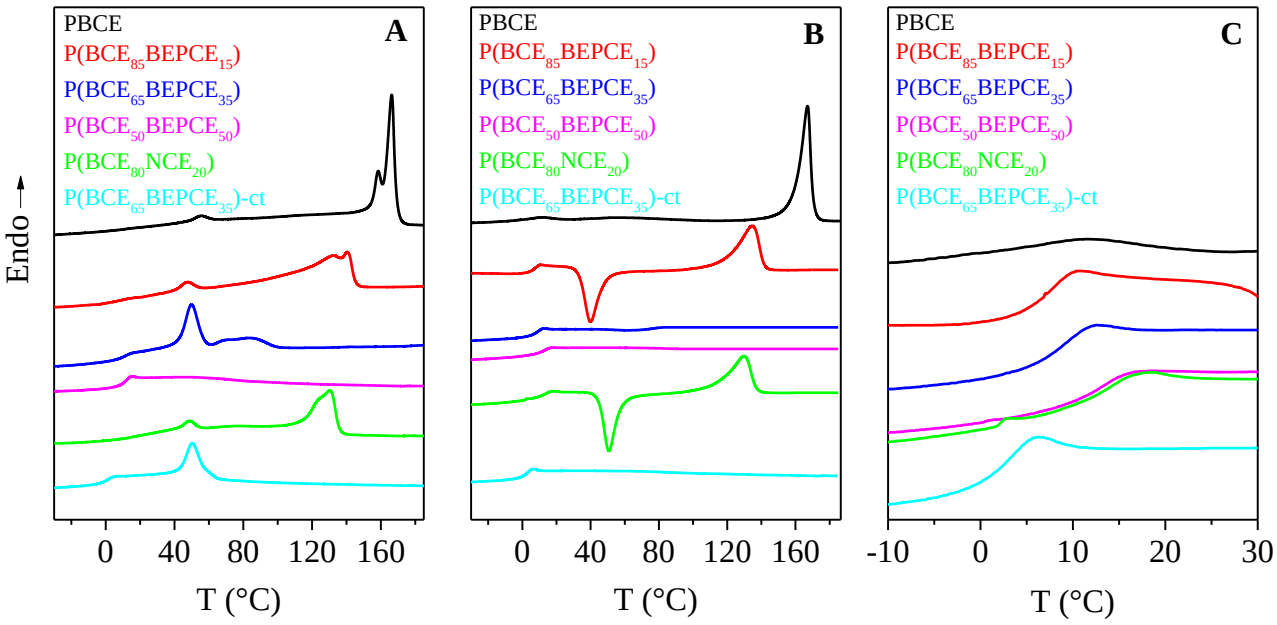

Figure 4.46. Calorimetric curves (20 °C/min) of PBCE, P(BCE_xBEPCE_y), P($BCE_{65}BEPCE_{35}$)-ct and P($BCE_{80}NCE_{20}$) copolymers: **A**) 1st scan; **B**) 2nd scan after melt quenching; **C**) magnification in the T_g region of 2nd scan.

As to the semicrystalline samples, two different endothermic phenomena can be observed. The first one is located at around 50 °C, its position is independent on the amount of comonomeric units and its intensity is directly proportional to the comonomeric unit content (from now on it is referred to as peak I). The second one, characterized by a double peak, is located at higher temperature, and both its position and area progressively decrease with the comonomeric unit amount (from now on referred to as peak II). The evolution of peak II is common in many copolymeric systems, in which the formation of a crystalline phase characterized by a lower degree of perfection is favoured. As concerns the double peak shape, it can be related whether

to melting-recrystallization processes of low ordered crystalline phases, which are common when the co-units hinder the crystallization process of the parent homopolymer, or to the presence of different crystalline lattices [Minakov et al., 2010; Kong et al., 2003; Soccio et al., 2009; Soccio et al., 2013].

As to peak I, its position and intensity's trend are unusual for polyesters, and therefore not easily explainable.

The calorimetric curve of the copolymer containing *cis/trans*-1,4-cyclohexanedicarboxylate moieties, P(BCE$_{65}$BEPCE$_{35}$)-ct and that of P(BCE$_{65}$BEPCE$_{35}$), which contains only *trans*-1,4-cyclohexanedicarboxylic acid, are very similar, differing only for the presence of the low melting peak at 85 °C in P(BCE$_{65}$BEPCE$_{35}$) trace. The absence of this phenomenon in the *cis/trans* copolymer can be due to the additional crystallization hindering of the *cis/trans* isomerism in the acid subunit, which decreases the structural regularity inside the macromolecular chain.

In conclusion, the melting behavior appeared to be very complex. X-ray diffraction analysis, whose results are presented and discussed below, will be able to provide more elements to identify the origin of the endothermic peaks I and II.

In order to study the influence of the chemical structure on the glass-to-rubber transition of the materials under investigation in the total absence of crystallinity, all the samples were subjected to melt quenching. The DSC traces of the sample after this thermal treatment are shown in Figure 4.46B, while the corresponding thermal characterization data are listed in Table 4.19.

As to the homopolymer, PBCE curves of I and II scan present the same trend, thus confirming that this homopolymer cannot be blocked in the amorphous state under the experimental conditions adopted because of its high crystallization rate. On the contrary, calorimetric curves of all the copolymers deeply change after melt quenching, thus confirming the effect of copolymerization on the thermal behaviour of PBCE homopolymer. First, the glass-to-rubber transition phenomenon becomes broader, because of a higher amorphous phase amount in the quenched materials. In addition, a different crystallization capability can be detected as the amount of comonomeric units is increased: the DSC traces of the samples containing up to 20 mol% of co-units (P(BCE$_{85}$BEPCE$_{15}$) and P(BCE$_{80}$NCE$_{20}$)) are characterized by the typical glass to rubber transition baseline deviation, followed by both an exothermic and an endothermic peak at higher temperatures. This trend is typical of materials that are able to undergo crystallization in the temperature range between T_g and T_m. At further higher

temperature, they show a melting peak related to the crystalline portion developed during heating. Moreover, the areas under these two peaks are equal ($\Delta H_{cc} = \Delta H_{II}$), as a proof that the copolymers had been successfully quenched, thus confirming that the presence of both long (BEPCE) and short (NCE) comonomeric units along the PBCE chains hinders the crystallization ability of the homopolymer. This behaviour is even more clear in the copolymers containing the highest amount of co-unit, P($BCE_{65}BEPCE_{35}$) and P($BCE_{50}BEPCE_{50}$): in this case only the glass to rubber transition step can be detected in the II scan curves. The sample containing both the *cis* and *trans* isomers, P($BCE_{65}BEPCE_{35}$)-ct shows the same phase behaviour of P($BCE_{65}BEPCE_{35}$) and P($BCE_{50}BEPCE_{50}$), as in its II scan trace only the glass transition phenomenon is present (Figure 4.46B).

The kind of co-unit affects also the polymeric chains mobility, as evidenced by the T_g and the corresponding Δc_p values listed in Table 4.19. It is commonly accepted that the presence of alkyl pendant groups hinders the rotation around the C–C σ bond, because of their high steric hindrance, thus reducing the macromolecular chains mobility (T_g rises). However, pendant groups sufficiently long are able to act also as an internal plasticizer, leading to a decrease of T_g values. This effect is proportional to the length of the side alkyl group. For the copolymers under investigation, both these opposite effects are supposed to affect chain mobility and, consequently, T_g position. As evidenced in Figure 4.46C, the T_g step, which is quite low for PBCE, becomes higher in the copolymers, because of the presence of the only amorphous phase after rapid cooling from the melt. Therefore, the T_g position is determined only by chain mobility, as any effect of crystal phase can be excluded. It is also interesting to notice that for all the copolymers, apart from P($BCE_{65}BEPCE_{35}$)-ct, the T_g is progressively shifted to higher temperature, despite the absence of any crystalline domain. In case of P(BCE_xBEPCE_y) copolymers, analogously to other copolymeric systems previously studied [Soccio et al., 2007; Soccio et al., 2008], the effect of chain stiffening, due to the steric hindrance of the alkyl side-groups, prevails over the internal plasticizing one.

Conversely, in the case of P($BCE_{80}NCE_{20}$), characterized by shorter pendant groups along the main macromolecular chain, the overall balance of steric hindrance and plasticizing effect is different. In fact, the same increase in T_g value is obtained with lower weight fraction of comonomeric units. Indeed, as it can be seen in Figure 4.46C, the calorimetric curve of P($BCE_{80}NCE_{20}$), which contains an amount of NCE co-units of 21 wt% is practically overlapped with that of P($BCE_{50}BEPCE_{50}$), which contains the 55 wt% of BEPCE co-units.

From this result, it is possible to conclude that in case of NCE co-units, the internal plasticizing effect is minor, probably because of the presence of shorter side chains.

The copolymer containing *cis/trans*-1,4-cyclohexanedicarboxylate moieties, P($BCE_{65}BEPCE_{35}$)-ct, shows a lower T_g compared to that of PBCE homopolymer: the reduced chain symmetry induced by the different ring isomerism probably hampers chain interactions, thus resulting in a decrease of glass transition temperature.

4.6.3 Structural characterization

X-ray diffraction analysis was carried out both to investigate the crystalline phase of the samples under study and to shed light on the complex endothermic behaviour revealed by DSC analysis.

In Figure 4.47, the XRD patterns of the polymers under study are shown. According to the results obtained, it is clear that copolymerization deeply affects crystallinity of PBCE homopolymer. As a matter of fact, PBCE is characterized by a well-defined pattern with several peaks located at 9.3°, 15.1°, 16.6°, 18.2°, 19.3°, 20.7°, and 22.7°. For the copolymers, a considerable decrease of XRD reflections even for low amounts of comonomeric unit contents was observed. For example, as to peaks located at 9.3°, 15.1°, and 22.7°, they are less defined but still present in P($BCE_{85}BEPCE_{15}$), whereas they disappear in P($BCE_{80}NCE_{20}$) copolymer: in this case, only the peaks at 16.6°, 18.2°, 19.3°, and 20.7° can be detected. Moreover, these reflections, further reduced in intensity, are the only ones detectable in the copolymers containing 35 mol% of BEPCE co-units: P($BCE_{65}BEPCE_{35}$) and P($BCE_{65}BEPCE_{35}$)-ct. According to previous studies reported in literature [Gigli et al., 2014 (b); Genovese et al., 2014], the selective reduction of some peaks can be due to the disappearance of an ordered phase whose presence is deeply compromised by the insertion of BEPCE and NCE co-units along the main polymeric chain.

In the case of the P($BCE_{50}BEPCE_{50}$) copolymer, no clear reflections in the WAXS pattern are present.

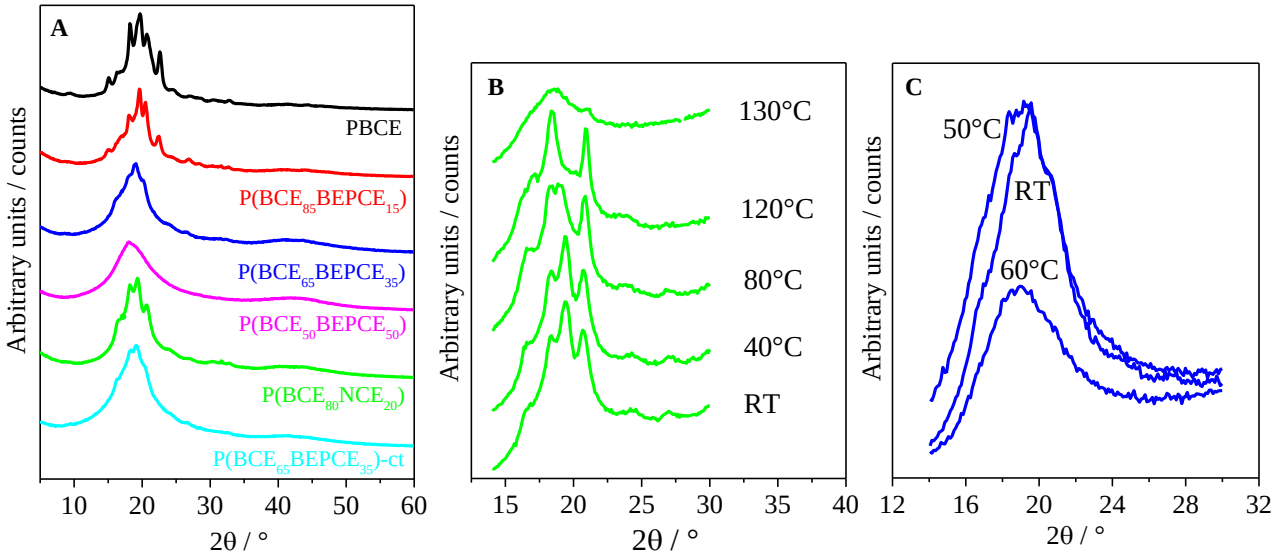

Figure 4.47. **A**) X-ray pattern at room temperature of all the samples under study; **B)**, **C**) XRD profiles at different temperatures of $P(BCE_{80}NCE_{20})$ and $P(BCE_{65}BEPCE_{35})$ films, respectively.

Moreover, according to diffractometric analysis, any co-crystallization phenomena, either in $P(BCE_{80}NCE_{20})$ or in $P(BCE_xBEPCE_y)$, can be excluded. This result agrees also with the calorimetric data listed in Table 4.19, in which a lowering of T_I proportional to the amount of co-unit and independently on its nature is shown.

By comparing $P(BCE_{65}BEPCE_{35})$ and $P(BCE_{65}BEPCE_{35})$-ct diffractometric patterns, it is possible to exclude any influence of the different isomerism of cyclohexane ring on the nature of the crystalline phase.

As the WAXS measurements carried out at room temperature are not able to clarify the origin of the complex melting behaviour, additional temperature scanning diffractometric experiments have been carried out in order to follow the ordered phase evolution of the samples under investigation. In Figure 4.47B, the XRD spectra of $P(BCE_{80}NCE_{20})$ collected at different temperatures are shown. From these patterns, it is possible to see how reflections at 18.2° and 20.7° progressively grow whereas the peaks at 16.6° and 19.3° decrease as temperature is increased. The disappearance of these last occurs at a temperature close to that of the endothermic peak I recorded by calorimetric analysis (Figure 4.46A). It is worth mentioning that peak I is the only one present in the $P(BCE_{65}BEPCE_{35})$ and $P(BCE_{65}BEPCE_{35})$-ct DSC traces. As the temperature is increased, an improvement of peak resolution can be seen, thus leading to hypothesize that the double DSC peak II could be due to melting/crystallization phenomena of crystals with a low degree of perfection.

In addition, in Figure 4.47C, WAXS patterns of P($BCE_{65}BEPCE_{35}$) collected at different temperatures are shown. At room temperature neither any defined peak reflection nor the typical bell shape of amorphous region are present, being the pattern characterized by the presence of a quite sharp peak, which becomes less defined at 50 °C and then disappears when a temperature of 60 °C is reached. At this temperature, the XRD pattern shows the bell-shape typical of the amorphous halo.

Among these interesting results, the evolution of the XRD pattern measured at 50 °C, not typical of a semicrystalline material, into the pattern at 60 °C, characteristic of a completely amorphous polymer, the presence of a 2D-ordered phase can be hypothesized. This hypothesis can be supported by previous studies [Chandrasekhar, 1992], including 1,4-cyclohexane moieties among the mesogenic groups.

4.6.4 Mechanical characterization

Tensile measurements have been performed on polymeric film samples to test their mechanical performances. The stress strain curves are shown in Figure 4.48, while the mechanical characterization data, including elastic modulus *E*, stress at break σ_b and elongation at break ε_b are reported in Table 4.20.

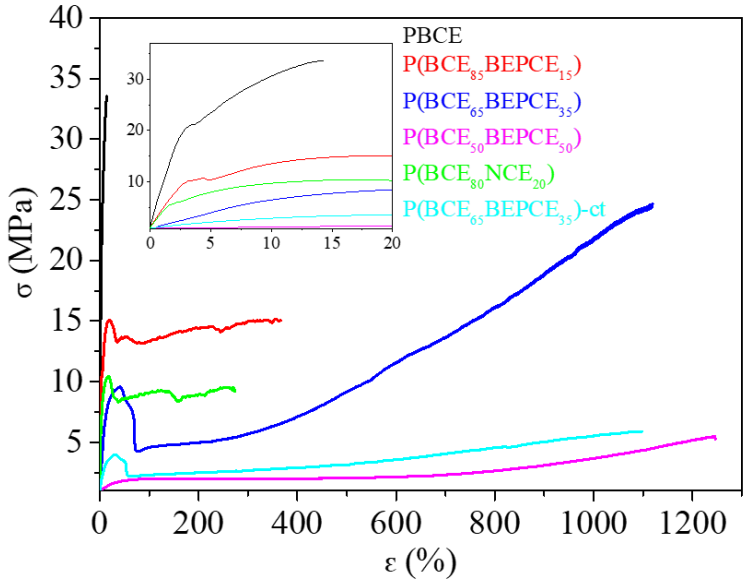

Figure 4.48. Stress-strain curves of PBCE, P(BCE_xBEPCE_y), P($BCE_{65}BEPCE_{35}$)-ct and P($BCE_{80}NCE_{20}$) random copolymers; In the inset: magnification of the low σ-ε region.

Table 4.20. Mechanical characterization and gas transmission rate (GTR) data for PBCE, P(BCE_xBEPCE_y), P($BCE_{65}BEPCE_{35}$)-ct and P($BCE_{80}NCE_{20}$) random copolymers (GTR measured at 23 °C, with N_2, O_2, and CO_2 dry gas test).

Sample	E MPa	σ_b MPa	ε_b %	GTR CO_2 cm^3 cm/m^2 d atm	GTR O_2 cm^3 cm/m^2 d atm	GTR N_2 cm^3 cm/m^2 d atm
PBCE	830±18	40±2	19.0±4	4.17239	1.29117	0.36585
P($BCE_{85}BEPCE_{15}$)	437±22	16±1	424±70	6.05463	2.05468	0.5544
P($BCE_{65}BEPCE_{35}$)	82±21	22±4	1198±176	0.01317	0.00517	0.00588
P($BCE_{50}BEPCE_{50}$)	6±1	4.0±0.4	1290±205	0.01722	0.00486	0.00705
P($BCE_{80}NCE_{20}$)	494±46	14±3	223±77	3.61667	0.88803	0.35319
P($BCE_{65}BEPCE_{35}$)-ct	38±3	6.6±0.5	1131±35	15.0923	7.53698	1.80443

The first interesting observation is that the mechanical characterization was possible also on P($BCE_{50}BEPCE_{50}$) copolymer, despite this material at room temperature is in its rubbery state and does not contain any crystalline phase. Taking into account all these aspects, the possibility of obtaining a freestanding film was possible thanks to the presence of a 2D-ordered phase, usually called mesophase.

Previous studies present in literature have shown that copolymeric materials containing in their main chain both mesogenic rings and an even number of flexible $–CH_2–$ groups, develop a smectic liquid crystal mesophase [Blumstein et al., 1982; Krigbaum et al., 1983]. The corresponding isotropization is detected in the calorimetric trace as an endothermic peak with low intensity located at a constant temperature between T_g and T_m. This peak can be seen both in PBCE homopolymer and in copolymers containing a higher amount of even number methylene group moieties (butylene ones) with respect to the odd number units, like $–CH_2–$ glycol units present in BEPCE, (P($BCE_{85}BEPCE_{15}$) and P($BCE_{65}BEPCE_{35}$)).

Conversely, PLCs containing an odd number of $–CH_2–$ groups, are characterized by the formation of a prevalent nematic mesophase [Blumstein et al., 1982; Krigbaum et al., 1983]. In DSC analysis this 1D-ordered phase can be detected at temperatures above T_m and the corresponding isotropization heat is lower than that of smectic mesophase. This nematic phase could be present in P($BCE_{50}BEPCE_{50}$), which is characterized by the presence of equimolar amounts of glycol sub-unit with even number of methylene groups, the butylene ones, and an odd number of $–CH_2–$ moieties, present in BEPD.

As to the mechanical characterization data (Table 4.20), PBCE turned out to be the most rigid material, with the highest values of elastic modulus E and stress at break σ_b, together with the

lowest elongation at break ε_b. Copolymerization deeply affects the mechanical properties of the so-obtained materials. More in details, the introduction of BEPCE co-units is responsible for a considerable decrease of both E and σ_b, being the entity of this variation directly proportional to the comonomeric unit amount. This behaviour can be probably ascribed to the progressive reduction of the crystallinity degree, X_c, in the copolymers with respect to PBCE. For example, in case of P($BCE_{50}BEPCE_{50}$), which is the copolymer containing the highest amount of BEPCE co-units, σ_b is ten times lower, while E decreases by more than two orders of magnitude, and ε_b reaches a value up to 1290% (for PBCE it was ε_b = 19%).

In order to evaluate the effect of alkyl pendant groups length on the mechanical properties of the final materials, P($BCE_{85}BEPCE_{15}$) and P($BCE_{80}NCE_{20}$) copolymers have been compared. It was observed that P($BCE_{80}NCE_{20}$), even though less crystalline, shows an elastic modulus comparable to that of P($BCE_{85}BEPCE_{15}$), but lower elongation at break. This trend can be ascribed to the minor plasticizing effect of the NCE comonomeric units, due to the shorter alkyl pendant groups.

As to the effect of *cis/trans* isomerism of the cyclohexane ring, P($BCE_{65}BEPCE_{35}$) and P($BCE_{65}BEPCE_{35}$)-ct copolymers, characterized by a similar composition but different acid co-units, have been compared. These two materials have the same crystallinity degree, which explain the similar mechanical behaviour in terms of elongation at break. However, the samples show different values of both E and σ_b, being P($BCE_{65}BEPCE_{35}$)-ct characterized by lower elastic modulus and tensile stress at break. This result can be probably due to the reduced structural symmetry that hampers the interactions between polymeric chains, thus facilitating their sliding under mechanical stretch.

4.6.5 Gas permeability studies

Gas permeability tests to dry N_2, O_2, and CO_2 gases were performed on polymeric films, in order to check their barrier performance as potential candidates for flexible packaging applications.

For all the samples under investigation, the Gas Transmission Rate (GTR) values are collected in Table 4.20 and shown in Figure 4.49.

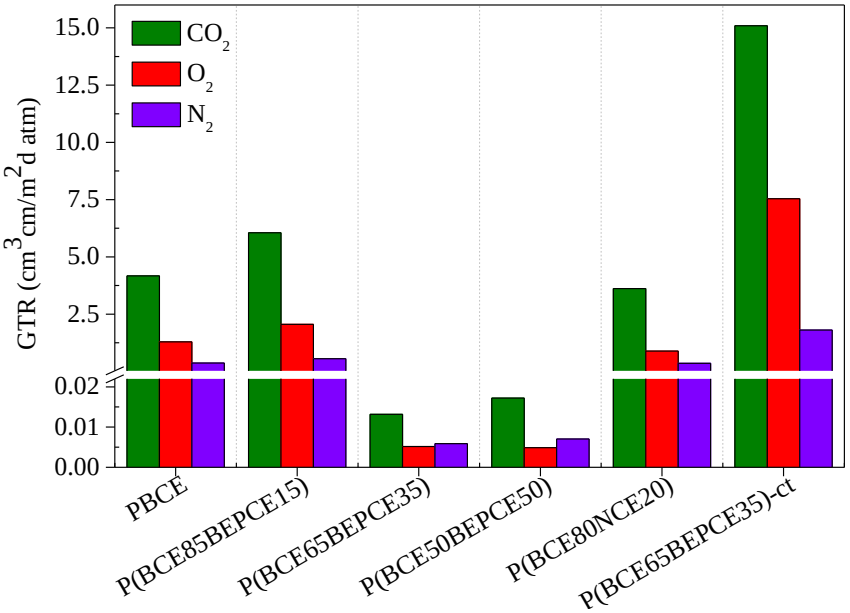

Figure 4.49. GTR through PBCE, P(BCE_xBEPCE_y), P($BCE_{80}NCE_{20}$), and P($BCE_{65}BEPCE_{35}$)-ct films of N_2, O_2, and CO_2 gases at 23 °C.

The results obtained show that copolymerization affects the barrier performances in a different way, according to the amount of BEP glycol co-units: the presence of up to 15 mol% of BEPCE comonomeric units, causes slight increase in gas permeability. Conversely, when the percentage of comonomer is of 35 and 50 mol%, a considerable improvement in the barrier performances is achieved: GTR values to N_2 are 50 times lowered and to O_2 and CO_2 even 250 times decreased. This result is of great interest considering that the P($BCE_{65}BEPCE_{35}$) sample is characterized by a considerably lower crystallinity degree than PBCE, and the P($BCE_{50}BEPCE_{50}$) copolymer is even amorphous. Crystallinity degree cannot be therefore responsible for these very low GTR values. In addition, considering that at 23°C, the temperature at which barrier tests were performed, P($BCE_{65}BEPCE_{35}$) and P($BCE_{50}BEPCE_{50}$) are in the rubbery state, the extraordinary low permeability cannot be ascribed to a low free volume. In this framework, a possible explanation can be the presence of a 2D-ordered structure, the already mentioned mesophase, which hampers the gas passage. The formation of this kind of 2D-organized phase is favoured by the simultaneous presence in the macromolecular chain of rigid units (i.e. aliphatic cyclohexane ring) together with flexible moieties (i.e. aliphatic glycolic unit). In addition, its presence seems to be confirmed by calorimetric and diffractometric data as well as by the mechanical response and the outstanding barrier properties.

In addition, to check the effect of side-chains length on the barrier properties of the copolymers, P($BCE_{85}BEPCE_{15}$) and P($BCE_{80}NCE_{20}$), characterized by similar composition but different alkyl pendant groups, have been compared. P($BCE_{80}NCE_{20}$) copolymer shows superior performance, in line with its higher macromolecular rigidity evidenced by calorimetric analysis. The explanation of this behaviour cannot be found in the crystallinity degree, being P($BCE_{80}NCE_{20}$) sample less crystalline than P($BCE_{85}BEPCE_{15}$) one. Instead, a possible reason could be the less effective arrangement present in P($BCE_{85}BEPCE_{15}$) copolymer, which contains longer and more sterically hindering ramifications. Conversely, the shorter ramifications inside the P($BCE_{80}NCE_{20}$) macromolecular chain favour a more effective chain packing which can more effectively limit gas flow.

The isomerism of the cyclohexane ring affects gas barrier properties too. More in details, the simultaneous presence of *cis* and *trans* isomers in P($BCE_{65}BEPCE_{35}$)-ct is responsible for a considerable increase of GRT values. It is well known that the *trans* isomer rings are more stable in the chair conformation, while the rings with *cis* isomerism tend to assume the boat conformation. Therefore, the mesogenic cyclohexane rings stacking, and thus the formation of 2D-ordered domains, is strongly limited by the presence of *cis* and *trans* cyclohexane rings. This less efficient packing leads to the presence of higher free volume (lower T_g), with a considerable increase in gas permeability for P($BCE_{65}BEPCE_{35}$)-ct sample.

Finally, in all cases under study, CO_2 is the gas that flows faster through the films despite its larger molecular diameter, probably due to the lower CO_2 solubility inside the highly hydrophobic polymeric matrix.

Lastly, both PBCE homopolymer and P($BCE_{50}BEPCE_{50}$) random copolymer, this latter the best performing sample among the materials investigated, were compared with some petrochemical-based polymeric packaging materials of common use and with some biopolymers (Figure 4.50). It is immediately clear that P($BCE_{50}BEPCE_{50}$) copolymer shows excellent barrier properties, with its lowest permeability values among the materials considered. Although this comparison is not exhaustive, it anyway highlights the potential of these new materials for applications as high barrier film packaging.

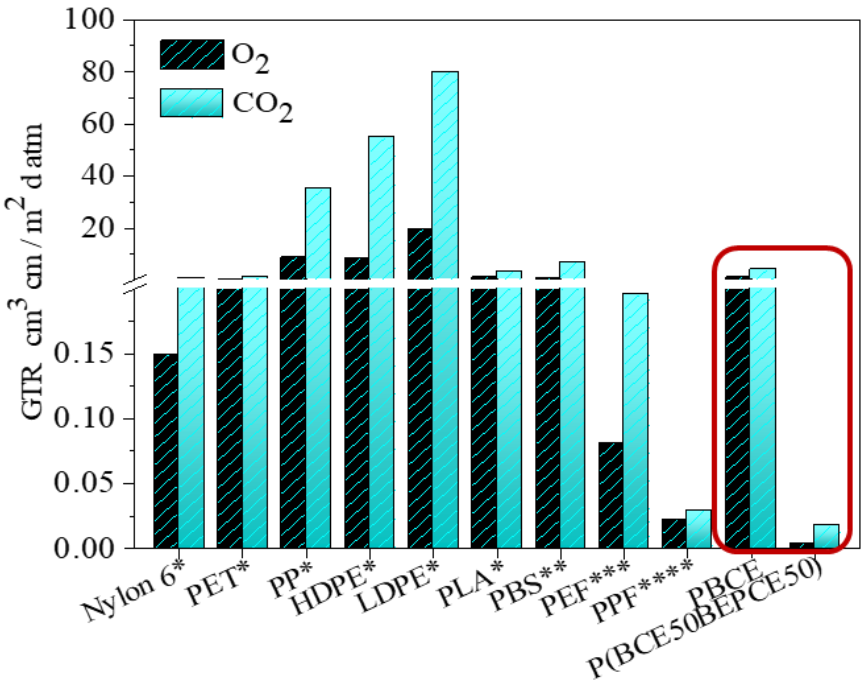

Figure 4.50. Gas transmission rate of O_2 and CO_2 gases for PBCE, P($BCE_{50}BEPCE_{50}$) compared to GTR of some traditional petrochemical-based polymeric packaging materials and GTR of some biopolymers [*Mensitieri et al., 2011; **Guidotti et al., 2017; ***Burgess et al., 2014; Burgess et al., 2015; ****Guidotti et al., 2018 (b)].

4.6.6 Conclusions

Novel poly(butylene 1,4-cyclohexanedicarboxylate)-based copolyesters containing side aliphatic pendant groups of different lengths along the main chain were successfully synthesized by melt polycondensation, a simple and solvent-free technique, which can also be scaled-up at industrial level. These new materials were designed in view of a possible application in the field of flexible packaging.

Trans-PBCE is an example of potentially bio-based aliphatic polyester, with very promising properties like resistance to heat, light, UV radiation and humidity, which make it a potential candidate as a material for food packaging, although the high rigidity of this homopolymer limited its development for this kind of applications. In this framework, copolymerization turned out to be a winning tool in order to improve PBCE final properties. More in details, by varying the copolymer composition, the length of aliphatic side chains, as well as the *cis/trans* isomerism of the aliphatic ring, it was possible to tune the thermal, structural, mechanical and barrier properties.

According to the results obtained, all the objectives of the research were achieved. The two copolymers richest in BEPCE co-units turned out to be particularly interesting, being characterized by exceptional barrier properties to O_2 and CO_2, better than those of poly(ethylene 2,5-furanoate) (PEF) and poly(propylene 2,5-furanoate), two bio-based materials with very high performances. Copolymers with a lower co-unit content or containing short side chains, although less performing, showed however a barrier behaviour similar to PLA and better than LDPE.

These outstanding barrier properties were hypothesized to be due to the presence of a 2D-ordered phase, referred to as mesophase, which was supposed to be predominant for P($BCE_{50}BEPCE_{50}$), as it can be processed as a freestanding flexible film despite being amorphous and showing a glass transition temperature below the room one.

Taking into account all the results obtained, the new materials under investigation can be considered an interesting alternative to traditional plastics for sustainable flexible food packaging.

4.7 Novel poly(butylene succinate)-based random copolymers containing aliphatic side chains for flexible food packaging applications.

Novel poly(butylene succinate)-based random copolymers with different composition and containing different glycolic sub-units were synthesized. The so-obtained materials are characterized by alkyl pendant groups of different length: neopentyl glycol (NG) in one case, 2-butyl-2-ethyl propanediol (BEPD) in the other. Aim of the work was the evaluation of the effect of the glycol sub-unit length on the material final properties.

The samples were characterized from the molecular, thermal, diffractometric and mechanical point of view. Copolymerization with short side methyl groups causes a more modest decrement of crystallinity degree: in this case, the co-units were included in the PBS crystal lattice. In addition, the introduction of side alkyl groups in PBS backbone did not affect the thermal stability, but significantly reduced the samples crystallinity degree, enhancing their flexibility. In order to evaluate the potential applications of these bio-based plastics in the field of food packaging, barrier performances to O_2, CO_2 and N_2 gases were also evaluated. Even though the barrier properties turned out to be worse than those of PBS, for most of the materials under investigation, they were still comparable or even better than those of LDPE (largely used as flexible food packaging material).

4.7.1 Synthesis and molecular characterization

PBS homopolymer, P(BSxBEPSy) and P($BS_{70}NS_{30}$) random copolymers have been synthetized following the procedure described in Paragraphs 3.2.1.2 and 3.2.1.3 respectively. At room temperature, all the synthesized polyesters appeared as semicrystalline light yellow solids. The samples are listed in Table 4.21, which also collects the molecular characterization data.

Table 4.21. Molecular characterization data of PBS and P(BS_xBEPS_y) and P($BS_{70}NS_{30}$) random copolymers.

Samples	BS (mol%) feed	BS (mol%) by ^{1}H-NMR	BS (wt%)	M_n (g/mol)	D
PBS	100	100	100	50000	2
P($BS_{90}BEPS_{10}$)	90	87	83	52000	1.9
P($BS_{80}BEPS_{20}$)	80	78	72	49000	2.1
P($BS_{70}BEPS_{30}$)	70	67	59	63000	2.2
P($BS_{70}NS_{30}$)	70	72	70	55000	2.1

GPC analysis was carried out to check the molecular weight and the polydispersity index D. As shown in Table 4.21, molecular weights are high and comparable, and the polydispersity index in all cases is around 2, confirming that no significant thermal degradation reactions occurred during polycondensation reaction.

^{1}H-NMR and ^{13}C-NMR analyses have been carried out to verify the chemical structure, calculate the actual composition and the degree of randomness b. In Figure 4.51 the ^{1}H-NMR spectrum of P($BS_{70}BEPS_{30}$) with the corresponding resonance assignments is shown. According to the spectrum, the following peaks can be noticed: as to the BS subunit, methylene protons, b (4H, t), of the butylene subunit located at δ 4.19 ppm, methylene protons, c (4H, m), of the butylene subunit located at δ 1.7 ppm and the singlet a (4H, s) of the acid subunit, situated at δ 2.63 ppm can be found. In addition, as to BEPS subunit, the presence of methylene protons, d (4H, t), located at δ 3.9 ppm, e (2H, m), located at δ 1.3 ppm, f (3H, t) located at δ 0.9 ppm, g and h (2H, m) partially overlapped and located at δ 1.25 ppm, i (2H, m) located at δ 1.2 ppm and j (3H, t) located at δ 0.8 ppm of the BEPD subunit can be observed, together with the singlet a (4H, s) of the acid subunit, situated at δ 2.63 ppm.

All the spectra are coherent with the awaited chemical structure, since no additional peaks are present. The copolymer composition was calculated from the relative areas of the resonance peak of the b protons of the butylene moiety, located at δ 4.19 ppm and of the peak related to d protons of the butyl-ethyl propylene sub-unit at δ 3.90 ppm (Figure 4.51). The actual composition is close to the feed one (Table 4.21) for all the materials under investigation, as a proof of a good control over the polymerization process.

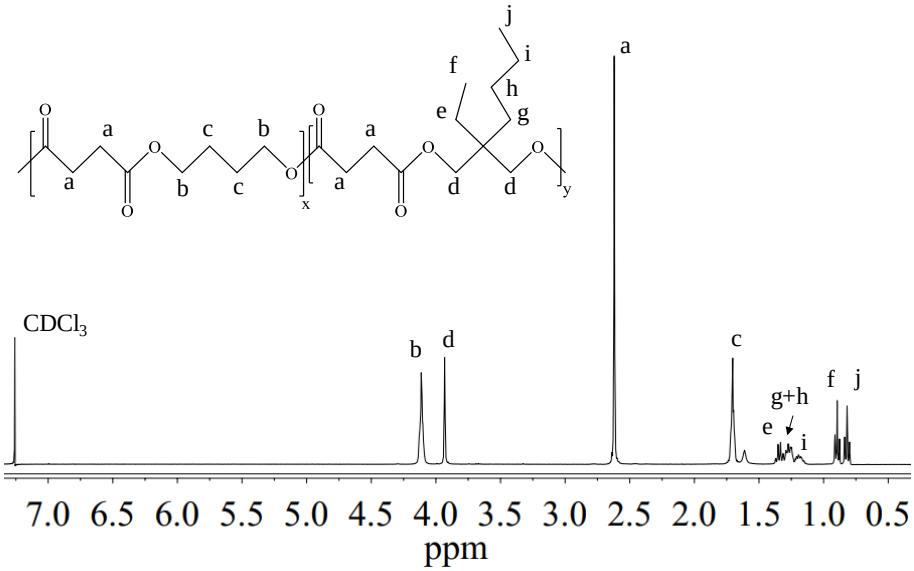

Figure 4.51. ^{1}H-NMR spectrum of P($BS_{70}BEPS_{30}$) with resonance assignments.

The degree of randomness b was calculated by means of ^{13}C-NMR spectroscopy. In Figure 4.52 the ^{13}C-NMR spectrum of P(BS$_{70}$BEPS$_{30}$) is shown, together with the peaks assignments (Figure 4.52A) and the magnification of the region in between δ 172.50 ppm and δ 171.80 ppm, where the signals of the ester groups carbons are located (Figure 4.52B).

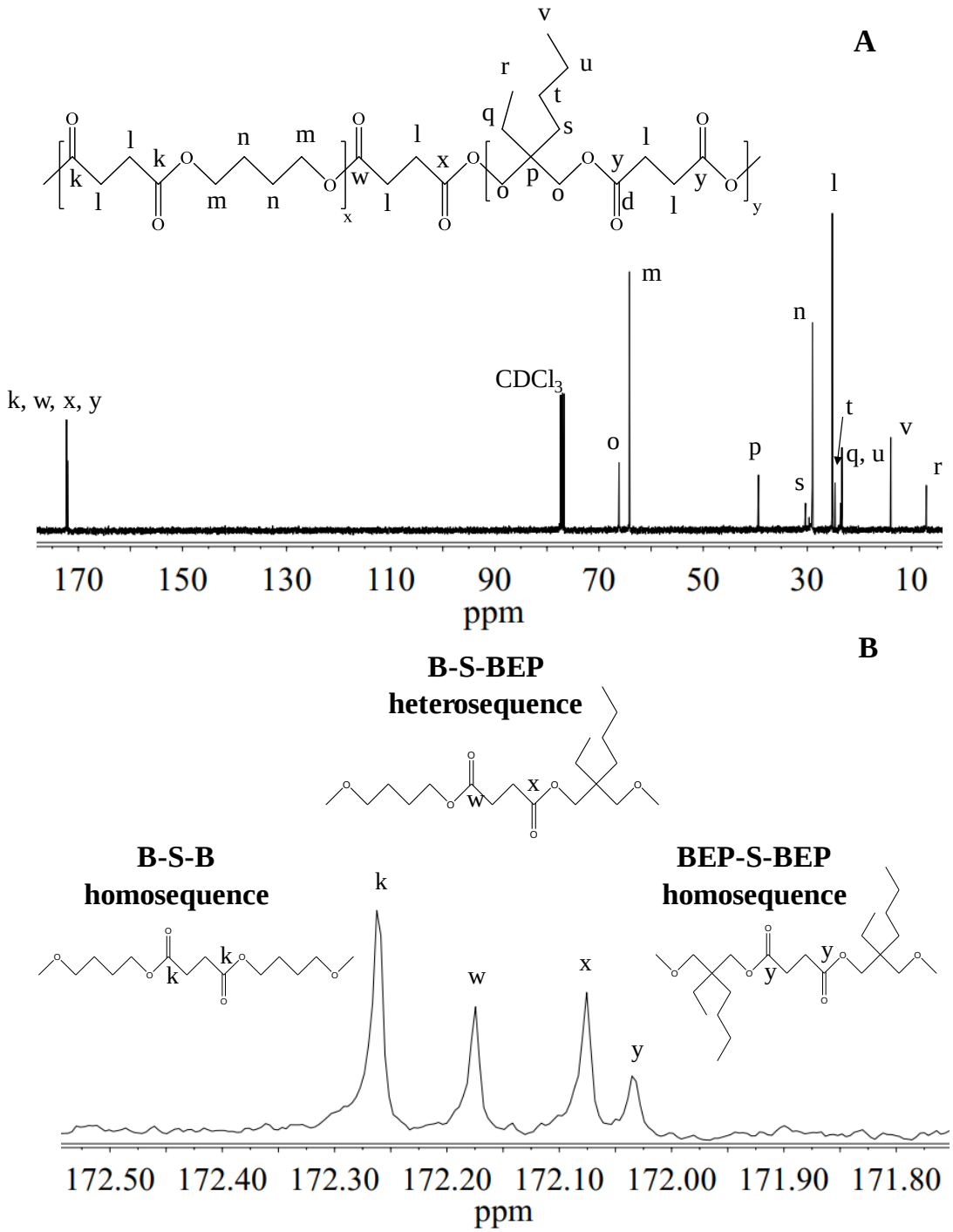

Figure 4.52. **A**) ^{13}C-NMR spectrum of P(BS$_{70}$BEPS$_{30}$) with resonance assignments; **B**) enlargement of ^{13}C-NMR spectrum in the region δ 172.50–171.80 ppm together with the schematic representation of B-S-B, B-S-BEP and BEP-S-BEP sequences.

In this region, together with the signals of the ester carbons at δ 172.26 and δ 172.03 ppm, related to B-S-B (k carbon) and BEP-S-BEP (y carbon) homosequences, respectively, two additional peaks in between are present. These signals are related to the B-S-BEP and BEP-S-B (w and x carbons) heterosequences, due to transesterification reactions.

The degree of randomness b was calculated from the intensity of the k, y, w and x peaks, according to Eqn. [28], where P_{X-Y} (P_{B-BEP}) and P_{Y-X} (P_{BEP-B}) are the probability of finding a B unit close to a BEP one and the probability of finding a BEP unit next to a B one, respectively. The two values can be obtained from Eqn. [29] and Eqn. [30], where I_{X-Y}, I_{Y-X}, I_{X-X} and I_{Y-Y} represent I_w, I_x, I_k, I_y, respectively (Figure 4.52B).

For all the copolymers, b was equal to 1, proving that through the experimental conditions adopted it was possible to obtain copolymers characterized by a random distribution of the comonomeric units.

4.7.2 Thermal and structural characterization

The thermal stability of the materials under investigation was checked through thermogravimetric analysis under nitrogen flow. In Table 4.22 the temperatures of peak onset (T_{onset}) and the temperatures corresponding to the maximum weight loss rate (T_{max}) are listed. In all cases, the weight loss is 100% and takes place in one-step. All copolymers under study show a behaviour similar to PBS parent homopolymer. All the samples under study are characterized by a very good thermal stability, as the weight loss starts above 380 °C. Copolymerization therefore does not affect PBS thermal stability, as T_{onset} and T_{max} are almost constant in the entire composition range studied.

As to calorimetric analysis, it is possible to exclude an influence of the molecular weight on the thermal transition, being the molecular weights of all the samples high and comparable to each other. The thermal data of the samples under investigation are listed in Table 4.22, while the relative calorimetric curves are shown in Figure 4.53.

As to the first calorimetric scan, all the samples are semicrystalline, being the corresponding DSC curves characterized by the presence of an endothermic baseline deviation around –30 °C, related to the glass to rubber transition, followed by an endothermic peak at higher temperature, due to the melting of the crystalline phase (Figure 4.53A).

Table 4.22. Thermal characterization data of PBS and $P(BS_xBEPS_y)$ and $P(BS_{70}NS_{30})$ random copolymers.

Samples	T_{onset} °C	T_{max} °C	I Scan				II Scan					
			T_g °C	Δ_{Cp} J/g*°C	T_m °C	ΔH_m J/g	T_g °C	Δ_{Cp} J/g*°C	T_{cc} °C	ΔH_{cc} J/g	T_m °C	ΔH_m J/g
PBS	385	407	-35	0.088	114	50	-35	0.192	-	-	114	51
$P(BS_{90}BEPS_{10})$	381	410	-33	0.155	99	38	-34	0.180	7	19	100	50
$P(BS_{80}BEPS_{20})$	382	416	-29	0.263	42 80	33	-31	0.444	31	34	81	34
$P(BS_{70}BEPS_{30})$	382	413	-28	0.354	43 60	22	-29	0.457	-	-	-	-
$P(BS_{70}NS_{30})$	386	415	-28	0.244	42 77	33	-29	0.456	27	30	79	30

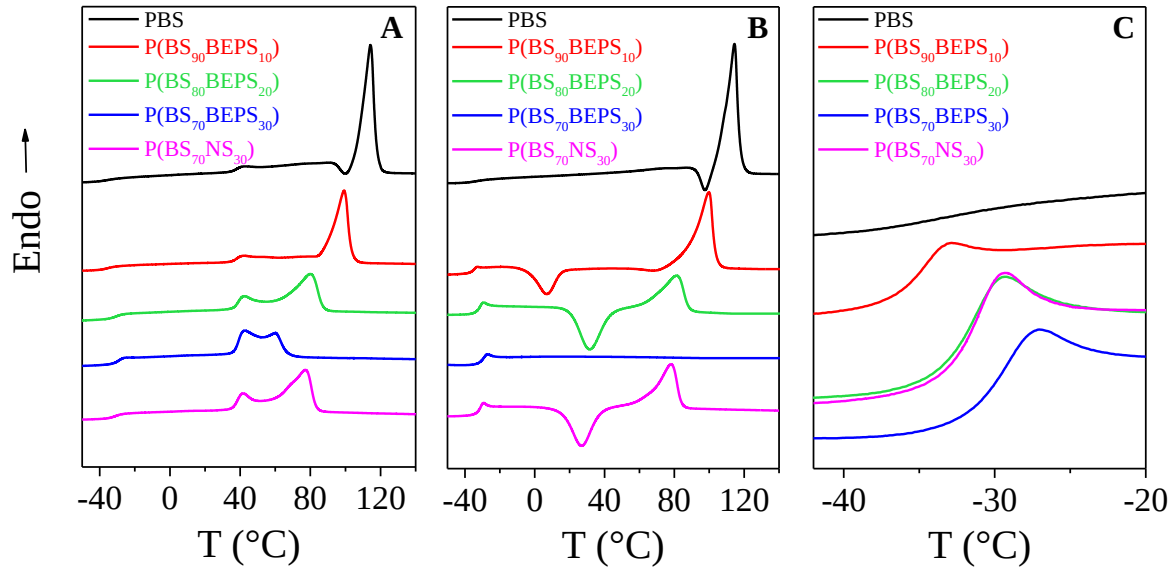

Figure 4.53. Calorimetric curves (20 °C/min) of PBS, $P(BS_mBEPS_n)$ and $P(BS_{70}BEPS_{30})$ copolymers: **A**) I scan; **B**) II scan after melt quenching; **C**) magnification in the T_g region of II scan.

Nevertheless, the curves show very different melting peaks, which progressively decrease in intensity (lower values of ΔH_m) and move towards lower temperatures as the comonomeric units amount increases, probably because of the formation of crystals with lower degree of perfection. Together with this phenomenon, an increase of the amorphous fraction can be noticed, as indicated by the increase of Δc_p values. Furthermore, in case of $P(BS_{80}BEPS_{20})$ and $P(BS_{70}BEPS_{30})$, i.e. the two copolymers containing the highest molar amount of BEPS comonomer, as well as $P(BS_{70}NS_{30})$, multiple melting peaks are present. This trend is typical

of melting/recrystallization processes of crystals with lower degree of perfection, whose presence is due to the hindering effect of the co-units during crystallization [Minakov et al., 2004; Kong et al., 2003; Soccio et al., 2009; Soccio et al., 2013].

It is well accepted that crystallinity acts like crosslinking, raising T_g values because of its restrictive effect on the motion of amorphous polymeric chains. Consequently, a partially crystalline material generally shows different glass transition behaviour than the same material but in a completely amorphous state. For this reason, to study the influence of chemical structure on the glass transition of random copolymers the phenomenon has to be examined in the total absence of crystallinity. In this view, all the samples were subjected to quenching from the melt. The DSC traces and the relative thermal characterization data of the so-treated samples are reported in Figure 4.53B and collected in Table 4.22, respectively.

PBS homopolymer shows practically the same calorimetric profile for both I and II scans: in fact, it cannot be quenched in the amorphous state under the experimental conditions adopted because of its high crystallization rate. Conversely, the DSC curves of all the copolymers deeply change after melt quenching in liquid nitrogen. First, the glass transition phenomenon becomes more evident, because of the higher amount of amorphous phase in the quenched samples. In addition, as the BEPS co-unit content is increased, a different crystallization capability is observed (Figure 4.53B). More in details, the samples containing up to 20 mol % of comonomeric BEPS units show DSC curves characterized by the glass to rubber transition step, followed by an exothermic peak together with an endothermic one at higher temperatures. This behaviour is typical of materials that have enough energy to crystallize in the temperature range between T_g and T_m and then undergo melting of the crystals formed during heating. Copolymer composition affects also the area under the exothermic (ΔH_{cc}) and the endothermic (ΔH_m) peaks. In case of P($BS_{90}BEPS_{10}$), for example, macromolecular chains cannot be locked in the disordered phase under the experimental conditions adopted, since the quantity of crystals melted is higher than the amount of crystals formed at T_{cc} ($\Delta H_{cc} < \Delta H_m$). For P($BS_{80}BEPS_{20}$) instead, the areas under the two peaks are equal ($\Delta H_{cc} = \Delta H_m$), thus indicating that the amount of BEPS co-units was high enough to hinder PBS crystallization capability. Quenching was even more successful in the copolymer containing the highest content of BEPS co-unit, P($BS_{70}BEPS_{30}$): in this case, only the glass to rubber transition step was detected in the II scan. The DSC curve of P($BS_{70}NS_{30}$) is very similar to the one of P($BS_{80}BEPS_{20}$), as they are both able to crystallize during the II heating scan, despite their different molar composition. This

result, which is in line with the diffractometric analysis, proves the higher hindering effect on PBS crystallization capability of the long pendants present in BEPS, with respect to NS short side-chains. The chemical structure of comonomeric unit influences the chain mobility too. As mentioned above for another copolymeric system investigated (see Paragraph 4.6), the presence of alkyl side-groups hinders the rotation around the C–C σ bond, because of their high steric hindrance, thus reducing the macromolecular mobility and causing an increase in T_g values. Nevertheless, if these pendant groups are long enough, they can act as internal plasticizers, leading to a decrement of the T_g values. This effect is more intense with longer side alkyl groups. In the copolymers under investigation, both these opposite effects are supposed to influence chain mobility, as well as T_g position.

In order to investigate the effect of the different co-units (BEPS and NS) on the glass transition temperature, in Figure 4.53C a magnification of the temperature range in between the glass to rubber transition is shown. T_g step, which is quite low for PBS, increases in height in the copolymers, as a consequence of the higher amount of amorphous phase. More in details, in case of copolymers containing the higher amount of BEPS co-units, which were successfully quenched in the amorphous state, any restriction related to the presence of crystalline net-points can be excluded, thus indicating that the T_g position is due only to macromolecular chain mobility. It is also interesting how, for these samples, the glass to rubber endothermic transition progressively moves towards higher temperatures, despite the complete absence of crystalline regions (Table 4.22). T_g of P($BS_{70}BEPS_{30}$) is 10 °C higher than the one of completely amorphous PBS, previously determined [Genovese et al., 2016]. This behaviour suggests that, for the class of P(BS_xBEPS_y) copolymers, the effect due to steric hindrance of the alkyl side chains prevails on their plasticizing one. Interestingly, the calorimetric trace of P($BS_{70}NS_{30}$), which contains 30 wt % of NS co-units, is practically overlapped with that of P($BS_{80}BEPS_{20}$), which contains 28 wt % of BEPS co-units (Table 4.21), despite the lower length of the neopentyl side chains.

In order to investigate the type and the amount of crystalline phase of the random copolymers under investigation, WAXS analysis was carried out. The X-ray diffraction patterns of all the samples are reported in Figure 4.54.

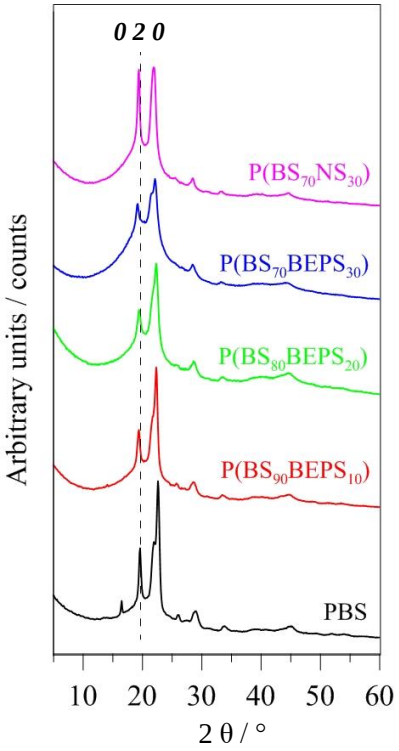

Figure 4.54. X-Ray diffraction profiles of the copolymeric system under study. The ***0 2 0*** reflection of PBS is indicated.

According to the patterns obtained, all the materials present the peaks characteristic of the α-PBS crystal phase [Ichikawa et al., 2000]. In addition, the higher the BEPS co-units amount, the more pronounced the area under the bell shaped background line. This behaviour is due to the relative decrease of crystalline portion and consequent relative growth of the amorphous one in the copolymers, according to the decrement of crystallinity degree values (Table 4.23). Moreover, along the series, the *0 2 0* reflection shifts to smaller 2θ angles, thus indicating bigger interlayer distances. The parameters of the unit cell, as well as width of the 0 2 0 reflection and the crystallinity index have been calculated and reported in Table 4.23.

An increase of the unit cell volume can be observed for $P(BS_xBEPS_y)$ copolymers. Anyway, this increase, although detectable, is too low to be compatible with the hypothesis of inclusion of BEPS segments inside the α-PBS crystalline lattice. More probably, the exclusion of the co-monomers at the surface of the crystal may cause changes in the crystal parameters. As already reported from previous studies [Gigli et al., 2012 (b); Genovese et al., 2016], the higher lattice volume in $P(BS_xBEPS_y)$ copolymers has to be related to the disorder induced by the presence of comonomeric units, also confirmed by the reflections broadening of *0 2 0* peak (Table 4.23).

Table 4.23. Crystallinity index (X_c), width of the *0 2 0* peak (FWHM) and unit cell parameters.

Samples	X_c %	FWHM °	*a* Å	*b* Å	*c* Å	β °	V $Å^3$
α-PBS*			5.23	9.12	10.90	123.9	431.5
PBS	46	0.43	5.24	9.09	10.85	123.7	429.9
P($BS_{90}BEPS_{10}$)	38	0.54	5.29	9.19	10.72	123.5	434.6
P($BS_{80}BEPS_{20}$)	31	0.66	5.27	9.22	10.70	123.3	437.7
P($BS_{70}BEPS_{30}$)	18	0.55	5.29	9.39	10.70	122.9	446.1
P($BS_{70}NS_{30}$)	31	0.43	5.31	9.26	10.87	122.2	451.3

According to the results obtained, the complete exclusion of the BEPS co-units from the PBS crystal lattice can be hypothesized.

As to the crystallization capability of the NS-containing copolymer, it is deeply different from that of the corresponding BEPS copolymer (P($BS_{70}BEPS_{30}$)). As a matter of fact, P($BS_{70}NS_{30}$) sample is more crystalline than P($BS_{70}BEPS_{30}$) one, being the X_c values equal to 31% and 18%, respectively (Table 4.23). In addition, as it can be seen from FWHM values, the peak broadening, which is an index of the overall order degree, is the same for PBS and P($BS_{70}NS_{30}$), whereas for P($BS_{70}BEPS_{30}$) is about 30% higher. Moreover, the cell volume is significantly higher (+20 $Å^3$) than that of PBS, even though it is not so big as the one calculated for P($BS_{70}BEPS_{30}$). Such increment empirically corresponds to one atom different from hydrogen one inside the crystalline lattice [Clegg, 2015]. This result leads to hypothesize the inclusion of NS unit in the PBS cell: in the presence of methyl substituents, as the case of NS moieties, the unit cell can expand and host them, increasing its final volume. The increase of only *a* and *b* parameters, *c* remaining constant, is coherent with the structure of α-PBS crystalline phase, in which the macromolecular chain is oriented in the *c*-axis direction. Consequently, NS-units insertion does not cause a chain extension, but rather a chain thickening.

To conclude, although in both copolymeric systems a similar crystalline lattice distortion is observed, its origin is different: for P(BS_xBEPS_y) copolymers the disorder may be due to longer substituents, whereas in P($BS_{70}NS_{30}$) it can be caused by the possible inclusion of the ramified units.

4.7.3 Mechanical characterization

Tensile measurements have been performed on both PBS and copolymeric films to test the suitability of these materials for the intended use. The stress–strain curves are shown in Figure 4.55, while the values of elastic modulus E, stress at break σ_b and elongation at break ε_b are collected in Table 4.24.

PBS homopolymer turned out to be the most rigid material among the investigated ones, being characterized by the highest elastic modulus E and stress at break σ_b, together with the lowest elongation at break ε_b. Thanks to the copolymerization with BEPS co-units, both E and σ_b decrease. The entity of variation is function of copolymer composition, being the effect more pronounced the higher the BEPS co-unit amount (Figure 4.55B). This result can be ascribed to the progressive reduction of the crystallinity degree in the copolymers with respect to the homopolymer. More in details, for P($BS_{70}BEPS_{30}$), which contains the highest molar amount of BEPS co-units, E is reduced by almost one order of magnitude, while σ_b is halved. In addition, the values of ε_b rise from 5% for PBS up to 1050% for P($BS_{70}BEPS_{30}$) (Figure 4.55A). Nevertheless, as already seen for thermal properties, the different pendant group length affects also the mechanical behaviour of the random copolymers under investigation. For example, P($BS_{80}BEPS_{20}$) shows lower E and σ_b values, together with a higher ε_b than P($BS_{70}NS_{30}$), despite their similar X_c values. Therefore, this trend must be ascribed to the higher chain flexibility and plasticizing effect given by the longer pendant groups inside the BEPS co-units.

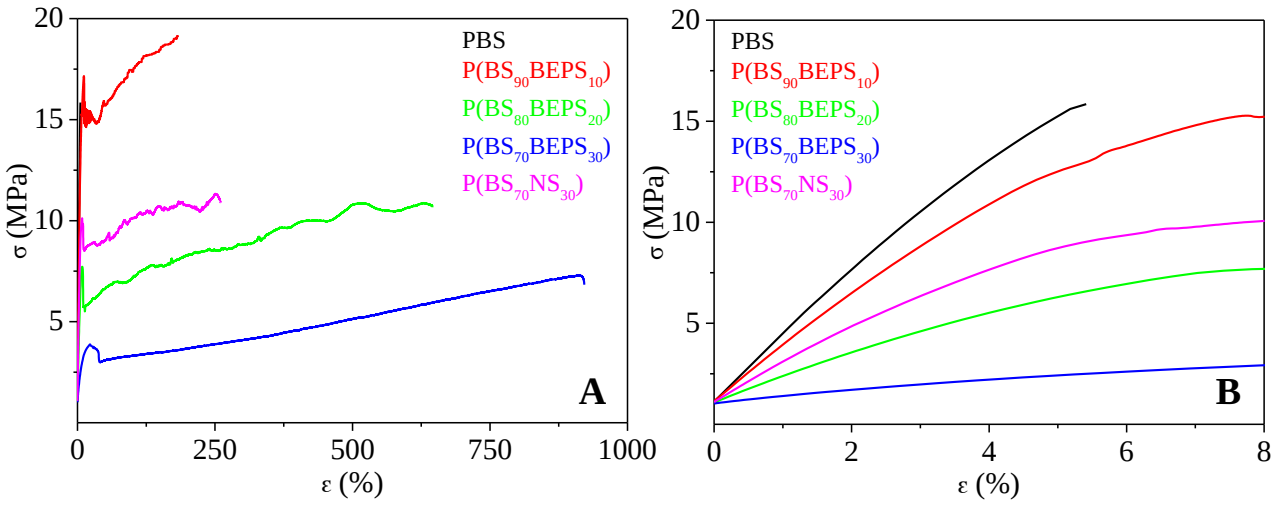

Figure 4.55. **A**) Stress–strain curves of PBS, P(BS_xBEPS_y) and P($BS_{70}NS_{30}$) random copolymers; **B**) magnification of the low σ-ε region.

Table 4.24. Mechanical characterization data of PBS, P(BS_xBEPS_y) and P($BS_{70}NS_{30}$) random copolymers.

Samples	E (MPa)	σ_b (MPa)	ε_b (%)
PBS	301±25	16±2	5±1
P($BS_{90}BEPS_{10}$)	282±17	17±2	166±26
P($BS_{80}BEPS_{20}$)	139±7	11±1	675±27
P($BS_{70}BEPS_{30}$)	47±7	7±1	1050±99
P($BS_{70}NS_{30}$)	219±12	18±1.0	340±34

4.7.4 Gas permeability studies

Gas barrier ability of PBS and its random copolymers was checked at 23 °C using dry N_2, O_2 and CO_2 gases, to investigate the performance of the materials for potential applications in food packaging.

The Gas Transmission Rate (GTR) values, which are an index of permeability through the polymeric matrix, are listed in Table 4.25 and shown in Figure 4.56.

Table 4.25. Gas transmission rate (GTR) data for PBS, P(BS_xBEPS_y) and P($BS_{70}NS_{30}$) random copolymers, at 23 °C, using N_2, O_2 and CO_2 as dry gas test.

Sample	Film Thickness µm	N_2-GTR cm^3 cm / m^2 d atm	O_2-GTR cm^3 cm / m^2 d atm	CO_2-GTR cm^3 cm / m^2 d atm
PBS	112 ± 11	0.3473	1.1327	6.8573
P($BS_{90}BEPS_{10}$)	102 ± 14	1.0286	3.6146	18.3380
P($BS_{80}BEPS_{20}$)	109 ± 15	1.8600	5.4080	26.6400
P($BS_{70}BEPS_{30}$)	137 ± 8	3.0444	8.9153	29.5840
P($BS_{70}NS_{30}$)	120 ± 10	0.7948	3.0351	13.6101
LDPE*	n.a.	n.a.	4.4079	18.4210

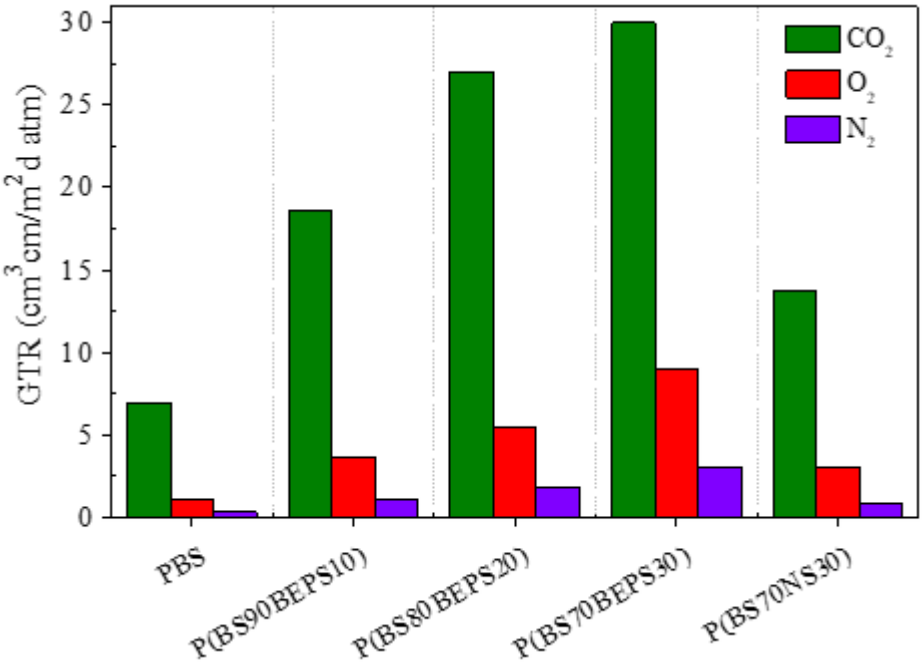

Figure 4.56. GTR of N_2, O_2 and CO_2 through PBS, P(BS_xBEPS_y) and P($BS_{70}NS_{30}$) films (T=23 °C).

As it can be seen from Figure 4.56, in all cases N_2-GTR shows the lowest values, while the CO_2-GTR the highest ones, despite CO_2 molecule diameter (3.4 Å) is bigger than N_2 molecule one (2.0 Å). Moreover, the permeability of all gases through the copolymeric films is higher than that of PBS film, highlighting that the presence of aliphatic side-chains negatively affects the final barrier properties. This trend can be ascribed to the lower crystallinity degree of the copolymers. In fact, it is well known that gas molecules diffuse and permeate more easily through amorphous regions, which are characterized by higher chain mobility, mainly if, as in this case, are in the rubbery state (Table 4.22). [Jamshidian et al., 2012].

Also the length of alkyl pendant groups affects the barrier performances: by comparing P($BS_{70}NS_{30}$) and P($BS_{70}BEPS_{30}$), which are characterized by a similar molar amount of comonomeric units, it is possible to notice that the former shows better barrier performances, which can be related to its higher crystallinity. It is also interesting to note that P($BS_{70}NS_{30}$) shows barrier performances even better than those of P($BS_{80}BEPS_{20}$), despite the same crystallinity degree value (31%). A possible explanation can be found in the higher stiffness imparted by the shorter aliphatic pendant chains. In addition, NS co-units are able to enter in crystalline lattice of PBS, thus making the crystal phase more packed. As a result, P($BS_{70}NS_{30}$) copolymer shows the best barrier performances with respect to N_2 and CO_2 among all the copolymers under study and O_2-GTR comparable to that of P($BS_{90}BEPS_{10}$).

The GTR values to O_2 and CO_2 of Low Density Polyethylene (LDPE), which dominates the flexible food packaging market and is characterized by a high degree of short-chain branching and long-chain branching, are reported in Table 4.25 for sake of comparison. Both PBS and P($BS_{70}NS_{30}$) copolymer display superior barrier properties than LDPE to both gases, whereas P($BS_{90}BEPS_{10}$) performances are comparable. By increasing the BEPS-units amount, the permeability values are slightly worse, proving that the chemical structure influences the final barrier behaviour.

4.7.5 Conclusions

Novel PBS-based random copolymers containing along the macromolecular chain different amounts of glycol sub-units with pendant alkyl groups of different length were successfully synthesized and investigated for applications in flexible food packaging. The synthetic strategy adopted, a 2-step melt polycondensation, is a simple and solvent-free technique, which can be easily scaled-up at industrial level. From the results obtained it is possible to say that copolymerization turned out to be a winning tool in order to modulate the final properties of PBS homopolymer, which is already used for food packaging applications, even though its high crystallinity and rigidity significantly limit its applications, in particular in the field of flexible food packaging.

As to thermal properties, the presence of different comonomeric units did not alter the thermal stability, while it deeply lowered the crystallizing ability of PBS homopolymer. This effect was less marked in case of comonomeric units characterized by the presence of short methyl side groups, which also turned out to be included in the PBS crystal lattice.

On the other hand, the long alkyl pendant groups deeply affect the mechanical properties, reducing the elastic modulus E and increasing elongation at break ε_b.

In order to check the potentiality of the so-obtained copolymers to be used for eco-friendly flexible food packaging applications, gas permeability tests to O_2, CO_2 and N_2 were performed. The results obtained showed that barrier properties can be nicely tailored, acting both on the pendant group length and on copolymer composition, in relation to the intended use. More in details, barrier performances decrease with the increase of the BEPS co-unit amount, because of a reduction of the crystallinity degree. This detriment was more consistent in case of CO_2 gas test, more modest for N_2 one. In addition, the barrier performances of some copolymers are

comparable or even superior than those of LDPE, which is widely employed in flexible food packaging.

Taking into account all the results obtained, the new materials under investigation can be considered a valid alternative to traditional plastics currently used in food packaging.

4.8 Novel PBS-based random copolyesters containing PEG-like sub-units for controlled drug release and soft tissue engineering applications

Random copolymers of poly(butylene succinate) PBS, (poly(butylene/triethylene succinate) (P(BSxTESy)), characterized by the presence of ether-oxygen atoms along the main chain, were synthesized by two-step melt polycondensation, starting from succinic acid, 1,4-butanediol and triethylene glycol. The copolymers were characterized from the molecular, thermal, structural and mechanical point of view.

Hydrolytic degradation studies and both indirect and direct biocompatibility tests were carried out to investigate the degradation profile and evaluate their potential use in soft tissue engineering.

Dexamethasone (DXM)-encapsulated nanoparticles were also prepared by oil-in-water miniemulsion and the release profile of Dexamethasone from nanoparticles was investigated.

The results obtained confirmed that solid-state properties, as well as biodegradation rate and Dexamethasone release profile, can be nicely tailored simply by varying copolymer composition. Moreover, the introduction of TES subunit does not negatively affect PBS biocompatibility.

4.8.1 Synthesis, molecular and surface characterization

PBS homopolymer and P(BSxTESy) random copolymers have been synthetized following the procedure described in Paragraphs 3.2.1.2 and 3.2.1.3 respectively. The samples are listed in Table 4.26, which also collects the data regarding molecular and surface characterization.

All the polyesters under investigation are characterized by relatively high molecular weights, indicating that appropriate synthesis conditions and a good polymerization control were achieved. ^{1}H-NMR analysis has been employed to verify the chemical structure, and in the case of copolymers, to determine the real composition [Soccio et al., 2012 (a)]. In all cases, the spectra are consistent with the awaited structure and the composition close to the feed one.

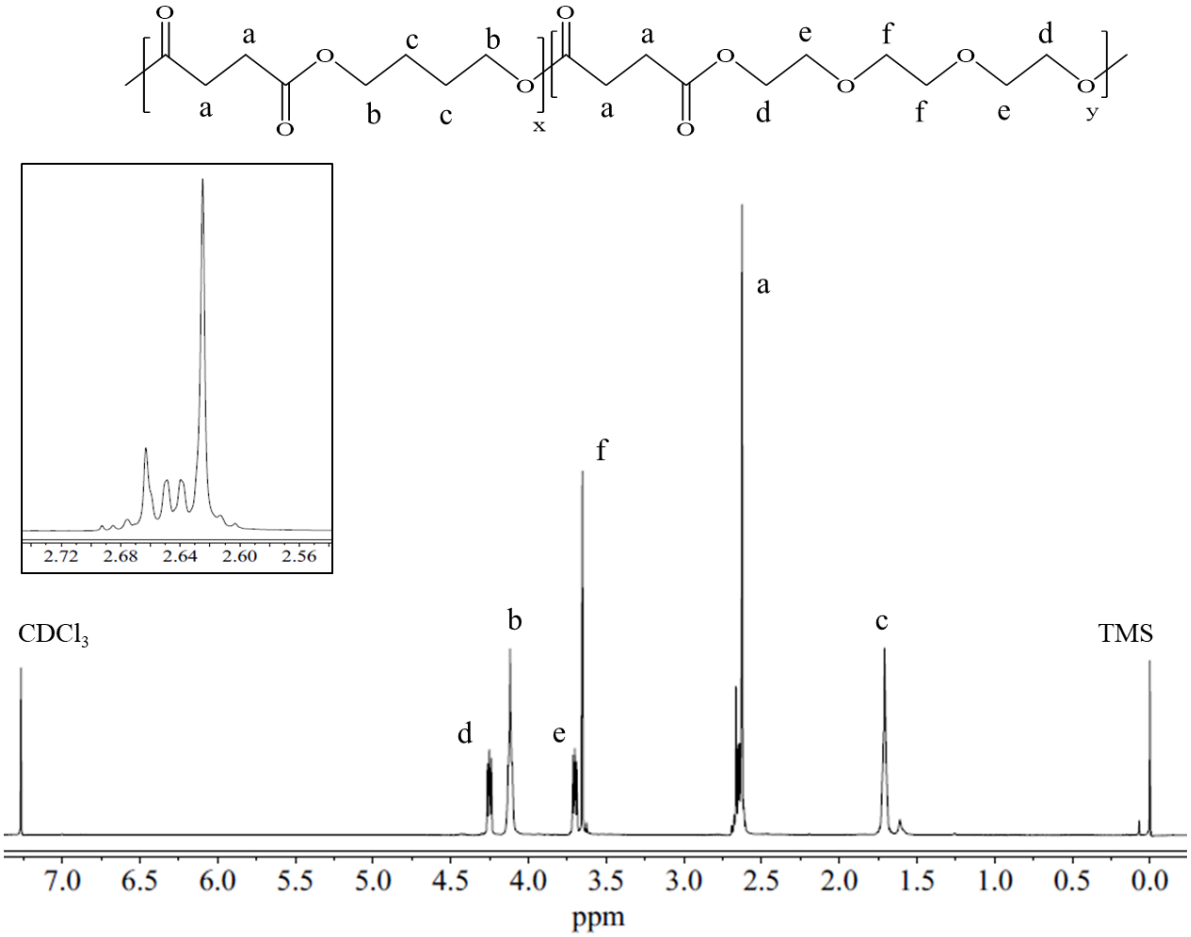

Figure **4.57**. ^{1}H-NMR spectra of P(BS70TES30) with resonance assignments.

As an example, ^{1}H-NMR spectrum of P(BS70TES30) copolymer is reported in Figure 4.57. Both the BS unit signals and TES unit ones are evident. The signals of b and c protons of methylene groups of butanediol subunit are located at δ 4.16 and δ 1.72 ppm, respectively. The resonance peaks d, e and f due to protons of the triethylene glycol moiety are detected at δ 4.24, 3.70 and 3.61 ppm, respectively, while a protons at δ 2.62 and δ 2.64 ppm corresponds to the succinic acid segments. The catalyst employed (titanium tetrabutoxide ($Ti(OBu)_4$)), as well as the high temperatures involved in the synthesis favour a random distribution of the comonomeric units [Guidotti et al., 2017; Guidotti et al., 2018 (a); Allen et al., 1989].

After molecular characterization, thin films were obtained by compression moulding. Before further characterization, they were let at room temperature for at least three weeks in order to uniform their thermal history providing them the same treatment.

Table 4.26. Molecular and surface characterization data of PBS and P(BSxTESy) copolymers.

Polymer	M_n (g/mol)	D	BS (mol%)	TES (mol%)	WCA (°)
PBS	48300	2.7	100	-	89 ± 2
P(BS95TES5)	44800	2.9	96	4	86 ± 1
P(BS80TES20)	42300	2.9	83	17	83 ± 1
P(BS70TES30)	49300	3.1	70	30	79 ± 1
P(BS60TES40)	40900	3.0	60	40	75 ± 1

As to wettability measurements, PBS turned out to be the most hydrophobic material (WCA = 89°), while P(BS60TES40) the most hydrophilic (WCA = 75°). The reduction of the WCA values by copolymerization (Table 4.26 and Figure 4.58) indicates that the introduction of PEG-like segments along the PBS chain determines an increase in the surface hydrophilicity. WCA decrement, directly proportional to the TES moiety amount, can be explained as due to the presence of highly electronegative ether-oxygen atoms in the TES co-units.

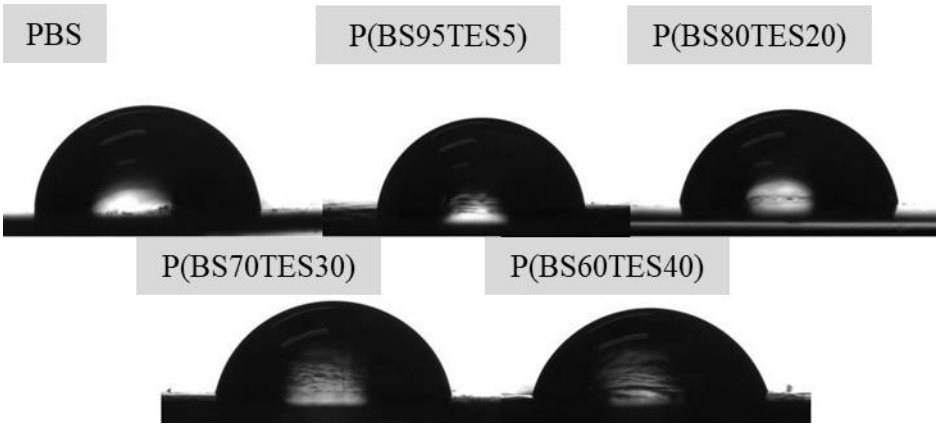

Figure 4.58. Water contact angle images of PBS and P(BSxTESy) copolymers.

4.8.2 Thermal and structural characterization

The synthesized polyesters have been subjected to thermogravimetric analysis, under pure nitrogen flow. The temperatures corresponding to initial decomposition (T_{id}) and to the maximum weight loss rate (T_{max}) were determined and collected in Table 4.27.

The thermal degradation is characterized by one-step weight loss, which starts above 380°C in all cases, evidencing a very good thermal stability for this family of materials. Thermal stability

is slightly affected by copolymerization, being T_{id} of copolymers up to 10°C lower. On the contrary, T_{max} remains almost constant in the whole composition range investigated.

The calorimetric curves obtained by DSC measurements and the corresponding thermal transitions data are reported in Fig. 4.59 and Table 4.27, respectively. In the first scan, glass transition temperature T_g is almost constant for all the materials, probably because of the very similar values of T_g of the two parent homopolymers (Fig. 4.59A) [Soccio et al., 2012 (a)]. Moreover, from the ΔH_m values, which are related to crystallinity degree, it is not possible to determine the effect of copolymerization on T_g.

As to the melting phenomenon, all the polymers under investigation are characterized by the same phase behaviour. In particular, they are semicrystalline, being the corresponding calorimetric traces characterized by a melting endotherm, whose intensity, location and width depend on copolymer composition. As expected, the melting temperature and the associated heat values both decrease, and the peaks become wider as the amount of TES sub-units increased, probably because of the formation of a crystalline phase with a lower degree of perfection (see Table 4.27). In addition, P(BS70TES30) and P(BS60TES40) show multiple endothermic peaks, related to melting-crystallization-melting processes typical of polyesters.

Table 4.27. Thermogravimetric and calorimetric characterization data of PBS and P(BSxTESy) copolymers.

			I scan				II scan						
Polymers	**T_{id}**	**T_{max}**	**T_g**	**ΔC_p**	**T_m**	**ΔH_m**	**T_g**	**ΔC_p**	**T_{cc}**	**ΔH_{cc}**	**T_m**	**ΔH_m**	**T_c**
	°C	**°C**	**°C**	**J/g°**	**°C**	**J/g**	**°C**	**J/g°**	**°C**	**J/g**	**°C**	**J/g**	**°C**
PBS	390	416	-32	0.077	115	62	-32	0.077	-	-	115	63	79
P(BS95TES5)	381	414	-34	0.066	111	60	-33	0.052	-	-	111	57	75
P(BS80TES20)	381	415	-35	0.132	96	43	-35	0.159	-	-	97	46	53
P(BS70TES30)	385	417	-34	0.313	78	34	-35	0.652	23	-33	78	32	-
P(BS60TES40)	385	419	-34	0.505	63	24	-33	0.665	-	-	-	-	-

As the glass transition temperature of a semicrystalline material is different from that of the same material but in a complete amorphous state, all the samples were rapidly cooled from the molten state, in order to check the effect of copolymerization on T_g values. After melt quenching (Fig. 4.59B), the calorimetric traces of PBS and the copolymers containing lower amounts of TES co-units (up to 20 mol%) are very similar to those of the first scan, evidencing the high crystallization rate of these samples, which cannot be quenched in the amorphous state.

Conversely, in the case of P(BS70TES30) and P(BS60TES40) copolymers, the glass transition phenomenon become more evident as a consequence of an increased amorphous phase amount. In addition, P(BS70TES30) curve presents an exothermic peak at 23°C, followed by an endothermic one at 78°C. Being the areas under the two peaks equal ($\Delta H_{cc} = \Delta H_m$), it is possible to say that the copolymer had been quenched into the amorphous phase, because of the presence of TES co-units that hinder the crystallization capability. This effect is even more evident in P(BS60TES40) copolymer, whose II scan DSC curve presents only the endothermic baseline deviation related to glass-to-rubber transition phenomenon.

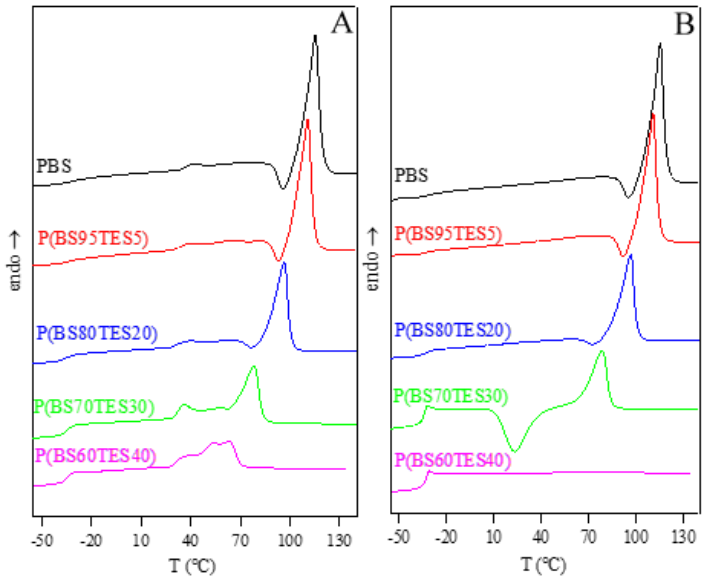

Figure 4.59. Calorimetric curves of PBS and P(BSxTESy) copolymers. **A**) 1st scan; **B**) 2nd scan after melt quenching.

To better understand the nature of the crystalline phase of the samples under investigation, WAXS analysis was performed (Figure 4.60). The profiles obtained are typical of semicrystalline materials, with well-defined peaks, overlapped to a bell-shape baseline characteristic of amorphous regions. All the copolymers are less crystalline than PBS, showing lower crystallinity degrees X_c, according to calorimetric data (Table 4.28).

All the samples show only the diffraction pattern of the α-PBS crystalline phase [Ichikawa et al., 2001].

With the increase of the TES co-units amount, peak *0 2 0* does not change its position, while peaks *0 2 1* and *1 1 0* shift towards lower angles and bigger distances. In addition, peak width

slightly increases: consequently, the *0 2 1* peak shoulder is no more detectable in P(BS60TES40) (Figure 4.60B).

Table 4.28. Crystallinity degree (X_c) and cell parameters calculated from WAXS data compared to crystallinity degree calculated from DSC (X_c^{DSC}).

Polymer	X_c (%)	*a* (Å)	*b* (Å)	*c* (Å)	β(°)	V (Å^3)	X_c^{DSC} (%)
PBS	43	5.21	9.10	10.79	123.0	428.2	56
P(BS95TES5)	40	5.21	9.12	10.82	122.9	431.6	54
P(BS80TES20)	36	5.21	9.17	10.77	122.2	433.5	39
P(BS70TES30)	31	5.21	9.17	10.78	122.4	435.2	31
P(BS60TES40)	25	5.20	9.19	10.77	122.2	435.3	22

This behaviour can be due to a higher disorder, caused by the longer TES co-units, which are not included in the crystal domains of PBS. Cell parameters and volume values, which are reported in Table 4.28, show an almost negligible increase in the overall cell volume, a confirmation of the hypothesis that TES segments are excluded from the crystalline lattice.

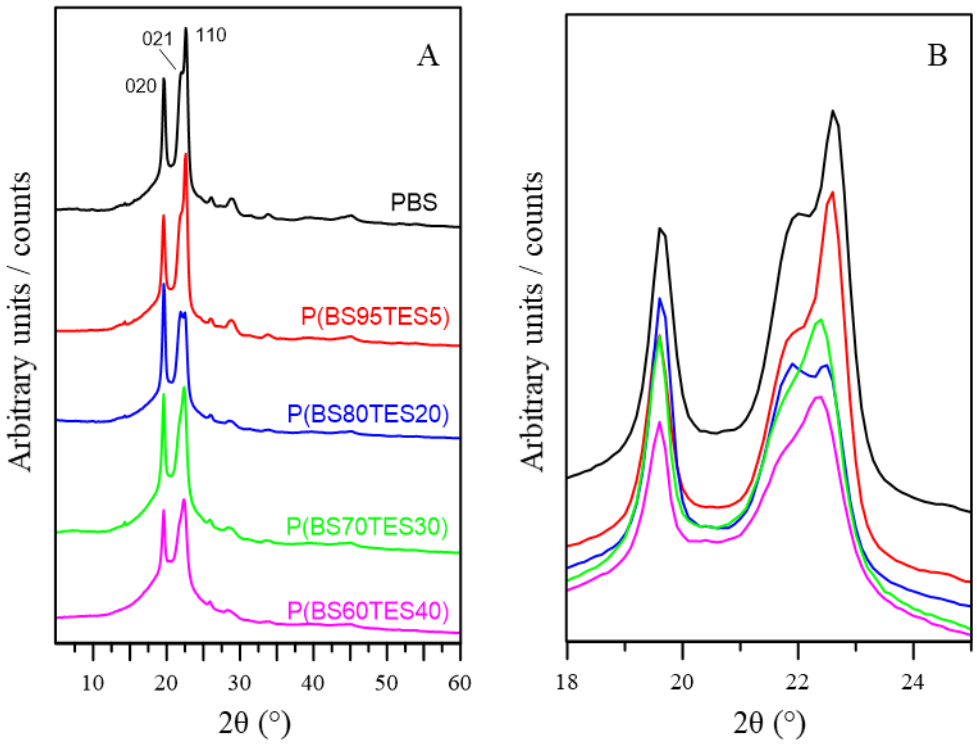

Figure 4.60. **A**) WAXS profiles of PBS and P(BSxTESy) copolymers. For PBS, the main reflections are indicated. **B**) zoom of the 2θ region between 18 and 25°.

In order to confirm that in the copolymers the crystallization capability decreases as the content of TES co-units is increased, non-isothermal experiments were carried out, subjecting the samples to a controlled cooling from the melt (5°C/min). The results are collected in Table 4.27 while the DSC curves are reported in Figure 4.61: T_c values change with the chemical composition, decreasing as the amount of TES co-units increases. The results obtained indicate that such co-units act as an obstacle towards PBS chain folding. In addition, in the case of the two copolymers containing the highest amount of TES units, P(BS70TES30) and P(BS60TES40), the crystallization process is completely suppressed.

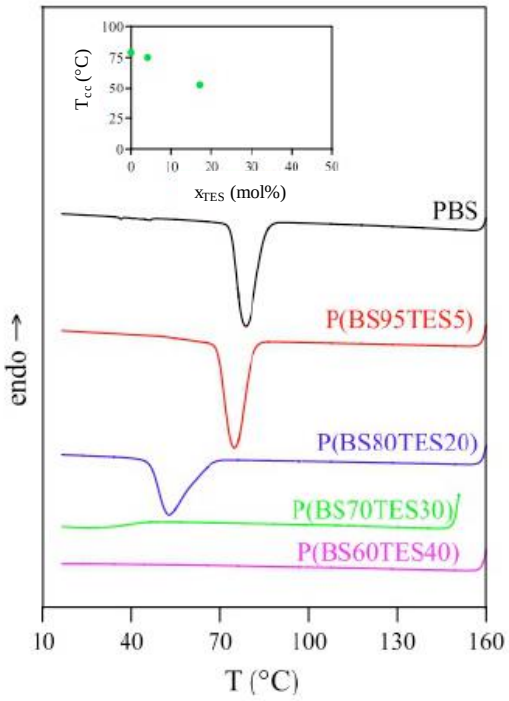

Figure 4.61. Crystallization curves of PBS and P(BSxTESy) copolymers.

4.8.3 Mechanical characterization

The mechanical properties of PBS and P(BSxTEsy) random copolymers were investigated subjecting the samples to stress-strain measurements. Table 4.29 collects the values of elastic modulus (E), stress and deformation at break (σ_b and ε_b, respectively) for all the samples under study.

From the data collected is clear that the presence of the TES co-units affects the mechanical behaviour of PBS homopolymer, which is characterized by the highest elastic modulus (E = 330 MPa) and stress at break (σ_b = 30 MPa), and the lowest elongation at break (ε_b = 23%). The

trend observed is probably due to the lower crystallinity degree in the copolymers with respect to the homopolymer.

Table 4.29. Mechanical characterization data (elastic modulus E, stress at break σ_b and elongation at break ε_b) of PBS and P(BSxTESy) random copolymers.

Polymer	E (MPa)	σ_b (MPa)	ε_b (%)
PBS	330±13	30±2	23±4
P(BS95TES5)	307±18	28±3	121±27
P(BS80TES20)	240±14	20±1	151±5
P(BS70TES30)	142±3	13±2	462±47
P(BS60TES40)	79±3	10±1	801±28

At the same time, copolymerization leads to a reduction of the short aliphatic segments of BS units together with an increase of ether linkages amount given by longer TES segments. As well known, crystal domains act as physical cross-links, which cause an increase of the elastic modulus, whereas long aliphatic segments together with the presence of oxygen atoms are responsible for a higher chain mobility (with the consequent decrease of E).

More in details, the higher the amount of TES co-units, the lower the E value, which is reduced by even 75% in the case of P(BS60TES40) with respect to the homopolymer. A parallel increment of ε_b (up to 800%) was recorded as χ_c decreased.

Moreover, from the mechanical data obtained for P(BS95TES5) copolymer, compared to those of PBS, it seems that the elastic modulus, which does not significantly change in the two samples, is mainly dependent on the crystallinity degree (very similar for PBS and P(BS95TES5)). Conversely, the presence of 5 mol% of TES co-units deeply affects the elongation at break, which is 5 times higher for P(BS95TES5). This behavior could be caused by the presence of both longer glycol subunits and oxygen atoms in TES segments, thus allowing a higher elongation at break [Papageorgiou et al., 2007; Papadimitriou et al., 2007; Vassiliou et al., 2010].

4.8.4 Hydrolytic degradation tests

Hydrolytic degradation experiments have been carried out under physiological conditions in phosphate buffer, according to the procedure reported in Paragraph 3.9. Figure 4.62 shows the percentages of residual gravimetric weight and number average molecular weight as a function of incubation time. As to gravimetric weight, after 200 days of incubation PBS and P(BS95TES5) did not evidence any relevant weight loss (around 2%), while P(BS80TES20) lost around 3% of its initial weight after 20 days of incubation, remaining almost constant from there on. The two copolymers richer in TES co-units, P(BS70TES30) and P(BS60TES40), showed a slow weight decrease, of about 8%, after 150 days of incubation, that became more pronounced in the last 50 days (15% and 22%, respectively).

Despite these small gravimetric weight losses, for all the samples under investigation molecular weight decrement determination was carried out. In fact, as it is well known [Gigli et al., 2013 (b)] during the first stages of hydrolytic degradation, a pronounced decrease in molecular weight can occur even though the gravimetric weight loss is negligible. As shown in Figure 4.62 bottom, in all cases a significant decrease in M_n was registered, confirming the occurrence of the degradation process. As to the degradation rate, during the first 20 days of incubation, no relevant differences between the samples can be highlighted. After that, it seems to be strongly affected by molecular composition: more in details, both PBS and the copolymers containing up to 20 mol% of TES co-units progressively degraded, being their M_n halved after 200 days of incubation. On the other hand, P(BS70TES30) and P(BS60TES40) copolymers degradation is much more significant after 200 and 110 days, respectively, and their M_n values reach the values typical of oligomers.

As it is well known, hydrolysis in polyesters is affected by many factors like chemical structure, molecular weight, hydrophilic/hydrophobic balance within the main chain, crystallinity and solid-state morphology [Bikiaris et al., 2008]. Taking into account all these factors, the trend observed can be related to a decrement in crystallinity degree and to the higher amount of ether oxygen atoms, in the copolymers with respect to PBS. In fact, both factors promote water access, thus accelerating the hydrolysis of ester groups. Furthermore, it is proven that hydrolysis rate is significantly higher when the difference between the polymer T_m and the temperature of hydrolysis is less than 30°C, as in the case of P(BS60TES40) [Marten et al., 2003; Abou-Zeid et al., 2004].

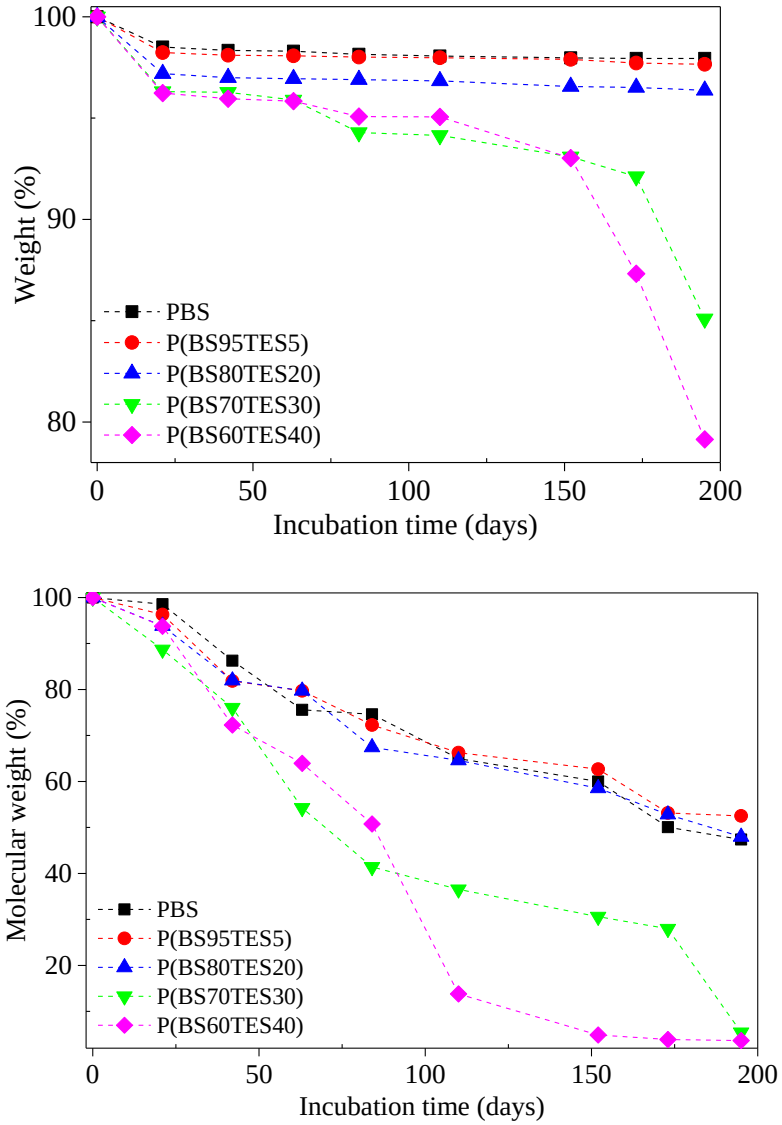

Figure 4.62. Residual percentage gravimetric (top) and residual molecular weight (bottom) as a function of incubation time for PBS and P(BSxTESy) random copolymers.

4.8.5 Biocompatibility and gene expression assay

As regards biocompatibility studies, both direct and indirect cytotoxicity assays were performed on PBS and P(BSxTESy) copolymers, using embryonic rat cardiac H9c2 cells obtained from the European Collection of Cell Cultures (ECACC) [Govoni et al., 2010], according to the ISO10993-5 international standard for biological evaluation of medical devices.

More in details, the PrestoBlue® fluorescence assay was used to estimate the potential indirect cytotoxicity. As shown in Table 4.30, where fluorescence values obtained are reported from cells grown both in standard DMEM medium and in DMEM medium previously incubated with polymeric samples, no evidence of potentially cytotoxic by-products released from the materials into the culture medium is reported. Indeed, cells grown for 72 h in PBS, P(BS95TES5), P(BS80TES20), P(BS70TES30) and P(BS60TES40) extraction medium exhibited comparable fluorescence outputs, which is equivalent to the value obtained for the standard DMEM control. Otherwise, when exposed to 1 mM H_2O_2 for 120 min, as a positive cytotoxicity control, all the cells were killed (data not shown).

PrestoBlue® fluorescence assay was also used to evaluate adhesion and proliferation of cells seeded (2 x 10^4 H9c2 cells) on both polymeric films and a polystyrene surface, which was used as control: quantification was performed by means of fluorescence measurements performed on medium aliquots collected up to one week (1, 3 and 7 days).

As reported in Table 4.31, after 24 h from cell seeding about the same number of cells survived on all the polymeric films, which is about half of the number of H9c2 cells adhered to the control polystyrene surface (17340 ± 945.5 a.u.).

Even though H9c2 cells continued to grow on the films up to 7 days in culture, PBS, P(BS95TES5) and P(BS80TES20) supported a better cell adhesion and proliferation than P(BS70TES30) and P(BS60TES40).

Cell adhesion to artificial materials is affected by surface properties such as wettability, roughness, surface charge, and chemical functionalization. In particular, a key role is played by the adsorbed protein layer, whose role is fundamental in the regulation of cellular function [Wilson et al., 2005]. It is generally assumed that protein adsorption to solid substrates is significantly better for hydrophobic surfaces. The results obtained are in accordance with previous studies, which reported that cell adhesion and spreading decrease as the amount of hydrophilic monomers increases [Anderson et al., 2017].

Table 4.30. Evaluation of indirect cytotoxicity. Fluorescence measurements are expressed in arbitrary units.

Extraction medium	Day 1	Day 3
DMEM control	12990 ± 598.2	26720 ± 602.9
PBS	11660 ± 536.3	26170 ± 597.0
P(BS95TES5)	11850 ± 452.3	24730 ± 651.9
P(BS80TES20)	13220 ± 286.4	26830 ± 447.5
P(BS70TES30)	12390 ± 261.2	24400 ± 602.1
P(BS60TES40)	12070 ± 230.0	24460 ± 623.4

Table 4.31. Proliferation assay. Fluorescence measurements are expressed in arbitrary units per day.

Polymer	Day 1	Day 3	Day 7
PBS	8751 ± 280.0	13900 ± 351.5	19580 ± 323.5
P(BS95TES5)	9327 ± 200.8	13780 ± 472.8	19200 ± 223.0
P(BS80TES20)	7775 ± 352.5	10700 ± 596.3	15910 ± 620.3
P(BS70TES30)	8340 ± 771.8	9437 ± 227.8	12840 ± 383.0
P(BS60TES40)	8333 ± 726.7	9360 ± 222.8	10600 ± 349.8

From real time PCR data, gene expression of myosin heavy chain, which is a marker related to the muscle phenotype expected to develop in H9c2 cells, shows up to twofold increase versus PBS homopolymer, when cells were cultured for 7 days on P(BS95TES5) and P(BS80TES20) films (Figure 4.63). The results obtained suggest that through copolymerization it is possible to tune the hydrophobic/hydrophilic ratio *ad hoc*, in order to initiate a phenotypic cell commitment.

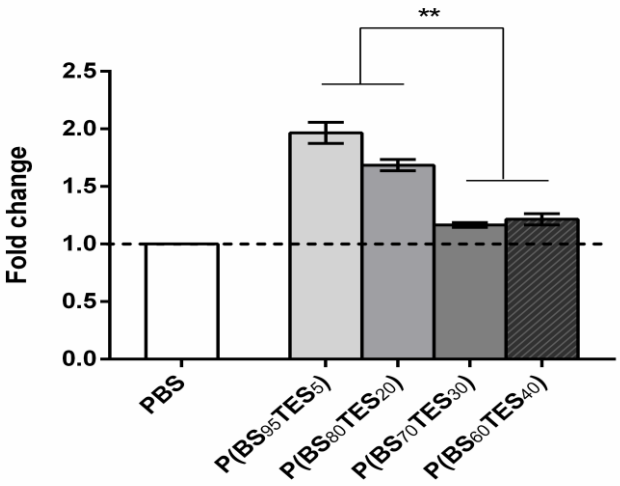

Figure 4.63. Real time PCR data on myosin heavy chain expression. Each copolymer vs. PBS: P < 0.01; P(BS95TES5) vs. P(BS80TES20) and P(BS70TES30) vs. P(BS60TES40): P > 0.05; P(BS95TES5) and P(BS80TES20) vs. P(BS70TES30) and P(BS60TES40): P < 0.01.

4.8.6 Nanoparticles characterization and drug release experiments

PBS and P(BS60TES40) Dexamethasone-loaded nanoparticles were obtained by oil-in-water miniemulsion technique. Nanoparticles size and size distribution were determined by means of dynamic light scattering (DLS). Both the particle types show a unimodal and comparable size distribution, being the diameters 290 ± 50 nm for the homopolymer and 320 ± 40 nm for the copolymer. The percentage encapsulation efficiency (EE%) calculated according to Eqn. [38] (see paragraph 3.11) is particularly different for the two samples, being 7.5% and 69% for PBS and P(BS60TES40), respectively. As it is well known, EE depends on many parameters, like hydrophilicity and crystallinity degree. According to the hydrophobic nature of DXM, its encapsulation should be favored in the more hydrophobic sample, i.e. PBS. However, the opposite trend observed could be explained with the different crystallinity degree of the two samples, three times lower for P(BS60TES40) than PBS: in fact, the drug is mainly encapsulated into the amorphous regions, more abundant in the copolymer, while is rejected from the crystalline ones, most present in the homopolymer.

In Figure 4.64 the release profile of DXM from PBS and P(BS60TES40) nanoparticles is shown: drug release is faster from copolymeric nanoparticles than from the homopolymeric ones. Drug release from biodegradable polymeric nanoparticles is affected by several factors,

such as the molecular weight, crystallinity degree, T_g and T_m, degradation rate of the polymeric matrix, as well as drug loading capacity, particle size and hydrophilicity [Fu et al., 2010; Karavelidis et al., 2010]. In some cases, they can also play contradictory roles.

In the present study, as both the materials show a high molecular weight, similar glass transition temperatures, well below room temperature, and particle size comparable as well, the effect of all these parameters can be excluded.

Nevertheless, the two materials significantly differ in melting temperature, crystallinity degree and hydrophilicity. More in details, PBS melting phenomenon is particularly pronounced, being related to a higher crystallinity degree, and occurs well above the physiological temperature. Conversely, P(BS60TES40) melting starts around 37°C, and in this case the transition is less pronounced. Moreover, the higher copolymer hydrophilicity favours the entrance of water in the polymeric matrix, thus enhancing DXM release.

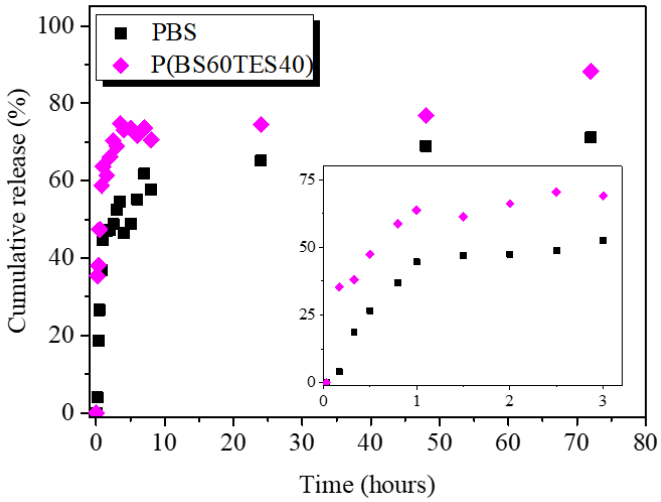

Figure 4.64. DXM release profile from PBS and P(BS60TES40) nanoparticles.

4.8.7 Conclusions

A new class of PEG-like sequence containing aliphatic polyesters based on succinic acid, 1,4-butanediol and triethylene glycol has been studied and characterized with respect to controlled drug delivery and tissue engineering applications.

The synthetic strategy consisted in a solvent-free and eco-friendly process. The so-obtained materials were characterized by the molecular, thermal, structural and mechanical point of view. All these properties, as well as surface wettability and hydrolysis rate have been nicely tailored simply by varying copolymer composition.

In fact, melting temperature and crystallinity degree regularly decrease with the increase of triethylene succinate (TES) mol %, while hydrophilicity presents an opposite behavior: surface wettability increases with higher amounts of TES co-units. All these parameters deeply affect hydrolytic degradation, confirming that a lower crystallinity degree and perfection, together with an improved hydrophilicity, strongly increase the hydrolytic degradation rate.

The release profiles of Dexamethasone from nanoparticles, which were obtained by oil-in-water miniemulsion process, have been affected by the same factors as well: P(BS60TES40), which is the richest in TES sequences, less crystalline and more hydrophilic material among all the copolymers, shows the fastest DXM release, together with the highest encapsulation efficiency with respect to PBS.

As to biocompatibility evaluation, even though all the materials investigated can be considered no cytotoxic, P(BSxTESy) copolymers containing up to 20 mol% of TES co-unit demonstrated good biocompatibility both at shorter (24 h) and longer incubation times (7 days), according to gene expression of myosin heavy chain, marker of a commitment towards the muscle phenotype, twofold increased with respect to PBS.

In conclusion, PBS copolymerization through the introduction of different amounts of ether-oxygen atoms along its backbone turned out to be a winning tool to modulate properly the properties of the so-obtained materials. The new copolyesters synthesized are characterized by a high versatility, as by varying their composition it is possible to tune properties in relation to many different potential applications, from tissue engineering to controlled drug delivery.

In particular, in the present study it was demonstrated that changing features like hydrophobic/hydrophilic ratio and crystallinity degree, it was possible to influence the phenotypic cell commitment as well as the drug release kinetics.

4.9 Novel biocompatible PBS-based copolymers for applications in myocardial tissue engineering: chemical structure and molecular architecture as efficient tools to modulate chemical and physical properties

As cardiac diseases are the first cause of death worldwide, soft tissue engineering, and in particular the cardiac one, can represent a valid alternative to traditional therapies like transplant and drugs. Thanks to the use of flexible devices in which cardiac cells can grow and proliferate, it is possible to repair damaged cardiac tissue, preventing in the same time the loss of cardiomyocytes, that can occur after severe injury. Among the materials used in soft tissue engineering, polylactic acid, polyglicolic acid, polycaprolactone and their copolymers are the most used, even though they are too rigid for soft tissue regeneration. Poly(butylene succinate) (PBS), which was recently FDA approved, could represent a promising alternative, thanks to its thermal stability, high melting temperature and, most importantly, its biocompatibility. In order to overcome its main drawbacks, related to its high crystallinity, rigidity and hydrophobic nature, the present work has as aim the synthesis of new PBS copolymers, characterized by a random and block distribution of comonomeric units for potential applications in the field of myocardial tissue engineering. In addition, different subunits were used: neopentyl glycol, characterized by short ramifications in the main chain, and Pripol 1009, a commercial product with a PE-like structure, containing also long ramifications. Through this particular design, it is possible to obtain materials with mechanical properties typical of thermoplastic elastomers and with improved biodegradability, to be used for the manufacture of scaffolds for myocardial tissue engineering.

More in details, the effect of the molecular architecture (statistical copolymer vs. multiblock copolymer) on the final properties, keeping the same amount and type of comonomeric unit was investigated. The effect of the type of comonomer introduced in PBS main chain (Pripol 1009 vs. neopentyl glycol), keeping the same molecular architecture, was also evaluated.

4.9.1 Synthesis and molecular characterization

OH-terminated poly(butylene succinate) PBS-OH, poly(butylene succinate/Pripol) P(BSBPripol)-OH, and poly(butylene/neopentyl succinate) P(BSNS)-OH were synthesized by two-step melt polycondensation, according to the procedure described in Paragraph 3.2.1.2, using $Ti(OBu)_4$ (TBT) as catalyst. Their molecular weight was determined by ^{1}H-NMR

spectroscopy. In Figure 4.65A P(BSBPripol)-OH spectrum is shown with the relative chemical shifts assignment, while in Table 4.32 the molecular weight of all the hydroxyl-terminated materials is reported.

Table 4.32. Molecular characterization data of PBS-OH, P(BSBPripol)-OH and P(BSNS)-OH obtained by ^{1}H-NMR.

Polymers	M_n (g/mol)	DP	BS (mol%)	BS (wt%)
PBS-OH	9700	55.6	100	100
P(BSBPripol)-OH	25800	63.6	52	22
P(BSNS)-OH	8000	44,0	45	43

The spectra were found to be consistent with the expected structure. As to PBS-OH spectrum, the methylene protons of the butylene subunit are located at δ 4.19 ppm and δ 1.7 ppm, respectively, while the singlet of the acid subunit is situated at δ 2.6 ppm. Besides the signals of the aliphatic protons of the inner repetitive units, the peak due to the outer glycolic subunit can also be detected.

The polymer degree of polymerization (DP) has been calculated according to Eqn. [33], from the normalized areas of a protons of central butanediol (I_a) and a' protons of terminal butanediol ($I_{a'}$).

The polymer molecular weight (M_n) was then obtained from Eqn. [34], where W_{ru} and W_{glycol} are the molecular weights of the BS repeating unit and the butanediol, respectively.

For PBS-OH, DP and M_n were 55,6 and 9700 g/mol, respectively (Table 4.32).

As to P(BSBPripol)-OH spectrum (Figure 4.65A), besides the signals of BS co-unit, the signals of BPripol co-unit are also present: the methylene protons, a' and b' of the glycol subunit are located at δ 4.2 ppm and δ 1.6 ppm, respectively, while the singlet d of the protons related to the acid subunit in α position with respect to the carboxylic group is situated at δ 2.3 ppm. At lower chemical shifts (1.5 ppm < δ < 0.7 ppm) the signals of R subunit of Pripol can be seen, while the peak due to the outer glycolic subunits, a'', is located at δ 3.68 ppm.

In this case, both DP and M_n were calculated and resulted 63.6 and 25800 g/mol, respectively (Table 4.32).

In addition, the P(BSBPripol)-OH copolymer composition was calculated from the relative areas of the ^{1}H-NMR resonance peaks related to c protons of succinic subunit, located at δ 2.6 ppm and d protons associated with the Pripol subunit, located at δ 2.3 ppm. The actual molar composition was very close to the feed one (BS: 52 mol%; BPripol: 48 mol%).

After the synthesis of the two hydroxy-terminated polymers PBS-OH and P(BSBPripol)-OH, chain extension reaction was carried out, according to the procedure described in Paragraph 3.2.3. ^{1}H-NMR spectrum of the chain extended PBSP(BSBPripol) multiblock copolymer is shown in Figure 4.65B, together with peaks assignment. As it can be seen, besides the signals of both BS and BPripol co-units, the chain extender peaks, indicated as e, f and g, are located at δ 3.1 ppm and δ 1.1 ppm.

The actual weight composition of the copolymer PBSP(BSBPripol) can be calculated taking into account the relative area of d protons of Pripol subunit at δ 2.3 ppm, and the relative area of c protons of succinic subunit at δ 2.6 ppm. To this latter, the contribution of succinic subunit inside P(BSBPripol) block, previously calculated, was subtracted. The molar amount of PBS and P(BSBPripol) turned out to be 45% (corresponding to 26 wt%) and 55% (corresponding to 74 wt%), respectively, resulting very close to the feed one (Table 4.33).

The molecular weight of this chain extended polymer was obtained by GPC analysis. As expected, the sample shows a higher molecular weight (M_n = 67000 g/mol) with respect to the prepolymers (Table 4.32) and a pretty narrow polydispersity (PDI = 2.2) was found, indicating a good control over both the polycondensation and the chain extension processes.

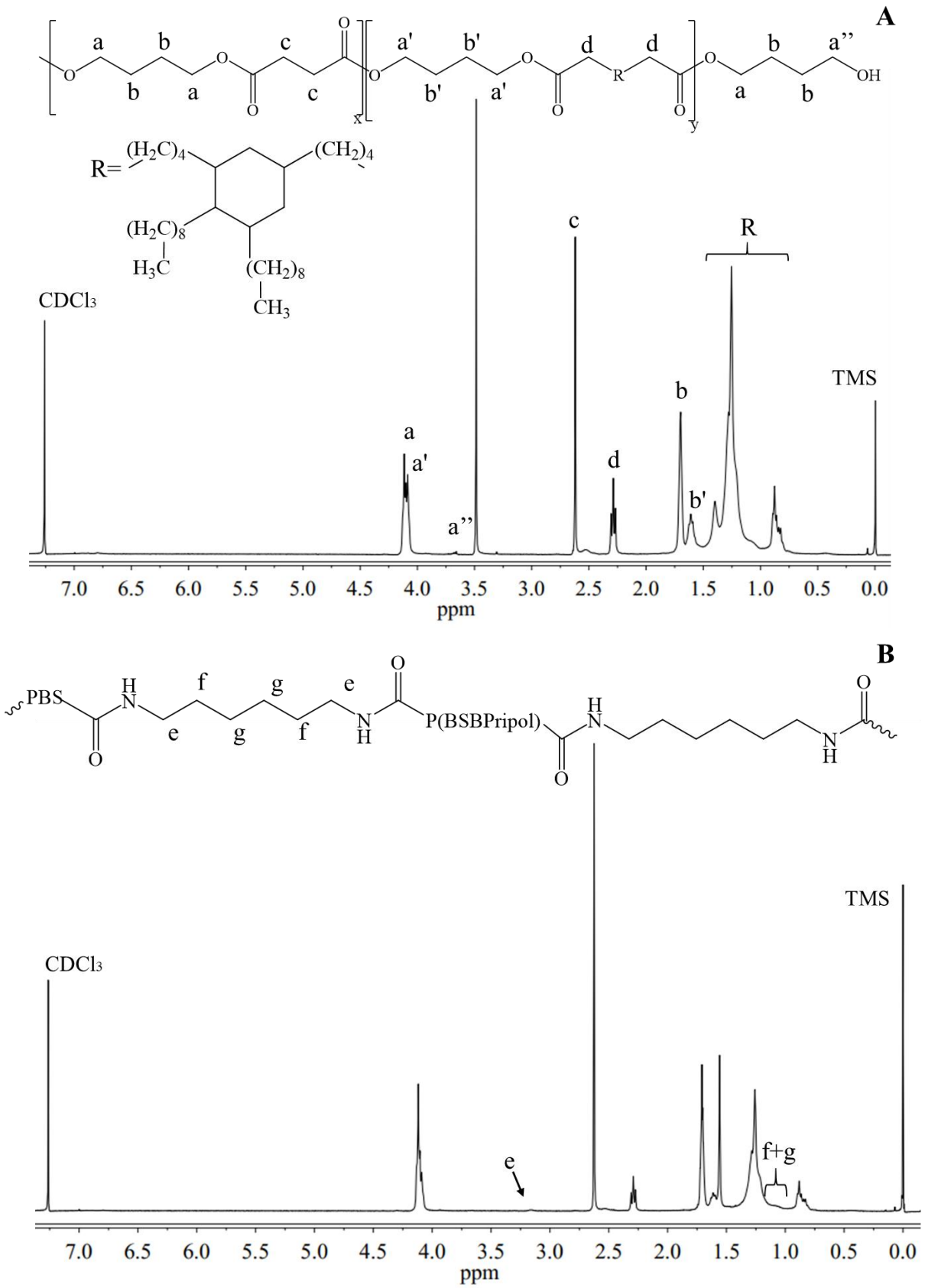

Figure 4.65. ^{1}H-NMR spectra of **A**) P(BSBPripol)-OH and **B**) PBSP(BSBPripol), together with peaks assignment.

In addition, chain extension between PBS-OH and P(BSNS)-OH was carried out, according to the procedure described in Paragraph 3.2.3. ^{1}H-NMR spectra of both P(BSNS)-OH prepolymer and the chain extended PBSP(BSNS) multiblock copolymer are shown in Figure 4.66, together with peaks assignment.

As to P(BSNS)-OH spectrum (Figure 4.66A), besides the signals of BS co-unit, the signals of NS co-unit can be seen: the methylene protons, d and e, of the glycol subunit are located at δ 3.9 ppm and δ 0.95 ppm, respectively, while the singlet f of the protons related to the acid subunit is situated at δ 2.6 ppm. Also in this case both DP and molecular weight were calculated, being 44.0 and 8000 g/mol, respectively (Table 4.32). In addition, the copolymer composition was obtained from the relative areas of the ^{1}H-NMR resonance peaks related to a protons of BD glycolic subunit, located at δ 4.1 ppm and d methylene protons associated with the NS subunit, located at δ 3.9 ppm. The actual molar composition was very close to the feed one (BS: 45 mol%; NS: 55 mol%).

^{1}H-NMR spectrum of PBSP(BSNS) multiblock copolymer (Figure 4.66B) shows, besides the signals of both BS and NS co-units, the chain extender peaks, indicated as g, h and i, located at δ 3.15 ppm and δ 1.25 ppm.

The actual weight composition of the copolymer PBSP(BSNS) can be calculated taking into account the relative area of d methylene protons of NS subunit at δ 3.9 ppm, and the relative area of a protons of BD subunit at δ 4.1 ppm. To this latter the contribution of BD subunit inside P(BSNS) block, previously calculated, was subtracted. The molar amount of PBS and P(BSBNS) turned out to be 29% (corresponding to 28 wt%) and 71% (corresponding to 72 wt%), respectively, resulting very close to the feed one (Table 4.33).

The molecular weight of this chain extended polymer was obtained by GPC analysis. As expected, the sample shows a higher molecular weight (M_n = 36000 g/mol) with respect to the prepolymers (Table 4.32) and a pretty narrow polydispersity (PDI = 2.5).

Table 4.33. Weight and molar composition data of PBSP(BSBPripol), PBSP(BSNS) and P(BSBPripol) obtained by ^{1}H-NMR, together with M_n and PD index obtained by GPC analysis.

Polymer	M_n (g/mol)	PDI	PBS_{block} (mol%)	PBS_{block} (wt%)
PBSP(BSBPripol)	67000	2,2	45	26
PBSP(BSNS)	36000	2,5	29	28
P(BSBPripol)	39000	2,4	60	28

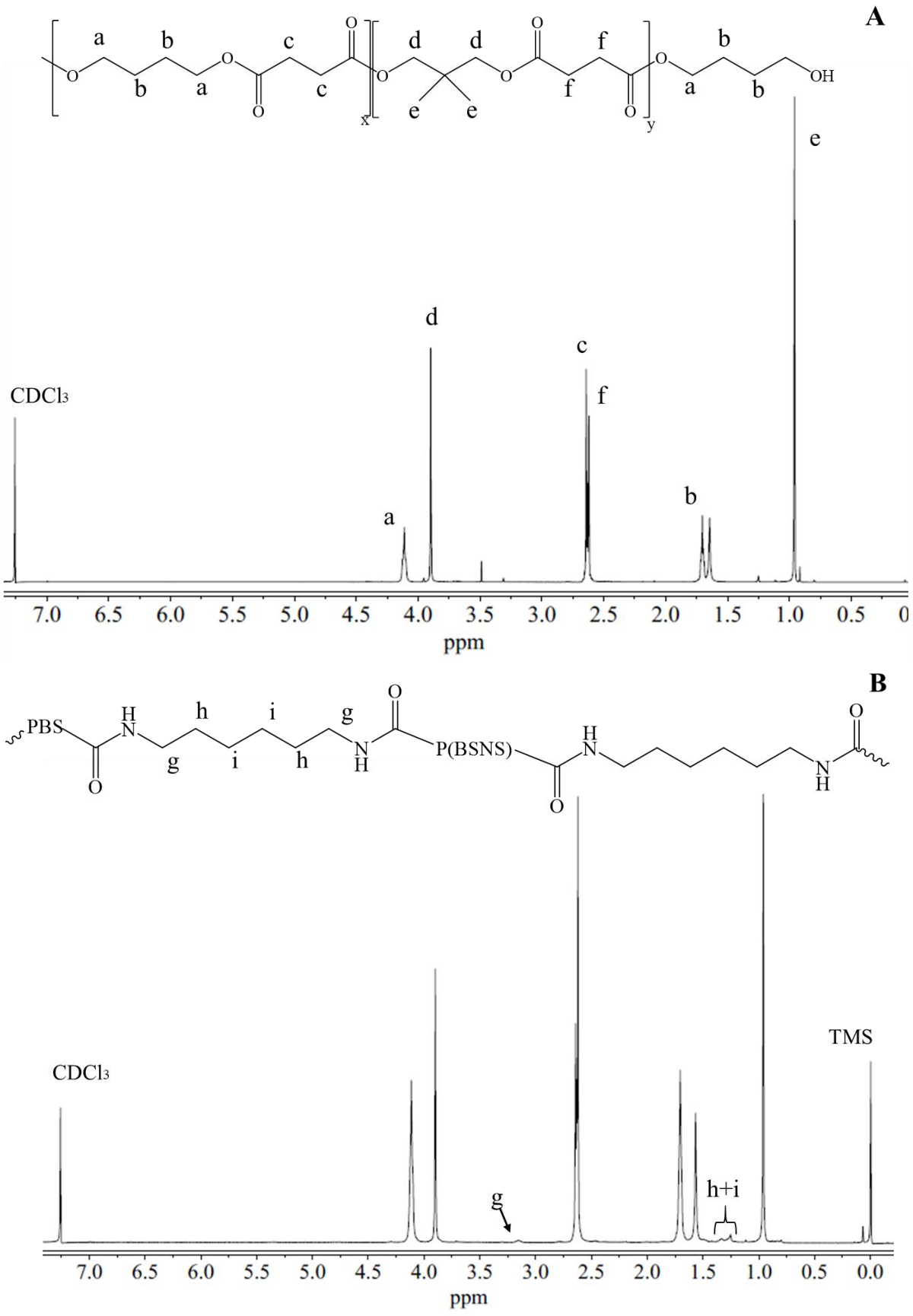

Figure 4.66. ^{1}H-NMR spectra of **A**) P(BSNS)-OH and **B**) PBSP(BSNS) with peaks assignment.

Together with the chain extended copolymers, also random P(BSBPripol) copolymer was synthesized by two-step melt polycondensation using $Ti(OBu)_4$ (TBT) as catalyst, according to the procedure reported in paragraph 3.2.1.2. The sample was then characterized by means of ^{1}H-NMR spectroscopy and GPC analysis. The molecular characterization data are collected in Table 4.33, while in Figure 4.67 the ^{1}H-NMR spectrum is shown.

As it can be seen, all the peaks of PBSP(BSBPripol) block copolymer (Figure 4.65B) are present, apart from those of chain extender. The chemical composition was calculated from the relative area of f methylene protons of Pripol subunit at δ 2.3 ppm, and the relative area of c protons of succinic subunit at δ 2.6 ppm. The molar amount of PBS turned out to be 60% (corresponding to 28 wt%), resulting exactly the feed one. Molecular weight obtained by GPC was of 39000 g/mol, with a PD index equal to 2.4 (Table 4.33).

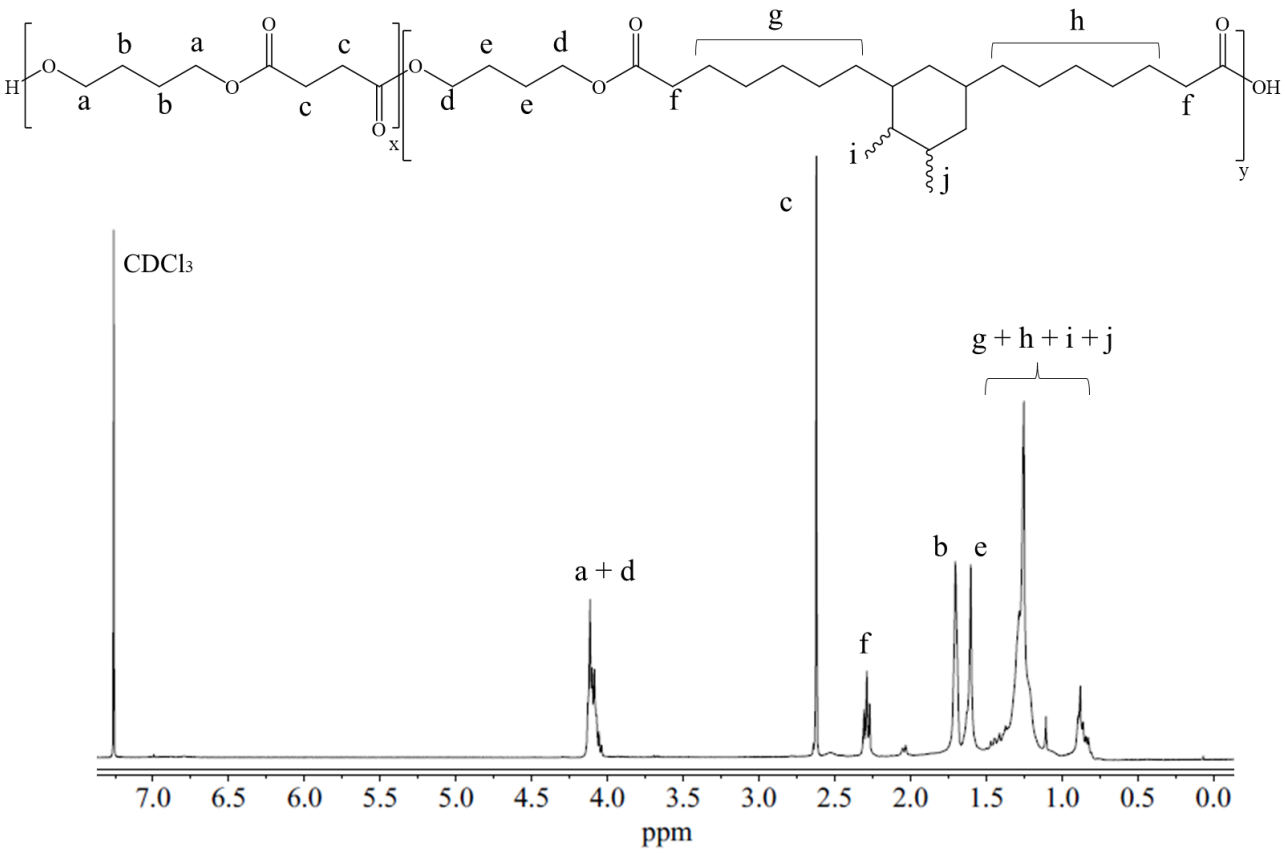

Figure 4.67. ^{1}H-NMR spectrum of P(BSBPripol) random copolymer, with peaks assignment.

In conclusion, the samples under investigation are characterized by the same weight percentage of PBS (≈28%), but different architecture (PBSP(BSBPripol) vs. P(BSBPripol)) or different chemical structure of comonomeric units (PBSP(BSBPripol) vs. PBSP(BSNS)).

4.9.2 Morphologic characterization of scaffolds

Nanofibrous scaffolds of all the materials under study were obtained through electrospinning (see Paragraph 3.4.2). SEM analysis was carried out on scaffolds in order to check the fibers morphology and to calculate their mean diameter. In Figure 4.68 a SEM picture of PBSP(BSBPripol) is shown as an example (12.00k X magnification). As it can be seen, no beads are present, as a proof of the good control over the electrospinning procedure. As a matter of fact, the development of crystallinity during solvent evaporation allows to avoid the formation of agglomerates, thus giving structural strength to the fibers. These fibers present quite different diameters, because of jet-splitting phenomena, which starts from the primary jet and cause secondary jets of smaller dimensions.

In all the samples analysed, the fibers are characterized by a non-Gaussian distribution, probably due to the above-mentioned jet-splitting phenomena, with dimensions ranging between 100 to 400 nm.

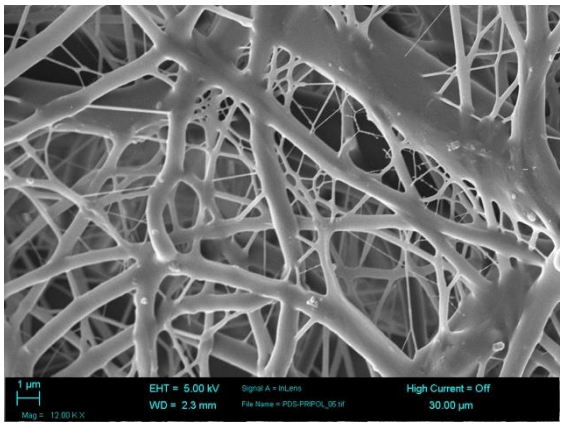

Figure 4.68. SEM picture of PBSP(BSBPripol) scaffold.

4.9.3 Thermal characterization

All the synthesized polymers, in the form of films and scaffolds, have been subjected to thermogravimetric analysis under dry nitrogen atmosphere. The temperature corresponding to the beginning of degradation (T_{onset}) and to the maximum rate of decomposition (T_{max}) are listed in Table 4.34. All the samples under investigation show a very good thermal stability (T_{onset} above 370 °C). Copolymerization improves thermal stability of PBS, even more when Pripol copolymeric unit is present. As to PBSP(BSNS), the higher thermal stability can be ascribed to the presence of the two methylene groups in NS co-unit, which limits β scission reactions, while

the higher thermal stability of Pripol-containing copolymers is probably due to the fewer carboxylic groups inside the macromolecular chains [Soccio et al., 2007]. In addition, P(BSBPripol) random copolymer is more thermally stable than its block counterpart, as a higher molar amount of Pripol sub-unit is present (40 mol% vs. 27 mol%, respectively). It has also to be noticed that electrospinning process does not affect the thermal stability of the materials under study, as the scaffolds do not show any difference in terms of T_{onset} and T_{max} with respect to films.

Table 4.34. TGA data (T_{onset} and T_{max}) of both OH-terminated polymers and high molecular weight ones.

Polymer	T_{onset} (°C)	T_{max} (°C)
PBS-OH	376	409
P(BSBPripol)-OH	407	440
P(BSNS)-OH	380	412
PBSP(BSBPripol)	386	418
PBSP(BSNS)	378	415
P(BSBPripol)	391	426

Calorimetric analysis of PBS-OH, P(BSBPripol)-OH and P(BSNS)-OH prepolymers was carried out immediately after synthesis, while in the case of high molecular weight materials, in the forms of films and scaffolds, DSC analysis was performed after three weeks of storage at room temperature, which are necessary to uniform the thermal history of the samples. I scan calorimetric data of all the materials under study are collected in Table 4.35, while in Figure 4.69, besides the I scan traces of the high molecular weight copolymers PBSP(BSBPripol), PBSP(BSNS) and P(BSBPripol), in the form of film and scaffold, the DSC curve of PBS homopolymer is also shown for sake of comparison. In case of block copolymers, the DSC profiles of the relative hydroxy-terminated prepolymers are included in the Figure.

The DSC trace of PBS-OH shows the typical behavior of semicrystalline materials, with a glass transition phenomenon at -29 °C, followed by a pronounced endothermic melting peak at 119 °C.

Copolymerization deeply affects both T_g and T_m: more in details, the plasticizing effect of the long aliphatic segments inside the Pripol comonomeric unit causes a decrease of T_g together with an increase of ΔC_p. In addition, the introduction of a so different comonomeric unit along

the PBS main chain deeply hampers the crystallization capability of BS segments, thus resulting in a multiple melting peak, which occurs at lower temperature and is less intense (lower ΔH_m) with respect to that of PBS homopolymer. This behaviour can be explained as due to the formation, in the copolymer, of a smaller amount of crystalline phase, characterized by a lower degree of perfection.

The double melting peak can be due to melting-crystallization-melting phenomena, in which crystals melt and crystallize in more perfect lattice during heating, analogously to other PBS-based copolymeric systems investigated in the present Thesis.

Table 4.35. Thermal characterization data of hydroxyl-terminated prepolymers and high molecular weight polymers, in form of films and scaffolds.

Polymer	I SCAN			
	T_g (°C)	ΔC_p (J/g °C)	T_m (°C)	ΔH_m (J/g)
PBS-OH	-29	0,155	119	67
P(BSBPripol)-OH	-52	0,409	36	15
P(BSNS)-OH	-26	0,459	43	16
PBSP(BSBPripol)*	-50	0,266	40; 110	27
PBSP(BSNS)*	-27	0,303	43; 104	41
P(BSBPripol)*	-50	0,194	42; 65	21
PBSP(BSBPripol)**	-50	0,151	37; 109	27
PBSP(BSNS)**	-26	0,365	45; 102	42
P(BSBPripol)**	-51	0,192	47; 64	23

*film; ** scaffold

The first DSC scan of PBSP(BSBPripol) film seems to be the sum of the calorimetric curves of the two prepolymers. It indeed shows the endothermic baseline deviation related to glass-to-rubber transition around -50 °C, together with two different melting peaks: the first one at 40 °C is related to the melting of P(BSBPripol) co-units, while the second one, at 110 °C, is due to the melting of PBS crystals (Figure 4.69A). This behaviour confirms that through chain extension it is possible to obtain copolymers in which both blocks are able to undergo crystallization. Moreover, the melting temperatures of the blocks are not significantly lowered by copolymerization.

It has also to be noticed that electrospinning does not alter the crystalline microstructure of the material, as the DSC profiles of both film and scaffold turned out to be very similar.

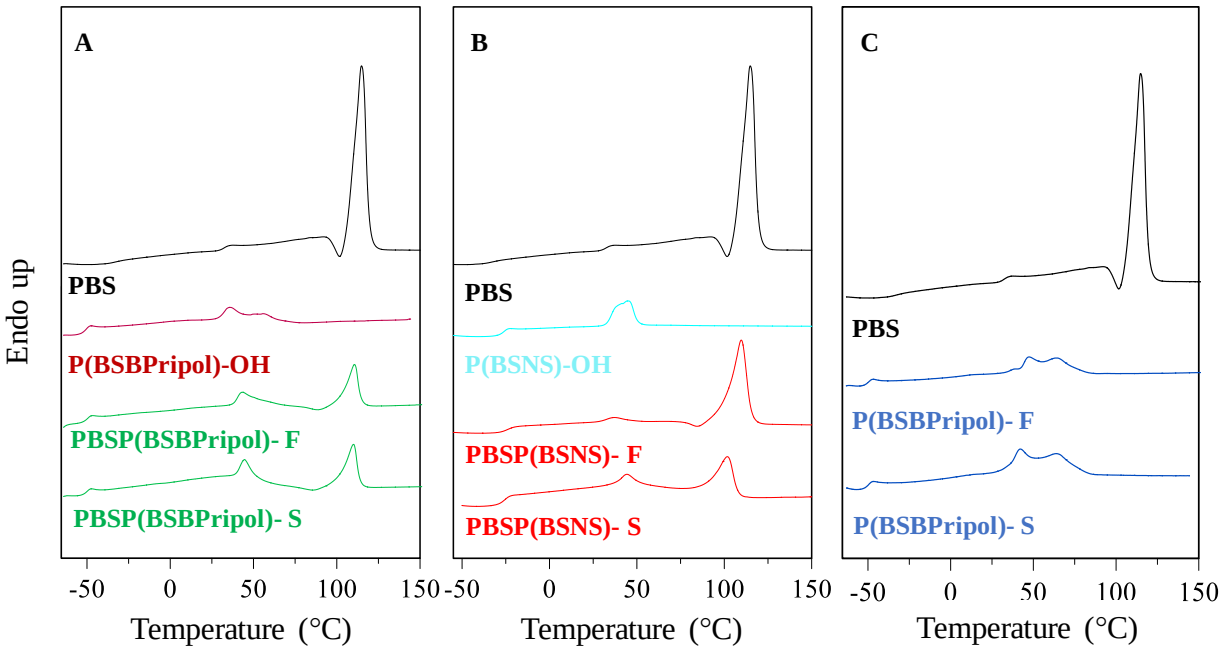

Figure 4.69. First scan calorimetric curves of **A**) PBSP(BPripol) (film and scaffold) and P(BSBPripol)-OH prepolymer; **B**) PBSP(BSNS) (film and scaffold) and P(BSNS)-OH prepolymer; **C**) P(BSBPripol) (film and scaffold). PBS DSC trace is added for sake of comparison.

In Figure 4.69B first scan DSC curves of PBS, P(BSNS)-OH and PBSP(BSNS) (film and scaffold) are shown. Also in this case the DSC curve of P(BSNS)-OH copolymer is significantly different from PBS one, as the NS co-unit is responsible for a slight increase of both T_g and ΔC_p. This behaviour is due to the presence of the two methyl groups along the glycolic subunit, which cause a decrease in the chain mobility, thus hindering the crystallization process, as already described in the copolymeric system reported in Paragraph 4.7. Indeed, the melting peak is shifted at lower temperatures and is less intense and broader than that of PBS homopolymer, because of the presence of a less perfect crystalline phase.

As to the PBSP(BSNS) film, T_g can be detected around -27°C, while two melting peaks are observed at T = 43 °C and T = 104 °C: the first one is related to the melting of the crystalline phase of P(BSNS) block, while the peak at higher temperature can be ascribed to the fusion of PBS block crystalline phase. Also in this case, chain extension allowed the synthesis of a copolymer containing two blocks capable to undergo crystallization, without any significant effect on the melting temperatures.

The DSC trace of PBSP(BSNS) scaffold (Figure 4.69B) turned out to be similar to that of the film, showing comparable melting temperatures, thus proving again that scaffold fabrication favours the crystallization of both short BS segments inside P(BSNS) block and long ones inside PBS block.

In Figure 4.69C first scan calorimetric curves of PBS and P(BSBPripol) random copolymer, in form of both film and scaffold are shown. The effect of copolymerization is the same already observed for the hydroxyl-terminated P(BSBPripol)-OH prepolymer (Figure 4.69A): lower T_g and higher ΔC_p values, together with a multiple and less intense melting peak located at lower temperature (Table 4.35). However, many differences can be noticed between the DSC profiles of P(BSBPripol) and PBSP(BSBPripol), because of their different molecular architecture, random *vs.* block. In fact, P(BSBPripol) DSC profile shows two endothermic peaks at T = 42°C and T = 65°C, quite near to each other, differently from PBSP(BSBPripol), whose melting peaks are distant, being located at T = 41°C and T = 110°C. In addition, the random architecture of P(BSBPripol) is responsible for a deeper reduction of PBS crystallinity.

4.9.4 Structural characterization

To get information on the nature and the amount of the crystalline phase present in the copolymeric films and scaffolds under investigation, WAXS analysis was performed. In Figure 4.70 the diffraction profiles are shown, while in Table 4.36 the values of crystallinity degree X_c are listed.

All the profiles obtained are typical of semicrystalline polymers, with well-defined peaks, overlapped with a bell-shape baseline characteristic of amorphous regions.

According to the patterns obtained, all the materials in the form of films and scaffolds are characterized by the α-PBS crystal phase [Ichikawa et al., 2000]. No other crystal phases are present. Peak position remains unchanged, proving that the co-units are excluded in the amorphous phase.

By comparing the X-Ray diffraction profiles of films, it is possible to notice that PBSP(BSNS) is the most crystalline among the copolymers under investigation (Table 4.36). This result is not surprising taking into account that neopentyl glycol has a chemical structure quite similar to that of butanediol.

Conversely, the copolymers containing Pripol subunit are characterized by a diacid moiety considerably different from that of succinic acid.

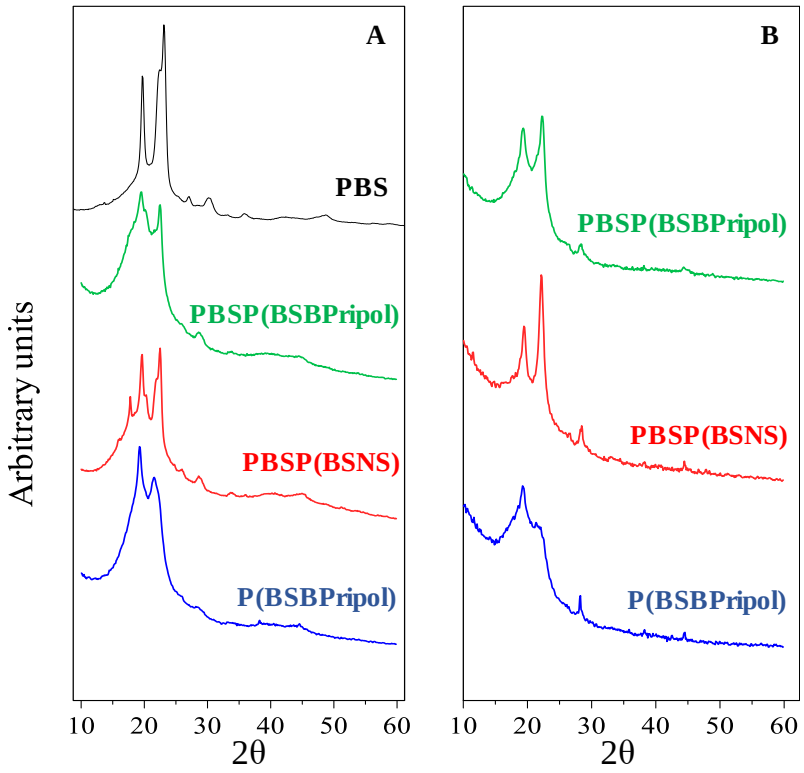

Figure 4.70. X-Ray diffraction profiles of PBS film and PBSP(BSBPripol), PBSP(BSNS) and PBSP(BPripol) copolymers: **A**) films; **B**) scaffolds.

In addition, a further decrease of crystallinity degree can be seen in the random copolymer P(BSBPripol) with respect to the block one PBSP(BSBPripol), evidencing that the distribution of comonomeric units also affects the crystallization capability.

More in details, the main PBS lattice reflections, located at 2θ = 19° and 2θ = 23°, change in intensity by copolymerization: in PBS pattern the reflection at 2θ = 23° is more intense than the peak at 2θ = 19°. In PBSP(BSNS) they are comparable, while for PBSP(BSBPripol) and P(BSBPripol) it is progressively inverted. Such change is more pronounced when the crystalline phase amount is decreased. It can be hypothesized that in P(BSBPripol) a partial lattice distortion occurs.

The behaviour of scaffold samples is similar to that of films: also in this case the reflection at 2θ = 23° is less intense for the random copolymer with respect to the block ones.

Lastly, the crystallinity indexes obtained from diffractometric analysis are consistent with the calorimetric data (Table 4.35).

Table 4.36. Crystallinity indexes of PBS film and of PBSP(BSBPripol), PBSP(BSNS) and PBSP(BPripol) copolymers (films and scaffolds).

Polymer	X_c film (%)	X_c scaffold (%)
PBS [Guidotti et al., 2017]	46	-
PBSP(BSBPripol)	27	28
PBSP(BSNS)	35	38
P(BSBPripol)	14	19

4.9.5 Mechanical characterization

To provide insight into the mechanical response of the polymers synthesized, tensile measurements were carried out. Stress-strain and cyclic measurements were performed on rectangular samples (50 x 5 x 0.3 mm for films and 50 x 5 x 0.05 mm for scaffolds, respectively) by measuring the variation of stress as a function of the strain applied. For cyclic measurements, the samples were subjected to 20 loading cycles upon a strain of 50%. The tensile testing data (elastic modulus E, stress at break σ_B and strain at break ε_B), are summarized in Table 4.37. In Figure 4.71 stress-strain curves for PBSP(BSBPripol), PBSP(BSNS) and P(BSBPripol) copolymers, in form of films and scaffolds, are shown, while in Figure 4.72 cyclic loading curves for the same materials are reported.

Table 4.37. Mechanical characterization data of PBS film and PBSP(BSBPripol), PBSP(BSNS) and P(BSBPripol) in form of films and scaffolds.

Polymer	σ_B (MPa)	ε_B (%)	E (MPa)
PBS [Guidotti et al., 2017]	16 ± 2	5 ± 1	301 ± 25
PBSP(BSBPripol)*	3,7 ± 0,5	185 ± 20	22 ± 2
PBSP(BSNS)*	15 ± 2	520 ± 27	78 ± 10
PBSP(BPripol)*	4,6 ± 0,3	460 ± 22	14 ± 2
PBSP(BSBPripol)**	3,3 ± 0,5	127 ± 20	5 ± 1
PBSP(BSNS)**	2,2 ± 0,8	120 ± 18	5 ± 1
PBSP(BPripol)**	1,9 ± 0,3	104 ± 16	10 ± 3

*film; **scaffold.

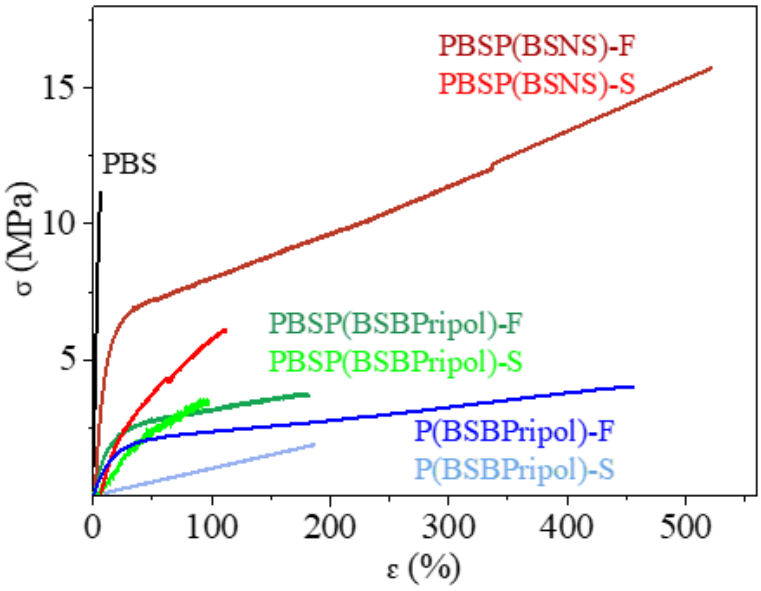

Figure 4.71. Stress-strain curves of films and scaffolds of PBSP(BSBPripol), PBSP(BSNS) and P(BSBPripol) compared to mechanical response of PBS.

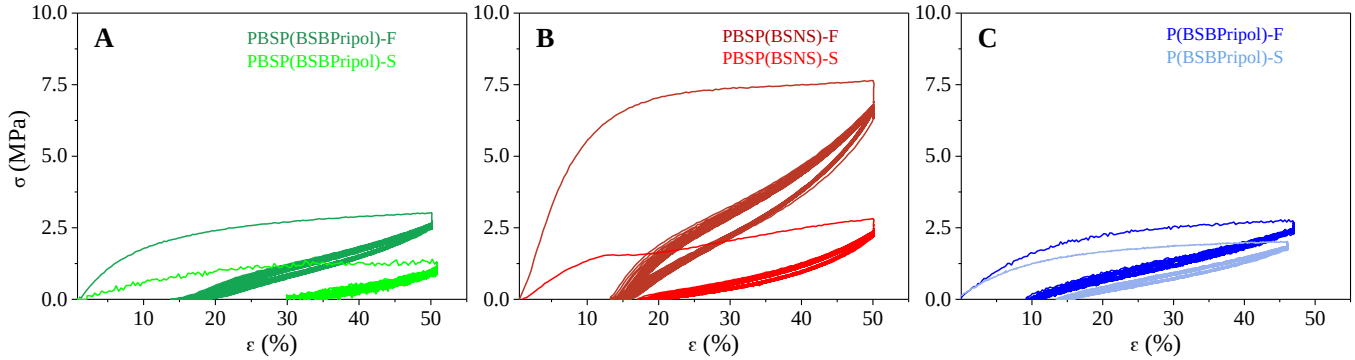

Figure 4.72. Cyclic loading curves of films and scaffolds of **A**) PBSP(BSBPripol); **B**) PBSP(BSNS) and **C**) P(BSBPripol).

As to PBSP(BSBPripol) block copolymer in the film form, it has an elastic modulus of about one order of magnitude lower than PBS one, together with three times lower σ_B value (Table 4.37). Even more interestingly, the value of ε_B increases from 5% for PBS to 185% for the copolymer, as an evidence of the high elasticity of this sample. These results can be ascribed to both the increase of chain mobility (lower T_g) and the reduction of the crystallinity degree (Figure 4.70A), due to the presence of Pripol subunit. It has also to be noticed that in the stress-strain curve of PBSP(BSBPripol) no yield is recorded, indicating a thermoplastic elastomeric behavior, thanks to the peculiar *soft-hard* multiblock molecular architecture.

Cycling stress-strain measurements were carried out in order to investigate the behaviour of the copolymer when subjected to cyclic stress (Figure 4.72A). The material shows good elasticity, even though a certain amount of permanent set, of about 35%, can be detected after each loading–unloading cycle. In addition, the stress–strain curve in the second cycle is more compliant than that observed in the first cycle. This behaviour, known as softening, can be due to a rearrangement in the crystalline microphase [Soccio et al., 2012 (b)]. Lastly, the hysteresis area of the second cycle is much smaller than that of the first cycle, thus indicating a good energy recovery.

As to the differences between film and scaffold, from the data collected in Table 4.37 a further decrease of elastic modulus can be observed, whereas the elongation at break does not change appreciably, being anyway good. Such trend can be related to the fibrous structure present in the scaffold, which is responsible for the higher elasticity. Anyway, scaffold structure is characterized by pores and defects, which determine the fracture of the sample at lower stress with respect to the film.

According to the cycling stress-strain curves shown in Figure 4.72A, PBSP(BSBPripol) scaffold shows a typical elastomeric behaviour as well. The elastic recovery, which in this case is lower than film (40% vs. 65%), is probably affected by the intrinsic structure of the scaffold: the random- oriented fibres, under the load applied, align along the same direction of the stress, thus irreversibly losing part of the elastic energy. Consequently, lower elastic recovery and higher hysteresis were recorded.

As to PBSP(BSNS) multiblock copolymer in form of film, a decrease of the elastic modulus can be observed with respect to PBS homopolymer, although in this case the reduction is less pronounced than for Pripol-containing block copolymer, probably because of the higher crystallinity degree and the higher T_g value. At the same time, the elongation and the stress at break are the highest among all the samples under investigation. This result can be correlated to the small size of the glycolic subunit, which may favour a more effective chain packing (i.e. higher density of the macromolecule). In addition, during mechanical stretching the polymeric chains can slide one on the other without the formation of any holes, being these latter responsible for early fractures. However, despite the higher stress at break and elastic modulus with respect to Pripol-based copolymers, PBSP(BSNS) shows a very good elasticity, as it can be seen from its cycling stress-strain curve (Figure 4.72B), characterized by an elastic return of 70%.

By comparing film and scaffold response, it is possible to see that electrospinning process does not negatively affect the mechanical behaviour of PBSP(BSNS) block copolymer in terms of elastic return, which turned out to be very similar to the film one (around 65%). In addition, both the elastic modulus and the stress at break are lower than those of film, thus confirming the influence of the porous 3D-structure on mechanical properties (Table 4.37).

As to the film prepared by the random PBSP(BPripol) copolymer, it also shows a significant different mechanical behaviour with respect to PBS homopolymer. In particular, a lower elastic modulus and a higher elongation at break, this latter even higher than that of PBSP(BSBPripol) block copolymer were measured. It is therefore possible to conclude that molecular architecture deeply influences the mechanical response. In addition, although the random distribution of comonomeric units, P(BSBPripol) does not show any yield (Figure 4.71C), probably because of the high sizes of Pripol co-units, which make them a kind of block themselves. From the cycling stress-strain measurements, it is clear that P(BSBPripol) is characterized by high elasticity, being the elastic recovery of 78% after 20 cycles, even superior than that of PBSP(BSPripol) block copolymer (Figure 4.72C).

From the comparison between the performances of film and scaffold after cyclic loading, it can be evicted that they are characterized by similar behaviour, although scaffold shows lower elongation at break (Table 4.37 and Figure 4.72C), because of the 3-dimensional porous structure, which breaks more easily under mechanical stretching. As to the cycling stress-strain measurements, PBSP(BPripol) scaffold exhibits a good elastic recovery too, around 67%.

To conclude, all the samples under investigation display the behaviour typical of thermoplastic elastomers. Moreover, the elastic modulus of the scaffolds ranges between 0.02 and 0.5 MPa, which is similar to that of cardiac muscle [Chen et al., 2008].

4.9.6 Hydrolytic degradation tests

Hydrolytic degradation experiments were carried out under the same physiological conditions previously employed for the copolymeric system discussed in Paragraph 4.8. At predetermined timepoints, sacrificial samples were collected, weighted, and their molecular weight was calculated by means of GPC analysis. In addition, the samples were subjected to ^{1}H-NMR, DSC and WAXS analyses, in order to check the residual composition and possible differences in crystallinity degree.

As already mentioned above, hydrolysis is a bulk phenomenon: the macromolecular chains are attacked by water and the molecular weight starts to decrease, while gravimetric weight loss occurs after longer times, as the hydrolysed chains are not able to solubilize during the first stages of degradation. In Table 4.38 both weight loss and molecular weight loss data for PBS and for all the copolymers (films and scaffolds) are reported, together with calorimetric data.
The hydrolytic degradation studies have been carried out also on P(BSNS) random copolymer, containing 70 weight % of BS co-units, previously described (see Paragraph 4.7). The copolymer is indeed characterized by high flexibility, which render it very promising for cardiac tissue engineering.

Table 4.38. Thermal characterization and hydrolytic degradation data of PBS, PBSP(BSBPripol), PBSP(BSNS), P(BSBPripol) and P(BSNS) in form of films and scaffolds.

Polymer	T_g (°C)	T_m (°C)	ΔH_m (J/g)	Weight loss (%)	Molecular weight loss (%)
PBS [Fabbri et al., 2018]	-32	115	62	2,0	35
PBSP(BSBPripol)*	-50	110	27	1,7	21
PBSP(BSNS)*	-26	104	41	1,3	23
P(BSBPripol)*	-51	65	21	2,0	47
P(BSNS)*	-28	77	33	3,0	42
PBSP(BSBPripol)**	-50	109	27	3,1	30
PBSP(BSNS)**	-26	102	42	3,9	31
P(BSBPripol)**	-51	64	23	5,2	60
P(BSNS)**	-28	77	33	4,8	45

*film, **scaffold

As regards the samples in the form of films, according to the data collected in Table 4.38, no appreciable weight losses were observed, the values ranging from 1 to 3%. As to the corresponding scaffolds, slightly higher weight loss percentages were measured (from 3% to 5%), because of the higher surface/volume ratio due to the nanofibrous structure.
As concerning the molecular weight, it is possible to notice that in this case the weight loss is more remarkable, thus confirming the bulky nature of the degradation process. By comparing

the films, two opposite trends have been observed depending on the copolymer architecture: block copolymers show a lower decrement, random copolymers a higher one with respect to PBS homopolymer film. In particular, block samples degrade slower than PBS despite their lower crystallinity degrees. In case of PBSP(BSBPripol) block copolymer, such result can be ascribed to the lower -COOR- groups density due to the presence of Pripol subunit; the PBSP(BSNS) multiblock copolymer behaviour can be, on the other hand, explained on the basis of its higher T_g value, which means less mobility and less accessibility to water of the macromolecular chains. It has to be emphasized that the two multiblock copolymers are characterized by similar molecular weight variation, which may be due to the combination of many different factors such as lower rigidity, crystallinity degree and ester group density in Pripol-containing copolymer, against higher crystallinity degree and presence of hydrolysable groups for the NG-containing copolymer.

As said above, both the random copolymers, despite the higher molar percentage of BS co-units in P(BSNS), degrade faster than PBS, showing a higher molecular weight variation. In particular, P(BSBPripol) random copolymer revealed to be the fastest degrading sample, with its lowest T_g, T_m and ΔH_m values. The slower degradation rate of random P(BSNS) copolymer can be correlated to its higher glass transition temperature, crystallinity degree and melting point.

From all the data available, it can be concluded that copolymer architecture affects the hydrolysis rate.

In all cases, ^{1}H-NMR analysis did not record any composition variation, evidencing no preferential attack of the two different comonomeric units. Analogously, DSC and WAXS analyses did not show any difference in the crystallinity degree, proving that degradation involves both the crystalline and the amorphous phase.

As to the scaffolds, the trend seems to be the same already observed for films, being even enhanced thanks to the higher surface/volume ratio of the electrospun structure.

4.9.7 Biocompatibility studies

4.9.7.1 Gene expression of pluripotency markers

To evaluate the pluripotency state of human iPSCs grown on each copolymeric scaffold after 6 days from the seeding, gene expression profiles were analysed for the pluripotency markers

OCT4, *NANOG*, *SOX2*, *hTERT*, *REX1*, *KLF4*, *cMYC* and *GDF3*. H1 and H9 (from WiCell Research Institute) and human iPSCs cultured under normal conditions (collected at day 0) were used as positive controls, while human fibroblasts were used as negative control (Figure 4.73).

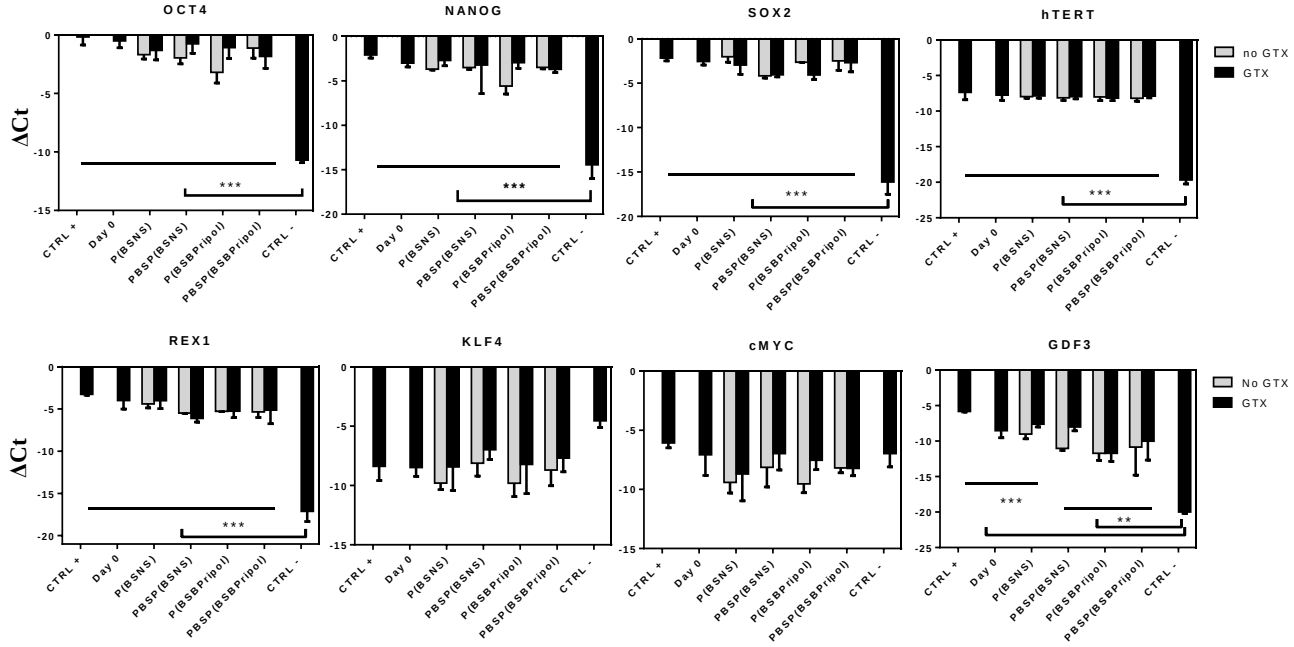

Figure 4.73. Gene expression profiles of the pluripotency markers *OCT4*, *NANOG*, *SOX2*, *hTERT*, *REX1*, *KLF4*, *cMYC* and *GDF3* of human iPSCs on scaffolds after 6 days of proliferation with and without GTX coating (data are representative of 3 independent experiments and expressed as mean ± SD). Significant differences are indicated as $P < 0.01$: ** versus control; $P < 0.001$: *** versus control.

As reported in Figure 4.73, it is possible to notice that iPSCs cultured on all the samples expressed many pluripotency factors analysed (*OCT4*, *NANOG*, *SOX2*, *hTERT*, *REX1*, *GDF3*). No relevant differences both between the 4 different scaffold types and between cells collected at day 6 compared to those collected at day 0 can be evidenced. Moreover, qRT-PCR data showed that the different scaffolds do not influence the pluripotency state, as the as the expression levels of the pluripotency genes are comparable to the standard control condition, even without the use of a thin Geltrex (GTX) coating.

4.9.7.2 Immunofluorescence analysis on human iPSCs on scaffolds

Human iPSCs pluripotency after 6 days of adhesion on GTX-coated copolymeric scaffolds was checked also by means of immunofluorescence analysis, in order to address the pluripotency at

the protein expression level (Figure 4.74). As a control, human iPSCs cultured feeder-free in Essential 8^{TM} medium after 6 days of adhesion were used.

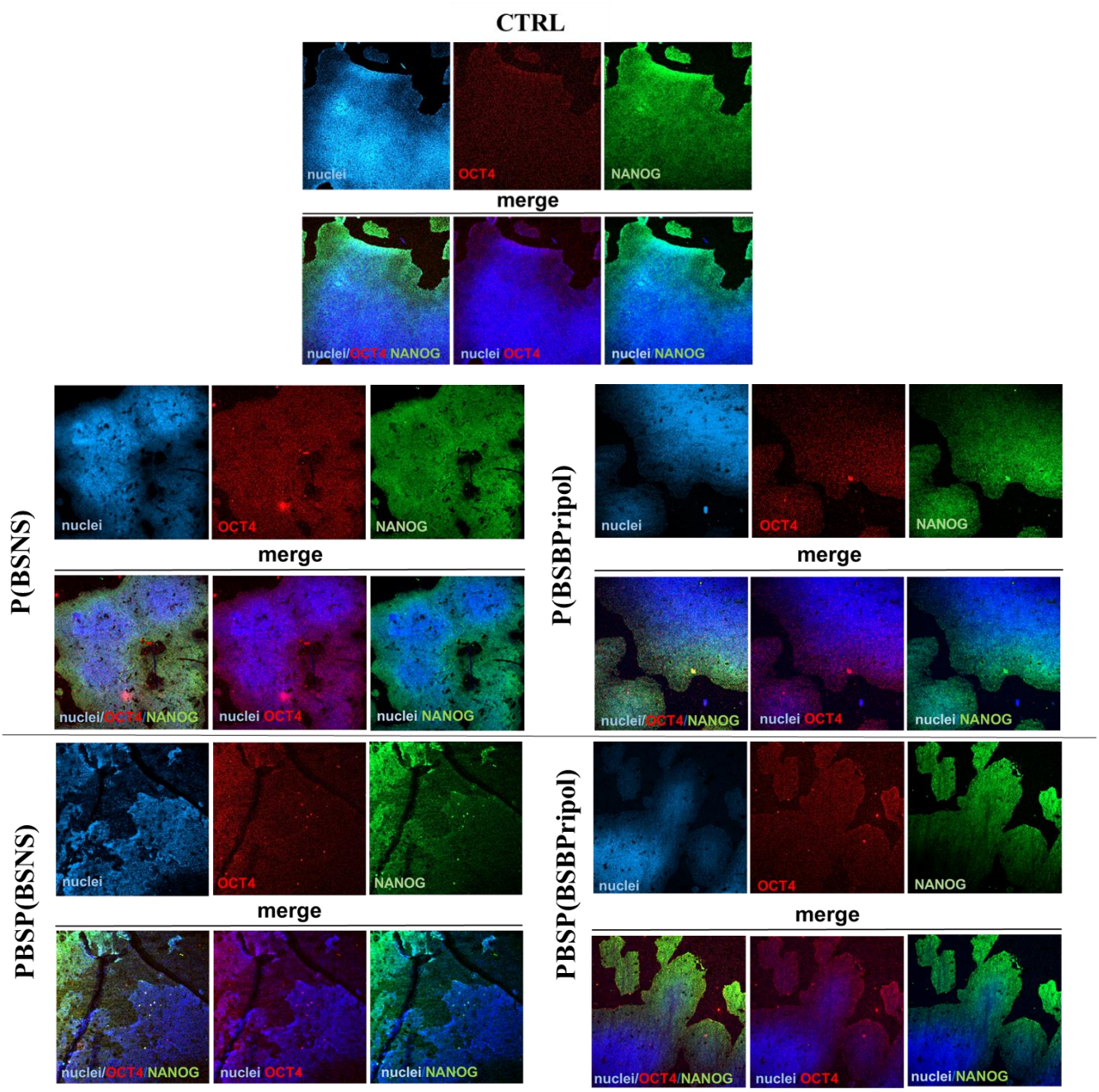

Figure 4.74. Immunofluorescence analyses for representative iPSC colonies after 6 days of proliferation expressing OCT4 (red) and NANOG (green). Nuclei were stained with Hoechst (blue). Magnification 5x.

Immunofluorescence analyses confirmed the pluripotency capacities of the iPSCs, expressing the markers OCT4 and NANOG, on the different scaffolds used for the present study.

Moreover, if compared to the control, iPSCs attempted to grow and proliferate properly in round and confluent colonies on each copolymeric support, which is particularly important for further differentiation experiments. Cell attachment on no coated scaffolds was lower (data not shown); for this reason, a thin layer of coating was used for further differentiation experiments, in order to obtain better adhesion.

4.9.7.3. Gene expression of HIPPO pathway

As reported from several studies the HIPPO pathway plays a key role in stem and progenitor cell expansion, in tissue regeneration and in the regulation of cardiomyocyte proliferation and maturation [De La Cruz et al., 2017]. HIPPO pathway has mechano-sensor properties, as its expression is influenced by the surface on which cells are cultured: YAP is an important regulator of the cell-matrix interface, as it controls the expression of genes involved in the composition and arrangement of the extracellular matrix, together with many components of cell mechanosome.

Moreover, this pathway is a kinase cascade involving mammalian STK3, STK4, LATS1 and LATS2. When it is activated, STK3 and STK4 phosphorylate activate LATS1/2 kinases, which directly inactivate Yes-associated protein (YAP) and transcriptional coactivator with PDZ-binding motif (TAZ), the two principal functional output. In this case, phosphorylated forms of YAP and TAZ are located in the cytoplasm, where they undergo degradation. Rather, active, thus unphosphorylated, YAP and TAZ migrate into the nucleus and regulate the expression of many target genes, including *CTGF, ANKRD* and *CYR61*.

To evaluate the activation of the HIPPO pathway in human iPSCs grown on each copolymeric scaffold after 6 days from the seeding, gene expression analysis was performed for the markers *YAP, TAZ, STK3, STK4, LATS2, CYR61, CTGF* and *ANKRD.* Human iPSCs collected at day 6 after seeding were used as control (Figure 4.75).

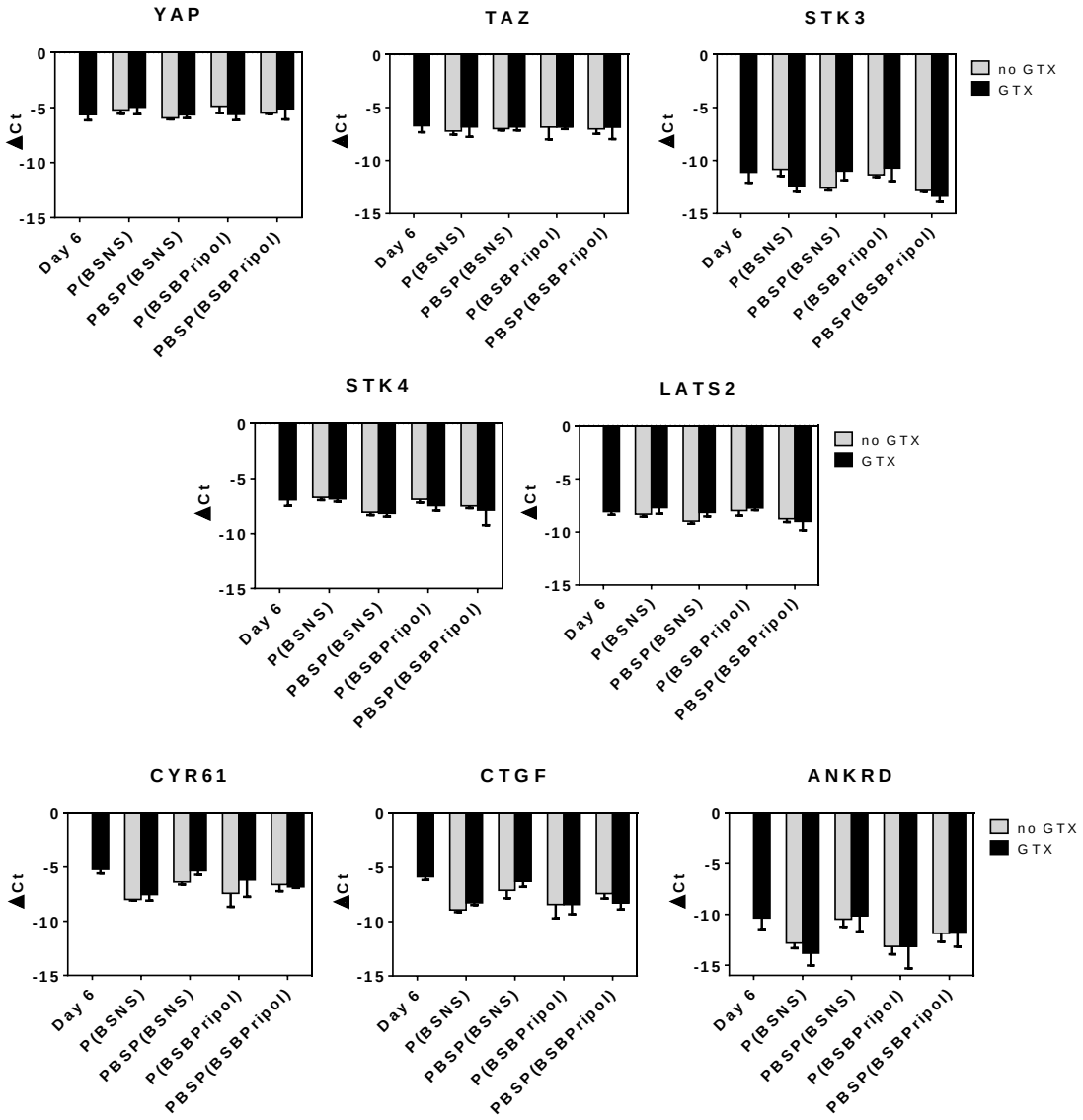

Figure 4.75. HIPPO pathway gene expression profiles (*YAP*, *TAZ*, *STK3*, *STK4*, *LATS2*, *CYR61*, *CTGF* and *ANKRD* markers) of human iPSCs on scaffolds after 6 days of proliferation with and without GTX coating (data are representative of ≥ 2 independent experiments and expressed as mean ± SD).

As regards pluripotency, it is possible to see that the thin GTX coating does not change the expression profiles of the HIPPO pathway mediators, thus meaning that it is possible to investigate the direct effect of the polymeric scaffolds on the pathway expression. This is true for all the scaffolds under study. From data shown in Figure 4.75, it seems that there are some differences between the four samples regarding gene expression of these markers. In particular, in the case of the two random copolymers P(BSNS) and P(BSBPripol), YAP seems to be more active, as *CYR61*, *CTGF* and *ANKRD* markers seem to be lower expressed if compared to the

values obtained from the block copolymers PBSP(BSNS) and PBSP(BSBPripol). As expected, gene expression of the markers *YAP, TAZ, STK3, STK4* and *LATS2* is the same for all the samples, because differences become relevant only at protein level.

4.9.7.4 Gene expression of integrins

Integrins are surface receptors involved in cells adhesion, migration and survival, as they are responsible for the interaction between cells and extracellular matrix (ECM). The binding between ECM proteins and integrin receptors is not specific: a ligand can interact with many different integrin receptors and, vice-versa, an integrin can bind with different ligands.
Integrins are also responsible for both ectodermal (α6, αv, β1, β3, β5), mesodermal (α5, α6, β1), and endodermal (α5, αv, β1, β3, β5) differentiation [Sun et al., 2013]. More in details, from the ectoderm germ layer starts the differentiation of neural tube and neural crest, the mesoderm one can potentially differentiate in skeletal, cardiac and vascular tissue, while the endoderm germ layer can develop into organs like liver, pancreas, intestines, and can also promote mesodermal differentiation.

In Figure 4.76 the gene expression analysis of some α and β integrins in human iPSCs grown on each copolymeric scaffold after 6 days from the seeding is reported.

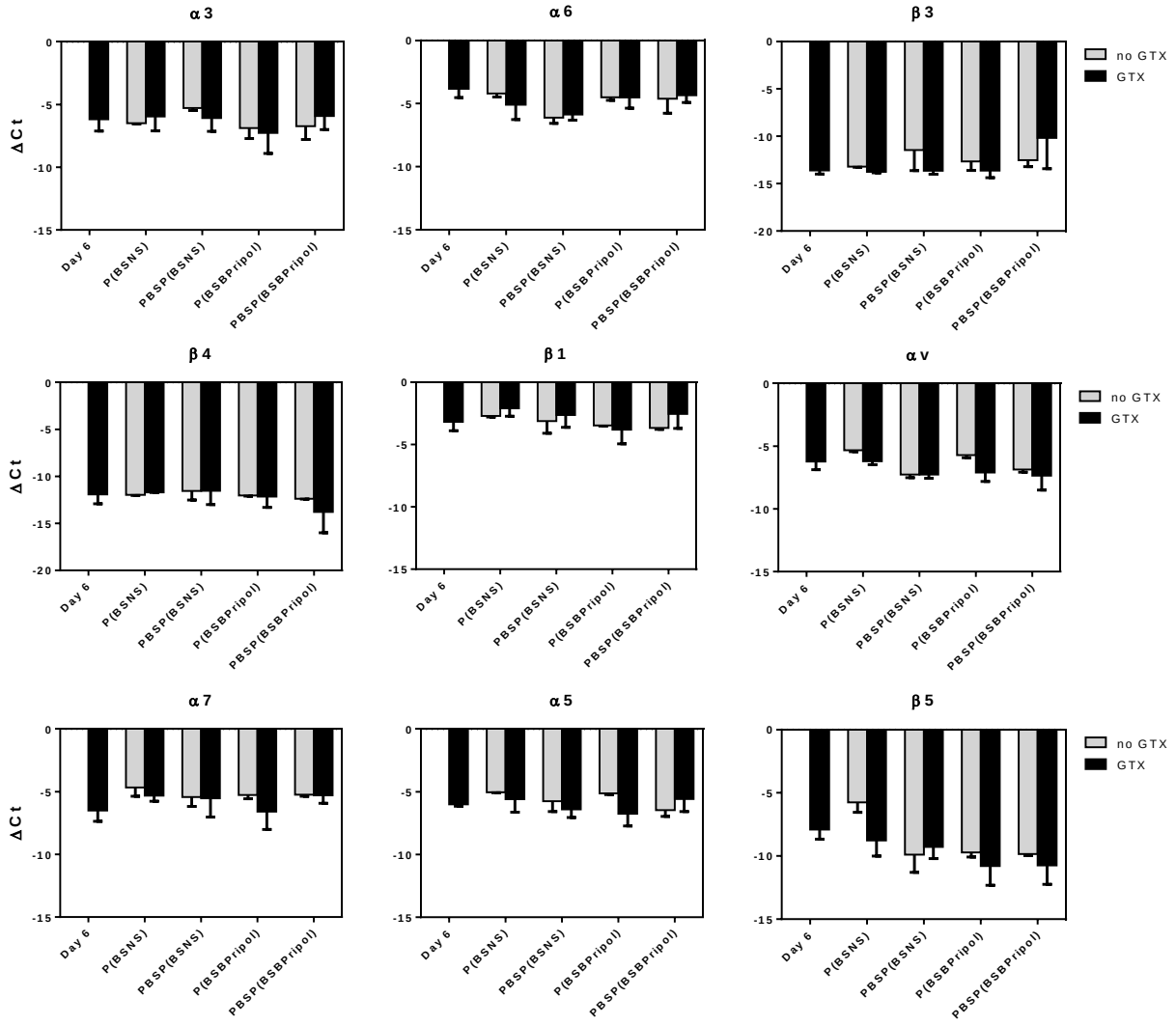

Figure 4.76. Gene expression profiles of the integrins α3, α6, β3, β4, β1, αv, α7, α5 and β5 of human iPSCs on scaffolds after 6 days of proliferation with and without GTX coating (data are representative of 3 independent experiments and expressed as mean ± SD).

From the data collected it seemed that there were no significant differences between all the scaffolds on undifferentiated iPSC samples, with or without the presence of GTX coating. As a result, copolymeric materials did not negatively affect human iPSCs attachment.

4.9.7.5 Human iPSCs cardiac differentiation: gene expression of differentiation markers

Cardiac differentiation experiments were carried out on random copolymeric scaffolds P(BSNS) and P(BSBPripol), in order to check if the presence of ramifications of different length, keeping the same molecular architecture, is capable to affect cells behavior.

As regards gene expression analysis on human iPSCs differentiated towards cardiomyocytes on scaffolds, some markers related to different stages of differentiation were taken into account: *OCT4* for the pluripotency, *BRACH* for early mesoderm differentiation, *NKX2.5* and *GATA4* for cardiac progenitors, and *MYHC* and *TNNT2* for later differentiation stages.

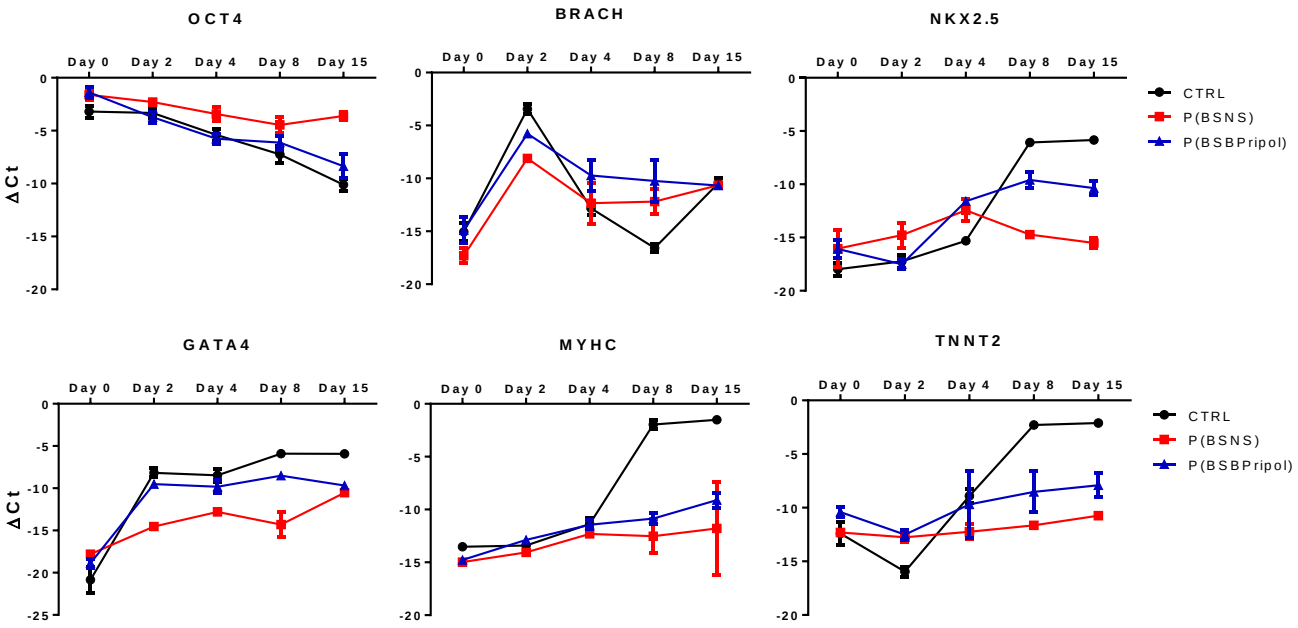

Figure 4.77. Gene expression profiles of the differentiation markers *OCT4*, *BRACH*, *NKX2.5*, *GATA4*, *MYHC* and *TNNT2* of human iPSCs-derived cardiomyocytes (iPSC-CMs) differentiated on scaffolds with GFR coating (data are representative of ≥ 2 independent experiments and expressed as mean ± SD).

As reported in Figure 4.77, the pluripotency marker *OCT4* gene expression is downregulated during cardiac differentiation both for iPSCs used as control and for iPSCs differentiated on P(BSBPripol) scaffolds, while it remains upregulated for cells differentiated on P(BSNS) scaffolds. In this latter case, the pluripotency is maintained, and the differentiation is delayed. The typical trend of *BRACH* gene expression during differentiation, which is characterized by an upregulation peak at day 2, is present for all the samples analysed, even though it is less remarkable for P(BSNS) sample. At the cardiac progenitor level (*NKX2.5* and *GATA4*) it is

possible to see an upregulation starting from day 2 for *GATA4* and at day 8 for *NKX2.5*, respectively. This trend is quite similar for both the control and P(BSBPripol) samples, while is more downregulated than P(BSNS), in particular from day 4 onwards. As to late differentiation markers, such as *MYHC* and *TNNT2*, there are many differences between the gene expression of the control and that of cells differentiated on scaffolds, particularly evident after day 4, when a remarkable upregulation of the control is evident. This behavior can be explained on the basis of the differences between copolymeric scaffolds, ascribable to the presence of side alkyl group with different length.

4.9.7.6 Immunofluorescence analysis on human iPSCs differentiated on scaffolds

Human iPSC differentiation towards cardiomyocytes on GFR-coated copolymeric scaffolds was checked by means of immunofluorescence analysis, in order to confirm the results obtained by gene expression after 6 days of differentiation (Figure 4.78). Human iPSCs differentiated under normal culturing conditions without scaffold at the same timepoint were used as control.

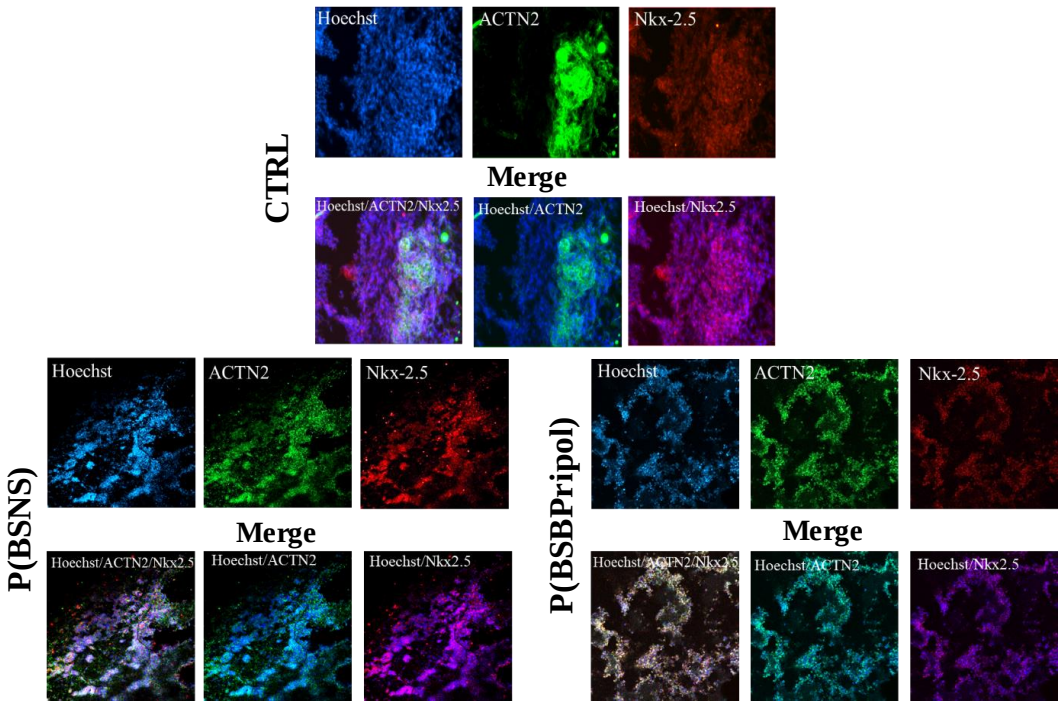

Figure 4.78. Immunofluorescence analyses for representative iPSC-derived cardiomyocytes (iPSC-CMs) expressing ACTN2 (green) and NKX2.5 (red). Nuclei were stained with Hoechst (blue). Magnification 20x.

Immunofluorescence analysis showed the presence of differentiated iPSC-CMs expressing the early cardiac progenitor marker NKX2.5 (red, inside the nuclei) and the later-stage cardiomyocyte marker ACTN2 (green, in the cytoplasm/cell membrane) on both the scaffolds under investigation. Protein expression levels of ACTN2 in cells differentiated on scaffold seemed to be less evident than those in cells differentiated under normal conditions, probably because on scaffolds, under the operating conditions adopted, later differentiation stages are more difficult to be reached.

4.9.7.7 Gene expression of HIPPO pathway on differentiated iPSCs

From the analysis of the expression of genes involved in the HIPPO pathway in human iPSCs differentiated on scaffolds (Figure 4.79), it is possible to notice that no significant differences between the samples and the control markers are present for *YAP*, *TAZ*, *STK4* and *LATS2*, as already observed for undifferentiated iPSCs, since, at this stage of differentiation, differences start to appear only at the protein level. On the contrary, gene expression of *CYR61*, which plays a key role in cell adhesion, migration, proliferation, survival, and differentiation through binding to integrin receptors [Mo et al., 2006] and *CTGF* is particularly interesting: cells differentiated on P(BSBPripol) scaffold had the same behaviour as the control. More in details, at day 0 of differentiation gene expression was upregulated, at day 2 becomes downregulated and then again upregulated from day 4 onwards. From these results, it seemed that YAP is active (located in the nucleus) at day 0, then phosphorylated at day 2 (in the cytoplasm) and again active at later stages (again in the nucleus). On the contrary, cells differentiated on P(BSNS) scaffolds did not show the downregulation peak at day 2, thus indicating that on this scaffold cells might keep more their pluripotency or that the mechanical properties of the copolymeric support (such as stiffness and elastic modulus) affect the mechanosensory activity of the HIPPO pathway.

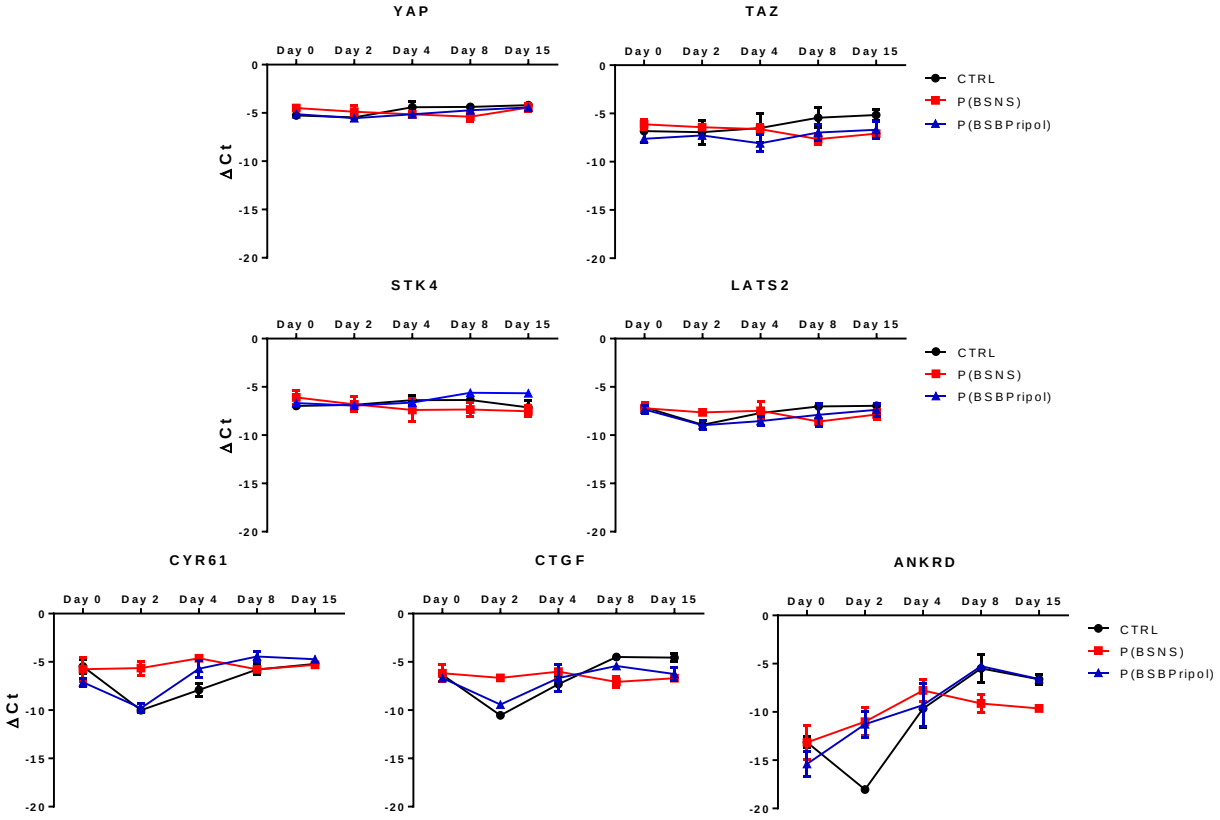

Figure 4.79. HIPPO pathway gene expression profiles (*YAP*, *TAZ*, *STK4*, *LATS2*, *CYR61*, *CTGF* and *ANKRD* markers) of human iPSCs-derived cardiomyocytes (iPSC-CMs) differentiated on scaffolds with GFR coating (data are representative of ≥ 2 independent experiments and expressed as mean ± SD).

To confirm this hypothesis, in Figure 4.80 the immunofluorescence analysis on control human iPSC-CMs differentiated at day 0 and day 2, respectively, for YAP, WNT and BRACH markers is reported [Duelen et al., data unpublished].

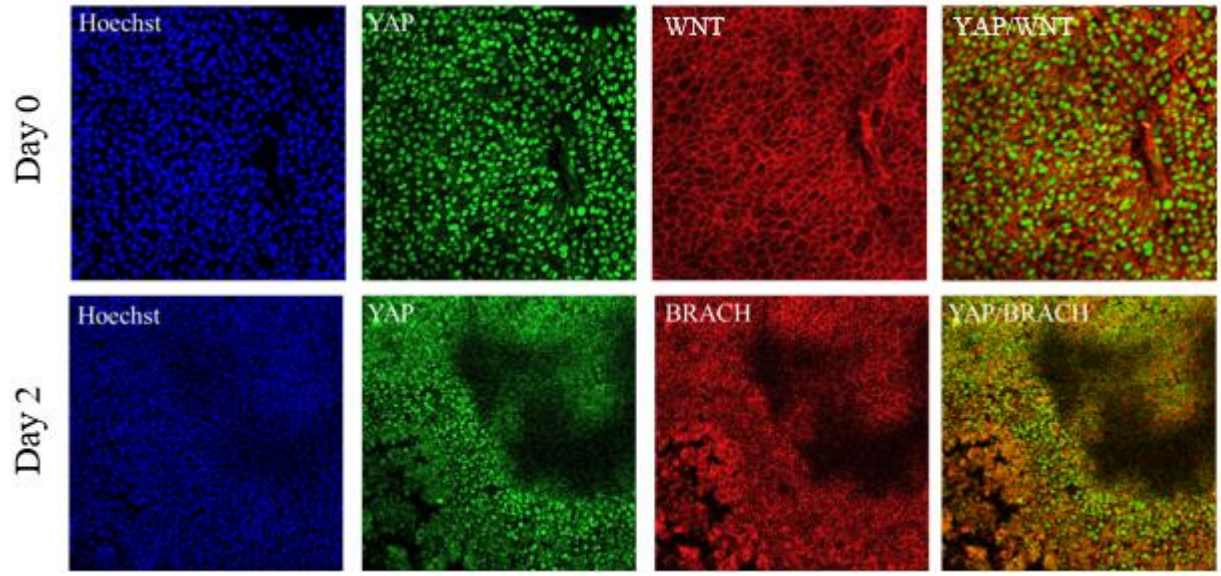

Figure 4.80. Immunofluorescence analysis on control human iPSCs differentiated at day 0 and day 2, respectively, for YAP, OCT4 and BRACH markers (magnification 20X).

As it can be clearly seen, at day 0 YAP is located inside the nuclei, while at day 2 is more spread also in the cytoplasm. Moreover, while WNT is located around cells at day 0, BRACH at day 2 is more spread also inside cells, thus indicating that at day 0 YAP is active, and becoming less active at day 2.

4.9.7.8 Gene expression of integrins on differentiated iPSCs

Gene expression of integrins on human iPSC-CMs differentiated on copolymeric scaffolds was carried out to understand whether copolymeric scaffolds support differentiation and to which germinal layer.

In Figure 4.81 gene expression analysis of some α and β integrins in human iPSCs differentiated towards cardiomyocytes on each copolymeric scaffold is reported. Cells differentiated under normal culturing conditions were used as control. As it can be seen, also in this case cells differentiated on P(BSBPripol) seemed to better mimic the behaviour of control cells. This is true for β1, β3, β5, α5 and αv. As to α5, which is responsible of endo- and mesodermal differentiation, its expression on P(BSBPripol) scaffold turned out to be upregulated as well as that of the control. For this reason, it seemed that P(BSBPripol) copolymeric scaffold supported better cardiac differentiation than P(BSNS), in which α5 gene expression was more downregulated.

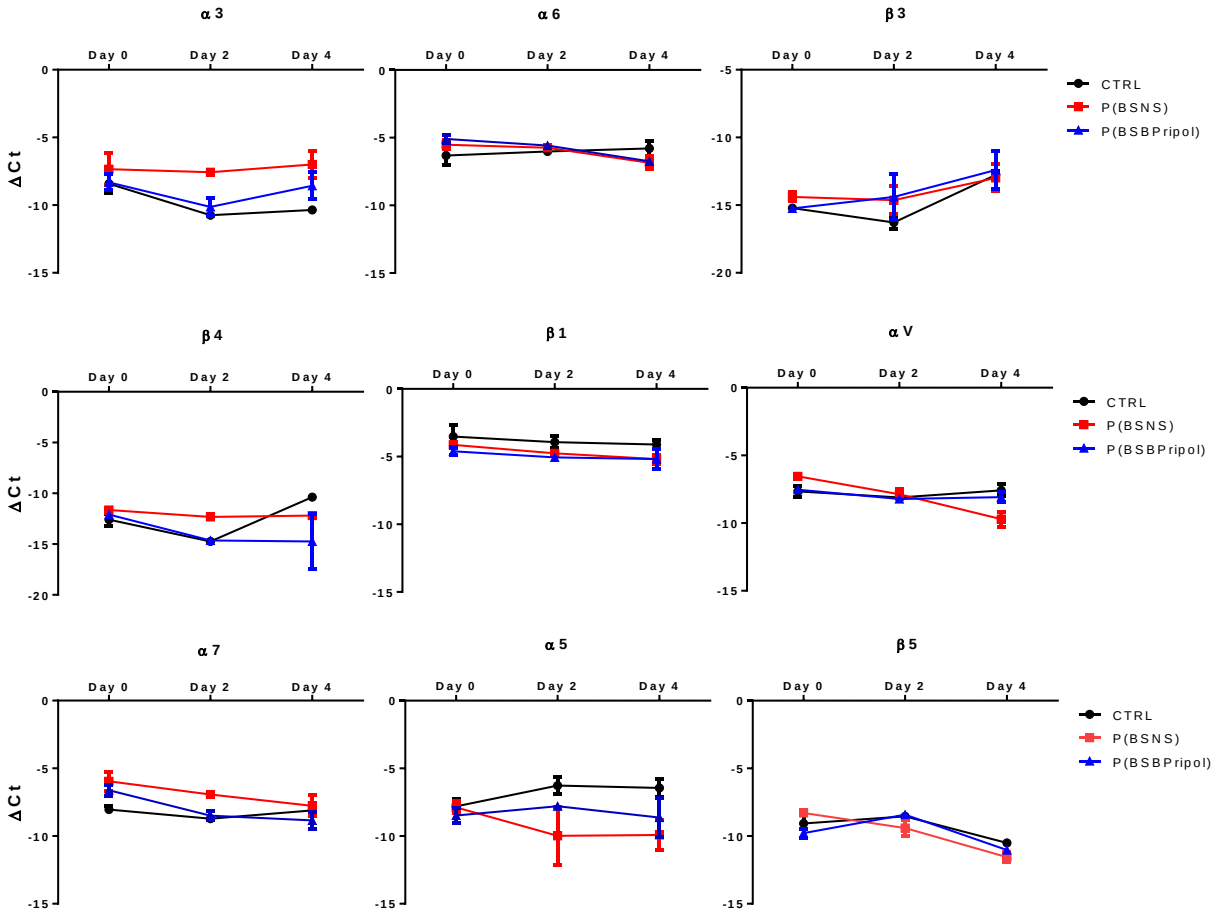

Figure 4.81. Gene expression profiles of the integrins α3, α6, β3, β4, β1, αv, α7, α5 and β5 of human iPSCs-derived cardiomyocytes (iPSC-CMs) differentiated on scaffolds with GFR coating (data are representative of ≥ 2 independent experiments and expressed as mean ± SD).

4.9.8 Conclusions

As cardiac disorders are the major cause of death in the world, many efforts have been made to find therapies that can heal and recover these diseases avoiding at the same time the irreversible loss of cardiac tissue. In this framework, a key role is played by tissue engineering, a multidisciplinary field that starting from 3-dimensional supports (scaffolds), cells and growth factors aims to regenerate functional tissues. As regards scaffolds, in the present study new poly(butylene succinate) (PBS)-based copolymers were synthesized and characterized as potential candidates for cardiac tissue engineering applications. Simply by varying the comonomeric units (containing both short and long ramifications) and the molecular architecture (random or block one) it was possible to obtain four different materials with

different chain flexibility and crystallinity degree, which are able to affect functional properties such as mechanical behaviour and biodegradation rate. In addition, the optimization of electrospinning process allowed the fabrication of nanofibrous scaffolds characterized by high flexibility and elastic modulus comparable to that of cardiac tissue. As to hydrolytic degradation studies, block copolymers showed a lower degradation rate than PBS, whereas the random ones, in particular P(BSBPripol), were characterized by the highest biodegradability. These results confirm that simply by acting on the chemical structure, as well as on the molecular architecture, it is possible to tailor ad hoc the degradation kinetics.

In addition, PBS-based copolymer scaffolds have been subjected to several biocompatibility studies: first, human induced Pluripotent Stem cells (iPSCs) growth and proliferation was checked by gene expression analysis and immunofluorescence staining. From this preliminary investigation, it is possible to say that all the materials supported cells growth and proliferation. Moreover, the pluripotency was kept in all cases. In addition, differentiation experiments were carried out on random copolymeric scaffolds. From gene and protein expression experiments, it is possible to say that P(BSBPripol) better supported differentiation into cardiomyocytes than P(BSNS), even though the protocol worked only until earlier differentiation stages, probably due to the inappropriate initial seeding density.

In conclusion, the copolymerization strategies adopted turned out to be successful: in fact, it was possible to improve the unsatisfactory properties of PBS, making it more suitable for soft tissue engineering applications. Furthermore, electrospinning has proved to be a simple and versatile technique, which allowed to obtain engineered constructs with controlled morphology, able to support cells growth, proliferation and even cardiac differentiation.

4.10 New nano- and microparticles from PLLA-based triblock copolymers for controlled drug release

Novel A-B-A triblock copolymers of polylactic acid (PLLA), with chemical structure designed *ad hoc* to prepare micro- and nanoparticles for controlled drug delivery, were synthesized. The A block is PLLA, whereas B block is an equimolar copolymeric system poly(butylene/triethylene succinate) with different sequence length: in particular, a block copolymer with long sequences and a random one with short sequences randomly distributed were prepared [Gualandi at al., 2012 (a)].

The so-obtained materials were characterized from the molecular and thermal point of view. In addition, to investigate the effect of both chemical structure and molecular architecture of the polymers synthesized on drug release kinetics, Dexamethasone-encapsulated micro- and nanoparticles were prepared by oil-in-water miniemulsion technique and subjected to thermal and morphological characterization. After that, drug release studies were carried out. The effect of particles size on release profile was also evaluated.

4.10.1 Synthesis, molecular and surface characterization

OH-terminated Poly(butylene succinate) (PBS-OH) and poly(triethylene succinate) (PTES-OH) were synthesized by two-step melt polycondensation, according to the procedure described in paragraph 3.2.1.2, using $Ti(OBu)_4$ (TBT) as catalyst. Their molecular weight, which is reported in Table 4.1, was determined by ^{1}H-NMR spectroscopy.

Both the spectra were consistent with the expected structure. As to PBS-OH spectrum, it was already described in Paragraph 4.9.1.

As to PTES-OH spectrum, the methylene protons of the glycolic subunit (4H, t), (4H, t) and (4H, s) are located at δ 4.25 ppm, δ 3.7 ppm and δ 3.64 ppm, respectively, while the singlet of the acid subunit (4H, s) is situated at δ 2.65 ppm. Besides the signals of the aliphatic protons of the inner repetitive units, the peak due to the outer glycolic subunits (2H, t) can also be detected at δ 3.68 ppm, partially overlapped with the inner glycolic peak.

The polymer degree of polymerization (DP) has been calculated from the relative areas of protons of central triethylene glycol and protons of terminal triethylene glycol, according to Eqn. [33].
The intensity of the hydrogens of the outer glycol subunit was calculated subtracting the area of the protons in α position with respect to the ester oxygen (δ 4.25 ppm), from the area of the peak of both protons in β position to the ester oxygen and protons of the outer glycol subunit (δ 3.70 ppm). The polymer molecular weight (M_n) has been obtained according to Eqn. [34], where in this case W_{ru} and W_{glycol} are the molecular weights of the TES repeating unit and the triethylene glycol, respectively.

After that, poly(butylene/triethylene succinate) P(BS_xTES_y)-OH copolymers with same composition (equimolar amounts of comonomeric units) but different block length (indicated by x and y) were obtained by reactive blending (see Paragraph 3.2.2). Both copolymers have been purified. In particular, P($BS_{13}TES_{12}$)-OH is a block copolymer, while P(BS_2TES_2)-OH is characterized by a random distribution of comonomeric sequences. Their molecular weight, as well as their actual composition, degree of randomness b and block length L were determined by ^{1}H-NMR spectroscopy. All these values are reported in Table 4.39, while in Figure 4.82 the P($BS_{13}TES_{12}$)-OH spectrum is shown with the relative chemical shifts assignment.

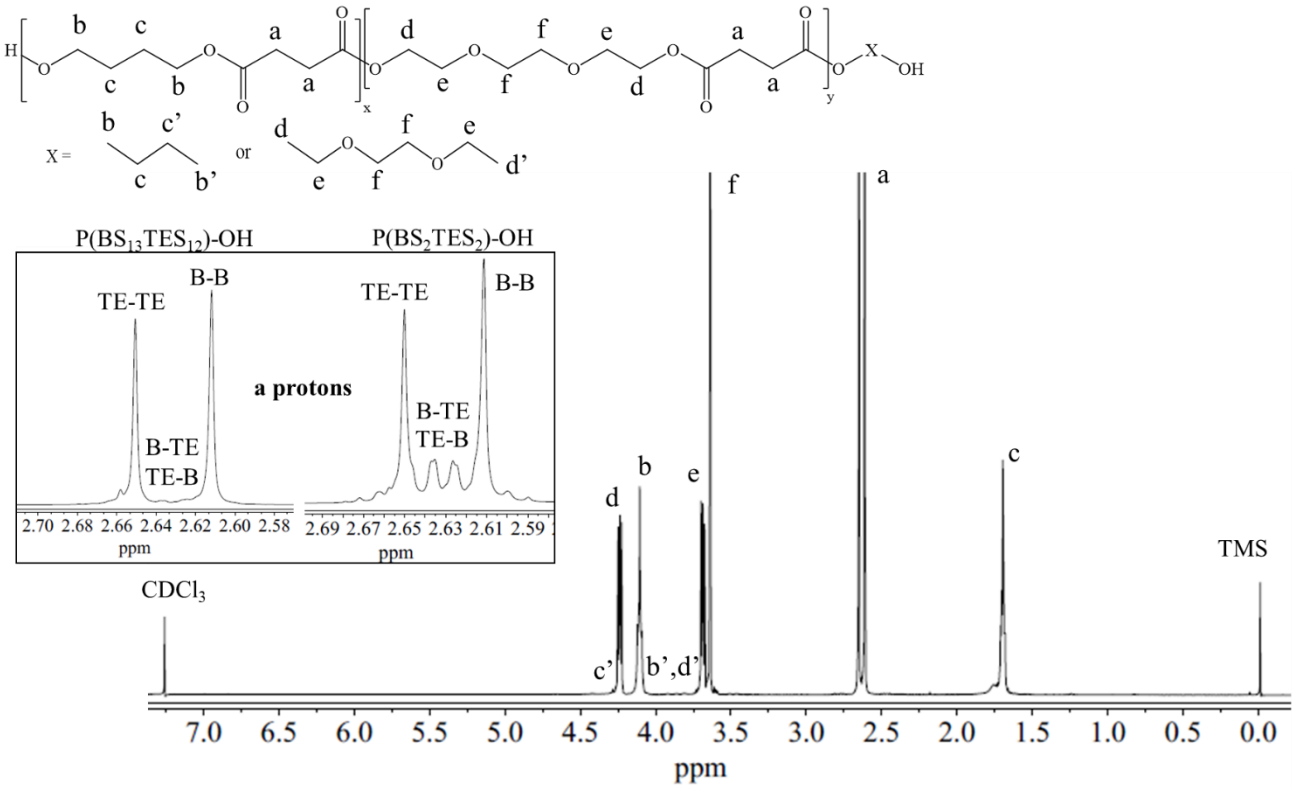

Figure 4.82. ^{1}H-NMR spectrum of P($BS_{13}TES_{12}$)-OH with peak attribution. In the insertion, a protons chemical shift of both P($BS_{13}TES_{12}$)-OH and P(BS_2TES_2)-OH is evidenced.

In the spectrum reported in Figure 4.82, the peaks related to both the BS and TES units are evident. The copolymer composition was calculated from the relative areas of the ^{1}H-NMR resonance peaks related to b protons of butanediol subunit, located at δ 4.19 ppm and d protons associated with the triethylene glycol subunit, located at δ 4.25 ppm. The actual molar composition was very close to the feed one (BS: 53 mol%; TES: 47 mol%).

The two copolymers differ in block length, as it can be seen from the region between 2.65 e 2.61 ppm in which the a protons related to succinic subunit are present (see insertion in Figure 4.82). In particular, the a protons related to succinic unit of BS segments are located at δ 2.61 ppm, while those of TES segments are located at δ 2.65 ppm. As it can be seen, other peaks are also evident, due to the presence of mixed sequences, (i.e. succinic unit linked to butanediol on one side and to triethylene glycol on the other). The intensity of these peaks increases with reaction time.

Copolymeric architecture is related to the degree of randomness b, which can be calculated according to the Eqn. [28], where P_{X-Y} (P_{TE-B}) represents the probability to find a TE subunit near a butylene one and P_{Y-X} (P_{B-TE}) represents the probability to find a butylene subunit near a

TE one. These parameters can be expressed according to Eqn. [29] and Eqn. [30], where I_{X-Y} (I_{TE-B}), I_{Y-X} (I_{B-TE}), I_{X-X} (I_{TE-TE}) and I_{Y-Y} (I_{B-B}) indicate the integral intensities of a protons in TE-B, B-TE, TE-TE and B-B sequences, respectively. TES and BS block length, L_{TES} and L_{BS}, whose values are listed in Table 4.39, were calculated from Eqn. [31] and Eqn. [32], respectively. From the results obtained, it is clear that L values decrease and b value increases with reaction time, according to transesterification reaction progress.

Also for P(BS_xTES_y)-OH copolymers the molecular weight M_n was obtained by ^{1}H-NMR analysis, according to Eqn. [34], and reported in Table 4.39. Also in this case, DP was calculated from Eqn. [33], where I_{Ext} corresponds to $I_{b'}$ and $I_{d'}$, which are the integrals related to protons of the outer glycol subunits b' e d', while I_{Int} corresponds to the integrals related to protons of the inner glycol subunits b and d (I_b and I_d). The intensity of d' integral was calculated subtracting the area of d protons from the area related to e + d' protons, as the relative areas of d and e protons present the same value.

Table 4.39. Molecular characterization data of PBS-OH, PTES-OH, P($BS_{13}TES_{12}$)-OH and P(BS_2TES_2)-OH obtained by ^{1}H-NMR.

Polymers	M_n	BS (mol%)	TES (mol%)	b	L_{BS}	L_{TES}
PBS-OH	4900	100	-	-	-	-
PTES-OH	14100	-	100	-	-	-
P($BS_{13}TES_{12}$)-OH	15900	53	47	0.16	13	12
P(BS_2TES_2)-OH	16700	53	47	1	2	2

After that, A-B-A triblock copolymers were synthesized by Ring Opening Polymerization (according to the procedure reported in Paragraph 3.2.3) between L-lactide, (A block) and the two P(BSTES)-OH copolymers (B block). PLLA homopolymer was also synthesized for sake of comparison, using a small amount of 1,4-butanediol as initiator. According to its ^{1}H-NMR spectrum (not shown), resonance peaks of Lactic acid repeating unit are present at δ 5.21 ppm and at δ 1.59 ppm; together with those at δ 3.76 ppm (4H, t) and at δ 1.74 ppm (4H, m), respectively, ascribable to the initiator (butanediol).

In Figure 4.83 ^{1}H-NMR spectrum of the triblock copolymer PLLAP(BS$_2$TES$_2$) is shown. In this case a, b, c, d, e and f peaks related to P(BS$_2$TES$_2$)-OH copolymer are present, as well as g and h signals of the lactic subunit.

The actual weight composition, calculated from the relative areas of the peak corresponding to g protons of PLLA and of a protons of the acid subunit in the central block P(BSTES), resulted very close to the feed one (Table 4.40).

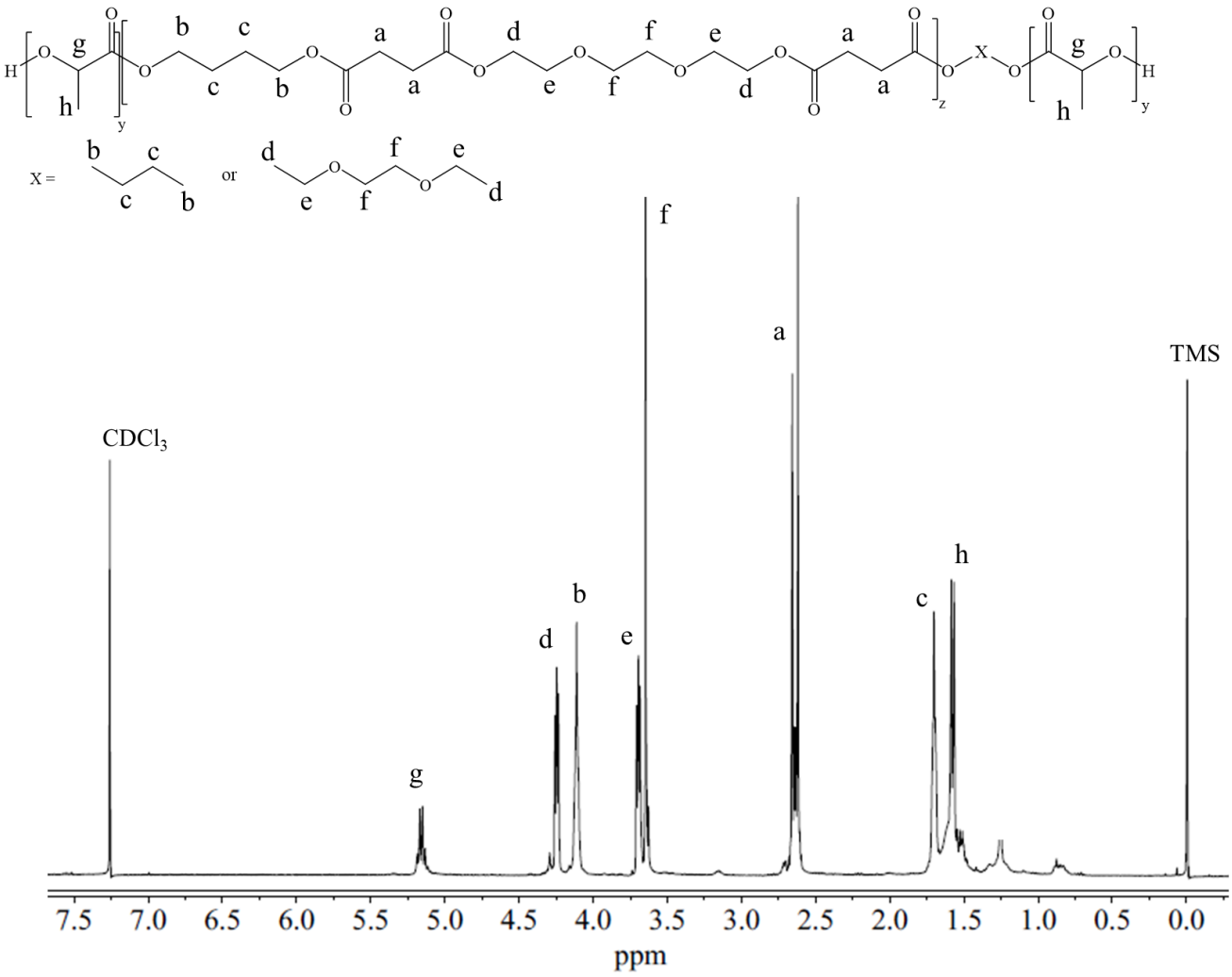

Figure 4.83. ^{1}H-NMR spectrum of PLLAP(BS$_2$TES$_2$) with peaks attribution.

In Table 4.40 the molecular weights of the so-obtained polymers obtained by GPC analysis are listed: in all cases, the polydispersity index D is low and the molecular weights comparable to each other.

Table 4.40. Surface and molecular characterization data of the homopolymer PLLA and of the triblock copolymers: *data obtained by GPC analysis and ** data obtained from ^{1}H-NMR analysis.

Polymers	M_n (g/mol)*	D*	PLLA (wt%)**	P(BSTES) (wt%)**	WCA (°)
PLLA	19300	1.2	100	-	95±3
PLLAP($BS_{13}TES_{12}$)	16600	1.4	30	70	80±4
PLLAP(BS_2TES_2)	17500	1.4	33	67	89±3

As to wettability measurements, WCA values are listed in Table 4.40: both the copolymers turned out to be more hydrophilic than the homopolymer PLLA. The reduction of the WCA values obtained by copolymerization can be explained as due to the introduction of ether oxygen atoms in the central B blocks. These oxygen atoms, which are characterized by high electronegativity, render the macromolecules more polar. Moreover, PLLAP($BS_{13}TES_{12}$), with its block structure, is more hydrophilic than PLLAP(BS_2TES_2) (WCA = 80° and 89°, respectively). Such behavior is in perfect agreement with previous studies, showing that in P(BSTES) block copolymers the TES sequences, characterized by higher water affinity, migrate towards the surface. Conversely, in P(BSTES) random copolymers TES and BS sequences are too short to rearrange and migrate [Gualandi et al., 2012 (a)].

4.10.2 Thermal and structural characterization

All the synthesized polymers have been subjected to thermogravimetric analysis under dry nitrogen atmosphere. TGA curves are shown in Figure 4.84. PBS-OH, PTES-OH, P($BS_{13}TES_{12}$)-OH and P(BS_2TES_2)-OH present a comparable thermal stability, in all cases higher than that of PLLA. Weight loss occurs in one step and is around 100%, apart from PTES, which loses only 92%. Regarding the triblock copolymers, TGA curves are located between those of PLLA and those of hydroxy-terminated polymers. In this case, thermal degradation takes place in two steps. The relative height of these two steps clearly depends on the composition: the higher the PLLA content, the more intense is the first weight loss. This is an indication that the second stage is due to P(BS_xTES_y) copolymers degradation. Anyway, the temperature of the initial degradation in the PLLA-based copolymers is comparable to that of PLLA homopolymer. In addition, PLLAP($BS_{13}TES_{12}$) is more thermally stable than PLLAP(BS_2TES_2).

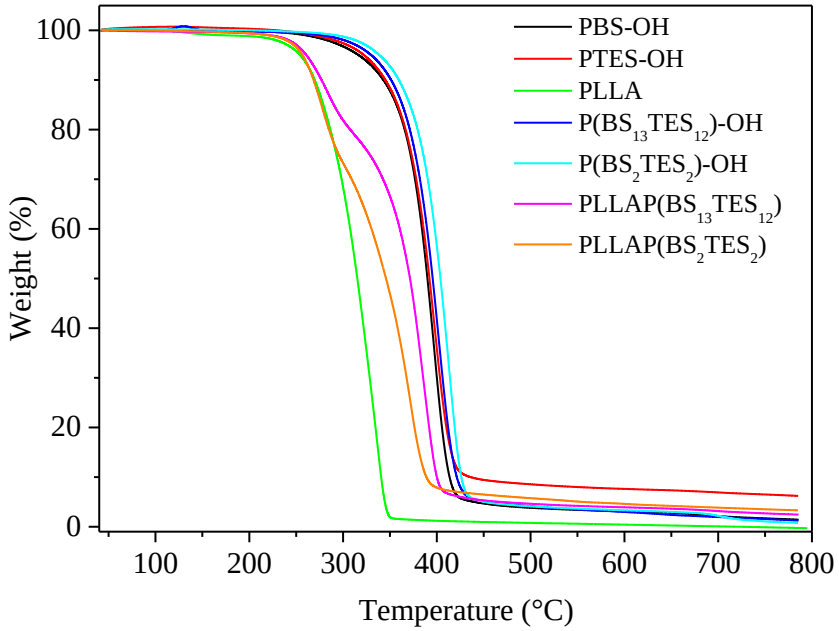

Figure 4.84. Thermogravimetric curves of the polymers under study (10°C/min).

Calorimetric curves of the materials under investigation are shown in Figure 4.85, while calorimetric data are listed in Table 4.41.

Table 4.41. Thermal characterization data by DSC analysis and crystallinity degree values by WAXS analysis.

Polymers	I scan						II scan						X_c %
	T_g °C	Δc_p J/g°C	T_m °C	ΔH_m J/g	T_c °C	ΔH_c J/g	T_g °C	Δc_p J/g°C	T_m °C	ΔH_m J/g	T_c °C	ΔH_c J/g	
PBS-OH	-22	0.275	115	82	-	-	-23	0.254	115	63	-	-	41
PTES-OH	-33	0.914	-	-	-	-	-33	0.853	-	-	-	-	-
P(BS$_{13}$TES$_{12}$)-OH	-30	0.473	113	42	-	-	-27	0.448	113	37	-	-	25
P(BS$_2$TES$_2$)-OH	-32	0.832	61	39	-	-	-31	0.568	-	-	-	-	24
PLLA	40	0.277	165	56	-	-	20	0.489	121	40	68	39	50
PLLAP(BS$_{13}$TES$_{12}$)	-18 40	0.357 0.132	106 132	30 3	-	-	-16	0.462	105 132	24 3	29	10	28
PLLAP(BS$_2$TES$_2$)	-28	0.458	55 144	9 13	-	-	-19	0.508	142	13	82	2	24

All the hydroxy-terminated samples, apart from PTES-OH, are characterized by the same phase behaviour: more in details, they are semicrystalline, being the corresponding calorimetric traces characterized by a melting endotherm (see Figure 4.85 left). Considering the amorphous

behaviour of PTES homopolymer, the endothermic peaks observed should be attributed to PBS crystalline phase.

In P(BS_xTES_y)-OH copolymers, both the position and the intensity of the endotherms are related to BS and TES block length: as a matter of fact, T_m and ΔH_m values are lower as the block length decreases. Moreover, peak width is higher than that of the parent homopolymer, thus suggesting the presence of a crystalline phase characterized by a wide range of degrees of perfection.

It is also interesting that T_m of ($BS_{13}TES_{12}$)-OH block copolymer is very similar to T_m of PBS-OH: the corresponding values are 113 °C and 115 °C, respectively. A possible explanation to this behaviour is the presence, in the copolymer, of BS segments long enough not be affected by the presence of TES sequences. On the other hand, DSC curve of the random copolymer P(BS_2TES_2)-OH shows multiple endothermic phenomena, which can be ascribed to fusion and recrystallization processes typical of polyesters.

As to the two triblock copolymers PLLAP($BS_{13}TES_{12}$) and PLLAP(BS_2TES_2), the DSC curves show multiple endotherms located at very different temperatures. More in details, peaks appearing at lower temperatures can be associated to the melting of BS segments, while peaks at higher temperatures are related to the melting of PLLA blocks.

From data collected in Table 4.41, it is clear that T_m of triblock copolymers are similar to those of their parent homopolymers, even though their relative ΔH_m values are much lower. This result confirms the good control over the ROP synthetic process, i.e. the occurrence of transesterification reactions between both BS and TES units and between PLLA and BS or TES units can be excluded.

Concerning the glass transition temperatures, both PBS-OH and PTES-OH homopolymers present T_g values below room temperature, a confirmation of the mobility of their amorphous phase. Conversely, PLLA is characterized by a rigid amorphous phase, being its glass transition well above room temperature (T_g = 40 °C).

P(BS_xTES_y)-OH copolymers have T_g values similar to those of their parent homopolymers, probably because of the very similar values of T_g of PBS-OH and PTES-OH. [Gualandi at al., 2012 (a)]. As to triblock copolymers, PLLAP($BS_{13}TES_{12}$) shows two different glass transitions at different temperatures, thus indicating the presence of two amorphous phases with different mobility. More in details, T_g at higher temperature corresponds to T_g of PLLA: this amorphous phase is characterized by the presence of pure PLLA. On the contrary, the other T_g value is

higher than that of the P(BSTES) central block (-18 °C *vs.* ≈ -30 °C, respectively). This behaviour indicates a partially miscible P(BSTES)-rich phase. As to the other triblock copolymer, PLLAP(BS_2TES_2), it is expected to present the same glass transition behaviour. However, in this case the T_g value at higher temperature is not visible, being hidden by the lower melting peak.

As it can be seen from the second scan traces, after melt quenching both the copolymers show only one glass transition, thus indicating a complete miscibility in the amorphous phase (Figure 4.85 right).

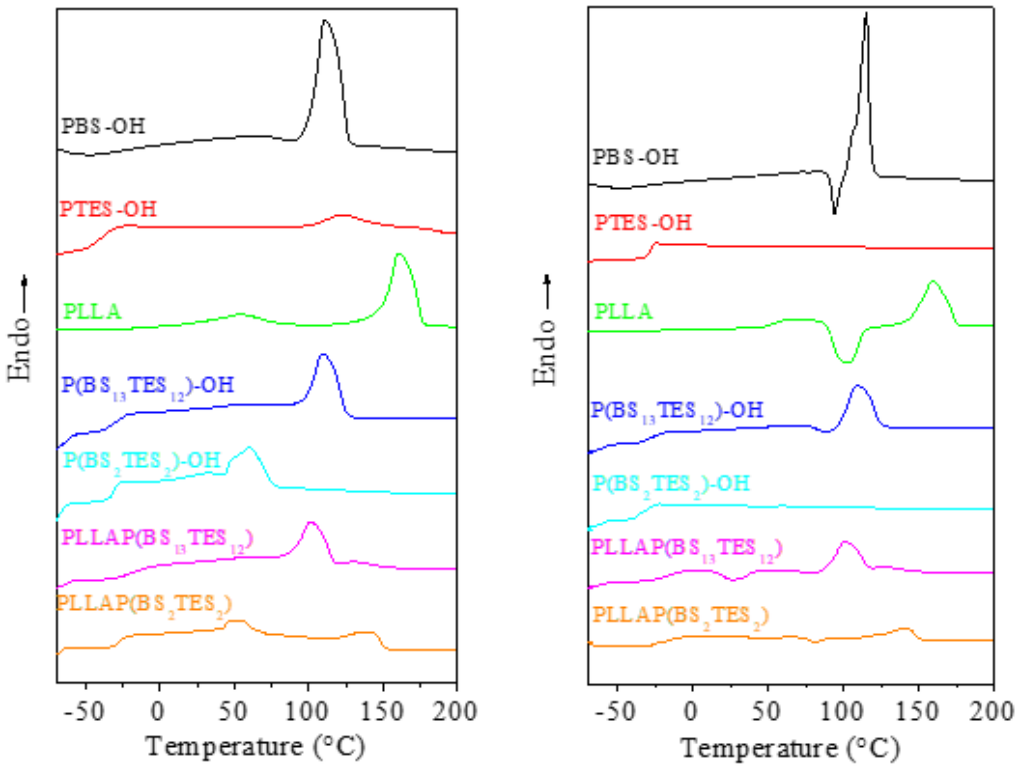

Figure 4.85. Calorimetric curves of the polymers under investigation: I scan (left) and II scan after melt quenching (right).

To better understand the nature of the crystalline phase present in the samples under investigation, WAXS analysis was performed. In Figure 4.86 diffraction profiles are shown, while in Table 4.41 the values of crystallinity degree X_c are listed.

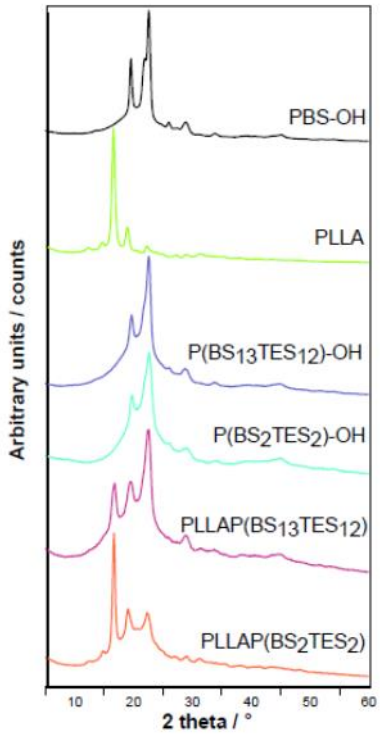

Figure 4.86. X-Ray diffraction patterns of the samples under investigation, obtained by WAXS analysis.

The profiles obtained are typical of semicrystalline materials, being visible some well-defined peaks related to the ordered portion of the material, overlapped with a bell-shape baseline characteristic of amorphous regions.

Both P($BS_{13}TES_{12}$)-OH and P(BS_2TES_2)-OH show the diffraction pattern of PBS crystalline phase. The presence of TES co-units is responsible for a reduced intensity and a slight increase of peak width, according to the values of X_c. listed in Table 4.41. As the position of the peaks does not change after the introduction of TES co-units, it is clear that the amorphous TES segments are completely excluded from the PBS lattice.

As the two triblock copolymers PLLAP($BS_{13}TES_{12}$) and PLLAP(BS_2TES_2), in their diffraction pattern both the peaks of PLLA and PBS crystalline phases are present. However, their relative intensity changes, in agreement with the calorimetric data reported in Table 4.41: in PLLAP($BS_{13}TES_{12}$), PBS peaks are more intense, vice-versa in the case of PLLAP(BS_2TES_2). As already observed from I DSC scan of P(BS_xTES_y)-OH copolymers, the patterns of triblock copolymers present wider peaks, due to the exclusion of the amorphous co-units from the crystalline lattice, which results in higher interplanar distances.

Anyway, their crystallinity degree X_c is lower than those of the parent homopolymers, being 28% for PLLAP($BS_{13}TES_{12}$) and 24% for PLLAP(BS_2TES_2).

In order to study the thermal transition of the samples in a complete amorphous state, a second calorimetric scan was performed after quenching from the melt. From DSC curves (Figure 4.85 right), two different crystallization kinetics can be evidenced. More in details PBS-OH and P($BS_{13}TES_{13}$)-OH cannot be quenched in the amorphous phase, as also in the II scan melting peaks related to BS crystalline phase are present. On the other hand, P(BS_2TES_2)-OH calorimetric curve shows only an endothermic baseline variation related to glass-to-rubber transition. In this case, macromolecular chains were blocked in a disordered conformation because of melt quenching.

PLLA homopolymer presents an exothermic peak at 68°C, followed by an endothermic one at 121°C. Being the areas under the two peaks equal ($\Delta H_c = \Delta H_m$), the quenching was effective.

As regards the two triblock copolymers, they show a behaviour similar to PLLA. However, being $\Delta H_m > \Delta H_c$, these materials are semicrystalline even after rapid cooling.

4.10.3 Micro- and nanoparticles characterization

PLLA, PLLAP($BS_{13}TES_{12}$) and PLLAP(BS_2TES_2) micro- and nanoparticles were obtained by oil-in-water miniemulsion technique, as described in Paragraph 3.10. Both empty and Dexamethasone-loaded particles, these last indicated as PLLA-d, PLLAP($BS_{13}TES_{12}$)-d and PLLAP(BS_2TES_2)-d, were prepared. As Dexamethasone (DXM) is a hydrophobic drug, it was quite easy to encapsulate it.

Empty and loaded microparticles were observed at optical microscope (Figure 4.87), through which it was possible also to evaluate the average sizes. In all cases, microparticles diameters ranged between 2 and 5 µm.

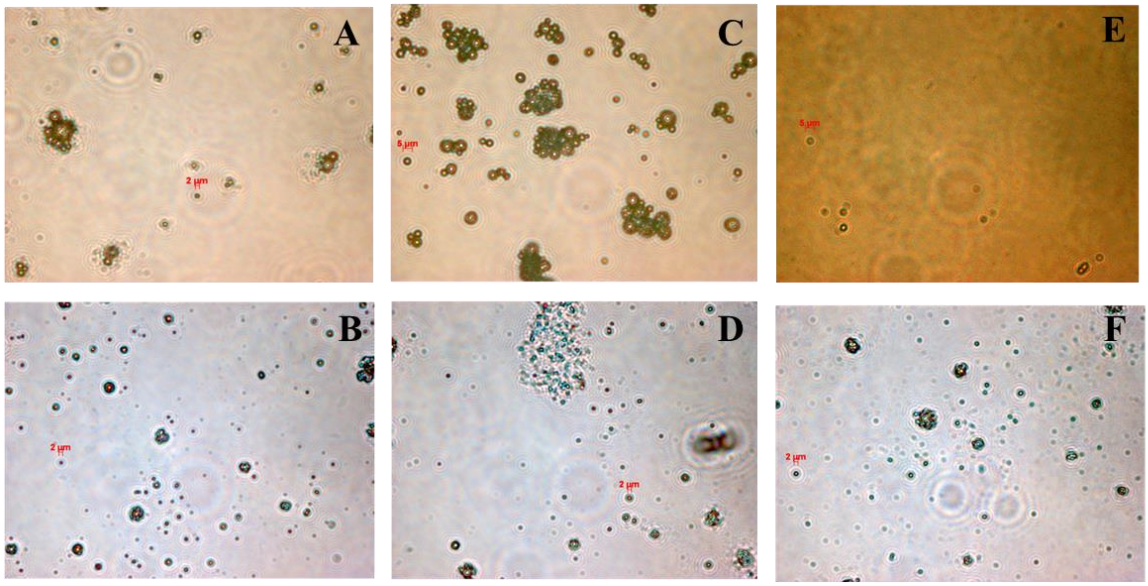

Figure 4.87. Optical microscope pictures of both empty and Dexamethasone-loaded microparticles: **A**) PLLA; **B**): PLLA-d; **C**): PLLAP($BS_{13}TES_{12}$); **D**): PLLAP($BS_{13}TES_{12}$)-d; **E**): PLLAP(BS_2TES_2) and **F**): PLLAP(BS_2TES_2)-d.

In Figure 4.88, histograms with diameter distributions of the polymeric nanoparticles are shown. The measurements were performed by dynamic light scattering (DLS). Mean diameter values turned out to be similar for all the particles types, ranging around 200 nm (Table 4.42).

Table 4.42. Mean diameter of both empty and Dexamethasone-loaded nanoparticles obtained by DLS analysis.

Polymers	Diameter (nm)
PLLA	223±35 nm
PLLA-d	227±47 nm
PLLAP($BS_{13}TES_{12}$)	220±27 nm
PLLAP($BS_{13}TES_{12}$)-d	258±37 nm
PLLAP(BS_2TES_2)	216±24 nm
PLLAP(BS_2TES_2)-d	210±27 nm

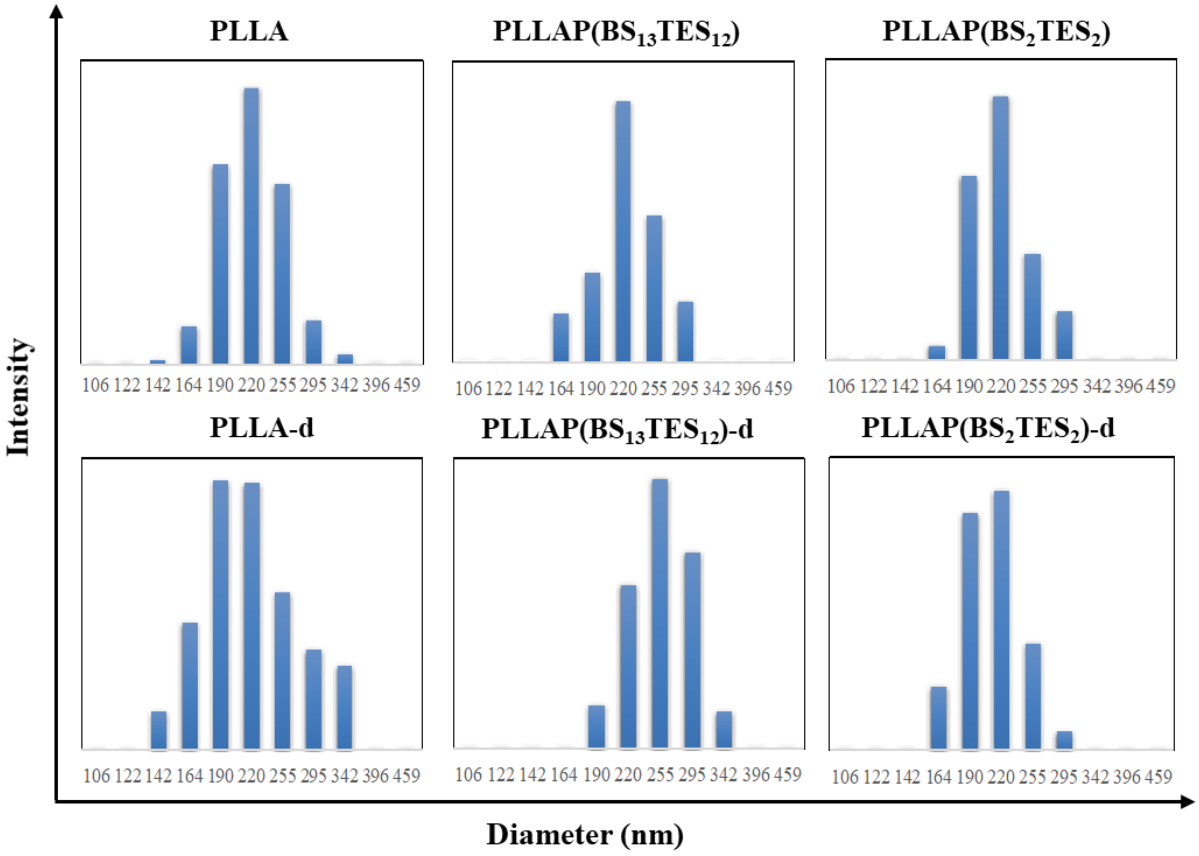

Figure 4.88. Diameter distribution of both empty and Dexamethasone-loaded nanoparticles obtained by DLS analysis.

The calorimetric curves of PLLA, PLLAP($BS_{13}TES_{12}$) and PLLAP(BS_2TES_2) powders, micro- and nanoparticles are shown in Figure 4.89. From the comparison among the DSC traces of the powders and of particles, it is evident how micro- and nano-confinements drastically depress the crystallizing ability of PLLA segments both in the homopolymer and in the copolymers. More in details, PLLA particles are amorphous, showing an exothermic peak, whose associated heat is equal to the heat of fusion of the melting peak at higher temperature. On the contrary, PLLAP($BS_{13}TES_{12}$) and PLLAP(BS_2TES_2) particles are semicrystalline, thus indicating that P(BSTES) segments keep their crystallization ability even in the particles form. According to the ΔH_m values of the two copolymers, PLLAP($BS_{13}TES_{12}$) particles turned out to be more crystalline than PLLAP(BS_2TES_2) ones, in agreement with the results obtained with the powders.

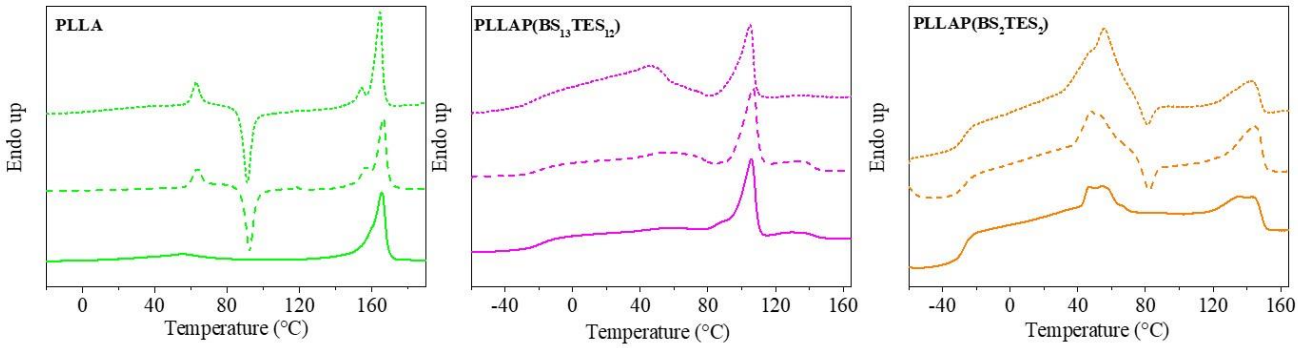

Figure 4.89. DSC curves of powder samples (solid line), microparticles (dashed line) and nanoparticles (short dashed line) for all the materials under investigation.

4.10.4 Drug release experiments

Drug release studies were performed in order to investigate the effect of both molecular architecture of the polymeric matrix and particles size on drug release kinetics, using Dexamethasone (DXM) as a model drug. As already mentioned in the experimental part, the amount of DXM released was calculated by absorbance measurements, using different solutions containing known concentrations of DXM as standards.

Before drug release experiments, encapsulation efficiency (EE%) of both micro- and nanoparticles was calculated. It is well known that drug loading depends on several factors, like particles size, amorphous phase mobility, hydrophilicity and crystallinity degree. From data collected in Table 4.43, it is possible to see that the higher the particles size, the higher the EE. As a matter of fact, microparticles are able to encapsulate more drug compared to nanoparticles obtained from the same polymeric material. In addition, according to the calorimetric data (Figure 4.89), lower T_g values are related to a more effective encapsulation efficiency: it seems that the amorphous phase mobility favours the entrance of the drug inside the particles. For example, both micro- and nanoparticles obtained from PLLA, whose T_g is the highest among the materials investigated, show the lowest EE values.

Table 4.43. Encapsulation efficiency (%) of Dexamethasone-loaded micro- and nanoparticles.

Polymers	Encapsulation efficiency (%)	
	Micro	Nano
PLLA-d	44	27
PLLAP($BS_{13}TES_{12}$)-d	77	54
PLLAP(BS_2TES_2)-d	90	39

In Figure 4.90, cumulative DXM release profiles from homo- and copolymeric microparticles are shown as a function of time. It is immediately clear that the so-obtained profiles present many differences.

As known, release rate is affected by several factors: among them, hydrophilicity, crystallinity degree and amorphous phase mobility are the most important. These parameters can influence both the diffusion of water molecules inside the polymeric matrix and the hydrolytic erosion of the material itself.

During the initial phase, controlled by diffusion processes (Figure 4.90B), both PLLA and PLLAP($BS_{13}TES_{12}$) show an induction phase of about 30 minutes before the drug starts to be released. For PLLAP(BS_2TES_2), this induction phase lasts about twice the time.

This trend can be explained considering that PLLA, although more crystalline, is characterized by a higher amount of hydrolysable ester groups than the copolymers, whereas PLLAP($BS_{13}TES_{12}$) is more hydrophilic (Table 4.40). Both these factors favour water diffusion inside the polymeric matrix, thus resulting in shorter induction times than that of PLLAP(BS_2TES_2).

At longer times, when Dexamethasone starts to be released (Figure 4.90B), release rate is higher from the block copolymer than from the random one. PLLA profile is located between these two. The higher PLLAP($BS_{13}TES_{12}$) release rate can be explained in terms of higher hydrophilicity and lower crystallinity compared to those of the homopolymer, which favour water diffusion. Conversely, the lower PLLAP(BS_2TES_2) release rate can be ascribed to the lower amount of hydrolysable ester groups.

After 8 hours of incubation in physiological conditions, drug release from the copolymers can be considered as complete (both the profiles reach a plateau value), while drug release from PLLA matrix continues for longer times, even though more the 80% of the drug incapsulated was already released after 8 hours of incubation. This trend seems to suggest that in copolymeric

microparticles, drug is released through a diffusion-controlled mechanism, which runs out after only 8 hours. On the contrary, drug release from PLLA microparticles seems to be affected also by erosion, which occurs during the later release phases.

It is also interesting to notice that drug release rate and drug release amount are inversely proportional to EE.

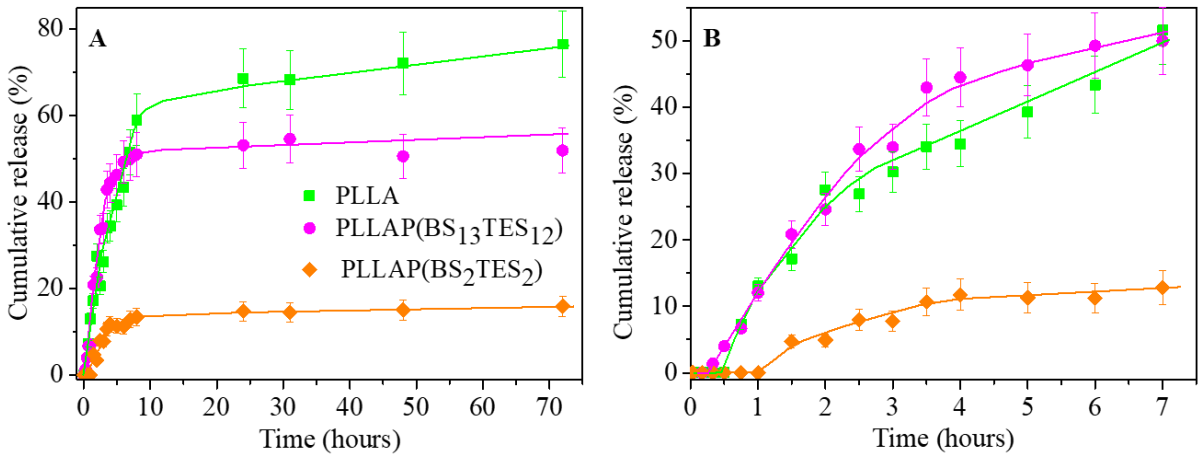

Figure 4.90. Cumulative DXM release from polymeric microparticles. **A**) Total time; **B**) Initial phase.

In Figure 4.91 Dexamethasone release profiles from both homopolymeric and copolymeric nanoparticles are shown as a function of time. Chemical structure, as already seen in case of microparticles, affects the release kinetics. However, from the differences between microparticles and nanoparticles profiles, it is clear that the dimension of the device is responsible for different behaviours.

During the first phase (Figure 4.91B), both PLLA and PLLAP($BS_{13}TES_{12}$) block copolymer nanoparticles show an induction time of about 30 minutes, whereas in case of PLLAP(BS_2TES_2) nanoparticles, Dexamethasone release starts almost immediately. This trend is opposite to the one observed for microparticles, where PLLAP(BS_2TES_2) showed the longest induction time (Figure 4.90B).

In addition, conversely from microparticles, in which there was a water diffusion-controlled mechanism, the release profile from nanoparticles is considerably affected by polymeric matrix erosion, which occurs even during the first phase of the process, as these particles are characterized by a higher surface/volume ratio.

In this framework, it is possible that the longer induction time observed for both PLLA and PLLAP($BS_{13}TES_{12}$) is due to their higher crystallinity degree with respect to PLLAP(BS_2TES_2), which slows down hydrolysis and erosion processes.

In addition, some other differences can be recorded during incubation time. Indeed, after 90 minutes from the beginning of the incubation, PLLA and random copolymer PLLAP(BS_2TES_2) are characterized by the same release rate. This behaviour can be due to the low crystallinity degree of these two materials, which favours water diffusion enhancing in the same time erosion mechanism.

After the first two hours of incubation, PLLA release profile is located between those of the copolymers.

As already observed for microparticles, after 8 hours of incubation in physiological conditions both copolymers reach a plateau value, while PLLA release continues slowly even after 24 hours of incubation. This trend indicates that for copolymeric nanoparticles the hydrolytic degradation rate is higher.

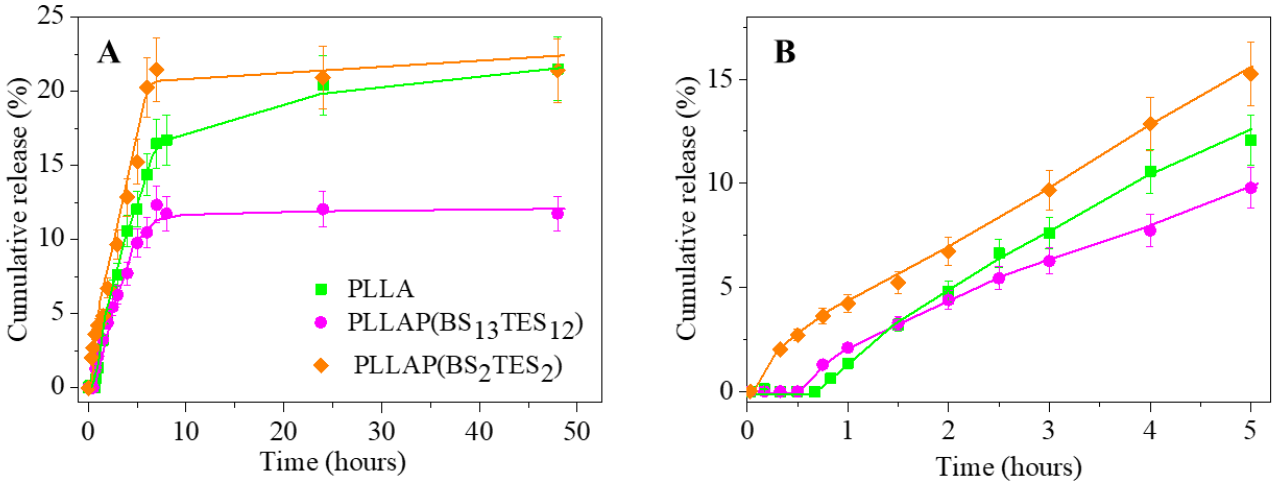

Figure 4.91. Cumulative DXM release from polymeric nanoparticles. **A**) Total time; **B**) Initial phase.

4.10.5 Conclusions

Novel A-B-A triblock copolymers where successfully synthesized for potential applications as controlled drug delivery devices. More in details, the side A block was made of PLLA, while the central B block was formed by two different PBS-based copolymers prepared *ad-hoc*, starting from equimolar amounts of poly(butylene succinate) and poly(triethylene succinate) homopolymers. One copolymer was characterized by a block molecular architecture, the other

by a random distribution of comonomeric units. The two copolymers contained sequences of different length, long sequences in block copolymer, short in random one.

Chain flexibility, crystallizing ability and surface wettability have been nicely tailored, simply by varying the molecular architecture of the central B block (block copolymer *vs*. random one). Moreover, the main crystalline phase present in the two copolymers was different: PLLA crystalline phase prevailed when the central block was made by the random copolymer, while PBS crystalline phase was more abundant when the central B block had a block structure.

Dexamethasone-encapsulated micro- and nanoparticles showed different drug release kinetics, which appeared to depend on both polymer chemical structure and particles size. The copolymeric particles were characterized by tunable release kinetics with respect to that of PLLA. Furthermore, the drug release rate as well as the release mechanism were strictly dependent on the dimensions of the realized vectors. In particular, it has been shown that in case of microparticles, the release profile is prevalently diffusion-dependent, while for nanoparticles also erosion processes had a role.

In conclusion, PLLA copolymerization through the introduction of comonomeric units designed *ad hoc*, playing on chemical structure as well as on molecular architecture, turned out to be a winning strategy to tune the properties of the so-obtained materials, which reveled to be very promising as controlled drug delivery systems.

4.11 New elastomeric PLLA-based triblock copolymer for vascular tissue engineering applications: annealing as efficient tool to tailor the solid-state properties

A novel high molecular weight polylactic acid-based aliphatic copolyester characterized by a A-B-A triblock architecture was synthesized. More in details, A block consists of polylactic acid (PLLA) homopolymer and B central block is an aliphatic biodegradable and biocompatible "PEG-like" random copolymer based on poly(butylene succinate) PBS and poly(triethylene succinate) PTES [Gualandi at al., 2012 (a)]. To achieve a high molecular weight, that guarantees good mechanical properties, hexamethylene diisocyanate (HDI), known chain extender, has been added to the reaction system. The material was characterized by the molecular point of view and after two different annealing treatments were applied to the polymer. From WAXS structural analysis, it was also possible to see that annealing deeply affects the main crystalline phase.

In order to explore the possible use of the so-obtained material in vascular tissue engineering, mechanical properties were investigated, and biocompatibility evaluated. Aim of the work was to study the effect of the different crystalline phase on functional properties.

4.11.1 Synthesis and molecular characterization

A-B-A triblock copolymer PLLAP(BSTES) was synthesized by Ring Opening Polymerization (according to the procedure reported in Paragraph 3.2.3) between L-lactide and P(BS_2TES_2)-OH copolymer, described in Paragraph 4.10.1. After ROP, in order to increase the molecular weight, chain extension reaction was carried out, according to the procedure described in Paragraph 3.2.3. Chain extended PLLA was also preprared for sake of comparison.

In Figure 4.92, ^{1}H-NMR spectrum of chain extended PLLA is shown. In addition to the singlets related to the solvent $CDCl_3$ and to the reference TMS, resonance peaks of lactic acid repeating unit are present. The quadruplet of g protons is located at δ 5.19 ppm, while the duplet of h protons appears at δ 1.57 ppm; b and c peaks of the initiator (butanediol), although less intense, can also be detected at δ 3.76 and δ 1.74 ppm, respectively, as well as HDI peaks i, k and j, visible at δ 3.18 and δ 1.55 ppm.

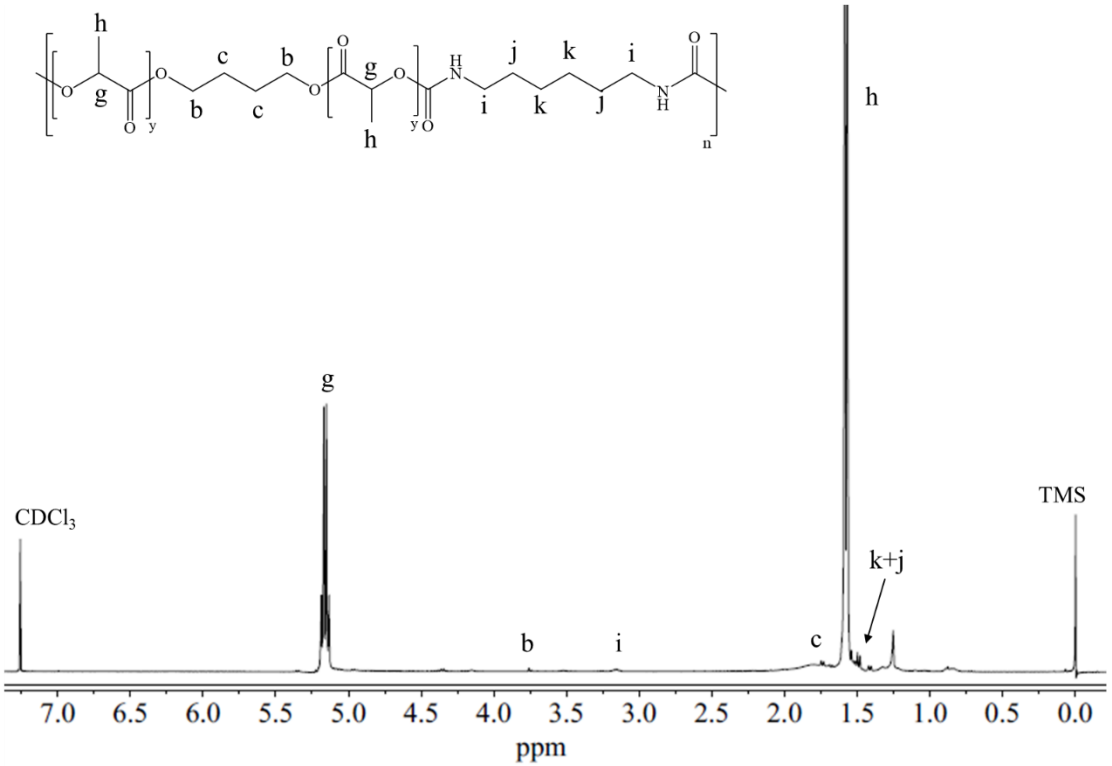

Figure 4.92. ^{1}H-NMR spectrum of chain extended PLLA homopolymer with peak attribution.

In Figure 4.93, ^{1}H-NMR spectrum of PLLAP(BSTES) copolymer is shown. It is possible to see g and h signals of the lactic subunit, i, k and j signals of HDI, and the peaks related to both the BS and TES counits. More in details, b and c multiplets of butylene subunit are located at δ 4.19 and δ 1.73 ppm, together with d and e triplets, and f singlet of TE subunit, at δ 4.25 ppm, δ 3.70 ppm and δ 3.65 ppm, respectively. The presence of a protons related to succinic subunit (present in both BS and TES segments) can be detected between 2.65 and 2.61 ppm. The actual weight composition of the copolymer PLLAP(BSTES), calculated taking into account the relative area of g protons of LLA subunit at δ 5.19 ppm, and the relative area of a protons of succinic subunit between δ 2.65 ppm and δ 2.61 ppm, resulted very close to the feed one (Table 4.44).

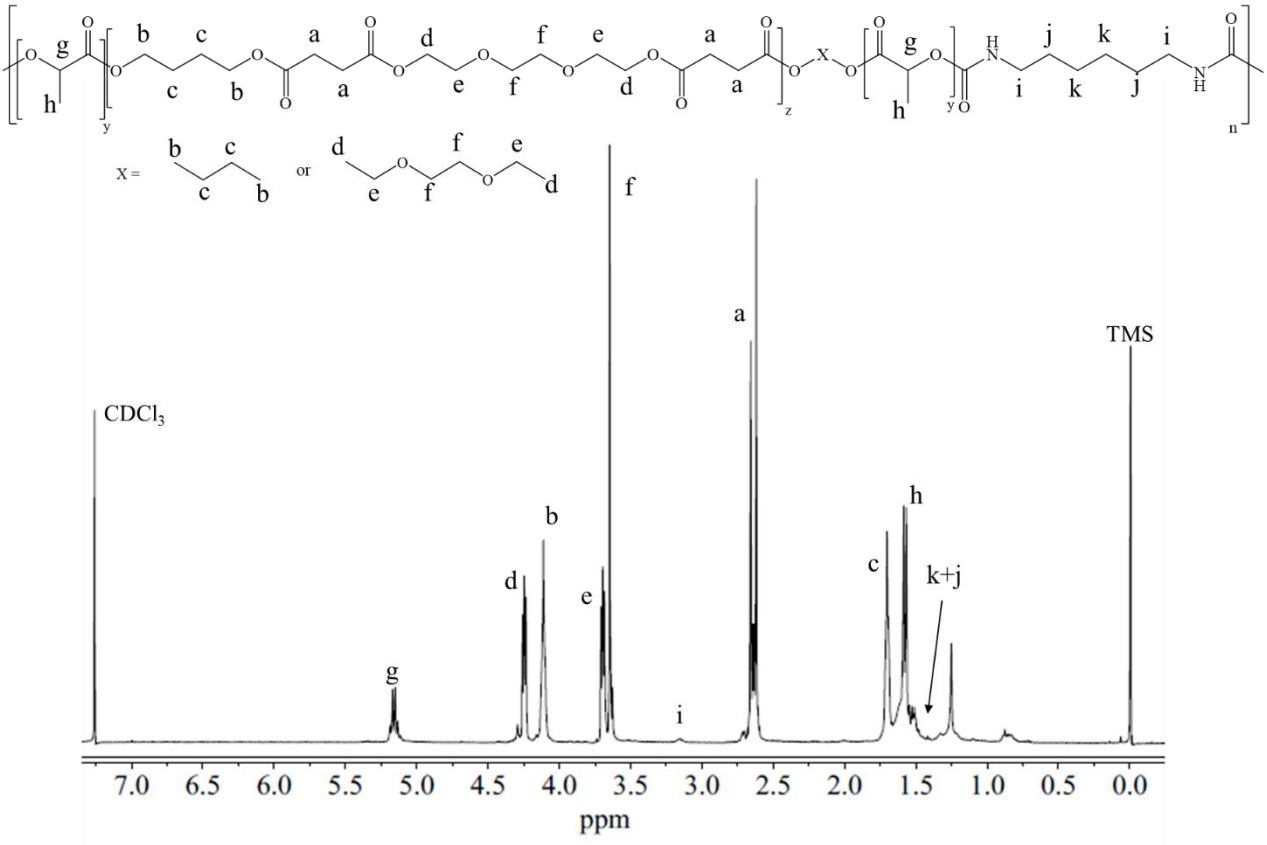

Figure 4.93. [1]H-NMR spectrum of PLLAP(BSTES) with peaks attribution.

In Table 4.44 the molecular weights of the chain extended polymers, obtained by GPC analysis, are listed. As expected, the samples show a higher molecular weight than the prepolymer (Table 4.39) and a pretty narrow polydispersity index, indicating a good control over both the ring opening polymerization and the chain extension process.

Table 4.44. Molecular characterization data of the homopolymer PLLA and of the triblock copolymer PLLAP(BSTES): *data obtained by GPC analysis and ** data obtained from [1]H-NMR analysis.

Polymers	**M_n (g/mol)***	**D***	**PLLA (wt%)****	**P(BSTES) (wt%)****
PLLA	31200	1.2	100	-
PLLAP(BSTES)	36200	1.2	24	76

4.11.2 Thermal and structural characterization

The chain extended polymers have been subjected to thermogravimetric analysis under dry nitrogen atmosphere. TGA curves are shown in Figure 4.94. Thermal stability is high in both cases, but the two samples present many differences: PLLA starts degrading at 250 °C, while PLLAP(BSTES) above 300 °C. Weight loss occurs in one step for the homopolymer and in two steps for the copolymer, being the first stage related to PLLA A-block degradation and the second one to the central B-block one, respectively. In conclusion, it is possible to affirm that copolymerization improves thermal stability.

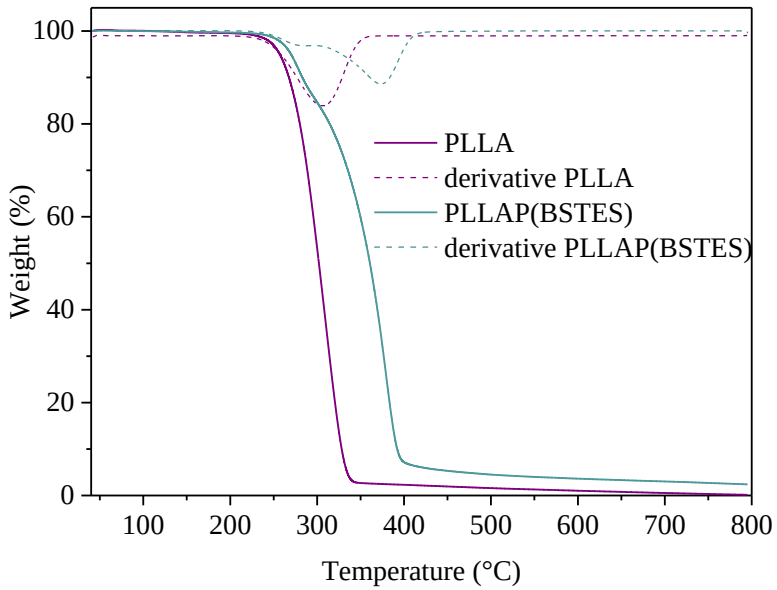

Figure 4.94. Thermogravimetric curves of the chain extended polymers and their derivatives.

After thermogravimetric analysis, films by compression molding were produced. Calorimetric analysis was performed immediately after film molding in the case of PLLA (Table 4.45). In fact, PLLA shows a T_g well above room temperature, which means that the macromolecular chains are blocked in the amorphous state, and they cannot rearrange themselves for storage at room temperature.

Conversely, PLLAP(BSTES) chains can undergo crystallization at room temperature, being the T_g of the copolymer around -20 °C. For this reason, copolymer film was analyzed after 0, 7 and 30 days after film molding. In Figure 4.95 I scan calorimetric curves of PLLAP(BSTES) are shown. The trace relative to the just made film shows the typical behavior of semicrystalline materials, with an intense glass transition phenomenon around -20°C, followed by a double

endothermic melting peak at higher temperature. After 7 days of incubation at room temperature, DSC trace remarkably changed: the glass transition phenomenon is less broad and shifted to higher temperatures, while the two melting peaks become more intense and sharper. This behavior can be ascribed to a higher amount of a more perfect crystalline phase, which develops during incubation at room temperature. In addition, ΔH_m, related to the amount of crystalline phase is increased, while ΔC_p decreased (see the insertion in Figure 4.95). DSC curve after 30 days of incubation is very similar to the previous one, with only a slight decrease of ΔC_p and a small increase of ΔH_m (Figure 4.95, insertion). According to this result, 30 days of incubation can be considered a time long enough for the material to develop a stable crystalline phase.

The double melting peak can be due to melting-crystallization-melting phenomena, during which crystals melt and crystallize in more perfect form during heating. As to glass transition, the presence of only one T_g proves the complete miscibility of the two PLLA and P(BSTES) blocks in the amorphous phase.

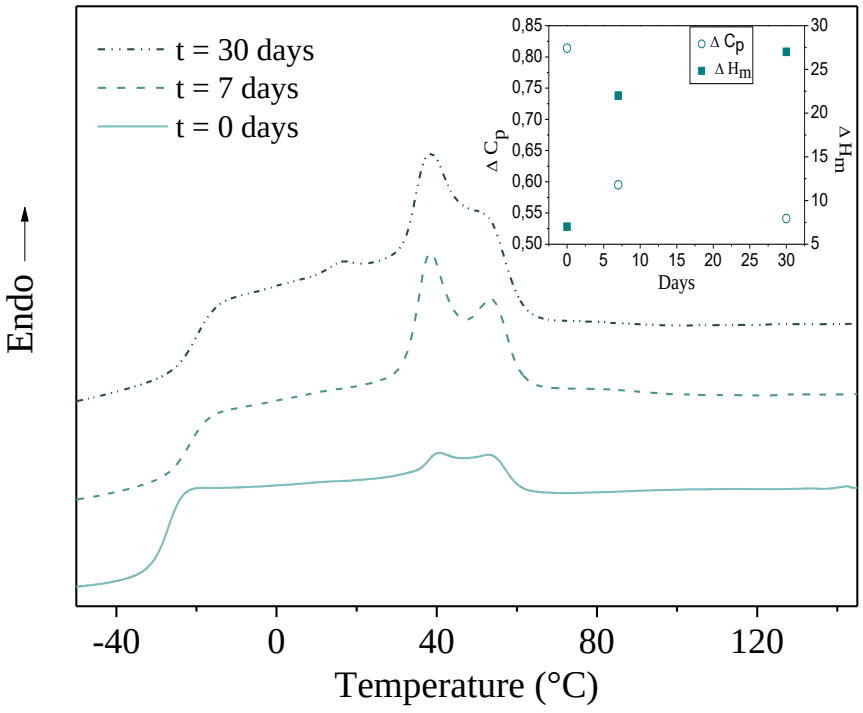

Figure 4.95. Calorimetric curves of PLLAP(BSTES) copolymer after different room temperature storage time (t_{Troom}). In the insertion the variation of ΔH_m and ΔC_p as a function of t_{Troom} are shown.

In addition, copolymer PLLAP(BSTES) has been submitted to thermal annealing, in order to check whether the amount and the kind of crystalline phase changes due to the effect of thermal treatment. In the first case, the sample was left for two weeks at room temperature. This sample from now onwards will be labelled as PLLAP(BSTES)1. The second sample, which will be indicated as PLLAP(BSTES)2, was left for two weeks at room temperature as well as PLLAP(BSTES)1, but then was left for 24 hours at 80°C. DSC scan was performed on PLLAP(BSTES)1 and PLLAP(BSTES)2. Figure 4.96 reports the I scan DSC traces of both such samples and of PLLA homopolymer, while in Table 4.45 the corresponding thermal characterization data are reported.

Table 4.45. Thermal characterization data and crystallinity degree values obtained by WAXS analysis for PLLA, PLLAP(BSTES)1 and PLLAP(BSTES)2.

Polymers	I scan						II scan						X_c %
	T_g °C	Δc_p J/g°C	T_m °C	ΔH_m J/g	T_c °C	ΔH_c J/g	T_g °C	Δc_p J/g°C	T_m °C	ΔH_m J/g	T_c °C	ΔH_c J/g	
PLLA	57	0.389	156 163	37	109	29	52	0.478	156 163	42	110	41	13
PLLAP(BSTES)1	-20	0.541	39 54	27	-	-	-21	0.819	-	-	-	-	24
PLLAP(BSTES)2	-28	0.612	36 96 132	4 15 1	-	-	-19	0.605	-	-	-	-	21

From Figure 4.96 it is possible to notice that all the samples under investigation show the typical profile of semicrystalline materials, with an endothermic baseline variation related to glass transition and an endothermic peak at higher temperature corresponding to the melting of the crystalline phase. In PLLA trace, between these two phenomena there is also an exothermic peak, which indicates that during heating a crystallization process occurs. Anyway, PLLA is semicrystalline, being $\Delta H_c < \Delta H_m$ (Table 4.45).

As to the copolymer, thermal treatment deeply affects the kind and the amount of crystalline phase. More in details, both the DSC traces of PLLAP(BSTES)1 and PLLAP(BSTES)2 show multiple endotherms, but at different temperatures. Peaks located at lower temperatures can be associated to the fusion of BS segments, while peaks at higher temperatures are related to the fusion of PLLA blocks. From data collected in Table 4.45, it is clear that T_m of PLLAP(BSTES)1 is similar to that of P(BSTES) parent homopolymer, while T_m values of PLLAP(BSTES)2 are more similar to that of PLLA, even if they are lower, because of the lower degree of perfection of the crystalline phase. In PLLAP(BSTES)2 DSC trace a small

endothermic peak at 36 °C is also present, thus indicating the residual presence of P(BSTES) crystalline phase (Figure 4.96).

Concerning the glass transition temperature, it does not significantly change as a consequence of thermal treatment, being -21 °C and -19 °C for PLLAP(BSTES)1 and PLLAP(BSTES)2, respectively.

As to the second scan after melt quenching, calorimetric data are listed in Table 4.45. PLLA shows a behaviour similar to that of I scan, keeping the same profile with both endothermic and exothermic peaks at the same temperatures. However, after rapid cooling from the molten state $\Delta H_c = \Delta H_m$, indicating that quenching was effective to get a completely amorphous polymer. As to the copolymer, regardless of the thermal treatment, the II scan shows only the endothermic transition associated to T_g, as a proof that also in this case it was possible to block the chains in a disordered state.

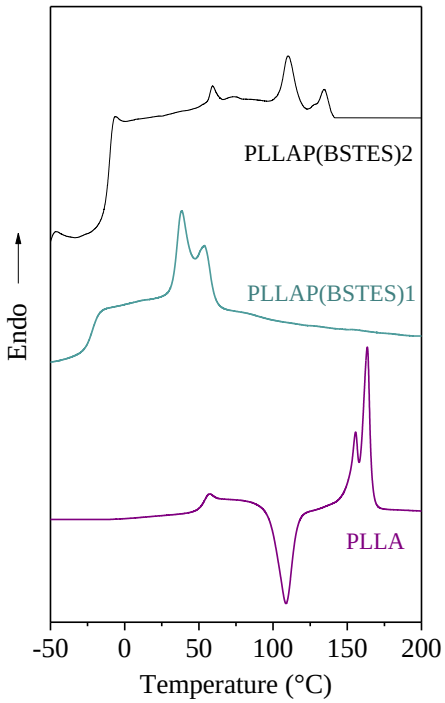

Figure 4.96. Calorimetric curves (I scan) of PLLA and PLLAP(BSTES)1 and PLLAP(BSTES)2 copolymers.

To better understand the nature of the crystalline phase present in the samples under investigation, WAXS analysis was performed. In Figure 4.97 diffraction profiles are shown, while in Table 4.45 the values of crystallinity degree X_c are listed.

All the profiles obtained are typical of semicrystalline materials, containing some well-defined peaks, related to the ordered portion of the material, overlapped to a bell-shape baseline characteristic of amorphous regions. However, the patterns present many differences in peak position and width, as well as in crystallinity degrees (Table 4.45).

More in details, in PLLA pattern only one intense and sharp peak at 17 ° (X_c = 13%) is present. PLLAP(BSTES)1 shows three well defined crystalline peaks: the two more intense can be ascribed to the PBS crystallyne phase of the central P(BSTES) block (see Figure 4.86), while the less intense is related to PLLA crystalline phase. An opposite behaviour is registerd for PLLAP(BSTES)1, whose pattern presents a sharp peak corresponding to PLLA crystalline phase, toghether with others less defined related to PBS crystalline phase. Anyway, in both cases, the degree of perfection of the crystals is lower (i.e. the peaks are more width), because of the presence of the co-units. Moreover, PLLAP(BSTES)1 turned out to be more crystalline than PLLAP(BSTES)2 (X_c = 24% and 21%, respectively), in agreement with calorimetric data (Table 4.45).

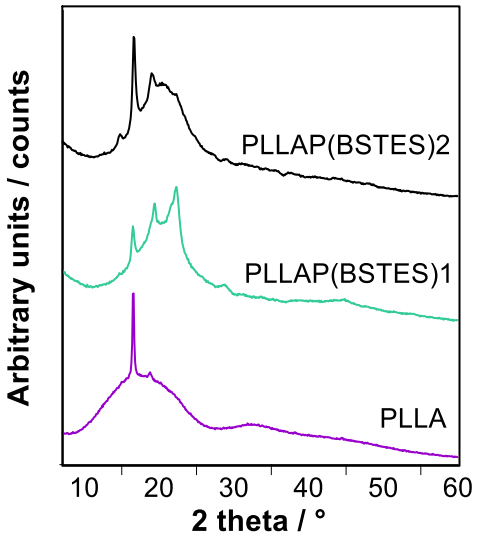

Figure 4.97. X-Ray patterns of PLLA and PLLAP(BSTES)1 and PLLAP(BSTES)2 copolymers.

4.11.3 Mechanical characterization

To provide insight into the mechanical response of the polymers synthesized, tensile measurements were carried out. Stress-strain measurements were performed on rectangular samples (50 x 5 x 0.3 mm) by measuring the variation of stress as a function of the strain applied. The tensile testing data (elastic modulus E, stress at break σ_B and strain at break ε_B), are summarized in Table 4.46, while in Figure 4.98 the stress-strain curves recorded for PLLA

homopolymer and PLLAP(BSTES) copolymer subjected to both thermal treatments are reported.

Table 4.46. Mechanical characterization data of PLLA and the copolymer PLLAP(BSTES) after the two different thermal treatments.

Polymer	E (MPa)	σ_b (MPa)	ε_b (%)
PLLA	2290±300	33.0±1.5	2.0±0.5
PLLAP(BSTES)1	25.0±1.7	2.0±0.2	100.0±10
PLLAP(BSTES)2	5.0±0.6	2.0±0.2	590.0±10

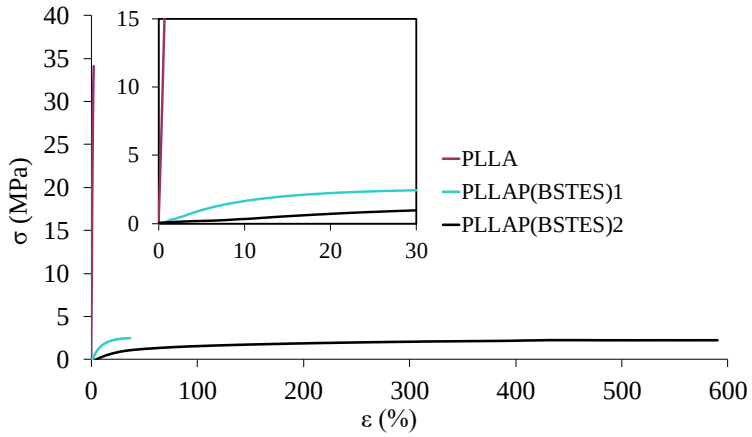

Figure 4.98. Stress-strain curves of PLLA and PLLAP(BSTES) copolymer after both thermal treatments. In the magnification: enlargement of the region corresponding to low σ-ε.

From the data reported in Table 4.46, it can be noticed that PLLA shows high values of elastic modulus E and stress at break σ_b, with a very low elongation at break ε_b (around 2%), confirming the remarkable stiffness of this homopolymer. Conversely, PLLAP(BSTES)1 is characterized by a completely different mechanical response: E decreases of about two orders of magnitude, σ_b decreases of almost one order of magnitude and a half, while ε_b is significantly improved, from 2% of PLLA to 100%. The thermal treatment is also responsible for a different mechanical behavior. In fact, PLLAP(BSTES)2 is even more flexible than PLLAP(BSTES)1: E is reduced by five other times and ε_b reaches almost 600%.

This result cannot be explained on the basis of differences in crystallinity degree, being both copolymers more crystalline than PLLA homopolymer. The observed trend is due to the

presence in PLLA of a glassy amorphous phase. In case of both PLLAP(BSTES)1 and PLLAP(BSTES)2 samples, the amorphous phase is on the contrary characterized by higher mobility being in the rubbery state (the presence of ether oxygen atoms significantly enhances chain flexibility). By comparing the two copolymers PLLAP(BSTES)2 and PLLAP(BSTES)1, the effect of annealing is evident considering the huge increment of elastomeric behavior: the elastic modulus of PLLAP(BSTES)2 is 5 times lower, whereas the elongation at break passes from 100 to 590 %. The thermal treatment at 80 °C, in fact, leads to a reduction in the amorphous portion of the stiff LLA segments, which are responsible for the earlier break of PLLAP(BSTES)1.

Overall, mechanical characterization demonstrated that the synthetic strategy adopted, as well as the thermal treatment applied, allowed to modify in a proper way the homopolymer mechanical properties.

It is also interesting to note that in stress-strain curves of PLLAP(BSTES)1 and PLLAP(BSTES)2 no yield is recorded (Figure 4.98), thus confirming a thermoplastic elastomeric behavior, which is fundamental for applications in soft tissue engineering.

Cycling stress-strain measurements were carried out in order to investigate the behaviour of the copolymer when subjected to cyclic stress. For PLLAP(BSTES)1 a deformation of 40% was applied, while for PLLAP(BSTES)2 the deformation was of 100%, in order to keep the strain well below ε_b. In both cases, 20 cycles were performed. As an example, in Figure 4.99 the hysteresis behaviour upon cyclic loading of PLLAP(BSTES)2, the more performing among the two copolymers, is shown.

In both cases, the sample shows good elasticity, even though a certain amount of permanent set could be recorded after each loading–unloading cycle. In addition, the stress–strain curves in the second cycle are more compliant than those observed in the first cycle. This behaviour, known as softening, can be due to a rearrangement in the crystalline microphase [Soccio et al., 2012 (b)]. Moreover, the hysteresis area of the second cycle is much smaller than that of the first cycle. The difference between the ascending curve of the first cycle and that of the second cycle can be due to reorientation of the macromolecules together with crystallization during straining [Andronova et al., 2006].

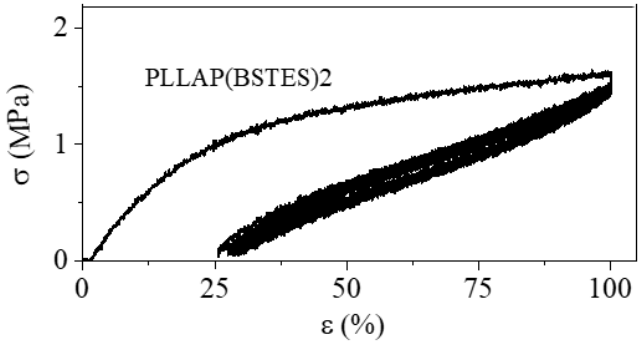

Figure 4.99. Hysteresis behaviour of PLLAP(BSTES)2 upon cyclic loading: cycles 1-20.

4.11.4 Hydrolytic degradation tests

Hydrolytic degradation experiments were carried out under physiological conditions (37°C, pH 7.4) in phosphate buffer to study the biodegradation kinetics of the synthesized materials in conditions mimicking the human body.

In Figure 4.100 the residual weight of PLLA, PLLAP(BSTES)1 and PLLAP(BSTES)2 is reported as a function of the incubation time.

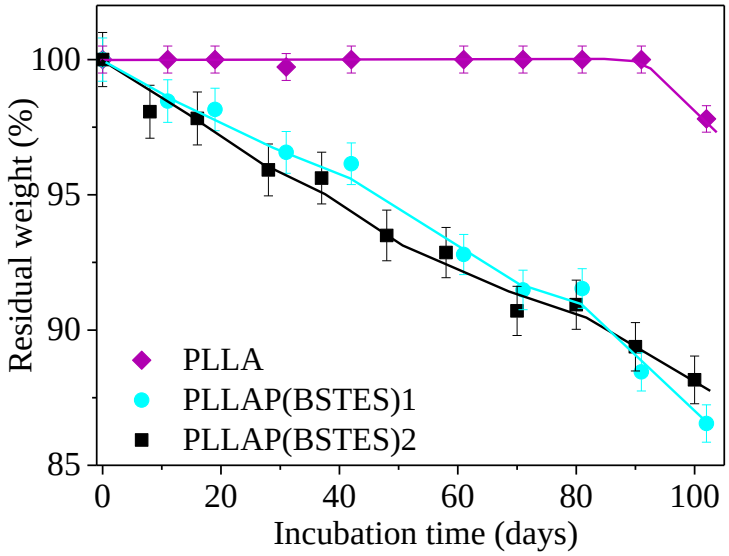

Figure 4.100. Residual weight (%) as a function of incubation time for PLLA, PLLAP(BSTES)1 and PLLAP(BSTES)2.

In the time scale explored (≈ 100 days of incubation), PLLA did not lose any weight and its residual weight is still above 95%. Conversely, both PLLAP(BSTES)1 and PLLAP(BSTES)2 copolymers show a gradual and similar decrease in gravimetric weight, around 13% after 100

days (Figure 4.100), thus indicating that the degradation rate is independent on the thermal treatment.

As it is well known, many factors affect the degradation rate, such as molecular weight, amorphous phase mobility, crystallinity degree, ester groups density, hydrophilicity and melting temperature. Although the correlation between all these factors and the effective degradation rate is complex, in this case amorphous phase mobility, as well as lower melting temperature and hydrophilicity of TES sequences, seem to play a key role in hydrolysis process [Gigli et al., 2012 (a); Gigli et al., 2013 (b)].

The partially degraded copolymeric samples were subjected to ^{1}H-NMR (Figure 4.101) and DSC (Figure 4.102) analyses, in order to check the residual copolymer composition and differences in crystallinity degree, making light on degradation mechanism. In Figure 4.101 the ratio between both TES/BS and L-LA/BSTES amount for the copolymers PLLAP(BSTES)1 and PLLAP(BSTES)2 are shown. For PLLAP(BSTES)1 (Figure 4.101A), a decrease of about 10% in the amount of the hard block (PLLA) with respect to the soft block (P(BSTES)) was registered. In addition, TES segment content in the soft block decreased during incubation (≈ 7%). On the other hand, for PLLAP(BSTES)2 (Figure 4.101B), it is possible to see a decrease of about 8% of the amount of the soft block (P(BSTES)) with respect to the hard block (PLLA). Moreover, also in this case TES segment content in the soft block decreased during incubation (≈ 5%).

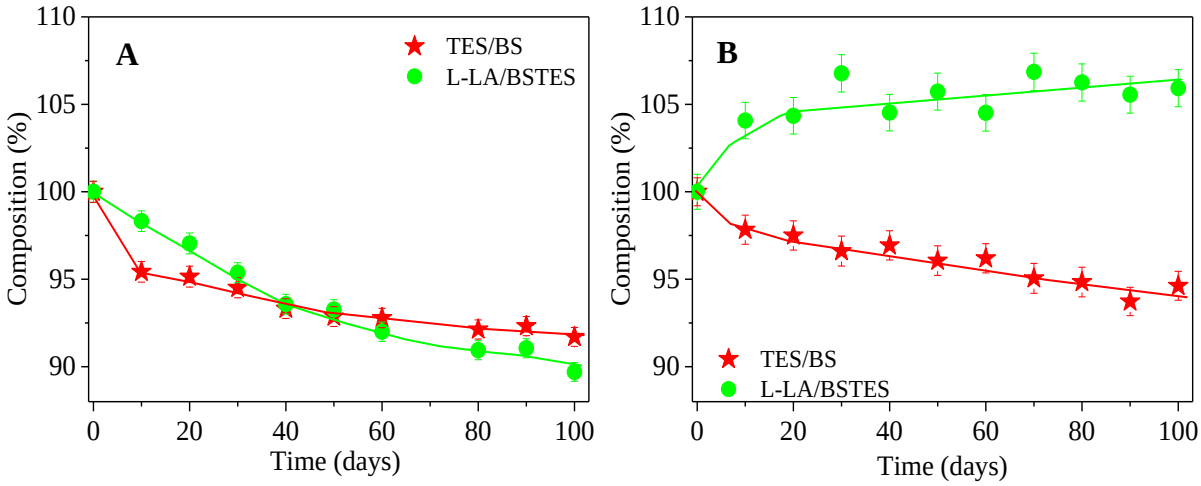

Figure 4.101. Residual TES/BS and L-LA/BSTES composition (%) as a function of incubation time obtained by ^{1}H-NMR analysis for: **A**) PLLAP(BSTES)1 and **B**) PLLAP(BSTES)2.

This behaviour can be ascribed to the preferential degradation of amorphous phases during degradation, which consists of PLLA blocks in PLLAP(BSTES)1 and P(BSTES) blocks in PLLAP(BSTES)2. As to the decrease of the amount of TES sequences in both the copolymers, this is due to their higher hydrophilicity, given by the ether oxygen atoms.

Calorimetric analysis was performed on partially degraded PLLAP(BSTES)1 and PLLAP(BSTES)2 copolymeric films. Incubation times of 0, 20, 60 and 100 days were considered. The relative DSC curves are shown in Figure 4.102. In the inset, the ratios $\Delta H_m/\Delta H_{m0}$ as a function of incubation time are reported.

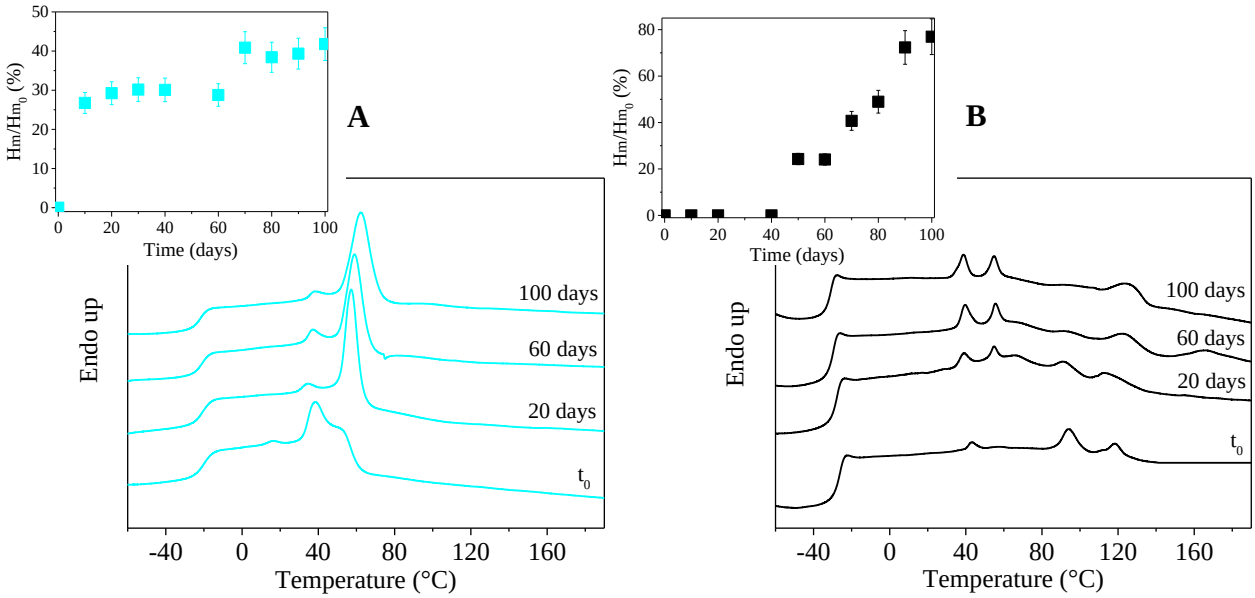

Figure 4.102. DSC curves at different incubation times for: **A**) PLLAP(BSTES)1 and **B**) PLLAP(BSTES)2. In the inset, the ratios $\Delta H_m/\Delta H_{m0}$ as a function of incubation time are reported.

It is interesting to notice that during incubation an increase in crystallinity degree is registered for both the samples, thus confirming that amorphous phases are preferentially attacked during hydrolytic degradation. These trends are confirmed also by the ratios between ΔH_m and ΔH_{m0}. For PLLAP(BSTES)2 copolymer this increment is more remarkable. A detailed analysis of endotermic phenomena indicates that in PLLAP(BSTES)1 an improvement of PBS crystal phase occurs. In case of PLLAP(BSTES)2 the development of PBS crystal phase is observed. Physiological temperature is the right annealing temperature of PBS crystalline phase present in the P(BSTES) soft block B. Its formation is therefore favoured at the expense of PLLA crystal phase. An alternative possible explanation considers that the crystallization process can

be favoured by the reduction of molecular weight of P(BSTES) blocks, which are preferentially attacked.

4.11.5 Biocompatibility studies

As reported in Figure 4.103, MTS assay on EA.hy926 cultured on both the control and PLLA and PLLAP(BSTES)2 polymeric films showed that, after 1 and 3 days of culture, there is no significant difference between cell viability on PLLAP(BSTES)2 and the polystyrene control, while viability is significantly higher on PLLA. After 7 days, the viability on the polystyrene control is very similar to that on PLLA, with a quicker growth with respect to that on polymeric films. Although viability on PLLAP(BSTES)2 after 7 days is lower with respect to other samples, there is an evident growth from day 1, meaning that PLLAP(BSTES)2, even though does not promote cell adhesion like PLLA, favors instead cell proliferation. On the other hand, PLLA seems to promote better adhesion with respect to other materials, with a worse behaviour in terms of proliferation with respect to both the control and the copolymer.

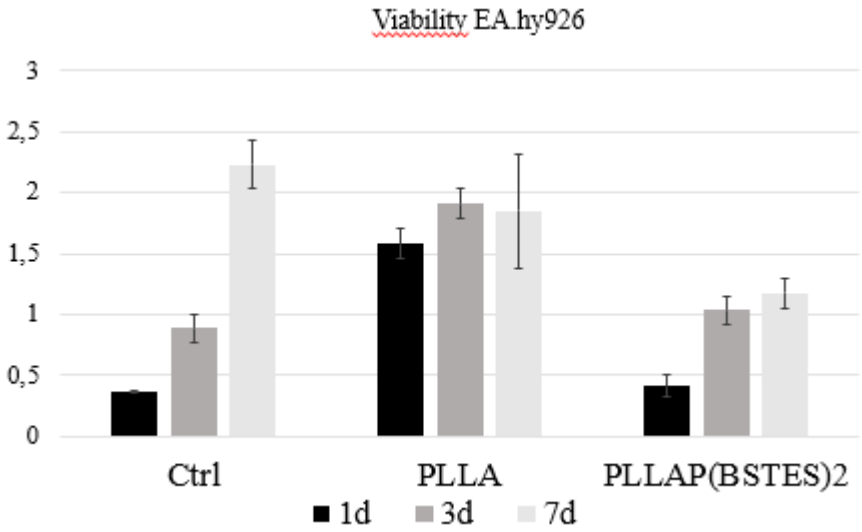

Figure 4.103. Viability data after 1,3 and 7 days of proliferation of cells grown on PLLA and PLLAP(BSTES)2, compared to the control.

In order to investigate cell morphology, phalloidin staining was used after 1, 3 and 7 days of proliferation. As it can be seen from Figure 4.104, at each time point there is no significative morphological difference in cells seeded on the polymers compared to those seeded on glass controls.

In addition, already after 3 days of culture all the cells reach full confluence, mimicking an endothelial layer and confirming a good proliferation rate on both PLLA and PLLAP(BSTES)2.

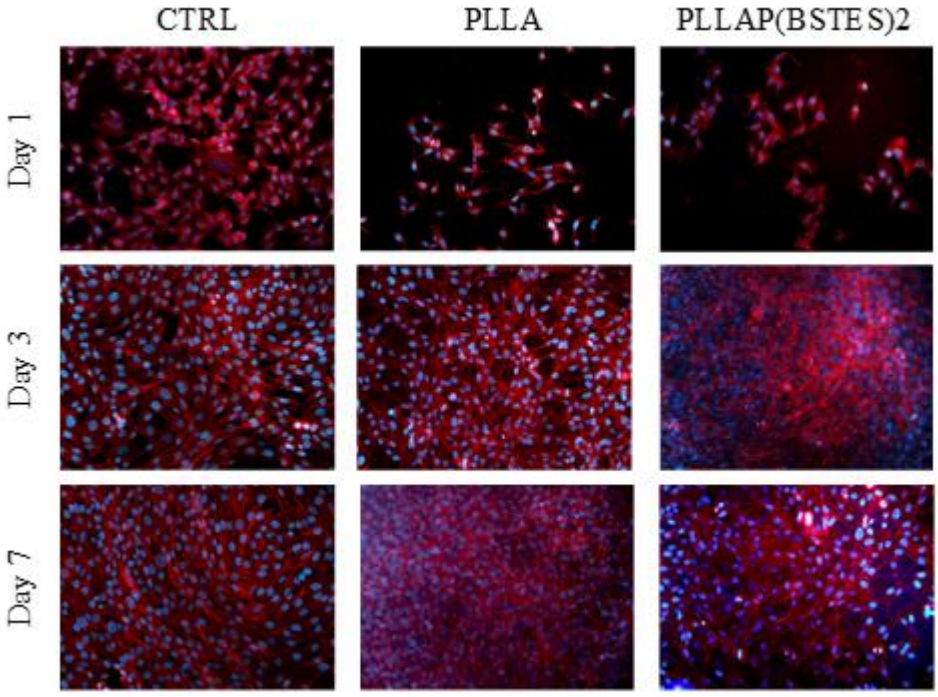

Figure 4.104. Phalloidin staining after 1, 3 and 7 days of proliferation on cells grown on PLLA and PLLAP(BSTES)2, compared to the control.

4.11.6 Conclusions

A novel high molecular weight PLLA-based aliphatic copolyester, PLLAP(BSTES), characterized by an A-B-A triblock architecture, has been *ad hoc* designed and successfully synthesized. The side A block consists of PLLA, whereas the central B block is an aliphatic statistical "PEG-like" copolymer based on PBS and PTES co-units. To achieve a high molecular weight, that guarantees good mechanical properties, hexamethylene diisocyanate (HDI) has been employed as chain extender.

The so-obtained copolymer was subjected to two different thermal treatments, which turned out to be effective in favouring the selective formation of different main crystalline phases, PBS and PLLA ones, respectively.

Aim of the work was to evaluate the effect of both copolymerization and thermal treatment on some functional properties and biocompatibility, in order to explore the possible applications in vascular tissue engineering.

Copolymerization revealed to be an efficient tool to significantly improve mechanical properties and degradation rate of PLLA homopolymer. In fact, it was possible to obtain thermoplastic elastomeric copolymers with a significative lower elastic modulus and higher elongation at break, characterized also by faster biodegradabilition rate under physiological conditions.

As to annealing treatment, it turned out to be a further efficient mean to tailor the final material properties, mainly the mechanical ones. In particular, through the second annealing treatment it was possible to improve further the elastomeric behavior of the copolymer, in terms of higher flexibility and lower hysteresis. As to the degradation process, even though the kinetics profile is not significantly influenced by the thermal treatment, this last is responsible for a different degradation mechanism. In addition, copolymerization did not negatively affect the biocompatibility, which was confirmed also for PLLAP(BSTES)2.

To conclude, annealing can be considered a valid alternative to modulate the final properties of a material, without changing neither chemical structure nor molecular architecture.

5.CONCLUSIONS

In the present PhD Thesis novel bio-based aliphatic and aromatic polyesters for applications in different fields such as flexible food packaging, soft tissue engineering and controlled drug release, have been successfully synthesized, by employing exclusively synthetic processes which were eco-friendly, i.e. solvent free, simple, and cost-effective and therefore easily scalable at industrial level. These new materials were obtained following two general approaches: *i)* through chemical modification of polyesters, possibly available on the market and already used for this kind of applications, such as PLA, PBS and furan-based aromatic polyesters; *ii)* alternatively, through the synthesis of new polymers starting from bio-based building blocks, like 1,4-cyclohexanedicarboxylic acid and 2,5-thiophenedicarboxylic acid.

The first strategy was necessary due to the fact that generally a polymer does not fulfil all the requirements needed for a specific application. In this view, copolymerization turned out to be a particularly effective tool to tailor *ad hoc* functional properties, improving the no optimal ones, without compromising those already satisfactory.

Of course, the new materials obtained through the second strategy, when no optimal for a specific application, have been also copolymerized to tune the final properties for the intended use.

The research activities carried out in the present Thesis have led to results of relevant academic as well as industrial importance. The main general result concerns the great versatility of the class of bio-polyesters, which can cover a wide range of different applications, from biomedicine to flexible food packaging. Several kinds of polymers are generally needed in order to fulfil the wide plethora of applications that plastics can cover. In this framework, the results obtained in the present research project are considerably outstanding: in fact, with only one class of high performing materials it was possible to cover very different fields such as flexible food packaging, soft tissue engineering and controlled drug release.

More specifically, according to the results obtained, solid-state properties have been nicely tailored acting on chemical structure as well as molecular architecture. As to the former tool, the introduction of short/long ramifications along the main chain, of different heterocyclic rings (furan vs. thiophene) and of flexible glycol sub-unit characterized by different length revealed to be very effective in changing in a controlled way some polymer final properties, like flexibility, biodegradation rate, mechanical and barrier performance. The molecular architecture, i.e. the distribution of comonomeric units, which was random, multiblock and triblock, also played a key role in determining the final polymer properties.

As to flexible food packaging application, the aliphatic copolyesters object of the present Thesis were characterized by good barrier properties, comparable or even better than those of LDPE and PLA. The aromatic furan- and thiophene-ring containing polyesters turned out to be however the best performing, with permeability values considerably lower than those of PET and PEF. This behaviour was ascribed to a 2D-ordered phase, generally defined as mesophase, whose influence on functional properties was deeply investigated. Eco-flex like aromatic/aliphatic copolyesters revealed to be particularly interesting as example of compostable flexible sustainable films.

As far as the biomedical field is concerned, PLLA- and PBS-based micro and nanoparticle were obtained for applications in controlled drug delivery: drug release experiments proved that release kinetics can be nicely tailored by acting on chemical structure, molecular architecture as well as on particle size. In addition, both PLLA-based triblock copolymeric films and PBS-based electrospun scaffolds turned out to be very promising for applications in soft tissue engineering: through copolymerization it was possible to prepare biocompatible thermoplastic elastomers, characterized by elastic modulus very close to cardiac one. Pluripotent stem cells showed even differentiation towards the cardiac phenotype.

Of course, the results herein presented, although very attractive, represent only a starting point: upscalability of the synthetic processes employed has to be tested and deeper investigation of the so-obtained polyesters is needed. As to packaging field, studies focused on the interactions with food and aimed at evaluating the ecotoxicity impact are necessary. As far as regenerative medicine is concerned, *in vivo* tests are mandatory to address the real utilization of a new material in this field.

References

A Plastic Bag Free World: www.plasticbagfreeday.org, 2018.

Abou-Zeid D.M., Muller R.J., Deckwer W.D, Biomacromolecules, 2004, 5, 1687.

Albertsson A.C., Varma, I.K., *Advances in Polymer Science*, Springer-Verlag Berlin Heidelberg, **2002**, 157.

Albertsson A.C., Srivastava R.K., *Advanced Drug Delivery Reviews*, **2008**, 1077.

Allen G., Bevington J.C., in *Comprehensive Polymer Science: the synthesis, characterization, reactions & applications of polymers*, Oxford, Pergamon Press, **1989**, Vol. 5, Chap. 17.

Allegra G., Marchessault R.H., Bloembergen S.J., *Polymer Science, Part B: Polymer Physics*, **1992**, 30, 809.

Amanatidou A., Slump R.A., Gorris L.G.M., Smid E. J., *Journal of Food Science;* **2000,** 65, 61.

Anderson C.R., Gambinossi F., DiLillo K.M., Laschewsky A., Wischerhoff E., Ferri J.K., Sefcik L.S., *Journal of Biomedical Material Research Part A*, **2017**, 105, 2416.

Andronova N., Albertsson A.C., *Biomacromolecules*, **2006**, 7, 1489.

Araujo C.F., Nolasco M.M., Ribeiro-Claro P.J.A., Rudić S., Silvestre A.J.D., Vaz P.D., Sousa A.F., *Macromolecules*, **2018**, 51, 3515.

Avantium: www.Avantium.com

Azevedo H.S., Reis R.L., in *Biodegradable Systems in Tissue Engineering and Regenerative Medicine*, Reis R.L., Roman J.S., Eds., CRC Press, Boca Ratón, FL (USA), **2004**, pp. 177–201.

Babensee J.E., Anderson J.M., McIntire L.V., Mikosa A.G., *Advanced Drug Delivery Reviews*, **1998**, 33,111.

Bajpai A.K., Shukla S.K., Bhanu S., Kankane S., *Progress in Polymer Science*, **2008**, 33, 1088.

Barry-Ryan C., O'Beirne D., *International Journal of Food Science + Technology*, **2000**, 35, 243. (a)

Barry-Ryan C., Pacussi J. M., O'Beirne D., *Journal of Food Science,* **2000,** 65, 726. (b)

BASF: product-finder.basf.com/group/corporate/productfinder/en/brand/ECOFLEX

Bastioli C., *Handbook of Biodegradable Polymers*, Rapra Technology, Crewe (UK), **2005**.

Baur V.H., *Makromolekulare Chemie*, **1966**, 98, 297.

BCC Research: https://www.bccresearch.com

Being wise with waste: the EU's approach to waste management, **2010**, Publications Office of the European Union, Luxembourg, **2010** (http://europa.eu).

Berti C., Colonna M., Finelli L., Lorenzetti C., Lotti N., Vannini M., Macromolecular Chemistry and Physics, **2004**, 205, 2473.

Berti C., Binassi E, Celli A., Colonna M., Fiorini M., Marchese P., Marianucci E., Gazzano M., Di Credico F., Brunelle D.J., *Journal of Polymer Science Part B, Polymer Physics*, **2008**, 46, 619. (a)

Berti C., Celli A., Marchese P., Marianucci E., Barbiroli G., Di Credico F., *Macromolecular Chemistry and Physics*, **2008**, 209, 1333. (b)

Berti C., Binassi E., Colonna M., Fiorini M., Kannan G., Kanaram S., Mazzacurati M., *Bio-Based Terephthalate Polyesters*, US 20100168461 A1, **2010**.

Bikiaris D.N, Achilias D.S., Polymer, **2008**, 49, 3677. (a)

Bikiaris D.N., Papageorgiu G.Z., Gillopoulos D.J., Stergiou C.A., *Macromolecular Bioscience*, **2008**, 8, 728. (b)

Blumstein A., Thomas O., Macromolecules, **1982**, 15, 1264.

Boland E.L., Shine R., Kelly N., Sweeney C.A., McHugh P.E., *Annals of Biomedical Engineering*, **2016**, 44, 341.

British Plastics Federation: http://www.bpf.co.uk/plastipedia/plastics_history/Default.aspx

Burgess S.K., Karvan O., Johnson J.R., Kriegel R.M., Koros W.J., *Polymer*, **2014**, 55, 4748.

Burgess S.K., Leisen J.E., Kraftschik B.E., Mubarak C.R., Kriegel R.M., Koros W.J., *Macromolecules*, **2014**, 47, 1383. (b)

Burgess S.K., Kriegel R.M., Koros W.J., *Macromolecules*, **2015**, 48, 2184.

Carothers W.H., *Journal of the American Chemical Society*, **1929**, 51, 2548.

Carothers W.H., *Chemical Reviews*, **1931**, 8, 353.

Carothers W.H., *Transactions of the Faraday Society*, **1936**, 32.

Catro G., Panilaitis B., Kaplan D., *Bioresource Technology*, **2008**, 99, 4566.

Cavallo D., Azzurri F., Floris R., Alfonso G.C., Balzano L., Peters G.W., *Macromolecules*, **2010**, 43, 2890.

Chandrasekhar S., *Liquid Crystals*, Cambridge University Press, Cambridge, UK, **1992**.

Chen C.C., White J.L.; *Polymer Engineering & Science*, **1993**, 33, 923.

Chen Q., Bismarck A., Hansen U., Junaid S., Tran M.Q., Harding S.E., Ali N.N., Boccaccini R., *Biomaterials*, **2008**, 29, 47.

Chen H.B., Wang X.L., Zeng J.B., Li L.L., Dong F.X., Wang Y.Z., *Industrial & Engineering Chemistry Research*, **2011**, 50, 2065.

Chen G.Q., Patel M.K., *Chemical Reviews*, **2012**, 112, 2082.

Chiou J. S., Paul D. R., *Journal of Polymer Science*, **1987**, 25, 1699.

Chrissafis K., Paraskevopoulos K.M., Bikiaris D.N., *Thermochimica Acta*, **2005**, 435, 142.

Chrissafis K., Paraskevopoulos K.M., Bikiaris D.N., *Thermochimica Acta*, **2006**, 440, 166.

Clegg W., *X-ray Crystallography*, 2nd ed., Oxford Chemistry Primers, Oxford, UK, **2015**.

Codou A., Guigo N., Van Berkel J., Jong E.D., Sbirrazzuoli N., *Macromolecular chemistry and physics*, **2015**, 215, 2065.

Cohn D., Lando G., Sosnik A., Garty S., Levi A., *Biomaterials*, **2006**, 27, 1718.

Compost Council of Canada: www.compost.org

Conn R.E., Kolstad J.J., Borzelleca J.F., Dixler D.S., Filer Jr. L.J., LaDu Jr. B.N., Pariza M.W., *Food and Chemical Toxicology*, **1995**, 33, 273.

Controlled Release Society: http://www.controlledreleasesociety.org

Cooper T.A., SPE FlexPackCon, **2017**.

Darney P.D., Monroe S.E., Klaisle C.M., Alvarado A., *American Journal of Obstetrics & Gynecology*, **1989**, 160, 1292.

De Azeredo H.M.C., *Food Research International*, **2009**, 42, 1240.

De La Cruz G.O., Nardone G., Vrbský1 J., Melajová1 K., Martini C., Caluori G., Pagliari S., Martino F., Stokin G.B., Forte G., *European Cells and Materials*, **2017**, 33.

De Winter J.C.F, *Practical Assessment Research & Evaluation*, **2013**, 18.

Diaz A., Katsarava R., Puiggalí J., *International Journal of Molecular Sciences*, **2014**, 15, 7064.

Dominguez de Maria P., *Industrial Biorenewables: A Practical Viewpoint*, John Wiley & Sons, Hoboken (New Jersey), **2016**.

Drumright R.E., Gruber P.R., Henton D.E., *Advanced Materials*, **2000**, 12, 1841.

Duda A., Penczek S., *Biopolymers*, Wiley-VCH, Weinheim (Germany), Vol. 3b, Ch.12, **2002**.

Duda J.L., Zielinski J.M., in *Diffusion in Polymers*, Neogi P. editor, Marcel Dekker, New York (N.Y), pp. 143–171, **1996**.

Eisenberg A., *Physical Properties of Polymers*, ACS, Washington, DC, **1984**.

Elisseeff J.H., Yamada Y., Langer R., in *Tissue Engineering and Biodegradable Equivalents Scientific and Clinical Applications*, Marcel Dekker Editors New York (N.Y.), **2002**.

EN 13.432, *Packaging –Requirements for Packaging Recoverable Through Composting And Biodegradation-Test Scheme and Evaluation Criteria for the Final Acceptance of Packaging, European Standard.* European Committee for Standardization, Brussels (Belgium), **2005**.

Endo T., in *Handbook of Ring-Opening Polymerization*, Dubois P., Coulembier O., Raquez J.M. eds., Wiley-VCH Verlag GmbH & Co. KGaA, **2009**.

European Bioplastics: www.european-bioplastics.org/market, **2017**.

Fabbri M., Gigli M., Gamberini R., Lotti N., Gazzano M., Rimini B., Munari A., *Polymer Degradation and Stability*, **2014**, 108, 223.

Fabbri M., Soccio M., Gigli M., Guidotti G., Gamberini R., Gazzano M., Siracusa V., Rimini B., Lotti N., Munari A., *Polymer*, **2016**, 83, 154.

Fabbri M., Guidotti G., Soccio M., Lotti N., Govoni M., Giordano E., Gazzano M., Gamberini R., Rimini B., Munari A., *Polymer Degradation and Stability*, **2018**, 153, 53.

Farber J.N., Harris L.J., Parish M.E., Beuchat L.R., Suslow T.V., Gorney J.R., Garrett E.H., Busta F.F., *Comprehensive Reviews in Food Science and Food Safety*, **2003**, 2, 142.

Flexible Packaging: state of the industry report, **2017**.

Flory P.J., *The Journal of Chemical Physics*, **1947**, 15, 684.

Fu S., Sanders E.S., Kulkami S.S., Wenz G.B., Koros W.J., *Carbon*, **2015**, 95, 995.

Fu Y., Kao W.J., *Expert Opinion on Drug Delivery*, **2010**, 7, 429.

Fujimaki T., *Polymer Degradation and Stability*, **1998**, 59, 209.

Gas Permeability Testing Manual, Registergericht Munchen HRB 77020, Brugger Feinmechanik GmbH, **2008**.

Genovese L., Gigli M., Lotti N., Gazzano M., Siracusa V., Munari A., Dalla Rosa M., *Industrial & Engineering Chemistry Research*, **2014**, 53, 10965.

Genovese L., Lotti N., Gazzano M., Finelli L., Munari A., *Express Polymer Letters*, **2015**, 9, 972.

Genovese L., Lotti N., Gazzano M., Siracusa V., Dalla Rosa M., Munari A., *Polymer Degradation and Stability*, **2016**, 132, 191.

Genovese L., Soccio M., Lotti N., Munari A., Szymczyk A., Paszkiewicz S., Linares A., Nogales A. Ezquerra T.A., *Physical Chemistry Chemical Physics*, **2018**, 20, 15696.

George S.M., Puglia D., Kenny J.M., Causin V., Parameswaranpillai J., Thomas S., *Industrial & Engineering Chemistry Research*, **2013**, 52, 9121.

Geyer R., Jambeck J.R., Lavender Law K., *Science Advances*, **2017**, 3: e1700782.

Gigli M., Negroni A., Soccio M., Zanaroli G., Lotti N., Fava F., Munari A., *Green Chemistry*, **2012**, 14, 2885. (a)

Gigli M., Lotti N., Gazzano M., Finelli L., Munari A., *Reactive and Functional Polymers*, **2012**, 72, 303. (b)

Gigli M., Lotti N., Gazzano M., Siracusa V., Finelli L., Munari A., Dalla Rosa M., *Industrial & Engineering Chemistry Research*, **2013**, 52, 12876. (a)

Gigli M., Negroni A., Zanaroli G., Lotti N., Fava F., Munari A, *Reactive and Functional Polymers*, **2013**, 73, 764. (b)

Gigli M., Lotti N., Vercellino M., Visai L., Munari A., *Materials Science and Engineering C*, **2014**, 34, 86. (a)

Gigli M., Lotti N., Gazzano M., Siracusa V., Finelli L., Munari A., Dalla Rosa M., *Polymer Degradation and Stability*, **2014**, 105, 96. (b)

Gigli M., Fabbri M., Lotti N., Gamberini R., Rimini B., Munari A.; *European Polymer Journal*, **2016**, 75, 431.

Gomes M., Gandini A., Silvestre A.J.D., Reis B., *Polymer Chemistry*, **2011**, 49, 3759.

Gopalakrishnan P., Narayan-Sarathy S., Ghosh T., Mahajan K., Belgacem M.N., *Physical Chemistry Chemical Physics*, **2013**, 16, 7946.

Göpferich A., *Biomaterials*, **1996**, 17, 103.

Govoni M., Bonavita F., Shantz L.M., Guarnieri G., Giordano E., *Amino Acids*, **2010**, 38, 541.

Govoni M., Berardi A.C., Muscari C., Campardelli R., Bonafè F., Guarnieri C., Reverchon E., Giordano E., Maffulli N., Della Porta G., *Tissue Engineering Part A*, **2017**, 23, 811.

Grassi M., Grassi G., *Current Drug Delivery*, **2005**, 29, 116.

Grima S., Bellon-Maurel V., Feuilloley P., Silvestre F., *Journal of Polymers and the Environment*, **2002**, 8, 183.

Gross R.A., Kalra B.; *Science*, **2002**, 297, 803.

Gross R.A., Ganesh M., Lu W., *Trends in Biotechnology*, **2010**, 28, 435.

Gualandi C., Soccio M., Saino E., Focarete M.L., Lotti N., Munari A., Moroni L., Visai L., *Soft Matter*, **2012**,8, 5466. (a)

Gualandi C., Soccio M., Govoni M., Valente S., Lotti N., Munari A., Giordano E., Pasquinelli G., Focarete M.L., *Journal of Bioactive and Compatible Polymers*, **2012**, 27, 244. (b)

Gualandi C., Govoni M., Foroni L., Valente S., Bianchi M., Giordano E., Pasquinelli G., Biscarini F., Focarete M.L., *European Polymer Journal*, **2012**, 48, 2008. (c)

Guidotti G., Soccio M., Siracusa V., Gazzano M., Salatelli E., Munari A., Lotti N., *Polymers*, **2017**, 9, 724.

Guidotti G., Soccio M., Siracusa V., Gazzano M., Munari A., Lotti N., *Polymers*, **2018**, 10, 866. (a)

Guidotti G., Soccio M., Lotti N., Gazzano M., Siracusa V., Munari A., *Polymers*, **2018**, 10, 785. (b)

Guidotti G., Gigli M., Soccio M., Lotti N., Gazzano M., Siracusa V., Munari A., *Polymers*, **2018**, 10, 167. (c)

Guidotti G., Gigli M., Soccio M., Lotti N., Gazzano M., Siracusa V., Munari A., *European Polymer Journal*, **2018**, 106, 284. (d)

Hakkarainen M., *Advance in Polymer Science*, **2002**, 157, 113.

Hamad K., Kaseem M., Yang H.W., Deri F., Ko Y.G., *eXPRESS Polymer Letters*, **2015**, 9, 435.

Harmand M.F., in *Biocompatibility Assessment of Medical Devices and Materials*, Braybrook J.H. Ed., John Wiley & Sons, New York (N.Y.), **1999**.

Hedenqvist M.S., in: M. Kutz, *Handbook of Environmental Degradation of Materials*, Elsevier Inc., 2nd ed., **2012**, pp. 833-862.

Helfland E., Lauritzen J.I., *Macromolecules*, **1973**, 6, 631.

Hillmyer M.A., Tolman W.B., *Accounts of Chemical Research*, **2014**, 47, 2390.

Holden G., Legge N.R., Zuirk R.P., Schroeder H.E., *Thermoplastic Elastomers, 2nd edition*, Hanser Gardner Pubns, Cincinnati, Ohio (U.S.A), **1996**.

Howe-Grant M., *Kirk-Othmer Encyclopedia of chemical technology*, John Wiley & Sons, New York (NY), **1991**.

Hotchkiss J.H., in: *Active Food Packaging*, Springer US, Chapter 18, **1995**.

Hu Y.S., Prattipati V., Mehta S., Schiraldi D., *Polymer*, **2005**, 46, 2685.

Hutmacher D.W., *Biomaterials*, **2000**, 21, 2529.

Ichikawa Y., Kondo H., Igarashi Y., Noguchi K., Okuyama K., Washiyama J., *Polymer*, **2000**, 41, 4719.

Ichikawa Y., Kondo H., Igarashi Y., Noguchi K., Okuyama K., Washiyama J., *Polymer*, **2001**, 42, 847; corrigendum to *Polymer*, **2000**, 41, 4719.

Ihn K.J., Yoo E.S., Im S.S., *Macromolecules*, **1995**, 28, 2460.

Ikada Y., Tsuji H., *Macromolecular Rapid Communications*, **2000**, 21, 117.

Ioakeimidis C., Galgani F., Papatheodorou G., in *Hazardous Chemicals Associated with Plastics in the Marine Environment*, Takada H., Karapanagioti H.K. eds., Springer International Publishing, **2017**, pp.93-120.

ISO 1997, *Biological evaluation of Medical devices- Part I: evaluation and testing. International Organization for Standardization*, Geneva (Switzerland).

Jacquel N., Saint-Loup R., Pascault J.P., Rousseau A., Fenouillot F., Polymer, **2015**, 59, 234.

Jalil R., Nixon J.R., *Journal of Microencapsulation*, **1990**, 7, 297.

Jamshidian M., Tehrany E.A., Cleymand F., Leconte S., Falher T., Desobry S., *Carbohydrates Polymers*, **2012**, 87, 1763.

Jang J, Hak Oh J., *Polymer*, **1999**, 40, 5985.

Jérôme C., Lecomte P., *Advanced Drug Delivery Reviews*, **2008**, 60, 1056.

Jiang H.L., Fang D.F., Hsiao B.J., Chu B.J., Chen W.L., *Journal of Biomaterials Science*, **2004**, 15, 279.

Jiang R., Quirk R.P., White J.L., Min K., *Polymer Engineering & Science*, **1991**, 31, 1545.

Jin H., Lee B.Y, Kim M.N., Yoon J.S., *Journal of Polymer Science, Part B, Polymer Physics*, **2000**, 38, 1504.

Jiang M., Liu Q., Zhang Q., Ye C., Zhou G., *Journal of Polymer Science Part A Polymer Chemistry*, **2012**, 50, 1026.

Karavelidis V., Giliopoulos D., Karavas E., Bikiaris D., *European Journal of Pharmaceutical Sciences*, **2010**, 41, 636.

Keum J. K., Kim J., Lee S.M., Song H.H., Son Y.K., Choi J.I., Im S.S., *Macromolecules*, **2003**, 36, 9873.

Ki H.C., Park O.O., *Polymer*, **2001**, 42, 1849.

Kim Y.J., Park O.O., *Journal of Applied Polymer Science*, **1999**, 72, 945.

Kint D., Alla A., Deloret E., Campos J.L., Munoz Guerra S., *Polymer*, **2003**, 44, 1321.

Komatsuka T., Nagai K., *Polymer Journal*, **2009**, 41, 455.

Kong Y., Hay J.N., *Polymer*, **2003**, 44, 623.

Kootstra M., Elissen H., Huurman S., ACRRES - Wageningen UR, **2017**. http://edepot.wur.nl/414011

Kricheldorf H.R., Stöber O., Lubbers D., *Macromolecules*, **1995**, 28, 2118.

Krigbaum W.R., Watanabe J., Ishikawa T., *Macromolecules*, **1983**, 16, 1271.

Lagaron J.M., Catala R., Gavara R., *Materials Science and Technology*, **2004**, 20, 1.

Lammers P., Kromer K., in*Proceeding of **2002** Annual International Meeting, ASAE Paper*, **2002**, ASAE Paper No. 026167, Chicago, Illinois, ASAE.

Landel R.F., Nielsen L.E., *Mechanical Properties of Polymers and Composites*, Second Edition, Taylor & Francis Group, **1993**, Boca Raton, Chap. 1-2.

Langer R.S., Wise D.L., *Medical applications of controlled released applications and evaluation*, CRC Press, **1984**, Boca Raton, FL, Vol I & II.

Langer R., Vacanti J., *Science*, **1993**, 260, 920.

Langer R., *Nature*, **1998**, 392, 5.

Lasprilla A.J.R., Martinez G.A.R., Lunelli B.H., Jardini A.L., Filho R.M., *Biotechnology Advances*, **2012**, 30, 321.

Lebreton L., Slat B., Ferrari F., Sainte-Rose B., Aitken J., Marthouse R., Hajbane S., Cunsolo S., Schwarz A., Levivier A., Noble K., Debeljak P., Maral H., Schoeneich-Argent R., Brambini R., Reisser J., *Scientific Reports*, **2018**, 8, 4666.

Lee S.H., Lim S.W., Lee K.H., *Polymer International*, **1999**, 48, 861.

Legras R., Dekoninck J.M., Vanzieleghem A., Mercier J.P., Nield E., *Polymer*, **1986**, 27, 109.

Leja K., Lewandowicz G., *Polish Journal of Environmental Studies*, **2010**, 19, 255.

Lensen D., Breukelen K.V., Vriezema D.M., Hest J.C.M.V.; *Macromolecular Bioscience*, **2010**, 10, 475.

Liu Z., in *Innovations in food packaging*, Elsevier, Amsterdam (Netherlands), **2005**, pp 318-337.

Lodge T.P., *Macromolecular Chemistry and Physics*, **2003**, 204, 265.

Lofgren A., Albertsson A.C., Dubois P., Jerome R., *Journal of Macromolecular Science – Reviews in Macromolecular Chemistry and Physics*, **1995**, 35, 379.

Lotti N., Munari A., Gigli M., Gazzano M., Tsanaktsis V., Bikiaris D.N., Papageorgiou G.Z., *Polymer*, **2016**, 103, 288.

Louhimies S., *Alternatives to Laboratory Animals*, **2002**, 30, 217.

Lourenço A.V., *Annales de Chimie et de Physique*, **1863**, 67 (3).

Lucas N., Bienaime C., Belloy C., Queneudec M., Silvestre F., Nava-Saucedo J.E. *Chemosphere*, **2008**, 73, 429.

Lutolf M.P., Hubbell J.A., *Nature Biotechnology*, **2005**, 23, 47.

Lv R., Na B., Tian N., Zou S., Li Z., Jiang S., *Polymer*, **2011**, 52, 4979.

Lv R., Zou S., Na B., Deng H., Yu Z., *Polymer Engineering & Science*, **2013**, 53, 2568.

Ma J., Yu X., Xu, J., Pang Y., *Polymer*, **2012**, 53, 4145.

Madhavan Nampoothiri K., Rajendran Nair N. John R.P., *Bioresource Technology*, **2010**, 101, 8493.

Marsh K.S., Bugusu B., *Journal of Food Science*, **2007**, 72, 39.

Marten E, Muller R.J., Deckwer W.D., *Polymer Degradation and Stability*, **2003**, 80, 485.

Matos M., Sousa A.F, Fonseca A.C., Freire C.S.R., Coelho J.F.J., Silvestre A.J.D., *Macromolecular Chemistry and Physics*, **2014**, 215, 2175.

Mazollier C., Taullet A., *Alter. Agri.*, **2003**, *59*, 10.

Melo F.C., F. de Souza F., Coutinho, P.L.A., O. de Souza M., *Journal of the Brazilian Chemical Society*, **2014**, 25, 12, 2378.

Mensitieri G., Di Maio E., Buonocore G.G., Nedi I., Oliviero M., Sansone L., Iannace S., *Trends in Food Science & Technology*, **2011**, 22, 72.

Michaels A.S., Vieth W.R., Barrie J.A., *Journal of Applied Physics*, **1963**, 34, 13.

Minakov A.A., Mordvinsted D.A., Schick C., *Polymer*, **2004**, 45, 3755.

Minelli M., Sarti G.C., Gas Transport in Glassy Polymers: Prediction of Diffusional Time Lag, *Membranes*, **2018**, 8, 8.

Mitsubishi Chemical: https://www.mcpp-global.com/en/mcpp-english-europe/products/brand/biopbsTM

Mo F.E., Lau L.F., *Circulation Research*, **2006**, 99, 961.

Mordor Intelligence, 2018: https://blog.mordorintelligence.com

Muller R.J., Kleeberg I., Deckwer W.D. *Journal of Biotechnology*, **2001**, 86, 87.

Muller R.J., Schrader H., Profe J., Dresler K., Deckwer W.D., *Macromolecular Rapid Communications*, **2005**, 26, 1400.

Muller R.J., *Process Biochemistry*, **2006**, 41, 2124.

Müller A.J., Balsamo V., Arnal M.L., *Lecture Notes in Physics*, **2007**, 714, 229.

Myriant Corporation: www.myriant.com

Nagata M., Goto H., Sakai W., Tsutsumi N., *Polymer*, **2000**, 41, 4373.

Nakajima H., Dijkstra P., Loos K., *Polymers*, **2017**, 9, 523.

Nair L.S., Laurencin C.T., *Progress in Polymer Science*, **2007**, 32, 762.

Novamont, 2016: www.novamont.com/leggi-comunicato-stampa/mater-biotech

Novamont e Genomatica alleati nel bioBDO, 2011: https://www.polimerica.it/articolo.asp?id=8890

Novepha; www.novepha.com

O'Brien F.J., Harley B.A., Yannas I.V., Gibson L.J., *Biomaterials*, **2005**, 26, 433.

Ohlsson T., Bengtsson N., *Minimal Processing Technologies in the Food Industry*, 1st ed. CRC Press, Washington, DC, **2002**.

Okada, M., *Progress in Polymer Science*, **2002**, 27, 87.

Owen S.C., Shoichet, M.S., *Journal of Biomedical Materials Research. Part A*, **2010**, 94, 1321.

Pankaj S.K., Bueno-Ferrer C., Misra N.N., O'Neill L., Jiménez A., Bourke P., Cullen P.J., *Innovative Food Science and Emerging Technologies*, **2014**, 21, 107.

Papadimitriou S., Bikiaris D.N., Chrissafis K., Paraskevopoulos K.M., Mourtas S., *Journal of Polymer Science Part A. Polymer Chemistry*, **2007**, 45, 5076.

Papageorgiou G.Z., Bikiaris D.N., *Biomacromolecules*, **2007**, 8, 2437.

Papageorgiou G.Z., Papageorgiou D.G., Terzopoulou Z., Bikiaris D.N., *European Polymer Journal*, **2016**, 83, 202.

Pasha I., Saeed F., Tauseef Sultan M. Rafiq Khan M., Rohi M. *Critical Reviews in Food Science and Nutrition*, **2014**, 54, 340.

Pasini A., Bonafè F., Govoni M., Guarnieri C., Morselli P.G., Sharma H.G., Caldarera C.M., Muscari C., Giordano E., *Cell Biochemistry and Biophysics*, **2013**, 67, 255.

Pathak V.M., Navneet, *Bioresources and Bioprocessing*, **2017**, 4, 15.

Paul D.R., in *Functional Polymers*, Bergbreiter D.E., Martin C.R. eds., Plenum Press, New York, **1989**.

Pawar R.P., Tekale S.U., Shisodia S.U., Totre J.T., Domb A.J., *Recent Patents on Regenerative Medicine*, **2014**, 4, 40.

Plastics – the Facts 2017 An analysis of European plastics production, demand and waste data www.plasticseurope.org

Plastic Change: https://plasticchange.dk/wcd2018/world-cleanup-day-2018.html

PSC Cardiomyocyte Differentiation Kit Prototype
https://tools.thermofisher.com/content/sfs/manuals/PSC_Cardiomyocyte_Diff_Kit_QR.pdf

Rabinovitch E., *Transactions of the Faraday Society*, **1937**, 33, 1225.

Ran S., Wang Z., Burger C., Chu B., Hsiao B.S., *Macromolecules*, **2002**, 35, 10102.

Reneker D.H., Yarin A.L., Fong H., Koombhongse S., *Journal of Applied Physics*, **2000**, 87, 4531.

Robertson G.L., in *Food Packaging: Principles and Practice*, 3rd ed., Taylor & Francis Group, Boca Raton, FL (USA), **2013**, chapter 4, pp. 91-130.

Rudnik E., *Compostable Polymer Materials*, Elsevier, Amsterdam (Netherlands), **2008**, Chapter 2.

Russo G.M., Simon G.P., Incarnato L., *Macromolecules*, **2006**, 39, 3855.

Ryan P.G., Moore C.J., Van Franeker J.A., Moloney C.L., *Philosophical Transactions of the Royal Society B: Biological Sciences*, **2009**, 364, 1999.

Rydz J., Sikorska W., Kyulavska M., Christova D., *International Journal of Molecular Sciences*, **2015**, *16*, 564.

Sanchez I.C., Eby R.K., *Journal of research of the Notional Bureau of Standards - A. Physics and Chemistry*, **1973**, 77, 353.

Sandhya; *LWT-Food Science and Technology*, **2010**, 43, 381.

Sangeetha V.H., Harekrishna Deka, Varghese T.O., Nayak S.K., *Polymer Composites*, **2016**, 81.

Schmid M., Zillinger W., Muller K., Sangerlaub S., *Food Packaging and Shelf Life*, **2015**, 6, 21.

Scott G., *Polymer Degradation and Stability*, **2000**, 68, 1.

Shah A.A., Kato S., Shintani N., Kamini N.R., Nakajima-Kambe T., *Applied Microbiology and Biotechnology*, **2014**, 98, 3437.

Shirahama H., Kawaguchi Y., Aludin M.S., Yasuda H., *Journal of Applied Polymer Science*, **2001**, 80, 340.

Shukla S., Bajpai A.K., Bajpai J.; *Macromolecular Research*, **2003**, 11, 273.

Showa Denko: http://www.showa-denko.com

Singh A., Koros W. J., in *Polymers, Laminations & Coatings Conference*, **1998**, San Francisco, CA.

Singh B., Sharma N., *Polymer Degradation and Stability*, **2008**, 93, 561.

Siracusa V., Rocculi P., Romani S., Dalla Rosa M., *Trends in Food Science & Technology*, **2008**, 19, 634.

Siracusa V., *International Journal of Polymer Science*, **2012**, 1, 1.

Siracusa V., Lotti N., Munari A., Dalla Rosa M., *Polymer Degradation and Stability*, **2015**, 119, 35.

Siracusa V., Ingrao C., *Polymer Testing*, **2017**, 59, 277.

Siracusa V., Genovese L., Ingrao C., Munari A., Lotti N., *Polymers*, **2018**, 10, 502

Sivasamy P., Palaniandavar M., Vijayakumar C.T., Lederer K., *Polymer Degradation and Stability*, **1992**, 38, 15-21.

Smart Packaging Market Size & Share, Industry Report
https://www.grandviewresearch.com/industry-analysis/smart-packaging-market

Smith M.D. Barbenel J.C., Courtney J.M., Grant M. H., *The International Journal of Artificial Organs*, **1992**, 15, 191.

SmithersPira, **2017** https://www.smitherspira.com/resources/2017

Soccio M., Lotti, N., Finelli L., Gazzano M., Munari A., *European Polymer Journal*, **2007**, 43, 3301.

Soccio M., Lotti N., Finelli L., Gazzano M., Munari A., *Journal of Polymer Science Part B Polymer Physics*, **2008**, 46, 170.

Soccio M., Lotti N., Finelli L., Munari A., *European Polymer Journal*, **2009**, 45, 171.

Soccio M., Lotti N., Finelli L., Munari A., *e-Polymers*, **2009**, ISSN 1618-7229. (b)

Soccio M., Gazzano M., Lotti N., Finelli L., Munari A., *Polymer*, **2010**, 51, 192.

Soccio M., Lotti N., Gigli M., Finelli L., Gazzano M., Munari A., *Polymer International* **2012**, 61, 1163. (a)

Soccio M., Lotti N., Gazzano M., Govoni M., Giordano E., Munari A., *Reactive and Functional Polymers*, **2012**, 72,856. (b)

Soccio M., Lotti N., Munari A., *Journal of Thermal Analysis and Calorimetry*, **2013**, 114, 677.

Soccio M., Costa M., Lotti N., Gazzano M., Siracusa V., Salatelli E., Manaresi P., Munari A., *European Polymer Journal*, **2016**, 81, 397.

Sokolsky-Papkov M., Agashi K., Olaye A., Shakesheff K., Domb A.J., *Advanced Drug Delivery Reviews*, **2007**, 59, 187.

Sousa A.F., Vilela C., Fonseca A.C., Matos M., Freire C.S.R., Gruter G.J.M., Coelho J.F.J., Silvestre A.J.D., *Polymer Chemistry*, **2015**, 6, 5961.

Stoclet G., Seguela R., Lefebvre J.M., Rochas C., *Macromolecules*, **2010**, 43, 7228.

Sturm R.N., *Journal of the American Oil Chemists Society*, **1973**, 50, 159.

Sun Y., Fu J., *Integrative Biology*, **2013**, 5, 450.

Tharanathan R.N., *Trends in Food Science & Technology*, **2003**, 14, 71.

Tserki V., Matzinos P., Pavlidou E., Panayiotou C., *Polymer Degradation and Stability*, **2006**, 91, 377.

Tuomela M., Academic dissertation in microbiology, *Degradation of lignin and other 14C-labelled compounds in compost and soil with an emphasis on white-rot fungi*, Helsinki, **2002**.

Ulery B.D., Lakshimi S.N., Cato T.L.; *Journal of Polymer Science Part B: Polymer Physics*, **2011**, 49, 832.

UNI EN ISO 10993-5 *Biological evaluation of medical devices. Part 5: Tests for in vitro cytotoxicity*

Van der Zee M., *Structure-biodegradability relationship of polymeric material*, Dissertation University of Twente, Enschede (The Netherlands), **1997.**

Van Krevelen D.W., Te Nijenhuis K., *Properties of Polymers: Their Correlation with Chemical Structure; their Numerical Estimation and Prediction from Additive Group Contribution*, Fourth edition, **2009**, Elsevier, Amsterdam (The Netherlands), pp 383-400.

Vandewijngaarden J., Murariu M., Dubois P., Carleer R., Yperman J., Adriaensens P., Schreurs S., Lepot N., Peeters R., Buntinx M., *Journal of Polymer and the Environment*, **2014**, 22, 501.

Vannini M., Finelli L., Lotti N., Colonna M., Lorenzetti C., Munari A., *Journal of Polymer Science Part B Polymer Physics*, **2005**, 43, 1441.

Varma I.K., Albertsson A.C., Rajkhowa R., Srivastava R.K., *Progress in Polymer Science*, **2005**, 30, 949.

Vassiliou A.A., Papadimitriou S.A., Bikiaris D.N., Mattheolabakis G., Avgoustakis K., *Journal of Controlled Release*, **2010**, 148, 388.

Vert M., *Biomacromolecules*, **2005**, 6, 538.

Von Burkersroda F., Schedl L., Göpferich A., *Biomaterials*, **2002**, 23, 4221.

Vroman I., Tighzert L., *Materials*, **2009**, 2, 307.

Ward I.M., Sweeney J., *Mechanical Properties of Solid Polymers*, Third edition, Wiley, UK, **2013**, Chapter 2, pp. 19-23.

Weinkauf, D. H., Paul D. R., in *Barrier Polymers and Structures*, Koros W. J. ed., American Chemical Society, Washington, DC, **1990**, Chapter 3, pp. 60-91.

Wenbiao Z., Yonghong H., Mengmeng L., Yan L., Jiaojiao L., Jingjing Y., Ying S., *Fluid Phase Equilibria*, **2014**, 375, 110.

Wendling J., Suter U.W., *Macromolecules*, **1998**, 31, 2509.

Werpy T., Petersen G., *Top value added Chemicals from biomass Volume I: Results of screening for potential candidates from sugars and synthesis gas*, **2004**, US Department of Energy.

Wijmans J.G., Baker R.W., *Journal of Membrane Science*, **1995**, 107, 1.

Wilson C.J., Clegg R.E., Leavesley D.I., Pearcy M.J., *Tissue Engineering*, **2005**, 11, 1.

Windle A.H., Viney C., Golombok C., Donald A.M., Mitchell G.R., *Faraday Discussions of the Chemical Society*, **1985**, 79, 55.

Witt U., Muller R.J., Deckwer W.D., *Journal of Macromolecular Science Part A Pure and Applied Chemistry*, **1995**, 32, 851.

Witt U., Muller R.J., Deckwer W.D., *Macromolecular Chemistry and Physics*, **1996**, 197, 1525.

Wu B., Xu Y., Bu Z., Wu L., Li B. G., Dubois P., *Polymer*, **2014**, 55, 16.

Wu L., Mincheva R., Xu Y., Raquez J.M., Dubois P., Biomacromolecules, **2012**, 13, 2973.

Xing Y., Li X., Xu Q., Jiang Y., Yun J., Li W., *Innovative Food Science and Emerging Technologies*, **2010**, 11, 684.

Xu J., Guo B.H., *Biotechnology Journal*, **2010**, 5, 1149.

Yang J., Pan P., Hua L., Zhu B., Dong T., Inoue Y., *Macromolecules*, **2010**, 43, 8610.

Yannas I.V., Lee E., Orgill D.P., Skrabut E.M., Murphy G.F., *Proceedings of the National Academy of Science of the United States of America (PNAS)*, **1989**, 86, 933.

Yield10 Bioscience: www.yield10bio.com

Yoo E., Im S.S.; *Journal of Polymer Science Part B: Polymer Physics*, **1999**, 37, 1357.

Yoshie N., Inoue Y., You H.Y., Okui N., *Polymer*, **1994**, 35, 1931.

Žagar E., Žigon M., *Journal of Chromatography*, **2004**, 1034, 77.

Zhihua G., Hideki A., Haruhiko K., Yoshiharu D., *Biomacromolecules*, **2001**, 2, 605.

Zheng Y., Yanful E.K., *Critical Reviews in Biotechnology*, **2005**, 25, 243.

Zhou W., Zhang Y., Xu Y., Wang P., Gao L., Zhang W., Ji J., *Polymer Degradation and Stability*, **2014**, 109, 21.

Zhu J., Cai J., Xie W., Chen P.H., Gazzano M., Scandola M., Gross R.A., *Macromolecules*, **2013**, 46, 796- 804.

Zielhuis S.W., Nijsen J.F.W., Seppenwoolde J.H., Bakker C.J.G., Krijger G.C., Dullens H.F.J., Zonnenbery B.A., Rijk P.P.V., Hennink W.E., Schip A.D.V., *Biomaterials*, **2007**, 28, 4591.

Zimmermann H., Chu D.D, *Faserforsch Textiltech*., **1973**, 24, 445.

Zimmermann H., *Developments in Polymer Degradation*, Elsevier Applied Science, London, **1986**.

Acknowledgments

E così, un'altra tappa del mio percorso sta per giungere al termine. Sono stati tre anni di intenso lavoro, di fatiche ma anche di grandissime soddisfazioni, in cui ho vissuto esperienze che non pensavo di essere all'altezza di affrontare e che mi hanno arricchito tantissimo, sia dal punto di vista professionale che da quello umano. Vorrei dunque dedicare questo piccolo spazio a chi innanzitutto ha reso possibile tutto questo, e a chi mi ha accompagnato, passo dopo passo, lungo questo cammino.

Grazie alla Prof. ssa Nadia Lotti e al Prof. Andrea Munari per avermi introdotto, già a partire dalla Tesi di Laurea triennale, nell'affascinante mondo dei polimeri e nel mondo accademico in generale, per avermi dato la possibilità di intraprendere questa esperienza di Dottorato e per il loro costante aiuto, supporto e la grande esperienza: ve ne sono davvero grata.

Grazie a tutto il gruppo di ricerca, prima fra tutti la Michi, con cui ho condiviso tantissime esperienze, di lavoro e non solo, per il suo aiuto costante e preziosissimo, per aver mantenuto sempre la calma anche quando non funzionava nulla, per le chiacchiere, le confidenze e le risate tra una *meso* e l'altra (ma anche per non avermi ancora mandato a quel paese soprattutto dopo queste ultime settimane). Grazie ai miei colleghi Silvia ed Emanuele, per il loro aiuto e supporto e per aver condiviso con me tutti i momenti di alta tensione e di divertimento che solo la vita da dottorando può regalare. In bocca al lupo per il vostro futuro: andrete alla grande!

Grazie a chi del gruppo ha fatto parte, con cui ho potuto condividere solo una parte del mio percorso ma che hanno comunque lasciato un bellissimo segno: Matteo, con cui ho mosso i primi passi al DICAM come tesista, e il cui aiuto è stato e continua ad essere veramente importante, anche dalla distanza, Laura, per la sua disponibilità e per la sua dolcezza, e per la serenità che riesce a infondere anche nelle situazioni più frenetiche, Martina e Michela, con cui ho condiviso i primi mesi da Dottoranda ma che mi hanno aiutato tantissimo già a partire dalla Laurea Magistrale.

Grazie a Vilma, indispensabile per il funzionamento del DICAM, per la sua infinita disponibilità. Grazie a tutto il DICAM, perché in questo dipartimento ho conosciuto persone splendide con cui ho condiviso la vita quotidiana tra laboratori, uffici, pause pranzo e caffè.

Grazie all'esperienza e alla disponibilità della Prof. ssa Valentina Siracusa, del Dr. Massimo Gazzano, della Dr. ssa Annalisa Aluigi, con cui ho avuto il piacere e l'onore di collaborare. Un

grazie speciale al Prof. Maurilio Sampaolesi dell'università KU Leuven, alle persone squisite dello SCIL e a tutto il Sampa Group, primo fra tutti al Dr. Robin Duelen, per avermi accolta con entusiasmo, pazienza e dedizione e per avermi permesso di vivere un'esperienza di vita e professionale a dir poco entusiasmante.

Un pensiero speciale alla mia famiglia, per il loro supporto, a chi c'è stato durante i momenti veramente bui, con una parola di conforto, con la propria presenza e con il proprio esempio, ma anche quando era il momento di festeggiare per un traguardo raggiunto.

Come non ringraziare gli amici di una vita, i Ziriot Imbariagot vicini e lontani, la mia sicurezza, con cui sono letteralmente cresciuta e su cui posso sempre contare. Non sempre do il meglio di me, ma davvero vi voglio un bene infinito. Grazie anche agli amici che ho incontrato lungo questo percorso, in Primis la mia Cumpi, Ale, Vale, Gabri, Ester, Puozz, la mia ancora di salvezza con cui ho condiviso l'esperienza di vita del periodo all'estero: senza di voi la maggior parte dei sorrisi e delle belle giornate belga non ci sarebbero mai state.

Dulcis in fundo, mille volte grazie a Elia, che è diventato un punto di riferimento nella mia vita, la mia forza, il mio supporto ed il mio rifugio: grazie per l'ottimismo, la pazienza, per avermi insegnato a prendere la vita con un briciolo di ottimismo in più e per spronarmi ogni giorno a fare di meglio. Grazie per aver vissuto con me questa esperienza, per aver superato insieme la prova della distanza, che ci ha rafforzato e unito ancora di più. È bello sapere che dopo le fatiche della giornata ci sei tu ad aspettarmi.

Se oggi posso gioire di questo traguardo, è anche grazie a tutti voi.